CRANFIELD UNIVERSITY

Aws Akram Mahmood Al-AKAM

MODELLING THE AERODYNAMICS OF AN AERO-ENGINE EXHAUST SYSTEM

SCHOOL OF AEROSPACE, TRANSPORT AND MANUFACTURING

PhD

Academic Year: 2017 - 2018

Supervisor: Dr Theoklis Nikolaidis
Prof. D. G. MacManus

April 2018

CRANFIELD UNIVERSITY

SCHOOL OF AEROSPACE, TRANSPORT AND MANUFACTURING

PhD

Academic Year 2017 - 2018

Aws Akram Mahmood Al-AKAM

Modelling the Aerodynamics of an Aero-engine Exhaust System

Supervisor: Dr Theoklis Nikolaidis
Prof. D. G. MacManus
April 2018

ABSTRACT

Aero-engine design is one of the most demanding tasks when the aircraft is constructed. The selection of the engine component's size and geometrical features depends on the assurance that the losses are minimal. The exhaust system is one of the main components that noticeably affect the overall propulsion-system performance because of its central role in the thrust production. Thus, it is essential to have an accurate performance assessment of the exhaust system in early design stages of the engine. However, to select the adequate design, a wide range of geometrical configurations of the exhaust system has to be covered. This task will increase the production cost and the time occupied during the construction of the engine. Therefore, it is essential to produce an evaluation tool can calculate the engine performance accurately, before making a commitment to the final design.

This research aims to generate a tool that predicts aero-engine performance during the preliminary design stages, with high sensitivity to the effect of the geometrical parameterisation of the exhaust system. To achieve this aim, a high fidelity assessment model for the exhaust-system performance was developed employing computational fluid dynamics method. This model was utilised to build a high degree of freedom maps of the performance metrics of a basic nozzle configuration (with a plug). These maps cover a range of geometrical parameters, in terms of the nozzle contraction ratio (CR) (the ratio of the nozzle charging area to the nozzle throat area) and the plug half-angle, alongside with the variation in the nozzle pressure ratio. Furthermore, correction factors were produced to take into account the impact of the bypass nozzle jet on the core nozzle performance.

The aerodynamic interference effect between the wing and the exhaust system was also considered by correcting the engine net thrust. This was achieved by generating correction factors to the nozzle gross-thrust as a function of the engine position and the local static pressure.

The derived nozzle performance maps were used to improve the calculations for a non-dimensional engine performance model, utilising response surface methods. Furthermore, the installation correction factors were employed to recalculate the performance data of an installed engine.

Through the use of the modified performance model of the engine, a 4.0% improvement was observed in the engine's gross thrust, and reduction in the specific fuel consumption by 10%, for a high-bypass-ratio engine runs under typical cruise conditions. Moreover, the effect of the wing pressure field on the exhaust-system improved the engine net thrust by a range of 2.3% at the start of the cruise and 2.1% at the end of the cruise segment. However, the net propulsive force of the engine was lower than the net thrust by a range of 0.28% to 0.6% across the cruise segment, despite the improvement in the exhaust-system performance.

The results of this project show the importance and suitability of building an assessment model of the nozzle performance and use it to improve the engine thrust calculations. They, also, highlight the discrepancies because of the simplifications in previous nozzle characteristic representations and the installed engine performance calculations.

Keywords: Propelling-nozzle, nozzle performance metrics, nozzle parameterisation, engine-aircraft aerodynamic interference.

ACKNOWLEDGEMENTS

First and foremost I would like to thank **God** the Almighty for blessing me and guiding me through my studies. Then I would like to thank the Iraqi Ministry of Higher Education and Scientific Research and Iraqi Cultural Attaché in London, for providing me with the opportunity and support to complete my PhD.

I would like to express my greatest gratitude, respect, and admiration to my supervisors **Dr Theokolis Nikolaidis** and **Prof David G. MacManus** for their richness in knowledge, experience and commitment, which they were always prepared to share, always had time to listen and was always open to discussion.

I would like to express my gratitude to **Dr Alvise Pellegrini** for his valuable help and backing. He was such a generous person, though out sharing his knowledge and time in contributing to the project.

I would also extend my thanks to all lecturers and member of staff at the Power and Propulsion Centre. They were very friendly helpful people and open to discussion.

I must thank all my colleagues at Cranfield University and my friends for supporting me in this endeavour; you have all been great people to be associated with.

Special thanks to my Father and Mother; words cannot express how grateful I am to you. Your prayers for me were what sustained me this far. I am very thankful to my brothers and sister, as I am sure that without their encouragement, patience and support, this work would not have achieved these results.

TABLE OF CONTENTS

LIST OF FIGURES

LIST OF TABLES

LIST OF EQUATIONS

LIST OF SYMBOLS

Symbols	Meaning	Units
A	Area	[m^2]
A8	Convergent-divergent nozzle throat area	[m^2]
A9	Convergent-divergent nozzle exit area	[m^2]
C	Chord length	[m]
C_d	Discharge coefficient	[-]
C_D	Drag coefficient	[-]
C_{fg}	Gross thrust coefficient	[-]
CFL	Courant–Friedrichs–Lewy	[-]
Cl	Lift coefficient	[-]
C_p	Pressure coefficient	[-]
C_v	Velocity coefficient	[-]
d	Diameter	[m]
D	Drag force	[N]
f	Physical property of interest	-
F	Engine thrust	[N]
Fga	Engine actual thrust (Gross propulsive force)	[N]
$F_x^{'}$	Axial balance force along the engine axis	[N]
H	Computational domain height	[m]
l_{bt}	Boat-tail length	[m]
L	Lift force	[N]
$\frac{L}{D}$	Lift-drag polar	[-]
M	Mach Number	[-]
k	turbulent kinetic energy	Joules
P0	Engine in position identifier	-
P	pressure	[pa]
p	Convergence order	
p	Static pressure	[pa]
R	Radius	[m]
R	Universal gas constant	[J/kg K]

Re	Reynold's number	[-]
T	Temperature	[K]
U	Flow velocity	[m/s]
W	Computational domain width	[m]
y	Observed value	-
$\hat{y}$	Predicted value	-

	Greek symbols	
α	Aero-line slop	[degrees]
β	Cone (Plug) half angle	[degrees]
βc	Boat-tail chord angle	[degrees]
δ	Boundary layer thickness	[m]
ε	turbulent dissipation	m2/s3
θ	internal aerodynamic forces of the stream tube	[N]
Φ	external aerodynamic forces	[N]
γ	Specific heat ratio	[-]
η	span wise distance ratio	[-]
τ	Viscous shear stress	[pa]
ω	specific dissipation	1/s
Δx	Axial distance from the wing leading edge to the cowl trailing edge	[m]
Δz	Radial distance from the wing leading edge to the cowl trailing edge	[m]

LIST OF ABBREVIATIONS

Alt.	Altitude [m]
AR	Area ratio [-]
Ap	Appendix
ARC	Aeronautical Research Committee
ASME	American society of mechanical engineering

AoA	Angle of Attack [degree]
BC	Boundary conditions
BPR	Bypass ratio
corr	corrected
CFD	Computational Fluid Dynamics
CNPR	Core Nozzle Pressure Ratio [-]
CV	Cross-Validation
CRM	Common Research Model
CRM-nacelle	CRM-separated flow nozzle nacelle configuration
CAD	Computer Aid Design
CR	Contraction ratio
CST	Classic-Shape-Transformation
CD	Convergent-divergent
DP	Design-point
GCI	Grid Convergence Index
DSFR	Dual Stream Flow Reference
F-D	Thrust minus drag [N]
LDA	laser-doppler anemometer
MFCR	Mass flow capture ratio
NPR	Nozzle Pressure Ratio
NPF	Net Propulsive Force [N]
RSM	Response surface method
HBPR	high bypass ratio
LPT	Low-pressure turbine
FNPR	Fan Nozzle Pressure ratio [-]
FPR	Fan pressure ratio [-]
OD	Off-Design point
OPR	Overall pressure ratio
PAW	Propulsion Aerodynamics Workshop
RAE	Royal Aircraft Establishment
RANS	Reynold's Averaged Naiver Stock's
SA	Spalart Allmaras
SST	Shear Stress Transport

SFC	Specific fuel consumption
SW	Swept -Wing
SW-nacelle	Swept wing separated flow nozzle nacelle configuration
TET	Turbine entry temperature [K]
TFN	Through flow nacelle
TPS	Turbine Powered Simulator
UHBPR	Ultrahigh bypass ratio
VHBPR	Very high bypass ratio
WB	Wing-body no tail
WBP	Wing-body and pylon
WBPTFN	Wing-body-pylon and through flow nacelle

SUBSCRIPTIONS

1	Highlight
a	actual
ab	After-body
A/C	aircraft
c	cold
c-c	Core-cowl
CF	Correction factor
Def.(1)	Thrust definition (1)
Def.(2)	Thrust definition (2)
e	Exit
fb	forebody
h	Hot
i	ideal
iso	isolated
inst	Installed
in	Inlet
j	jet
max	Maximum

nac	nacelle
ref	reference
s	isentropic
t	Total
th	Throat
upwash	Upwash the wing leading edge
up	upstream

1 Introduction

1.1 Rationale of the project

The engine nacelle components, in particular, the intake and exhaust system, have a direct influence on the overall performance of the propulsion system. The intake and nozzles interact with the external flow field in order to provide the required operating conditions for the engine, and their performance has a direct influence on the engine cycle. Therefore, having these components properly designed is one of the main tasks the concerns the engine designer. However, to achieve the sufficient design, an adequate number of test cases have to be implemented to cover a wide range of geometrical configurations, and to have an accurate assessment to the flow interaction impact on them.

Moreover, the growing need for more fuel-efficient engines, which produce less noise and fewer emissions, has led to the demand for higher by-pass ratio aero-engines as they have high propulsive efficiency [1, 2]. There is thus an ongoing development in turbofan configuration design for an intake diameter larger than that for conventional engines. The new large-size engine design has led to a close coupling to the wing [2–4] to provide adequate ground clearance. This means that the aerodynamic interference between the wing and engine is intensified [5].

Thus, capturing the correct performance of the engine through the evaluation of its components in isolated and combined with the wing is essential for a proper indication of engine fuel consumption and overall operating costs for each single-flight trajectory. However, this engine performance information should be produced with lowest costs, and short periods possible.

The exhaust system has a complex flow field, surrounding it, with many of the aerodynamic flow features [6]. These features are, currently, of ongoing interest to be modelled to assess engine performance efficiently using several low-order models [4,5,7]. However, the current low-order engine performance models do not capture most of the multi-dimensional flow features in the assessment of engine performance especially around the exhaust system.

Several studies were concerned with the prediction of the interference effect on the intake, nacelle, and engine/aircraft configuration using the low-order models [4,5,7]. However, the sensitivity of the engine thrust to nozzle performance is higher than the other engine components [8]. Therefore, low-order models of the engine performance prediction need to be adapted to be more sensitive to the aerodynamic interaction impact on the nozzle performance. To achieve that, multi-degree of freedom nozzle characteristics maps are required, which provide the combined effect of more than single geometrical or aerodynamic parameter.

Such types of enhanced performance models will lower the production cost and the time occupied during the early design stages of the engine, and provide a better indication of the engine performance. Therefore, quantifying the exhaust system performance in both isolated and under the wing cases, and identifying which geometric and aerodynamic parameters play the most significant roles, is crucial, and will provide a considerable contribution to the current performance models.

1.2 Novel aspects

1.2.1 Enhanced aero-engine nozzle performance maps

The variation of the aerodynamic parameters alongside with the geometrical features of the exhaust system influences the assessment of the nozzle performance and the design decisions to be taken. The currently available nozzle maps provide a single degree of freedom performance metrics. In the current project, aerodynamic performance evaluation for the nozzle and an assessment of the impact of the aerodynamic interaction between nozzle jet and the external flow have been conducted to produce characteristic maps. These maps provide flexibility to select the appropriate nozzle metrics for design and off-design conditions for the chosen geometry characteristic. These maps were constructed using modified thrust definitions so that they were able to capture more of the effects of the external flow interactions with the nozzle flow. Furthermore, the effect of the bypass nozzle flow on the core nozzle

aerodynamics was expressed in terms of a set of correction factor as a function of geometrical parameters.

1.2.2 Engine performance sensitivity to the nozzle geometrical features

The use of a simulation tool to predict the aero-engine performance before committing to a final engine design has become one of the most cost-saving approaches in this field. However, most of these tools are based on one-dimensional thermodynamic equations. The previous research aimed to modify these “low-order” models by employing experimental and computational approaches to capture much of the three-dimensional behaviour of the flow at each stage throughout the engine. The lack of a full set of data for different nozzle geometrical parameters that enable prediction of performance in a more generic and multidimensional manner means that current performance maps are oversimplified. The nozzle performance maps currently in use could either over- or under-predict nozzle performance under off-design operational conditions. This gap has been bridged by modifying engine performance model to be sensitive to the aerodynamic and the geometric parameters of the nozzle. This model was based on the employment of response surface methods that were used to interpolate the missing performance data.

1.2.3 Generic installed exhaust nozzle performance prediction

The impact of the presence of the wing on the exhaust system is significant. The impact of the engine installation under the wing on the engine is a function of the angle of incidence and engine position as they alter the pressure field of the wing. The current project suggests a method to predict the impact of the installation on the nozzle performance by generating a correlation that assesses the variation in the nozzle performance as a function of the local static pressure generated by the wing. This has been done by simulating the flow around a two-dimensional wing (infinite swept wing) and a more advanced aircraft configuration (Common Research Model (CRM)[9]). In this case, the only information required to predict the interaction effect is the value of the static

pressure produced by the wing configuration under cruise conditions, to determine the aerodynamic interference effect on the nozzle.

1.3 Aim and Objectives

The research aim is to modify a simulation model to improve the prediction of the performance of the propulsion system by considering the aerodynamic impact of the nozzle parameterisation and the engine installation under the wing.

Key objectives necessary to achieve this aim are:

1. To develop a method to estimate the performance of an aero-engine nozzle;
2. To perform an aerodynamic and geometric parameterisation for a basic nozzle configuration employing a Computational Fluid Dynamics (CFD) analysis;
3. To develop a method to quantify the impact of aerodynamic interference due to the engine installation on the nozzle performance as a function of engine position and angle of attack;
4. To validate the CFD method with the currently available experimental data;
5. To establish nozzle performance maps as a function of a range of geometrical and aerodynamic parameters;
6. To modify a low-order engine performance model (Turbomatch[9]) to capture the multi-dimensional impact of the external and the nozzle flow interaction on the exhaust-system characteristics using a multi-dimensional response surface methods (RSM);
7. To validate the RSM using Cross Validation approach; and
8. To assess the engine/aircraft performance model results using installed nozzle performance corrections;

1.4 Project structure

The project began by sizing the engine nacelle using data that were extracted from a non-dimensional performance model. The geometry was then generated

using these data and the nacelle basic design methods. A Computational Fluid Dynamics (CFD) approach was used to extract the performance data as a function of several aerodynamic and geometric parameters for both the isolated and installed engine. Validations of the CFD method and the employed mesh results were also conducted. The nozzle performance maps were then established using a modified definition of the nozzle performance. A response surface methods (RSM) were employed to integrate the new performance data into the non-dimensional engine performance code. The RSM was then validated using a cross-validation approach (leave-one-out). An engine performance model was modified to predict propulsion system performance in a more enhanced way. The extracted correction of the nozzle performance due to the installation is utilised to correct the results of an engine/aircraft performance model. The thesis structure is presented in Figure 1.1.

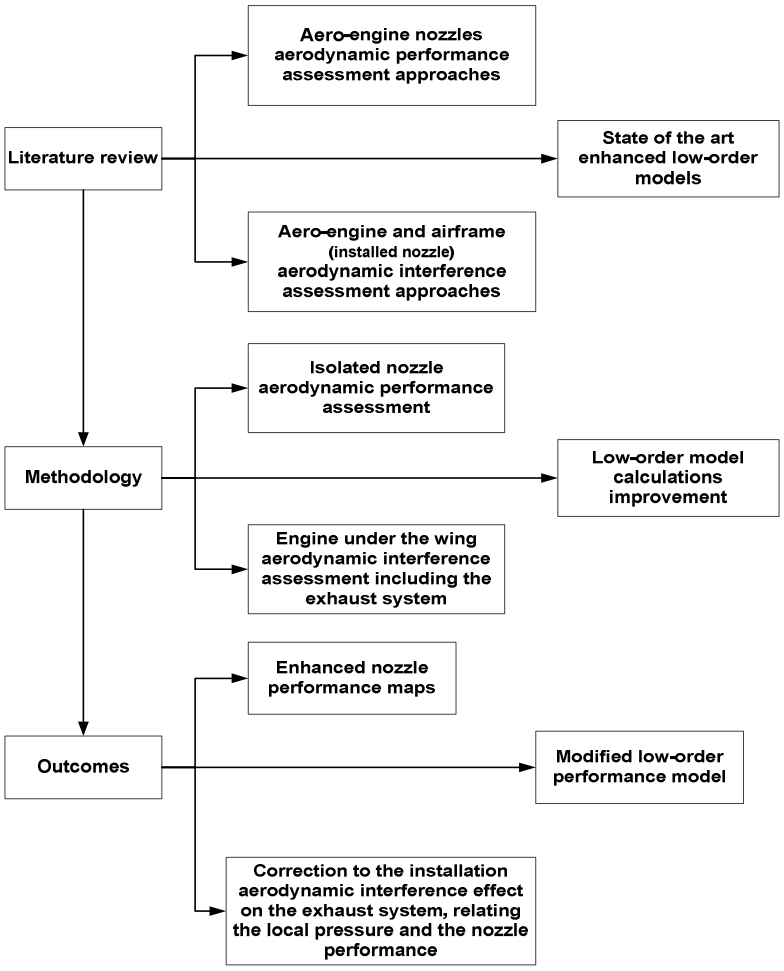

Figure 1.1 Roadmap of the current project.

2 Literature review

The objective of this chapter is to provide a review of the most relevant prior methods of evaluating the performance of the exhaust system of aero-engines in isolated and installed situations. The review includes a discussion of experimental, numerical and low-order analytical approaches that were used for this purpose. Furthermore, an explanation of the fundamental aspects of the aerodynamics of the isolated and installed exhaust system is illustrated. This includes a presentation of the main sources of flow interactions that influence gas turbine performance. This chapter concludes with a summary of the current findings and identifies the lack of knowledge addressed in this research.

2.1 Aero–engine exhaust system aerodynamics

The exhaust system is one of the main parts of the propulsion system that plays the main role of converting the gas potential energy into kinetic energy in terms of the thrust of the nozzle [10,11]. When this transformation takes place perfectly, nozzle exit static pressure will equal the free-stream pressure and the nozzle is fully expanded. However, a fully-expanded nozzle is not the usual case for the convergent nozzle of civil aero-engines at certain flight phases [10]. Usually, this type of nozzle runs in under- or over-expanded conditions depending on the function of the aero-vehicle and the operational conditions.

The convergent, rather than convergent-divergent nozzles, are sufficient for both subsonic and supersonic applications [10]. However, the most common installation of the convergent nozzle is with subsonic commercial and military transport aero-engines [10]. The preference comes from the fact that these types of nozzles are lightweight [10].

Typically, the convergent nozzle expands with high exit static pressure when the pressure ratio of the nozzle is higher than the critical nozzle pressure ratio (NPR). Consequently, the gross thrust will lose part of its momentum flux based on imperfect expansion. However, according to the ARC Technical Report [12], when the jet expands in supercritical cases (under-expanded), there will be an

expectation to calculate additional thrust owing to the expansion process of the jet, which is known as “recovery thrust or pressure thrust”.

The flow features that downwash the exit of the nozzle is significantly complex. They include a variety of flow features, mainly subsonic, transonic and supersonic flow separated by compression and expansion waves and shear flows [13],(Figure 2.1) [14]. These flow features influence the pressure distribution surrounding the exhaust-system nozzle, mainly the fan and core nozzles. Moreover, the presence of the wing affects the flow field around the nozzle and the pressure distribution over its components, (Figure 2.2) [15]. As a result, it will affect the forces that are generated on the core cowl and plug.

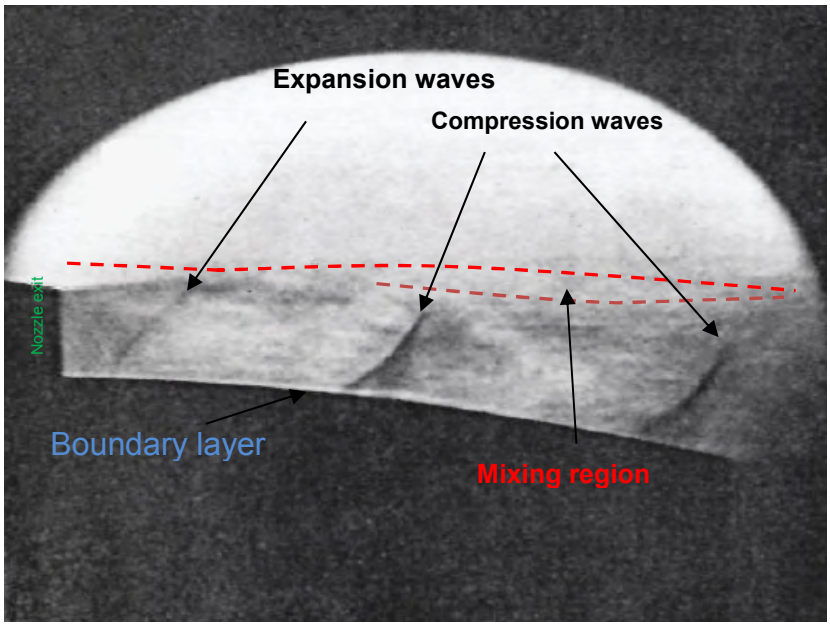

Figure 2.1 Schlieren photograph of the flow structure of the RB211 aero-engine at NPR of 2.8[14].

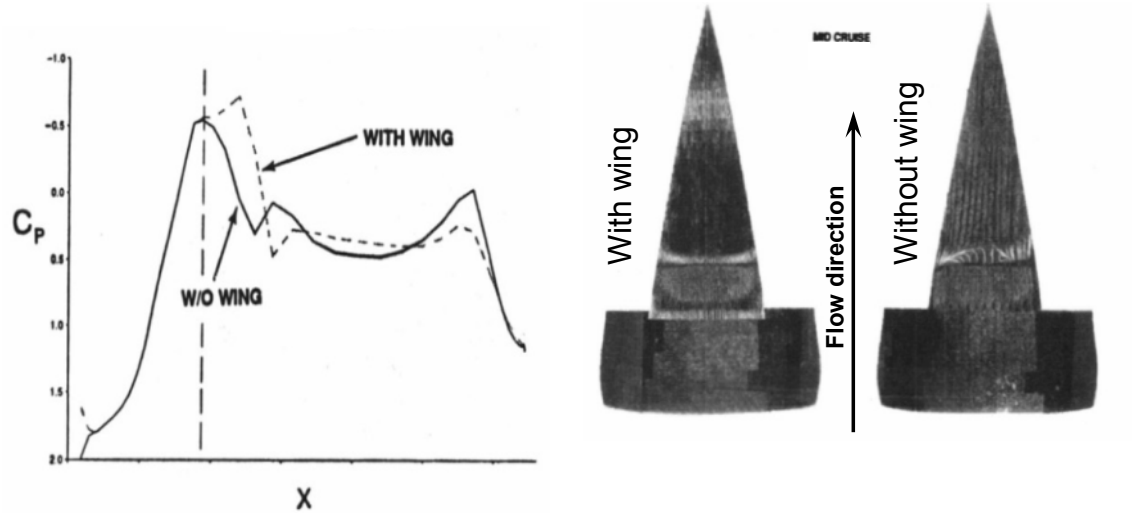

(a) (b)

Figure 2.2 (a) Predicted pressure distribution over the plug surface of an engine [15], (b) Core nozzle plug in two cases, with and without the wing [15].

The alteration of the pressure field surrounding the nozzles influences the back pressure, and as a result, it will affect the choking pressure ratio of the nozzle. It was reported by Munniksma and Jaarsm [16] that the choking nozzle pressure ratio of the fan nozzle increased to 2.31 at free stream Mach number 0.8 (air with specific heat ratio (γ) of 1.33). This means when the nozzle runs at an un-choked condition the internal flow of the nozzle will be altered by the pressure field of the surrounding flow.

The effect of the back pressure could be on the other way around; Salmi [17] reported that at flight Mach number 0.9, the interaction of the external flow with the jet flow caused a reduction in the base pressure. Thus, this pressure reduction increases the nozzle pressure ratio and consequently produces an overexpanded nozzle jet, intensifies the base drag and reduces the nozzle performance for a single-stream nozzle. As a result of that, the nozzle thrust losses increased by 8.0% as the Mach number increased from 0.6 to 0.9.[16]

However, when a supercritical condition of the nozzle is achieved, the nozzle internal flow field is in isolation from the outside flow. The only expected loss is due to the generation of the boundary layer over the internal walls.

To analyse the performance of the exhaust systems, the aerodynamic and thermodynamic characteristics of the nozzle have to be evaluated. Different

approaches have been employed previously to assess nozzle performance and examine the aerodynamics of the exhaust system. The following sections present these various approaches starting from experimental, analytical methods and numerical approaches.

2.1.1 Experimental exhaust-system characteristic assessment studies

Single-stream nozzle

In the past, experimental investigation played a vital role in the evaluation of nozzle performance. Initial studies at the preliminary design stages were carried out in the laboratory to capture the effects of the flow features on the aero-engine components. In 1957, James and Cubbage [18] executed an experimental test for a single stream with a circular-arc boat-tail nozzle to examine the effect of flight operating conditions in terms of the flight Mach number and nozzle pressure ratio (NPR). The M_∞ was changed from 0.6 to 1.28 and NPR from off-jet to 8.0. The findings showed there to be little impact of the NPR on the drag values at a low boat-tail angle (≈15˚) and M_∞ across a range of 0.6 to 1.20. The results demonstrated that the boat-tail pressure drag increases with the NPR up to a value of 2.0, then the drag coefficient started to decrease after that [18].

To be consistent and study the effect of the jet on the nozzle performance, a measurement of the local Mach numbers and flow angles was made by Abeyounis and Putnam [19] for a circular-arc boat-tail nozzle under subsonic operational conditions of free stream Mach number (M_∞) 0.6 to 0.8. A solid jet simulator was used to simulate the jet plume, to capture the blockage effect of the jet stream tube on the after-body and separate the entrainment effect from other measurements. The results indicated that there is an increase in the pressure over the boat-tail surface with the reduction in M_∞ because of the presence of the jet simulator.

Moreover, Mathur and Yajnik [20] studied the effect of the NPR and M_∞ on an axisymmetric conical after-body configuration, (Figure 2.3). The tests were conducted across M_∞ 0.6 to 1.1, with a jet pressure ratio that varied from 1.0 to

6.0. The findings suggested that the under-expanded jet plume affected the after-body pressure distribution and, accordingly, the pressure drag of the after-body. The influence of the jet extended up to the location of the maximum configuration diameter, and it is dominant in the location, where the shock over the after-body takes place, at transonic speeds.

On the other hand, as the boat-tail angle was elevated, the shock wave over the boat-tail occurred at lower M_∞ than the small boat-tail angle configurations [18]. This behaviour increased the levels of the drag with an increase in Mach number for each configuration [18]. Furthermore, the shock location was altered during the variation of M_∞, where with the increase in the free-stream velocity, the shock wave shifted upstream, (Figure 2.4) [20].

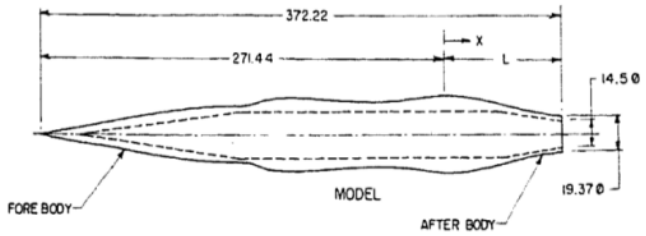

Figure 2.3 Axisymmetric sketch for the single-stream model (all dimensions in mm) [20].

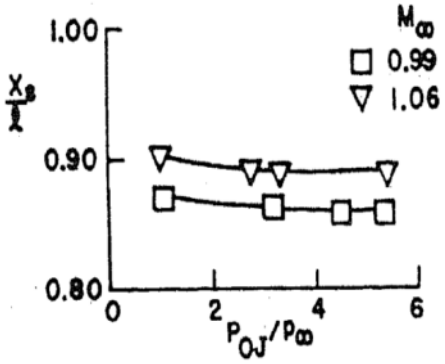

Figure 2.4 Shock location as a function of the NPR and M_∞. The vertical axis represents the axial distance over the boat tail surface, and the horizontal axis is the total nozzle pressure ratio [20].

Regarding nozzle boat-tail angle impact, Reubush et al., [21] extended the investigation to include the effect of the nozzle fineness ratio (the ratio of the boat tail length to the maximum diameter of the nozzle ($\frac{l}{D_m}$)), Figure 2.5, on aerodynamic characteristics. Three different nozzle fineness ratios, 0.8, 1.0 and 1.77, were examined. The results showed that as ($\frac{l}{D_m}$) increased, the separation was delayed, and the drag forces were reduced. The drag coefficient was diminished by 4.0% at M_∞ of 0.95 when the fineness ratio increased from $\frac{l_{bt}}{D_{max}}$

of 0.8 to 1.77. The drag-rise Mach number increased from 0.85 at $\frac{l}{D_m} = 0.8$ to 0.905 at $\frac{l}{D_m} = 1.77$ [21].

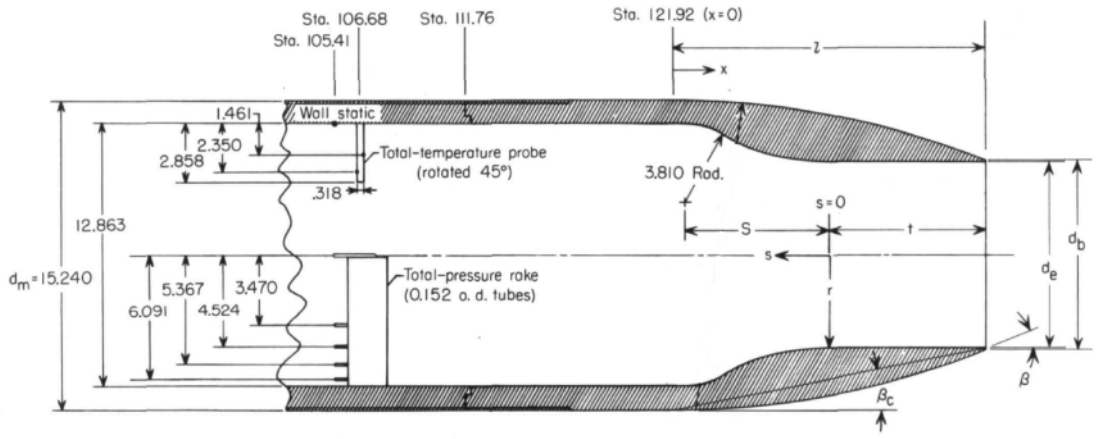

Figure 2.5 Sketch of the circular arc-boat tail single stream nozzle (all dimensions in cm) [21].

As it was observed before, when M_∞ was increased to supersonic values, a shock wave appeared over the after-body. Moreover, the location of the shock wave moved upstream with a decrease in the fineness ratio and increase of M_∞ [21]. James and Cubbage [18] demonstrated that the rise in the boat-tail angle (reduction in the fineness ratio) elevated the impact of the nozzle pressure ratio ($\frac{H_j}{P_\infty}$), and M_∞ on the boat-tail drag, (Figure 2.6).

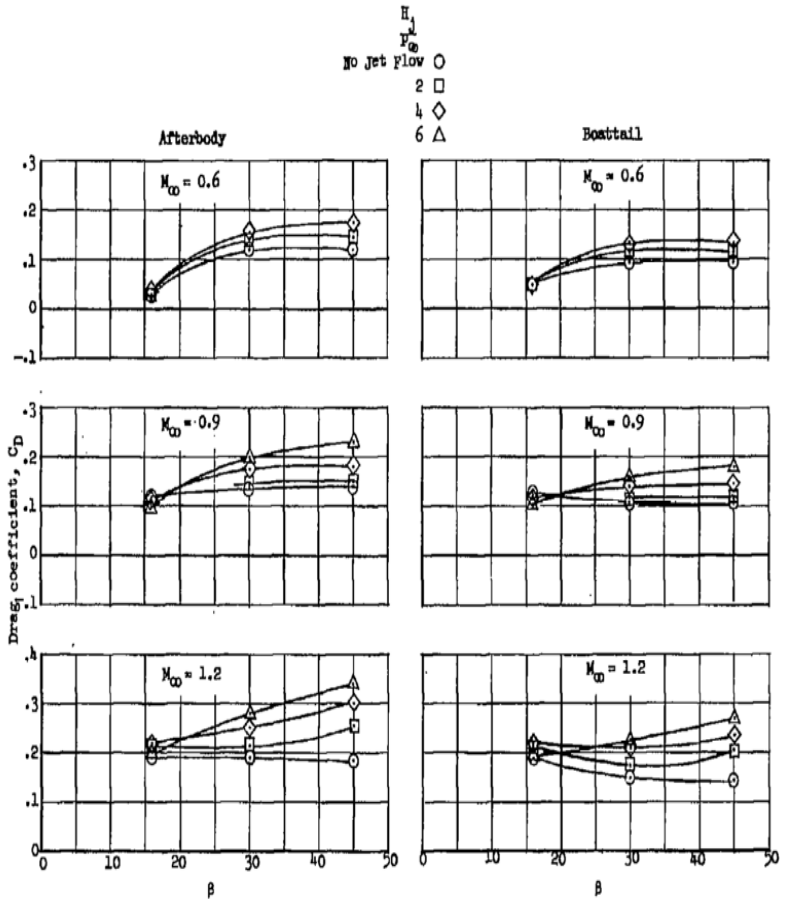

Figure 2.6 Variation of the after-body and boat-tail drag coefficient with the boat-tail angle at several values of nozzle pressure ratio ($\frac{H_j}{P_\infty}$), M_∞ and after-body angle (β) for the nozzle with a base diameter to maximum diameter ratio of 0.55; (the after-body drag represents the drag of the boat-tail and the base) [18].

The increase in the base area (the area between the boat tail rim and the edge of the nozzle exit plane) reduced the effect of the NPR and free-stream Mach number and intensified the impact of the boat-tail angle on the drag coefficient of the boat-tail, (Figure 2.7). The geometry of a smaller base area has a range of boat-tail angles less than that of a larger base area. However, its length was greater, and so the separation effect and disturbance to the flow over the after-body was smaller [18].

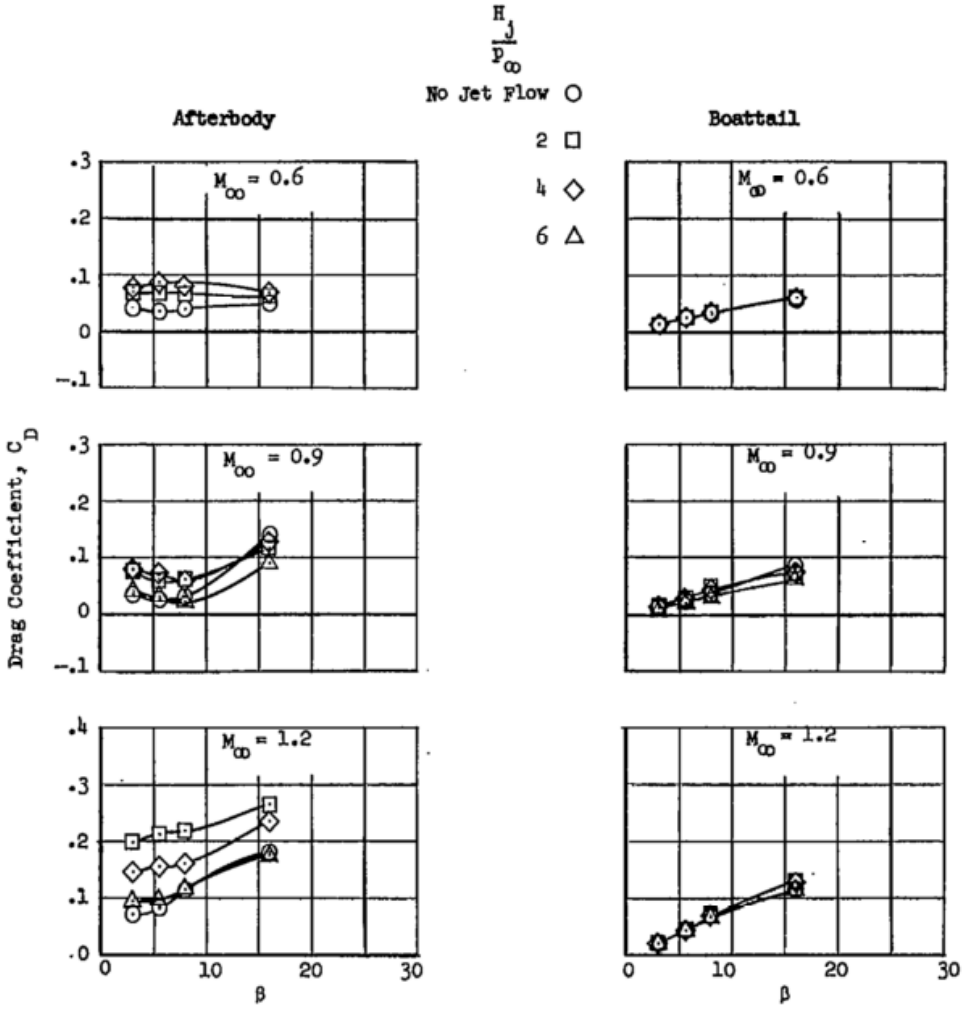

Figure 2.7 Variation of the afterbody and boat-tail drag coefficient with the Boat-tail angel at several values of $\frac{H_j}{P_\infty}$, and M_∞, for the nozzle with a base to maximum diameter ratio of 0.85 [18].

Wilcox et al., [22] examined the effect of the boat-tail angle and the Reynolds number (Re) on the boat-tail drag. The author noticed that the drag force increased with the increase in the boat-tail angle. The results showed an increase in the drag with Re to a peak drag value across the range $20x10^6$ < Re < $30x10^6$, after that the drag reduced, (Figure 2.8). Moreover, the angle of attack affected the drag coefficient of the boat-tail. The effect is little or insignificant at low M_∞ for small and large angles of attack. This behaviour persisted until the M_∞ reached transonic levels where the drag started to increase with angle attack [22].

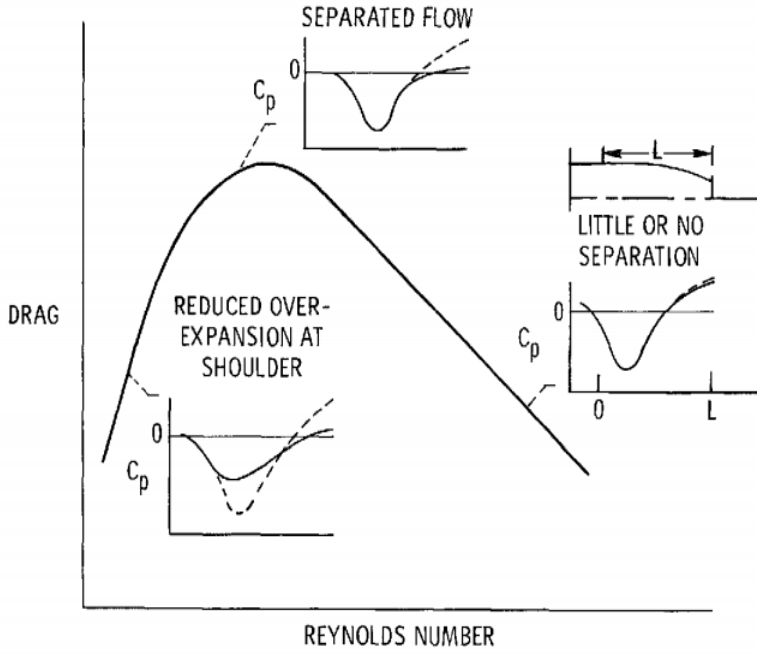

Figure 2.8 Boat-tail drag as a function of the Re showing different pressure distribution behaviour over the boat tail at difference Re the solid line represents (Viscous flow), and the dashed line represents the (inviscid flow) [22]

Apart from the parameters that affect the boat-tail of the nozzle were mentioned earlier, the properties of the exhaust gases are also of importance. The effect of exhaust gas properties on a single-stream nozzle drag has been investigated by Compton [23]. Since the gas properties are affected by the temperature of the gas, four different jet temperatures (300, 646, 810 and 1013 ˚K) were examined. An increase in the drag value by 20% was observed when cold air was used as a replacement for the turbojet exhaust gases [23]. However, this effect was noticed only at high NPR (5.0-9.0), and high boat-tail angles [23].

To consider the effect of temperature in the measurement of boat-tail drag, Mathur [24] suggested a correlation that relates the temperature effect in terms of the gas-specific heat ratio and drag coefficient, (Equation 2-1). Mathur [23] observed that a reduction in the boat-tail drag accompanied an increase in the temperature of the jet flow. The author noted that there is a reduction in the boat-tail drag by 10-25% between the use of hot and cold gases during the test.

$$C_{Dab(h)} = {C_{Dab(c)}}\Big/{\left(\gamma_{jc}/\gamma_{jh}\right)^2} \tag{2-1}$$

where γ_j is the specific heat ratio of the jet gases and the subscripts (c and h) denote the cold and the hot jets.

In terms of nozzle performance metrics, Reubush et al. [21] measured nozzle efficiency using the thrust–minus-drag term. The results demonstrated there to be an increase in nozzle performance with NPR (nozzle pressure ratio) [21]. This increase was attributed to the decrease in the boat-tail drag with NPR [21]. The impact of the fineness ratio on nozzle performance was seen to be noticeable with an increase in M_∞. At M_∞ =0.6, the efficiency rose by 0.9% between the two extreme nozzle fineness ratios (0.8 and 1.77), whereas at M_∞=0.9, the change was +5.0% [21].

Ashwood [25] put forth a set of nozzle gross thrust coefficients as a function of the NPR. This set of thrust coefficients was developed for two types of nozzles convergent and convergent-divergent (Con-Div). The Con-Div nozzle was parameterised by changing the divergent angle (5˚, 10˚, 30˚ and 50˚) and the NPR from 4.0 to 10.0 in steps of 2.0 [25]. The nozzle performance data showed peaks at a specific NPR for each nozzle configuration. The results revealed that maximum performance was achieved when the divergent angle was equal to 10˚, (Figure 2.9). Ashwood [25] attributed the degradation in the performance at high NPR and high divergence angles to the presence of shock waves in the flow and showed that the shock has fixed location and not affected by the variation in the NPR.

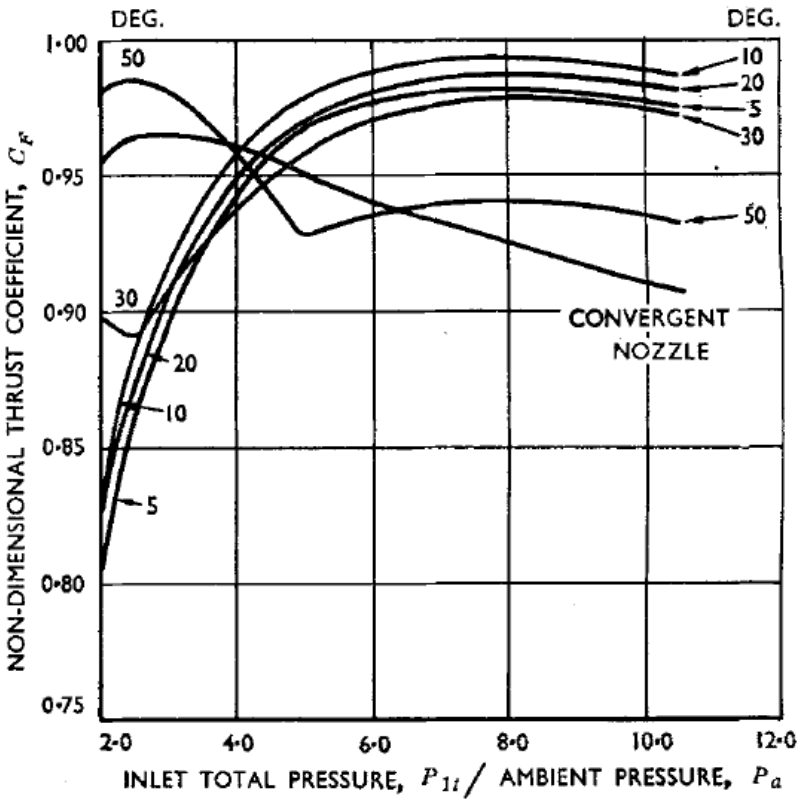

Figure 2.9 Variation of the gross thrust coefficient with nozzle pressure ratio for the chosen divergent angle [25].

Thornock and Brown [26] performed a study of the effect of the internal angle on nozzle performance. A simple conical nozzle configuration was used; three internal angles were investigated 15˚, 25˚ and 40˚. The NPR was varied between 1.4 and 7.0. The results showed there to be an increase in the discharge coefficient values with the reduction of nozzle angle across the entire range of NPR, and this was in contrast to the thrust coefficient (see Figure 2.10 and Figure 2.11). A measurement of the sonic line location showed there to be a downstream movement as the angle increased and shifted upstream with NPR for each internal angle, (Figure 2.12 and Figure 2.13).

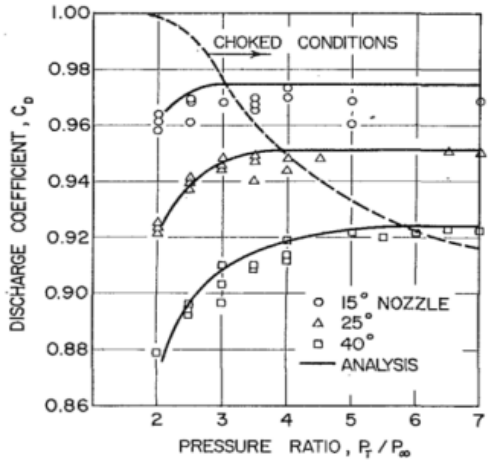

Figure 2.10 Discharge coefficient as a function of internal angle and NPR of the nozzle [26]; theoretical analysis by Brown [27].

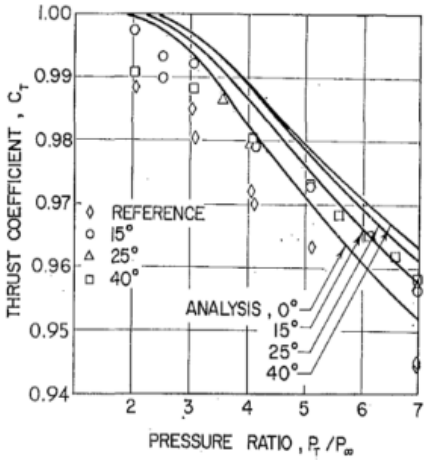

Figure 2.11 Thrust coefficient as a function of internal angle and NPR of the nozzle [26]; theoretical analysis by Brown [27].

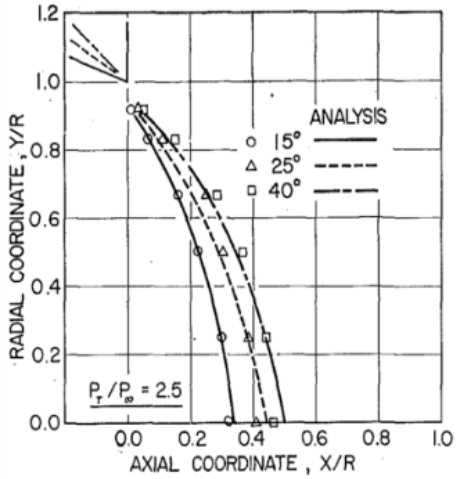

Figure 2.12 Sonic line location for the chosen internal wall angles [26]; theoretical analysis by Brown [27]

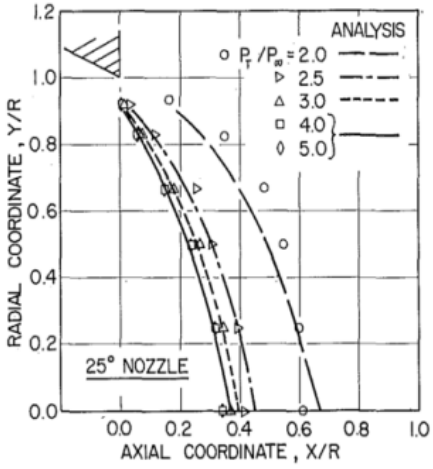

Figure 2.13 Sonic line location for the chosen value of NPR [26]; theoretical analysis by Brown [27].

Single stream with a plug (centre body)

Several engine types have a plug-shaped centre body, whether it is in the centre of the primary nozzle, such as those in military engines, or in the middle of the core nozzle in civil engines. The function of the plug is to provide extra thrust to the engine when the nozzle runs in under-expanded conditions [28].

Contradictory behaviour was noticed by Harrington et al. [29]. Specifically, they investigated three different nozzle configurations, (Figure 2.14): a single-stream nozzle with circular-arc boat-tail (with different exit areas), a circular-arc boat-tail

nozzle with a plug and a plug nozzle with a straight boat-tail. The experiment was conducted over a range of M_∞ from 0.0 to 1.97. The nozzle efficiency was presented in terms of thrust-minus-drag (F-D) as a function of nozzle ideal thrust ratio. The F-D term was measured using a load cell. Nozzle efficiency at NPR=2.80 and M_∞=0.9 of the single-stream nozzle was equal to 0.982 whereas the same configuration with a plug had an efficiency equal to 0.973 under the same conditions [29]. The efficiency of the single-stream nozzle increased with NPR up to 8.0 and reduced after that. Conversely, the plug nozzle exhibited a reduction in performance throughout all ranges of NPR[29]. This meant that the plug nozzle could contribute positively or negatively, depending on operating conditions.

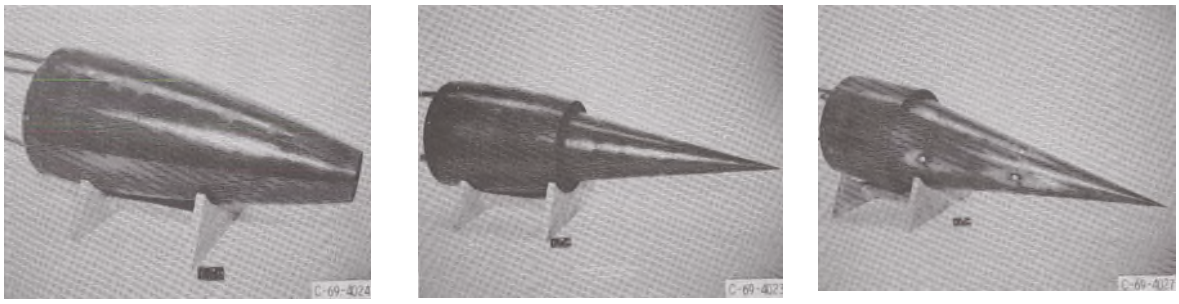

Single stream | Circular-arc boat tail with plug | Straight boat-tail with plug

Figure 2.14 Various configurations of the test nozzle, [29].

Several factors can affect nozzle performance based on the presence of the plug, including the effect of the jet shape along with entrainment. This was clarified by Bergman [30] where a boat-tail drag of a convergent and plug nozzle was evaluated. The tests were conducted at different flight Mach numbers of 0.55, 0.70 and 0.85, and NPR ranged from 0.0 to 4.0. The experiment was carried out to capture the plume shape and entrainment impact. The jet entrainment was sensible when the jet velocity exceeded the speed of the free stream [30]. As the NPR kept increasing, the entrainment effect reduced the boat-tail pressure and thus increased the drag. The jet shape showed there is a beneficial impact for the NPR as it moved the upcoming streamlines over the boat-tail away from the engine axis; this will cause a strong recompression region over the boat-tail. The comparison between convergent and plug nozzles showed that the convergent nozzle had a greater plume-shape impact and less

entrainment [30]. Consequently, the plug-nozzle boat-tail drag was higher than the convergent nozzle, (Figure 2.15). It should be noted that the "Simulated Convergent Nozzle" in Figure 2.15, shares the same geometrical exit area as the plug-nozzle, with the only difference being that the jet flow is directed axially [30]. In this case, the comparison between their performances is valid.

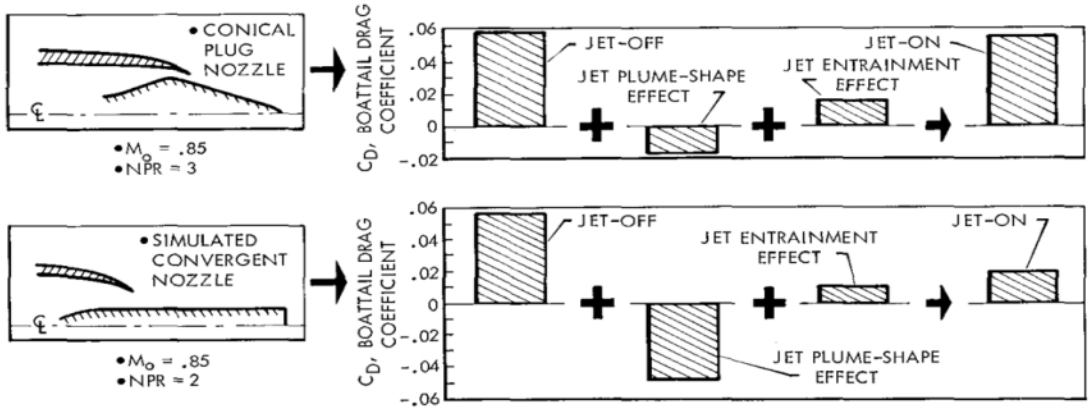

Figure 2.15 Comparison between the jet effect on the boat-tail drag between the conical plug and the simulated convergent nozzle [30].

The impact of the variation of plug length and boat-tail angle of a plug-nozzle on nozzle performance was evaluated experimentally by Berrier [31]. The author used a gas combination of 10% air and 90% hydrogen peroxide with a specific-heat ratio of 1.266 at a temperature of 1013 ˚K to simulate the gas properties. Three boat-tail angles were examined -8.0˚, 20˚ and 30˚. The operating conditions were changed across a range of M_∞ from 0.5 to 1.30 and NPR up to 16.5 at a zero-angle of attack. The results were compared with the performance characteristics of an isentropic plug nozzle. The F-D term was calculated by adding the internal pressure and the skin friction forces to the forces obtained by force balance. The nozzle with plug half-angle of 15˚ exhibited better performance as compared with the isentropic nozzle. However, the performance of the nozzle with plug half-angle of 15˚ was lower than the nozzle with an angle of 10˚ as a function of M_∞. Reducing the length of the plug degraded the nozzle performance by less than 1.0% for a configuration with a plug truncated by 30% and a plug angle of 15˚ [31].

Dual stream nozzle

High bypass ratio turbofan engines of modern commercial aircraft have a dual-stream nozzle [28]. This type of nozzle consists of the primary stream nozzle (core) and the secondary nozzle (fan nozzle) [28]. This type of nozzles has a very small area ratio Con-Div nozzles [28].

Welge et al. [32] assessed the performance of a dual-stream nozzle in isolated and installed cases with M_∞ of 0.0 and 0.8 and a range of NPR from 1.0 to 3.0. The results showed that there is a notable effect of the variation of M_∞ when the nozzle runs under unchoked conditions. This was attributed to the impact of the high pressure of the external flow on the low-pressure region inside the nozzle [32]. On the other hand, the choking NPR_{crit} increased with the rise in M_∞ compared with static conditions. A reduction in the thrust coefficient with the external flow was observed, and the thrust coefficient was reduced by 0.3% when the M_∞ was increased from 0.0 to 0.8.

Mikkelsen et al. [33] presented performance data in terms of thrust and discharge coefficients for the Dual Separate Flow Reference (DSFR) model. This model represents a scaled civil engine turbo-fan with a bypass ratio from 10-12. All the tests were conducted in static conditions across a range of fan NPR from 1.2 to 2.8. The discharge coefficient results showed that the curve levelled-off after choked NPR was achieved, of which it was 2.1 for the bypass nozzle and 1.8 for the core nozzle. The thrust coefficient showed an increase across a range of fan NPR from 1.2 to 2.2; the thrust coefficient decreased with further elevations in NPR. It should be noted that the actual thrust was calculated by measuring the resultant force of the vertical and horizontal force components that were derived from a three-component force balance, (Figure 2.16).

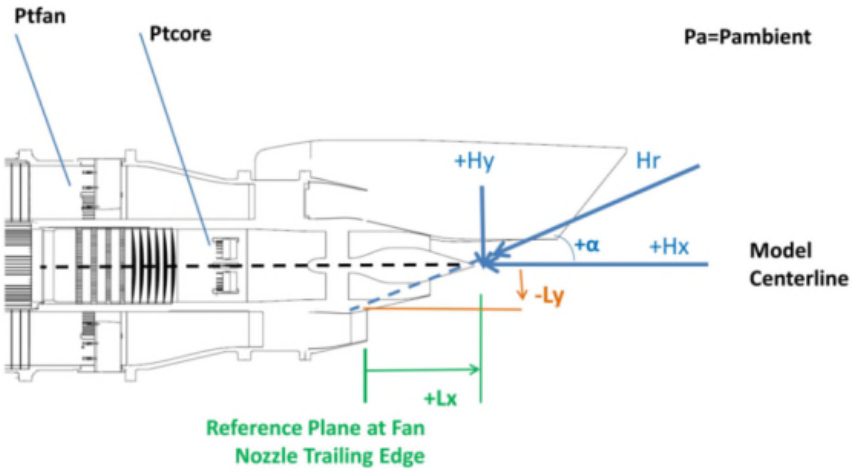

Figure 2.16 Schematic of ASME DSRF model and the forces components [33].

2.1.2 Analytical exhaust-system characteristics evaluation studies

An analytical method based on boundary-layer calculations was developed by Hall [34]. More specifically, this method was used to calculate the flow coefficient (C_d) as a function of the Reynolds number by assuming the internal walls of the nozzle as two parallel flat-plates, (Figure 2.17) [34].

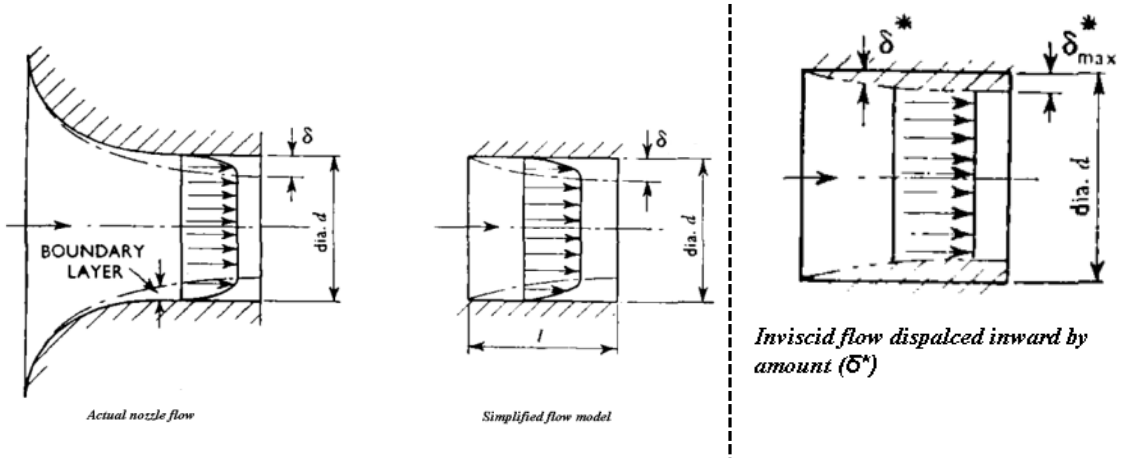

Figure 2.17 Hall's simplification of the nozzle geometry during the calculation of the nozzle discharge coefficient using boundary-layer theory [34].

The flow was assumed to be incompressible and separates at the nozzle exit only [34]. Laminar, turbulent and transitional boundary-layer theories were applied in the calculations for displacement thickness and then the discharge coefficient (C_d), (Equations (2-2) and (2-3)). For the transitional flow, Hall [34] mixed the laminar and turbulent flows to simulate the boundary-layer. The location of the

transition point was assumed first at the nozzle exit and moves upstream with the increase in Re (assuming the transitional Re is 10^5). As a result, three discharge coefficient (C_d) correlations were derived. The results showed there is an increase in the C_d with the three correlations with the same Re. The theoretical data followed the same trend as the experimental data that was used to validate the results.

$$C_{d(laminar)} = 1 - 6.92Re_{th}^{-0.5} \quad (2\text{-}2)$$

$$C_{d(turbulent)} = 1 - 0.184Re_{th}^{-0.2} \quad (2\text{-}3)$$

Mikkelsen et al. [35], based on the calculations of Hall [34], developed an analytical model for the calculation of C_d and thrust coefficients (C_T) based on an empirical set of data used for ASME circular-throat nozzles. The model, Equations (2-4), (2-5) and (2-6), was developed as a function of Re and NPR. The C_d equation was taken from Hall's [34] work based on the laminar and turbulent boundary-layer theories. The formula of C_T was founded upon the transition boundary-layer theory across a range of Re values from $0.5x10^6$ to $2.0x10^6$.

$$C_{d\ (Trans)} = C_{d\ (lam)} - (C_{d\ (lam)} - C_{d\ (Turb)}) \left[\frac{Re \quad - Re_{th(Lam)}}{Re_{(Turb)} - Re_{(Lam)}} \right] \quad (2\text{-}4)$$

$$C_{T\ (NPR=1.89)} = 1 - 0.109Re_{th}^{-0.2} \quad (2\text{-}5)$$

$$C_{T(NPR\geq 1.89)} = \frac{(f \quad - \frac{1}{NPR})}{(C_d \left(\frac{m_{inlet} V_{inlet}}{P_t A_{th}} \right))} \quad (2\text{-}6)$$

where $f = 0.52828(1 + 1.4(C_d - \frac{C_d}{1.6855} + \frac{C_d^2}{1.6855}))$

An ASME nozzle was used by the FluiDyne Laboratory to calibrate the force balance and measure the mass flow rate of thrust rigs [35]. The factor (f) was employed to extrapolate the formula in order to calculate the thrust coefficient at NPR (λ)>1.89. The models were validated against available sets of experimental data. The results showed there to be agreement with the available

experimental data in terms of C_d and C_T ,(Figure 2.18). These equations could be useful for predicting single-stream nozzle performance metrics but are limited for this type of nozzle within a specific range of Re. Furthermore, as the model was based on flat-plate boundary-layer theory, there is no inclusion of any geometrical parameter to parameterise the nozzle geometry except nozzle length.

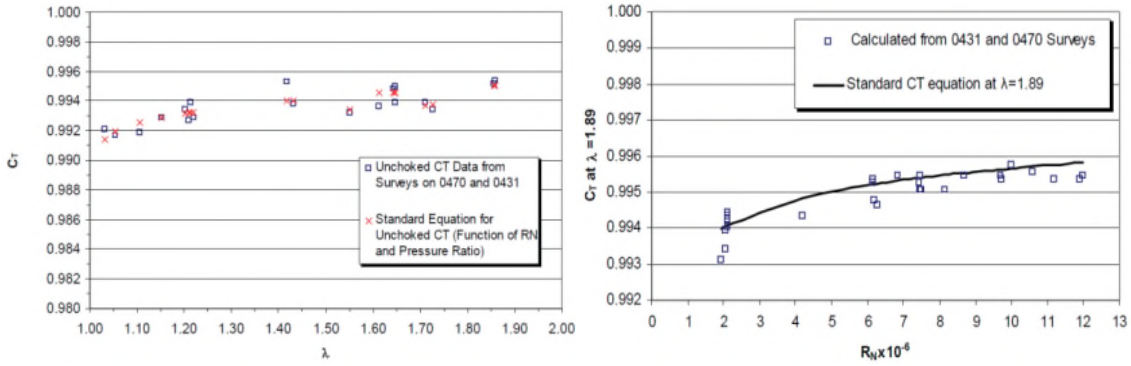

(a) **(b)**

Figure 2.18 (a) C_T comparison between the analytical formula results and the experimental data for an ASME nozzle as a function of NPR [35]; (b) C_T comparison between the analytical formula and the experimental data for an ASME nozzle as a function of Re at NPR =1.89 [35].

Olson [36] derived a C_d equation analytically based on the calculations of laminar boundary-layer displacement thickness. The boundary-layer characteristic equation was derived based on Walz's approximation. The density change in the boundary layer was considered using the temperature-velocity profile assuming the radial pressure variation is zero. The nozzle operational conditions were varied across a range of exit Mach number from 0.1-0.98. The results showed there to be agreement with empirical data within 0.1% at exit Mach number 0.1. Increasing exit Mach number from 0.1 to 0.98 elevated nozzle blockage by 10%. The results indicated there was agreement with the experimental data extracted from the investigation of the ASME long-radius nozzle running at NPR from 1.0 to 3.0. It was also reported by Olson [36] that there was insensitivity of the displacement thickness to the boundary-layer conditions at the entrance of the nozzle.

Ignoring the viscous effect and considering the flow to be irrotational, nozzle performance calculations were carried out by Brown [27]**.** Equations (2-7) and

(2-8) were developed to consider the effect of sonic-line curvature on conical nozzle performance in terms of C_d and C_T. The equation was derived from two-dimensional Euler's momentum equations. The C_d equation relates the shape of the sonic line with the radius of the nozzle exit. The effect of the curvature of the sonic line on the nozzle was, mainly, on the effective aerodynamic nozzle area, which is the nozzle discharges the exhaust gases through it. The C_T equation is related to the sonic-line curvature (to predict the exit flow angle), NPR and critical NPR. It should be noted that these equations were derived for a conical nozzle running at supercritical conditions only, to achieve sonic conditions at the exit. The results were compared with the experimental data of Thornock et al. [26], with the theoretical C_d and C_T data agreeing with the experimental data, (Figure 2.10 through Figure 2.13).

$$C_d = \frac{2}{R^2}\int_s y(sin\theta dx - \cos\theta dy) \tag{2-7}$$

$$C_T = \frac{\frac{P^*}{P_t}\left[1+\frac{2k}{R^2}\int_s y\cos\theta(\sin\theta\, dx - \cos\theta dy)\right] - \frac{P_\infty}{P_t}}{C_d\frac{2k}{k-1}\left(\frac{P^*}{P_t}\right)^{1/k}\left\{\left[1-\left(\frac{P^*}{P_t}\right)^{(k-1)/k}\right]\left[1-\left(\frac{P_\infty}{P_t}\right)^{(k-1)/k}\right]\right\}^{1/2}} \tag{2-8}$$

where: R is the radius of curvature, y is the radial position measured from the centre line, x is the axial coordinate measured from the exit plane, k is the specific heat ratio, θ is the flow angle and P*, P_t and P_∞ is the critical total and the free stream pressure, respectively.

Linear relationships were developed by Beans [37]. These relationships allow the determination of two performance coefficients from empirical data (C_d and C_T) for a third performance coefficient, such as the nozzle efficiency (η_{nozzle}). The relationships also allow the prediction of flow properties that are difficult to be measured at the nozzle exit, such as actual exit-static pressure (p_e) for a choked nozzle. This relationship works in combination with other empirical performance data. By knowing the nozzle efficiency, Beans [37] calculated the C_d and C_T of the nozzle for choked and unchoked cases for both convergent and Con-Div nozzles, (Equations (2-9) and (2-10)).

$$C_d = 1 - \frac{\gamma}{2}(1 - \eta_{nozzle}) \tag{2-9}$$

$$C_T = (\frac{p_e}{p_\infty})(\frac{A_e}{A_{th}})(1 + \gamma M_e^2) \tag{2-10}$$

L'Ecuyer et al. [38] applied compound-nozzle-flow theory to investigate the impact of the variation of the engine bypass ratio (during flight phases) on the nozzle performance of a turbofan engine equipped with a convergent nozzle. The test results showed that the gross C_T varied by up to 3.0% across a range of nozzle pressure ratio (NPR) from 1.18 to 1.7 owing to the variation of M_∞ (the ram pressure), (Figure 2.19) [38]. L'Ecuyer et al.[38] applied the theory to the exhaust system of a mixed-nozzle turbofan assuming no mixing between the engine bypass and the engine core streams. The correlated value of the theoretical gross thrust coefficient demonstrated there to be a variation by 1.0% with the same of NPR (Figure 2.20).

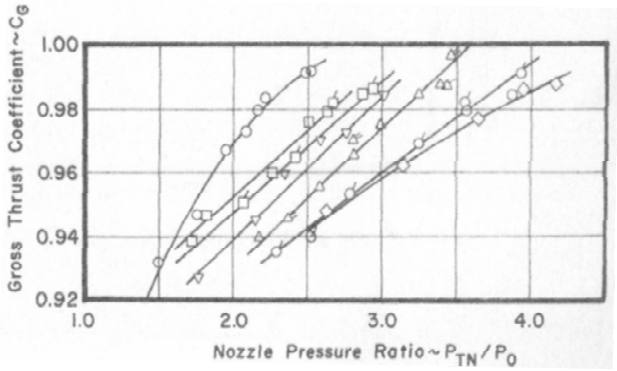

Figure 2.19 Variation of gross thrust coefficient with NPR at specific altitudes using the theoretical gross thrust as a function of NPR only. (The different curves represent the various altitudes).

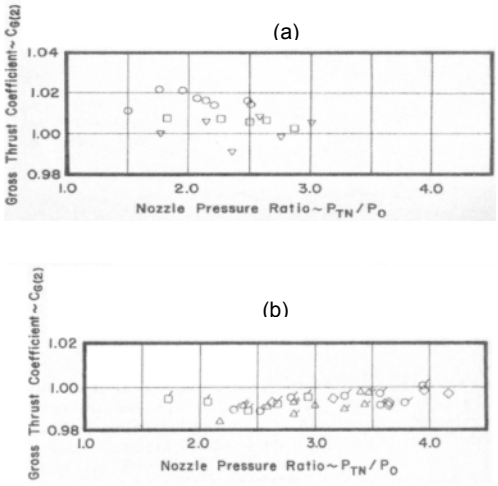

Figure 2.20 Variation of gross thrust coefficient with NPR at (a) low altitude; and (b) high altitude, using the gross thrust as a function of NPR and by-pass ratio.

Although, there is a number of attempts have been made to produce an analytical model to simulate the flow features surround the nozzle, still, there is a lack of full representation for the parameters that affect the performance. The reason behind that is owing to the difficulty of combining the wide range of parameters that affect nozzle performance into a single analytical model.

Therefore, the use of an analytical model to produce sufficient nozzle maps is still insufficient.

2.1.3 Numerical exhaust-system characteristics evaluation studies

Numerical approaches now play a significant role in the preliminary design stages of aero-engines and aircraft. CFD approaches are employed in the evaluation of aero-engine performance and show there to be an acceptable level of agreement with the available empirical data. Most early CFD studies for exhaust systems were intended to validate CFD codes, and some of them are now being extended to include some parameterisation of operational and geometrical features of the exhaust system.

Single-Stream Nozzle

Swanson [39] utilised a numerical model to simulate the transonic flow around a boat-tail element of the nozzle. A solid cylinder was attached to the configuration to simulate the jet boundaries. Swanson [39] neglected the effect of jet entrainment on the boat-tail aerodynamics. Three different boat-tail configurations were investigated for fineness ratios of $\frac{l_{bt}}{\mathrm{D_{max}}} = 0.8, 1.0 \text{ and } 1.77$. For transonic flow ($M_\infty$=0.8) and the small fineness ratios (0.8 and 1.0) configurations, the results showed there to be agreement with the experimental data, though in the region of flow expansion over the boat-tail. Moreover, an-over prediction was observed in the separation region [39]. At a high fineness ratio value (1.77), the numerical model predicted the expansion and separation region accurately [39]. Furthermore, the high value of the fineness ratio in the supersonic M_∞ (1.3) had the best agreement of the numerical model with the experimental data [39]. At supersonic flow, the shock location moved downstream with the fineness ratio, with shock taking place at ≈0.76l_{bt} for a fineness ratio of 0.8 and at ≈0.88l_{bt} at a fineness ratio of 1.77.

Another validation for the same nozzle was performed by Carlson [40], however, this time without a solid cylinder. The numerical model was built in PAB3D Navier-Stokes code. The employed turbulence model was the two-equation standard k-ε. The discharge coefficient results showed agreement with the

experimental data within a range of deviation of ±0.5%. The F-D coefficient had ±1.0% agreement with the experimental data [40], (Figure 2.21). Yet, the calculated boat-tail drag values did not agree with the experimental data [40], (Figure 2.22).

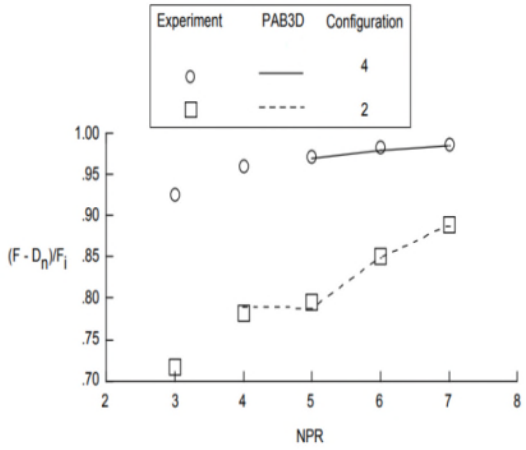

Figure 2.21 Comparison between the calculated and the measured nozzle efficiency as a function of NPR at M_∞= 0.90 and zero angles of attack [40].

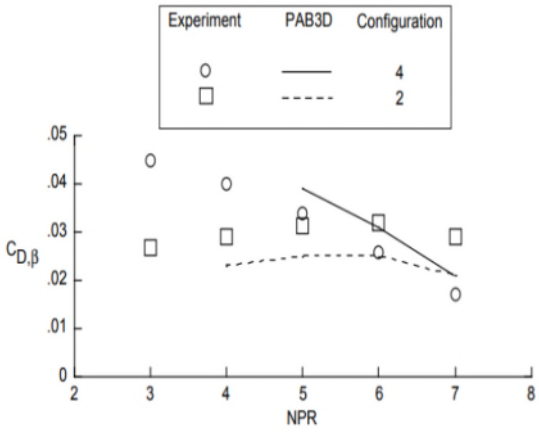

Figure 2.22 Comparison between the calculated and the measured boat tail drag coefficient as a function of NPR at M_∞= 0.90 and zero angles of attack [40].

Dalbello et al. [41] evaluated the capability of different turbulence models in simulating the transonic flow around and through a Con-Div nozzle. The study was for M_∞ of 0.9 and 1.2 and NPR of 4.0 and 6.0. Reynolds Averaged Naiver-Stocks (RANS) equations were solved to conduct this analysis using Wind Code. The extracted aerodynamic characteristics were the pressure coefficient over the external surface, local static pressure over the internal surface and Mach number contours to determine the underlying flow behaviour. The results showed the flow separation over the internal walls of the nozzle move upstream as the NPR increases. However, the separation region was not affected by the variation in M_∞ [41]. The comparison between the different turbulence models concluded that the k-ω SST model was the best for predicting the external and internal flows, (Figure 2.23) [41].

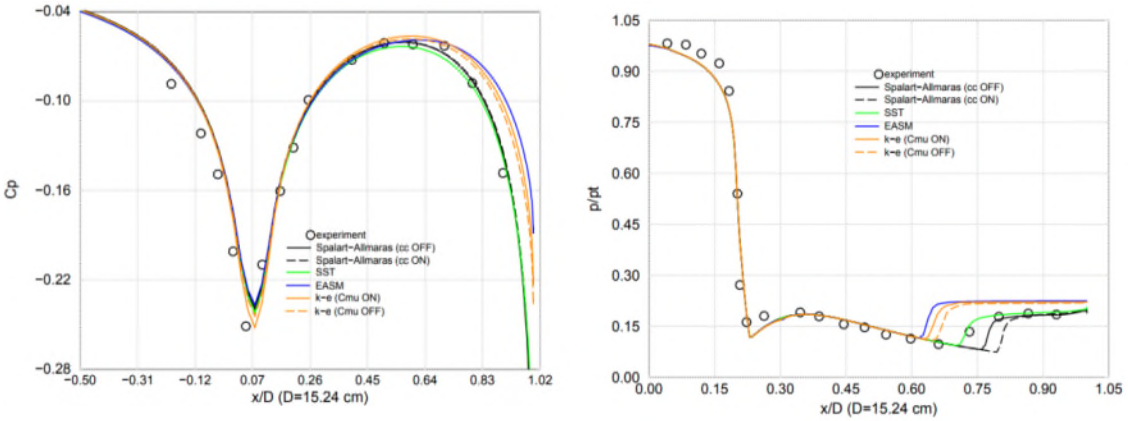

(a) (b)

Figure 2.23 (a) (a) Mean pressure coefficient (Cp) distribution on the external surface at NPR=4.0 and M_∞=0.9[41]. (b) Pressure distribution on the internal surface of the nozzle at NPR=4.0 and M_∞=0.9[41].

A numerical method was used by Wehofer et al. [42] to simulate transonic flow through a conical convergent nozzle. The goal was to evaluate the effect of inlet flow non-uniformities on nozzle performance. The data were compared with a set of experimental data for the convergent conical nozzle regarding the discharge and thrust coefficients. The simulation covered a range of NPR from 2.0 up to 4.0, and then the numerical data was extrapolated to cover higher NPR. The results were in line with the experimental data, (Figure 2.24). The inlet flow non-uniformity was examined using experimental data obtained from a turbofan engine. Wehofer et al. [42] stated that the existence of the non-uniformity in the flow increased the performance in terms of C_d by 1.0% and C_T by 0.1%.

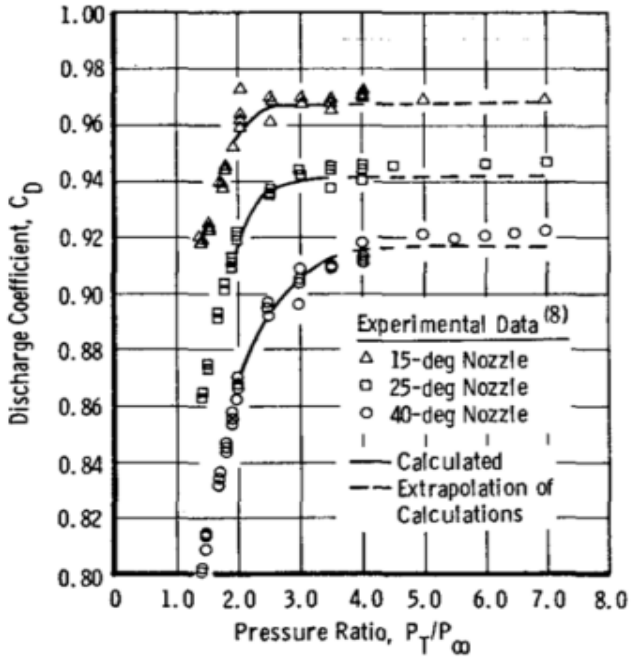

Figure 2.24 Calculated discharge coefficients compared with experimental data for a conical single stream nozzle, as a function of NPR and internal angle of the nozzle [42].

Dual-Stream Nozzle

Malecki and Lord [43,44] used CFD calculations to analyse the performance of three different nozzle configurations (single stream, plug and dual stream). The single stream and plug nozzle experimental data were extracted from Harrington's [29] work. The CFD calculations were performed using a RANS solver employing the standard k-ε model. The single-stream results indicated there was an over-prediction of nozzle efficiency at static free-stream conditions and M_∞=0.9 by 1.0% for static conditions and 0.2% for wind-on conditions, (Figure 2.25 (a)). For the plug nozzle, the results showed there to be a discrepancy of -1.2% from the measured data for the static conditions, and -1.0% for wind-on, (Figure 2.25 (b)). Nozzle efficiency agreed within ±0.2% with the experimental data for the dual-stream nozzle calculations, Figure 2.25 (c), for the two different configurations.

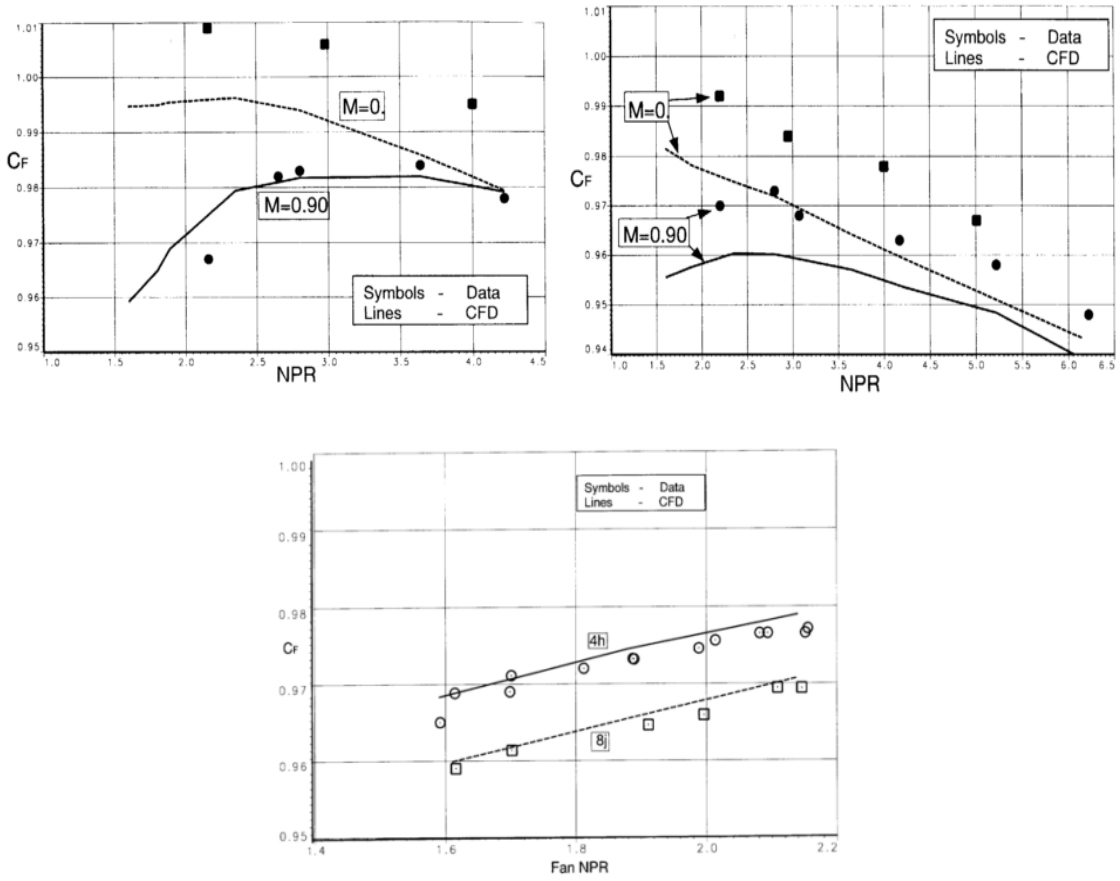

Figure 2.25 Comparisons of the calculated nozzle efficiency with experimental data [43]; (a) single-stream nozzle; (b) plug nozzle; and (c) exhaust nozzle of high-bypass turbofan [43].

Peery and Forester [45] conducted a validation study of the numerical model for single-stream, plug and multi-stream nozzles using the two-dimensional Navier-Stokes equations. A wall function was employed to represent the viscous flow over the nozzle solid surfaces. The pressure distribution over the cowl after-body surfaces for the multi-stream nozzle generally agreed with the experimental data; the percentage pressure difference was -0.3% at the nozzle edge. However, an under-prediction of the shock wave's strength was observed over the after-body surface as well as an over-prediction over the plug surface, (Figure 2.26).

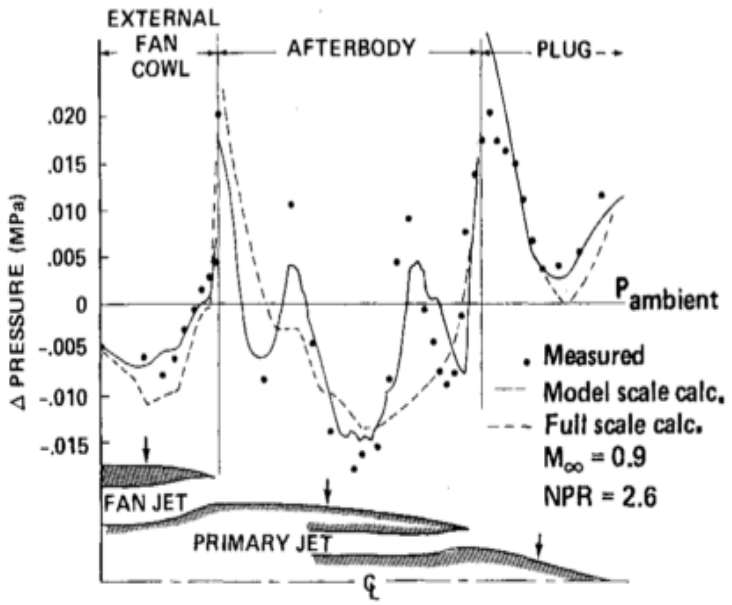

Figure 2.26 Gauge pressure distribution over a multi-stream nozzle compared with the experimental and flight data [46].

Keith et al. [47] developed a CFD code (ENS3D) to estimate the aerodynamic characteristics of an exhaust system and pylon configuration in a three-dimensional and axisymmetric domain, (Figure 2.27). The code solves Navier-Stocks equations. The code was validated against the available experimental data in terms of the pressure distributions around the exhaust system components. The simulations were run at both static and cruise conditions of M_∞=0.80 with a fan nozzle pressure ratio (FNPR) of 2.40 and core nozzle pressure ratio (CNPR) of 2.0. The pressure distribution over the core-cowl and plug surfaces exhibited fluctuating behaviour owing to the presence of the shock wave series over the entire surface. On the other hand, Keith et al. [47] reported an effect of M_∞ on the shear layer over the external surface of the configuration.

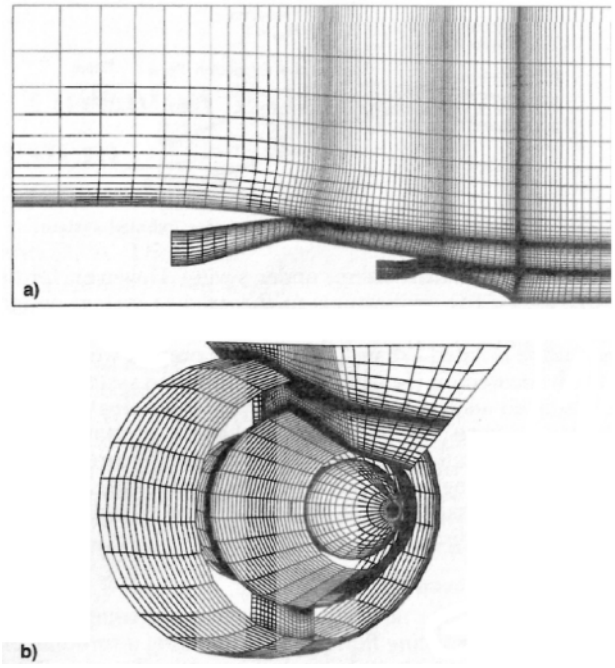

Figure 2.27 Separated flow exhaust nozzle: a) X-R planar grid; and b) isometric view - three-dimensional surface grid [47].

Abdul–Hamid et al.[48] modified the PAB3D code to solve the turbulent flow and evaluate the aerodynamic characteristics of a civil engine exhaust system. Three-dimensional CFD simulations for the turbofan using the Navier-Stokes equations coupled with the standard k-ε turbulence model was performed. The main aim was to assess the performance of the PAB3D code in simulating such flow features. The performance metrics calculations were carried out using a package that was developed by Carlson [40].

The performance of mixed and separate exhaust systems, combined with a pylon, were investigated. For a separated nozzle, the results showed that the mass flow rate of the fan nozzle and thrust coefficient were comparable to experimental data by -0.2% and +0.2%, respectively, (Figure 2.28 (a)). For a mixed nozzle, the discharge and thrust coefficient deviated from the experimental data by ∓0.1% and +0.6, respectively, (Figure 2.28 (b)).

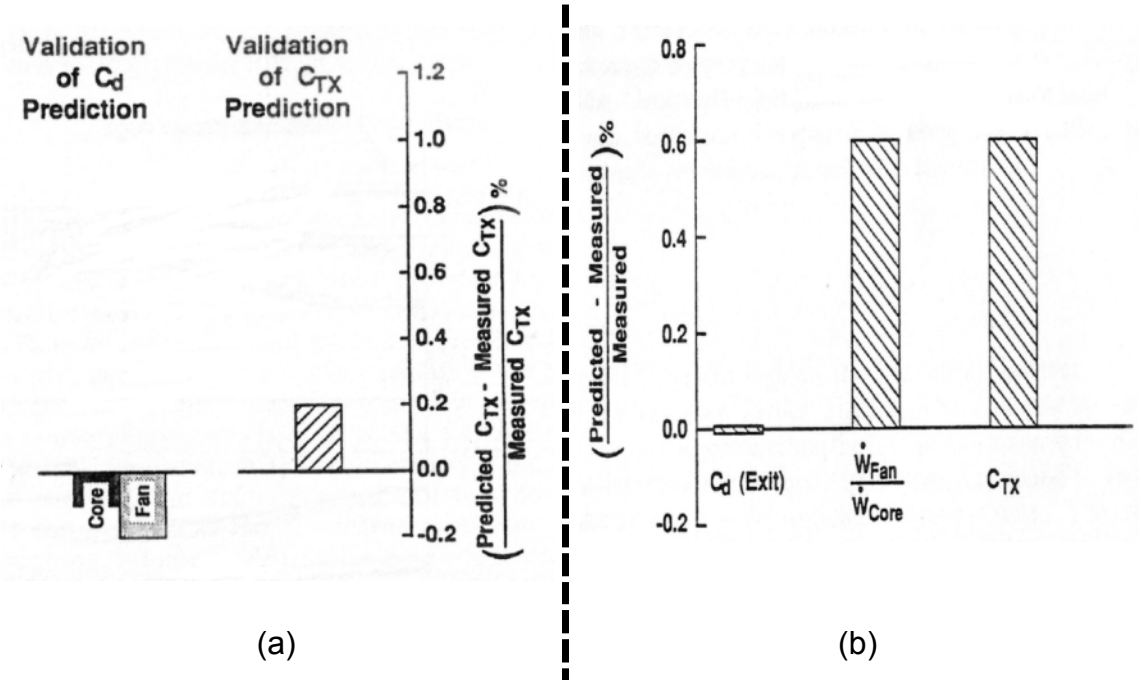

Figure 2.28 (a) Comparison between measured and predicted discharge and thrust coefficient (C_d, C_T) for separate flow configuration, (b) Comparison between measured and predicted discharge and thrust coefficient (C_d, C_T) for a mixed flow turbofan. [48]

Hebert and Ponsonby [49] described a CFD study for the exhaust nozzle at cruise and in the descent phase of a civil aero-engine. The results extracted were the pressure distribution over the core-cowl and an evaluation of the strength of the shock wave, which was the main source of drag in this region. The results were compared with the experimental data and demonstrated robust agreement, (Figure 2.29 and Figure 2.30).

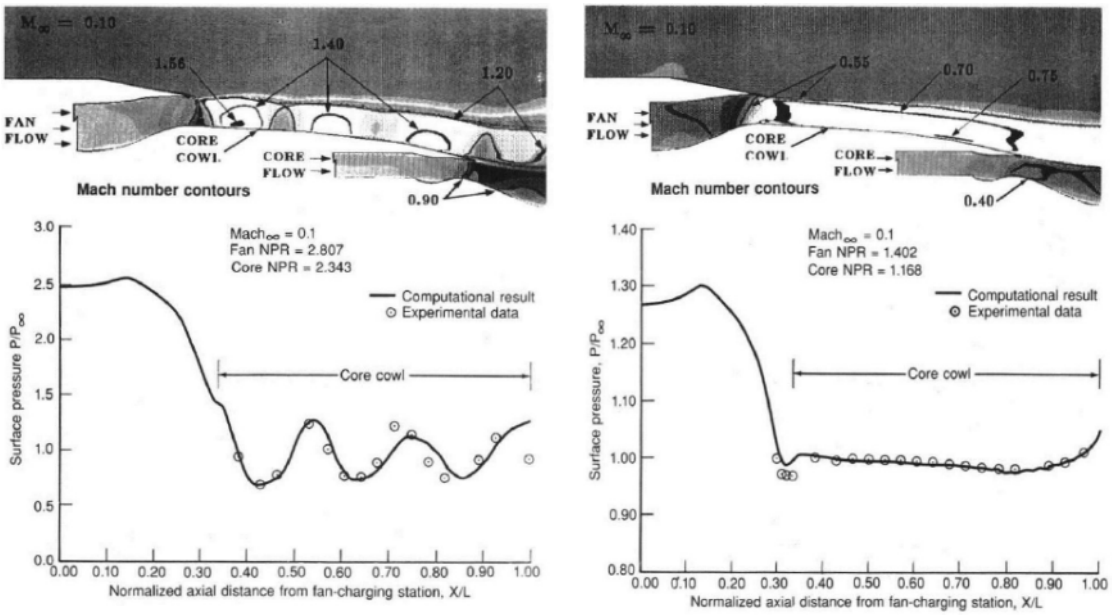

Figure 2.29 Mach number contour and pressure distribution along nozzle core-cowl compared with the experimental data at cruise nozzle running conditions [49].

Figure 2.30 Mach number contour and pressure distribution along nozzle core-cowl compared with the experimental data at decent nozzle running conditions [49].

An additional goal of this analysis was the prediction of nozzle performance coefficients (velocity coefficient: Cv). The comparisons with the experimental data suggested there to be a thrust coefficient difference of approximately 0.2-0.3% [49] through different NPR values, (Figure 2.31).

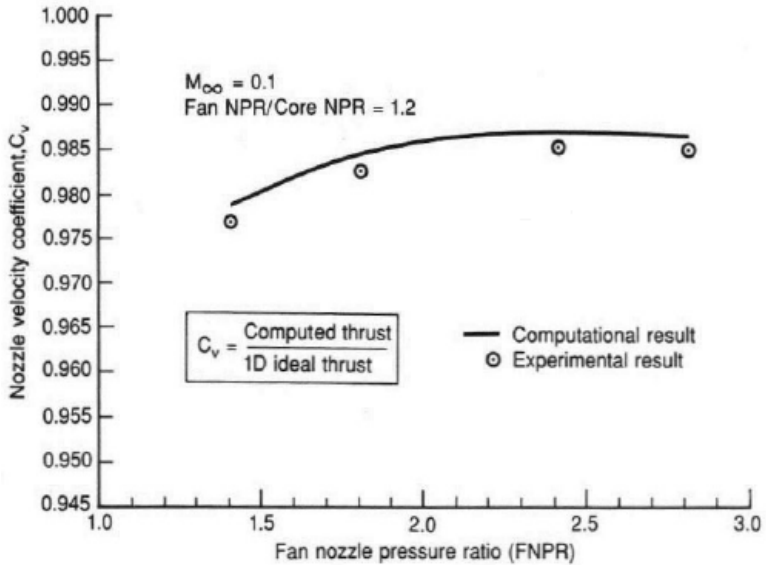

Figure 2.31 Comparison of the calculated nozzle velocity coefficient, Cv, with experimental data [49]

The geometrical features of the exhaust nozzle affect the aero-engine performance [50,51]. It was put forth by Eltis et al. [52] that the modification of the core-cowl angle from 11° to 15° of the RB211-22B engine improved the specific flying range by 5.5%. This was attributed to a reduction in the weight and favourable engine-wing interactions [52]. On the other hand, Lennard et al. [50] showed that the change in by-pass and core nozzle internal profile curvatures (Figure 2.32) enhanced the thrust coefficient under cruise conditions (high NPR) and deteriorated the discharge coefficient. The CFD results showed the gross thrust coefficient improved by 0.4% at FNPR of 2.74 [51] as compared with the baseline configuration results.

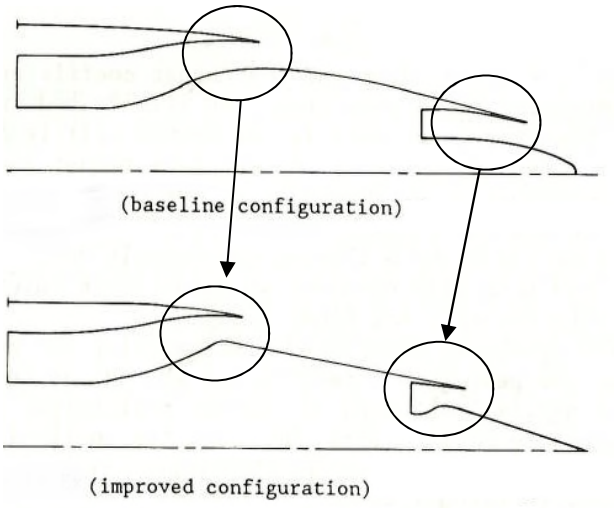

Figure 2.32 Baselines and improved geometry definitions of the exhaust system [50].

Zimmermann et al. [6,53] investigated the effect of changing the length of the core-cowl of an ultra-high by-pass ratio turbofan as well as evaluating the impact of the static back pressure on nozzle C_d with various numerical methods. The numerical scheme included employing the Reynolds-averaged Navier-Stokes equations and computing turbulent eddy viscosity by the standard k-ε model. The results showed that as the core-cowl length was increased, there was a reduction in the discharge coefficient of the fan nozzle and an increase in the thrust coefficient by 0.4% and 1.2%, respectively. On the other hand, the core nozzle showed an increase in the flow coefficient by 10% and reduction in the thrust coefficient by 4.3%.

In another work, Zimmermann et al. [53] compared the gross thrust of two different bypass ratio engines (12.2 and 18.2). The comparison was performed between the thrust and drag components of the two configurations, and the results showed there to be insignificant effects of the bypass ratio on the percentage gross thrust of the engine, (Figure 2.33). On the other hand, Zimmermann et al. [6] reported that the actual static back pressure of the core nozzle differed from the theoretical one.

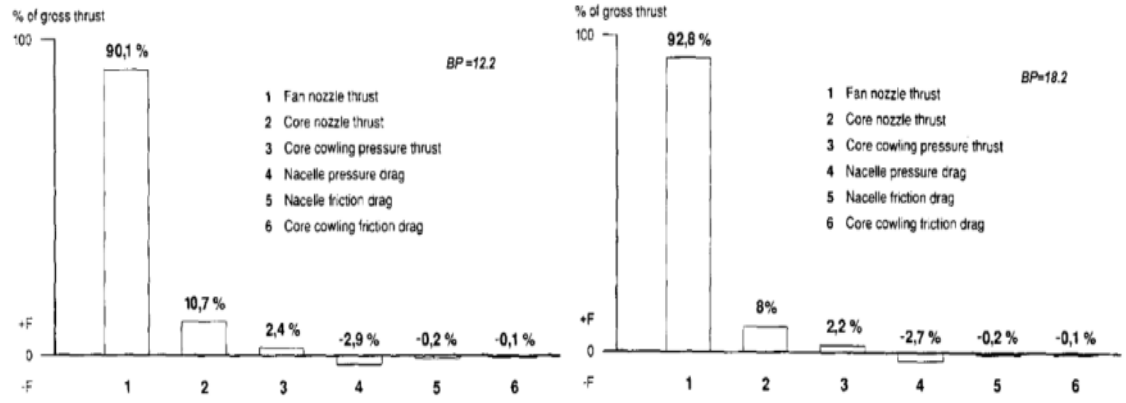

Figure 2.33 Thrust balance between two different engine by-pass ratio(12.2 and 18.2[53]).

First AIAA Propulsion Aerodynamics Workshop (PAW01)

The objective of the **PAW01** was the validation of a CFD simulation for a convergent-conical nozzle. The experimental data for this type of nozzle were taken from the work of Thornock et al. [26], including three different internal wall angles and one curved internal wall configuration, (Figure 2.34). CFD validation cases were set out for the workshop participants so that various numerical schemes and approaches could be compared. The achievement of three objectives was required from the PAW01 participants. The first was the comparison of the calculated nozzle performance metrics (discharge (C_d) and thrust (C_{fg}) coefficients) with the experimental ones. The second was the three-dimensional simulation of the nozzle with a 25˚ internal wall angle, splitter plate and NPR=4.0, and the results for the density gradient contour compared with the jet structure shadowgraph. The third goal was to produce unsteady vortex shedding using unsteady numerical calculations and compare the simulated results with the experimental shadowgraph.

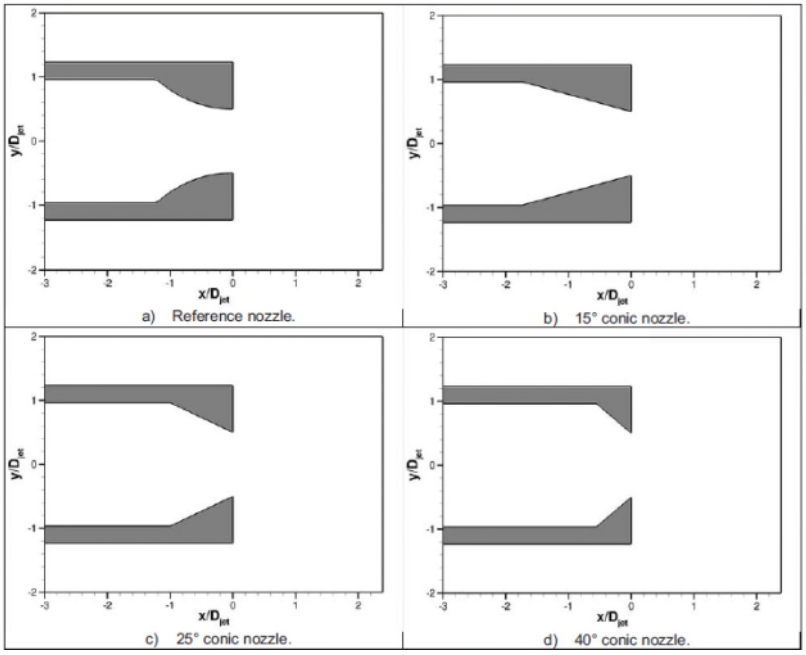

Figure 2.34 Nozzle aero-lines used by PAW01[54].

Spotts et al. [55] and Dippold [54] examined the performance of the **PAW01** nozzle using a CFD model built in CFD++ and Wind-US flow solver. The CFD++ code solves the RANS equations via a density-based solver. Three turbulence models were employed realisable k-ε, Menter shear-stress transport and Goldbrigd's realisable q-L. The results showed there to be little impact of these turbulence models on aerodynamic characteristics [55]. The validation results showed that the CFD++ calculated performance metrics over-predicted the discharge and thrust coefficients. No attempt was made by Spotts et al. [55] to predict unsteady vortex shedding. Dippold [54] utilised a second-order Roe numerical scheme and SST turbulence model in the investigation of nozzle performance for the steady state. The results showed the numerical calculations over-predicted the thrust coefficient within a range of 0.25% and 1.0%. Both authors ran their simulations at M_∞=0.0 within a range of NPR from 1.4 to 7.0. Dippold [54] simulated unsteady vortex shedding behind the nozzle with a splitter using URANS and detached eddy simulation (DES) models. Similarities with the experimental data were observed, but both numerical models showed flow dissipation earlier than the experimental results, (Figure 2.35) [54].

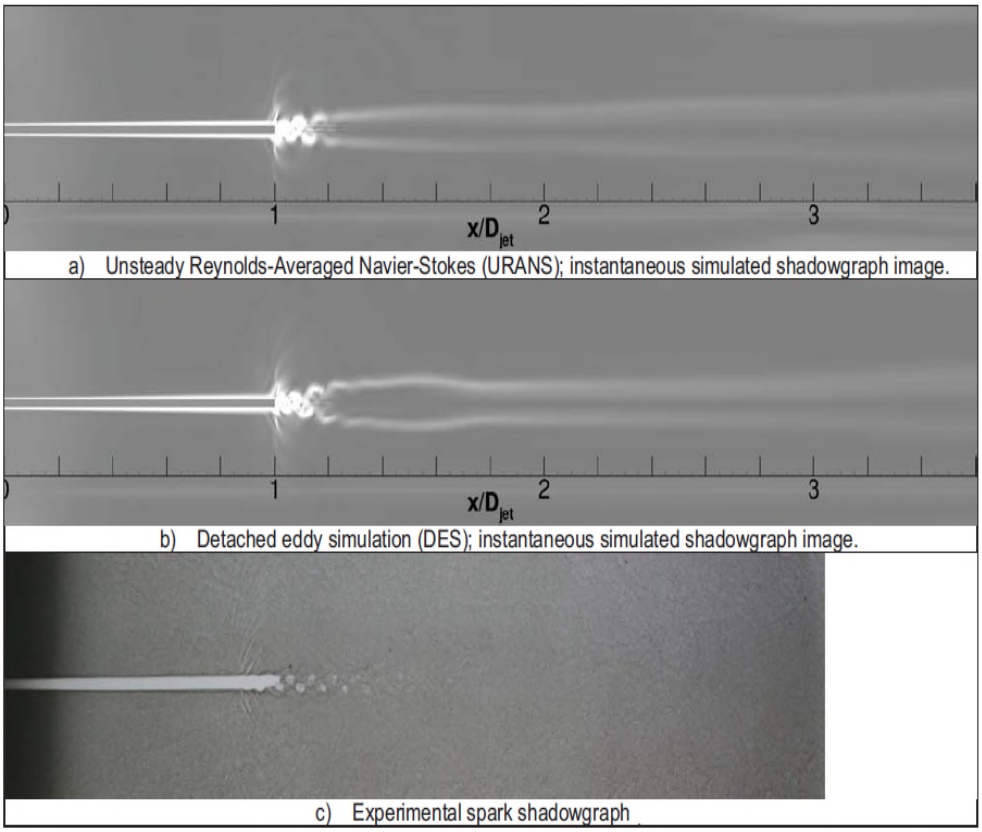

Figure 2.35 Vortex shedding at the trailing edge of a splitter plate used at the exit plane of a 25° conic nozzles at NPR=1.6 [54].

Zhang et al. [56] utilised the **PAW01** nozzle geometry and the coarse mesh to validate the NSAWET CFD code. They employed numerical model based on the finite volume discretization method. The employed turbulence model was k-ω SST. The results indicated that the CFD results compared with the experimental data within a range of -0.2% to -0.5% accuracy for C_d and C_{fg}, respectively. Zhang et al. [56] extended the work to include an unsteady simulation to capture the unsteady vortex shedding. The comparison between the CFD density gradient contour and the experimental shadowgraph suggested close agreement, (Figure 2.36).

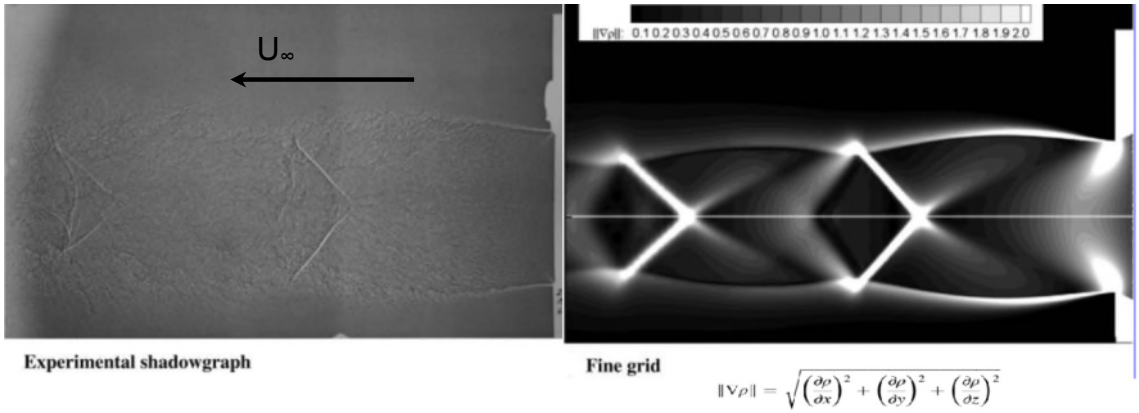

Figure 2.36 Comparison between the experimental shadowgraph and the CFD method data for the conical convergent nozzle [56].

Second AIAA Propulsion Aerodynamics Workshop (PAW02)

The objective of the **PAW02** was to assess the accuracy of CFD models in simulating multi-stream exhaust-system flows and review the **PAW01** nozzle simulation results. Domel [57] used LM Aero's Falcon CFD code to simulate the DSFR nozzle and produced initial performance data. The simulations were carried out through a range of FNPR from 1.4 to 2.6. The results were compared with other solvers' results by Domel [57]. The largest deviation was observed in the thrust coefficient for those simulations that were based on the coarse hybrid grid provided by the workshop for the given high NPR, which was roughly +0.25% greater than other simulations.

Li et al. [58] used the NSAWET code to simulate the flow around the DSFR at different FNPR (1.4 to 2.6) with a ratio of the total fan pressure to total core pressure (extraction ratio) of 1.2. Several turbulence models were employed in the simulations, including Spalart-Allmaras (SA), Wilcox k-ω, Menter k-ω-SST and the transitional k-kl models. The code was run for two different CFD domain types (three-dimensional and axisymmetric). The experimental data was not available at the time for the validation of these simulations. However, the results revealed a consistency. The three-dimensional computations agreed with the axisymmetric simulation in terms of the trends of the results.

The experimental work of **PAW02** was then carried out on the DSFR nozzle in the ASE FluiDyne Laboratory [33]. Afterwards, CFD calculations were performed

to validate the ability of the numerical model to predict nozzle performance [33]. A pressure-based solver (FLUENT) coupled with realisable k-ε turbulence was applied to perform the three-dimensional CFD simulations. The CFD domain was discretised using a hybrid mesh, (Figure 2.37). The computed nozzle performance results showed that the C_d when compared with the measured data, had a difference of -0.35% at NPR of 2.60 and -0.67% at NPR of 1.40 for the fan nozzle, and a relative difference of +0.6% for the core nozzle. The overall thrust coefficient differed from the experimental data by 0.03%, (Figure 2.38).

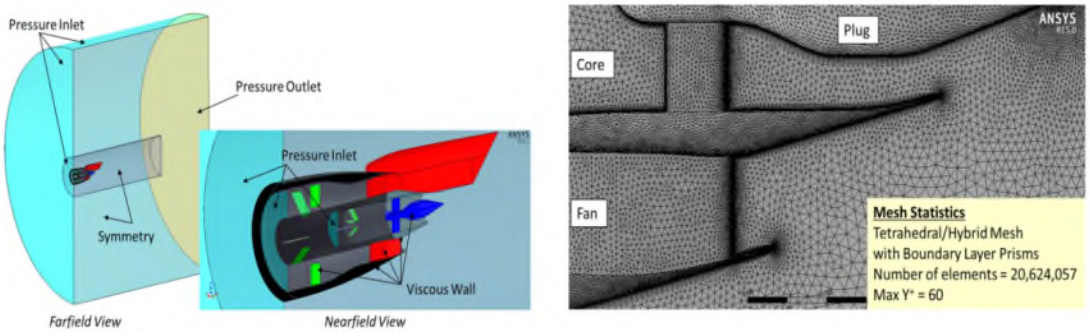

Figure 2.37 Mikkelsen's [33] CFD domain and Mesh.

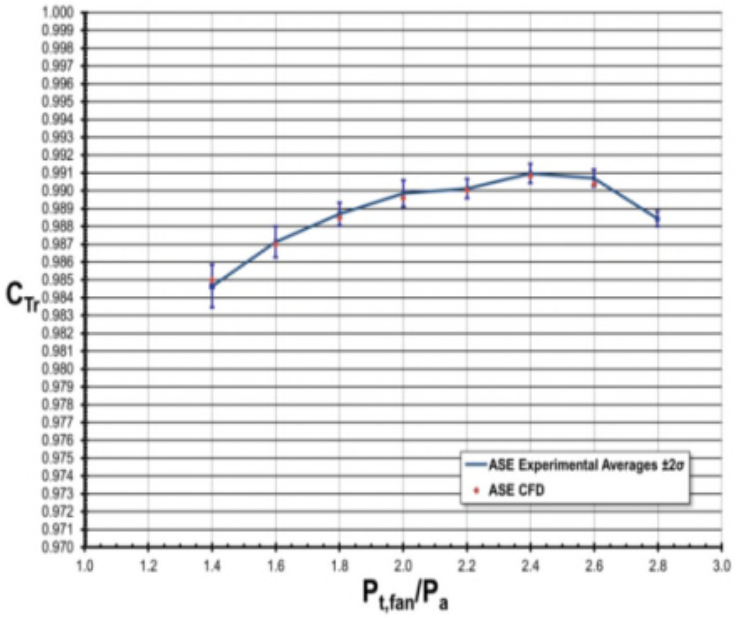

Figure 2.38 Thrust coefficient comparison between CFD and experimental data of DSFR nozzle [33].

2.2 Installed aero-engine aerodynamics

The state-of-the-art turbofan engine has a larger mass that goes through the bypass of the engine. This new development produced an engine that is environmentally efficient with low emissions, low noise, low fuel consumption and high performance. It was noticed by Kuchemann [59] that the provision of the large fan stream improved the propulsive efficiency of the engine itself by 25% at high-subsonic speeds compared to turbojet engines. The increase in engine mass flow compensated the reduction in the momentum flux owing to the velocity reduction of the exhaust jets [4]. The increase in the bypass mass led to an increase in engine size. The engine size was changed from a conventional Turbofan (TF) with the by-pass ratio (BPR) from 5.0 to 6.0 to higher BPR ranging from 9.3 for the Rolls Royce Trent to over 12 for the most modern Airbus designs. Thus, a large engine casing recognises a cutting-edge engine. The newly enlarged size of the engines has made the engine installation process problematic due to the aerodynamic interaction between the nacelle components and the wing at transonic free-stream Mach numbers. As a result, the interaction drag between the engine and the wing increased, (Figure 2.39).

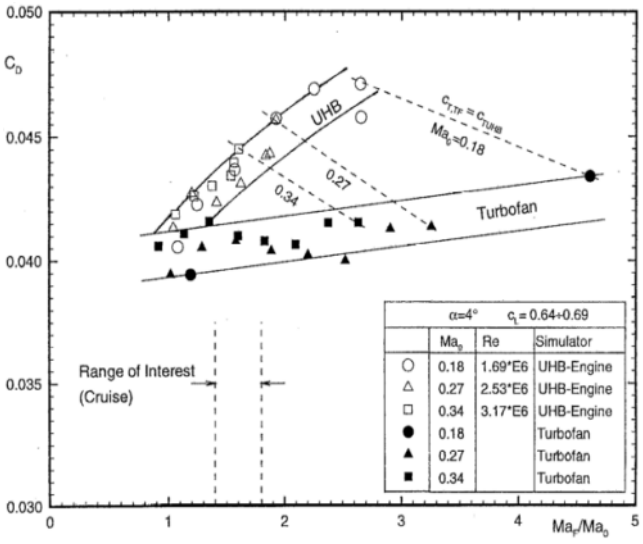

Figure 2.39 Measured jet interference drag as a function of the ratio of the fan exit Mach number to M_∞ [60].

The benefit of increasing the bypass ratio of the engine should outweigh the associated high engine drag and the interference penalties over the full range of the flight envelope. Therefore, it is important to evaluate the installed engine

performance at an early stage of the design process to quantify the impact of the installation process on the overall engine and its components' performances.

Although the current project is mainly focused on the effect of the installation on the performance of the exhaust system, the drag and flow field features in the interaction region between the wing and the nacelle are discussed here. As there is a noticeable interaction between the nozzle jet and after-body of the nacelle, it is important to rate the impact of the installation on the overall nacelle drag as the afterbody is included in the drag domain. Furthermore, the channel flow between the engine and the wing is of importance seeing that it represents the main region of interaction between the wing and the external flow field that surrounds the nozzle. The components of the nacelle in this region (boat-tail and pylon junction) are considered in many drag-accounting methods and are included in bookkeeping techniques [12,61–63]. However, recent accounting methods of nozzle performance include the after-body as a part of the nozzle thrust control volume [64]. Evaluation of the installation impact is achieved by employing wind tunnel investigation on scaled wing-body-engine models in addition to using CFD.

2.2.1 Experimental studies for the assessment of installed engine aerodynamic interactions

One of the earliest experimental rigs used to simulate engine installations was a 610 mm x 460 mm (2.0ft by 1.5ft) transonic wind tunnel at RAE Bedford. The experimental configuration consisted of a powered exhaust system with a dual-stream nozzle and two-dimensional wing (infinite wing with a span extended from side to side of the wind tunnel), (Figure 2.40) [65].

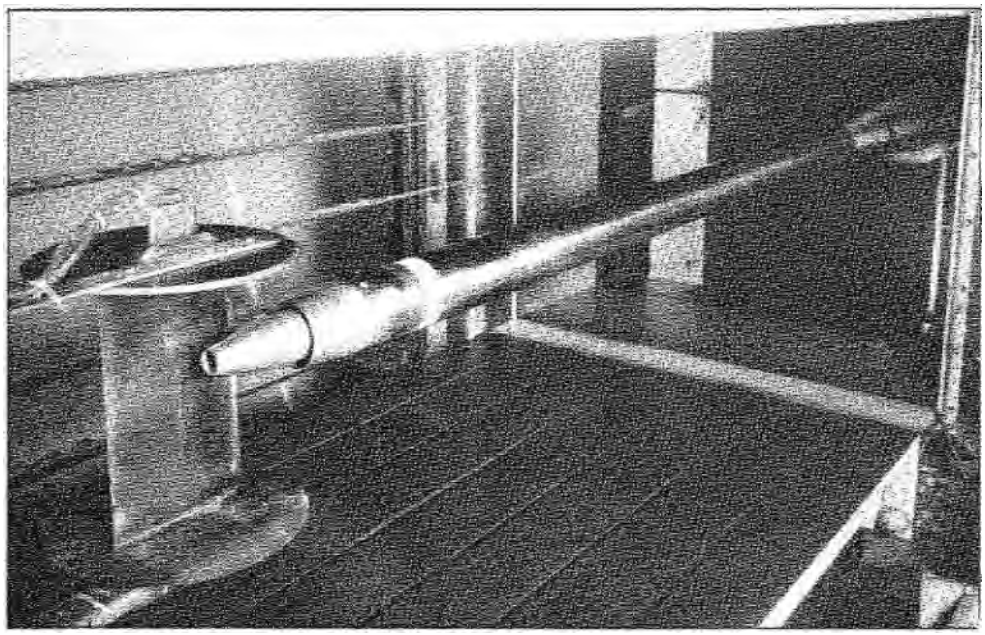

Figure 2.40 Wind tunnel model including the exhaust system and two-dimensional wing configuration [65].

Although the work was aimed at understanding the effect of the jet on wing aerodynamics, Raney et al. [65] provided a shadowgraph describing the flow structure of the jet from the bypass nozzle, (Figure 2.41). It was observed that the increase in the nozzle pressure ratio (NPR) strengthened the intensity of the shock series. Moreover, Raney et al. [65] observed the dependence of the nozzle jet on M_∞, NPR and wing incidence.

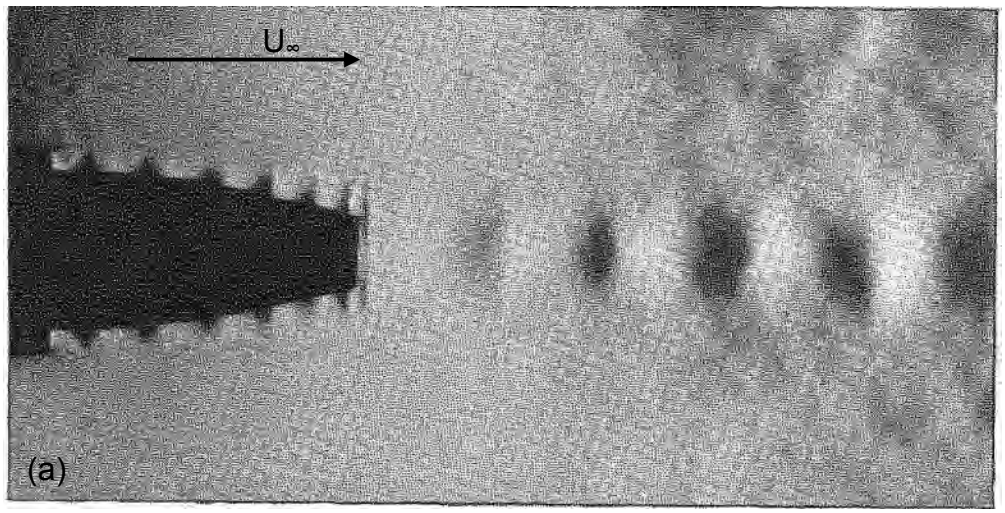

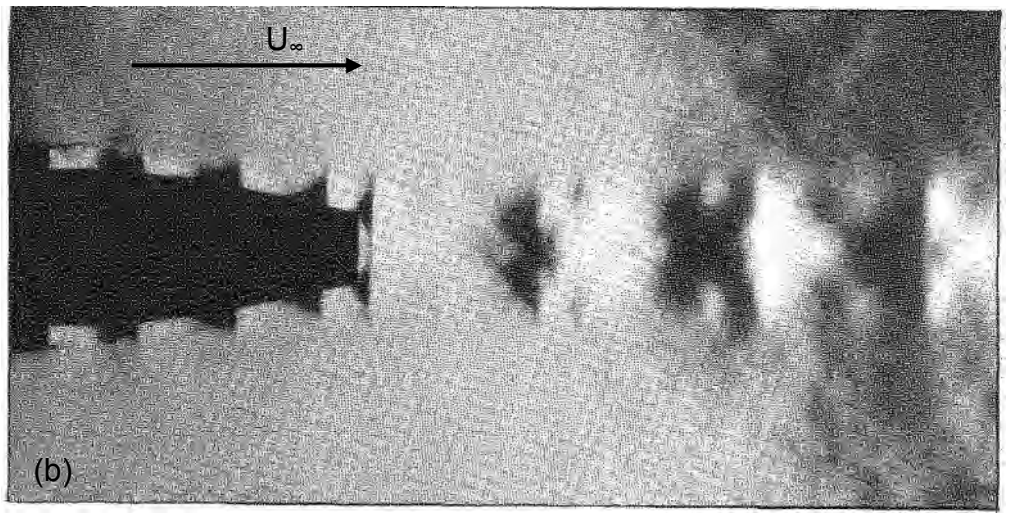

Figure 2.41 Schlieren photographs of flow exhausts from bypass nozzle: (a) M_∞=0.7, NPR=2.4; (b) M_∞=0.7 and NPR=3.0 [65].

Patterson et al. [66] conducted an experimental investigation using the NASA wind tunnel facility for a powered nacelle installed on a transport aeroplane, (Figure 2.42). The result was compared with certain through-flow nacelle configurations for the sake of understanding jet interference. Patterson et al. [66] reported a pressure fluctuation at the outboard pylon-engine junction owing to the presence of the jet flow of the engine, (Figure 2.43).

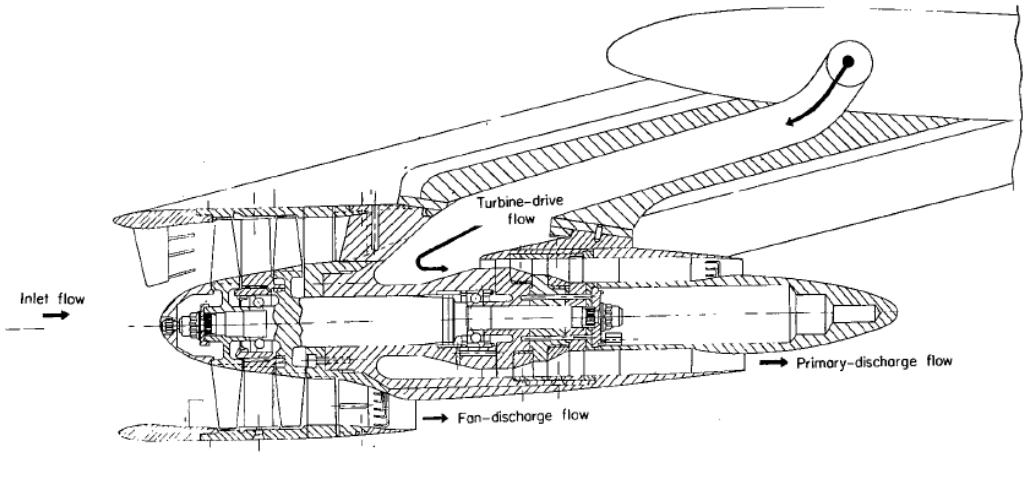

Figure 2.42 Powered engine-wing configuration [66]

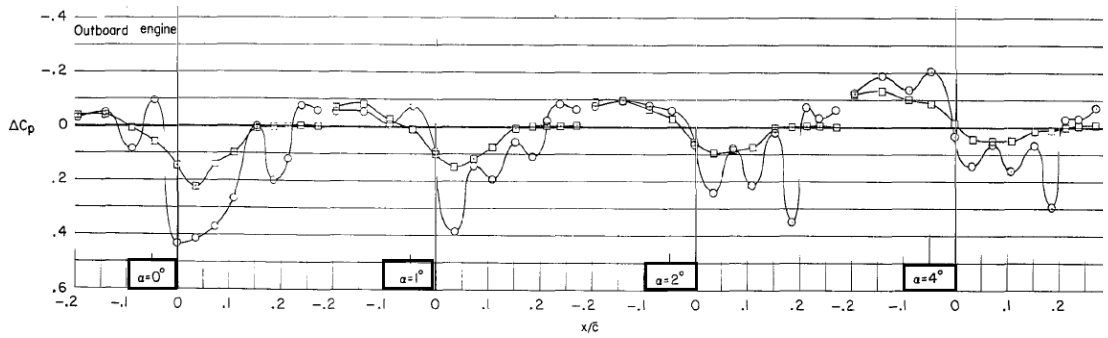

Figure 2.43 Pressure distribution at the engine pylon junction; the comparison between jet-on and jet-off operating conditions at a various angle of attack (α) [66].

An experimental test was conducted in the NASA Ames 3350 mm (11.0 ft) wind tunnel with a long duct nacelle installed on DC-8-50 and -60 aircraft models by Callaghan et al. [67]. Four different external geometry profiles were examined in the presence of the pylon. The results demonstrated there to be an increase in the local Mach number in the region of the channel flow (the region between the engine and wing) as the lift coefficient increased. As C_L was decreased from 0.4 to 0.3 at M_∞=0.82, a reduction in the local Mach number of the channel flow was detected, (Figure 2.44).

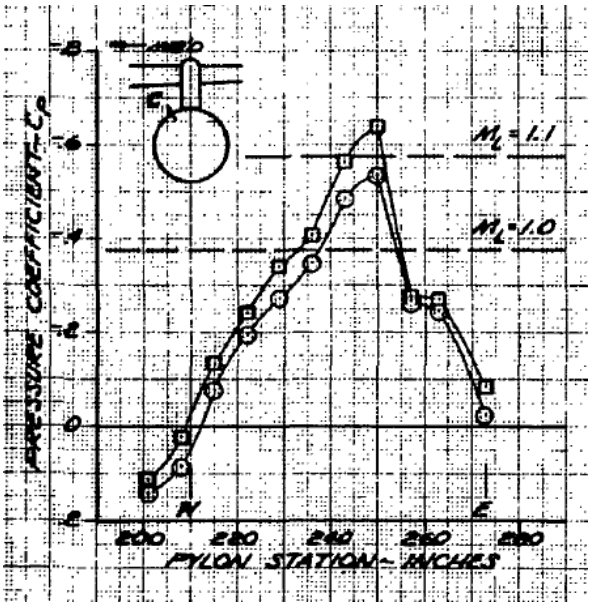

Figure 2.44 Effect of the lift coefficient variation on channel pressure distribution over the nacelle surface extended from wing leading edge (w) to nacelle exit plane (E) at M_∞=0.82 (square symbols: C_L=0.3; circles: C_L=0.4) [67].

The powered testing technique was employed in the ARA wind tunnel for determining drag force interaction and nozzle/after-body performance [68].

Several powered models were made use of to simulate isolated and installed engines on a full span and half-span wing-body with a nozzle/after-body system [68]. The latter was employed to measure the performance of low- and high-speed flight for a dual-stream nozzle, (Figure 2.45). The nozzle performance data presented by Harris et al. [68] were for different M_∞. The presence of the external flow retarded the performance of the fan nozzle, (Figure 2.46). Harris et al. [68] stated that the thrust coefficient derived from this test model included the free-stream effect on the drag of the nozzle after-body (core-cowl) and fan-cowl after-body and changed its contributions to the performance.

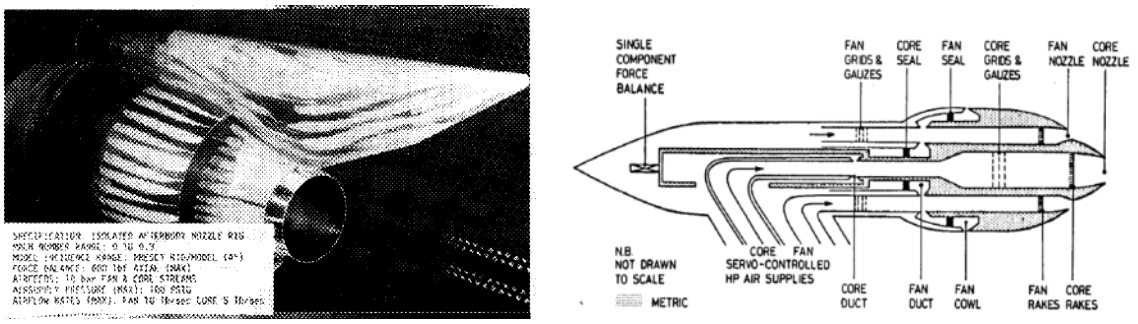

Figure 2.45 Schematic of after-body nozzle performance measuring rig [68].

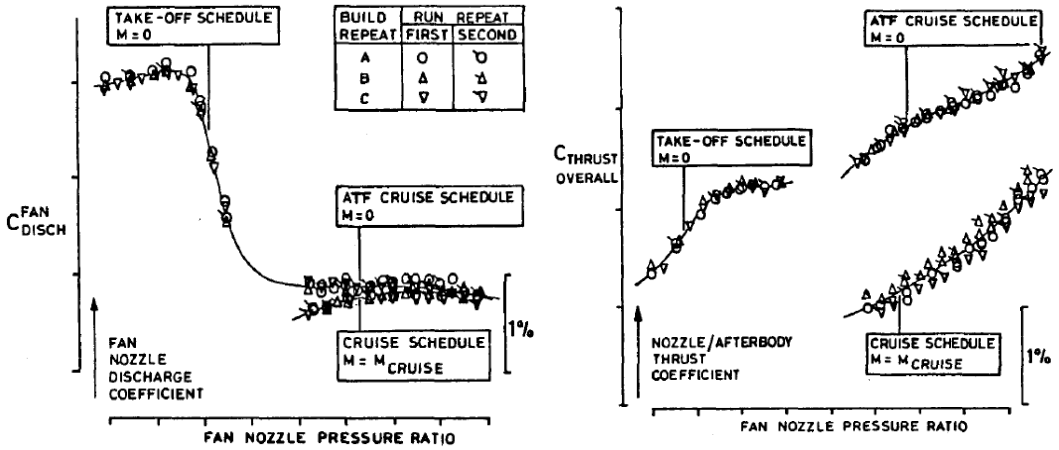

Figure 2.46 (a) Fan nozzle discharge coefficient as a function of NPR and M_∞. (b) Fan nozzle thrust coefficient as a function of NPR and M_∞ [68].

Hoheisel et al. [69] measured the velocity components and turbulence intensity using a three-component laser-doppler anemometer (LDA) within the bypass jet flow of a CFM56-5 engine installed on an A320 wing. Static conditions and different engine non-dimensional rotational speeds of 60%, 70%, 80% and 85%

were the test conditions. The aerodynamic flow description was taken from this measurement in terms of several profiles of velocity components provided for different fan rotation speeds, (Figure 2.47). In addition to the speed component at the exit of the nozzle, the flow angle was also presented, (Figure 2.48). Hoheisel et al. [69] concluded that for this set of data, the quality of the jet flow of the particular engine could be described. Furthermore, the presence of the wing and the pylon increased the spreading rate of the nozzle jet flow and diminished the NPR variation effect on the upper region of the engine relative to the lower part of the engine. Furthermore, for this engine, the flow deviated from the engine axis by an angle of 3.5˚.

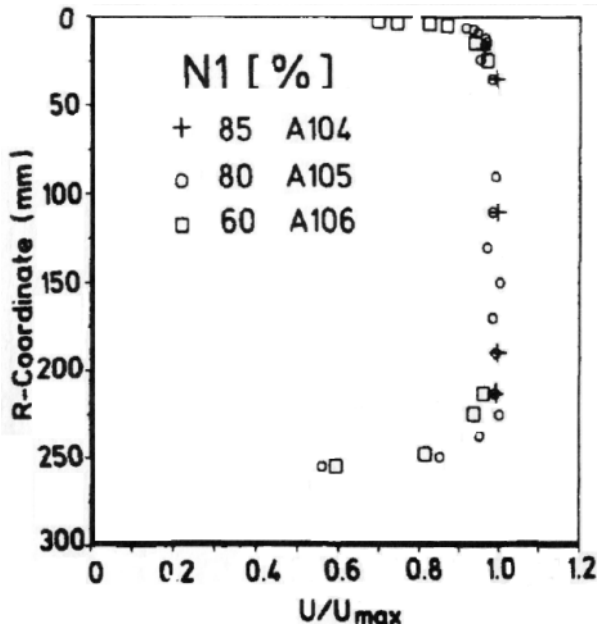

Figure 2.47 Radial velocity profile at the fan nozzle exit [69].

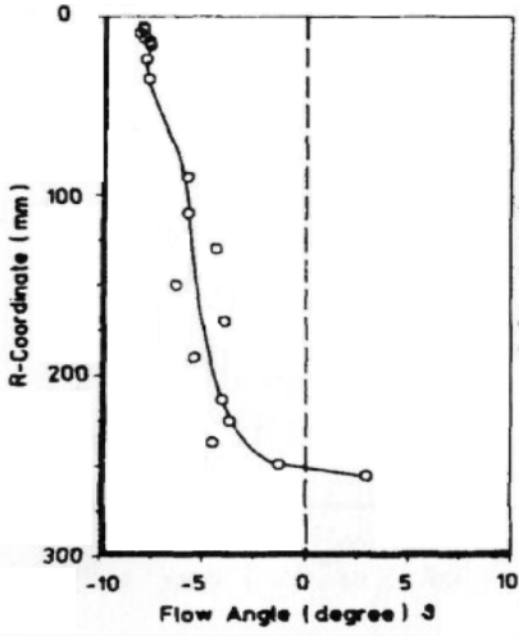

Figure 2.48 Flow angle profile at the fan nozzle exit [69].

Another test was carried out to measure the velocity and turbulence intensity at the core nozzle using LDA rig for an engine installed in the testbed with a pylon [70], (Figure 2.49). It was noticed that the velocity component at the core nozzle lip was lowest (closest to the tip of the low-pressure turbine hub). Conversely, the turbulence had the highest value close to the axis of the engine, (Figure 2.50) [70].

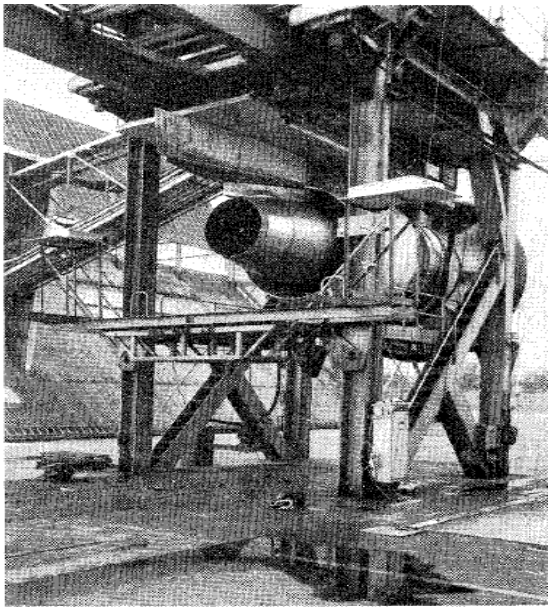

Figure 2.49 RB211 installed on a test bed [70].

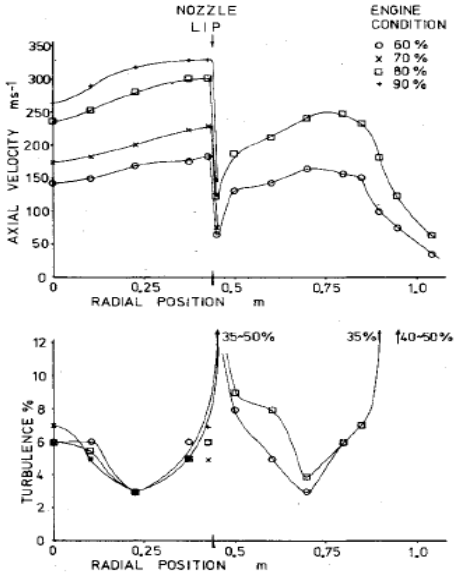

Figure 2.50 Axial velocity profile (upper) and turbulence profile (lower) [70].

Currently, several facilities exist around the world to experiment on both isolated and installed engines and aircraft. The development of the transonic wind tunnel has enabled engine installations to be investigated and estimate the drag at high-subsonic conditions. This has led to a series of aeroplane design modifications, including a variation of engine size and installed engine placement. For instance, several wind tunnel tests have been conducted using the half span of a scaled aircraft. The ONERA NASA Ames and ARA wind tunnels, equipped with turbine power simulators (TPS), were employed to evaluate the installation impact on jet flow and aircraft performance. Consequently, the development of a number of conventional engine and aeroplane designs was achieved, (Figure 2.51) [71, 72].

Figure 2.51 Half-span aircraft model with TPS mounted on the ONERA (left) and Ames wind tunnels (right) [59,71].

DLR-ALVAST Model

The ALVAST is a generic civil aircraft model equipped with a turbine-driven engine and has been used to study the interference effect between an engine exit jet and a wing [2]. Maximum operating free-stream Mach number for this model was 0.75 with a C_L of 0.5. This model was evaluated during the EU project, ENIFAIR.

The ALVAST-model, (Figure 2.52), equipped with TPS, was used to simulate the installation effect of HBPR, VHBPR and UHBPR (CRUF (Counter-Rotating Ultra-high Bypass Fan)) engines on aircraft performance for a range of angles of attack from 0.0°-8.0°. The experiment was carried out in a German-Dutch wind tunnel [2]. The results suggested there were noticeable drag interactions between the engine and aircraft where exhaust jet affected approximately 60% of the wingspan length.

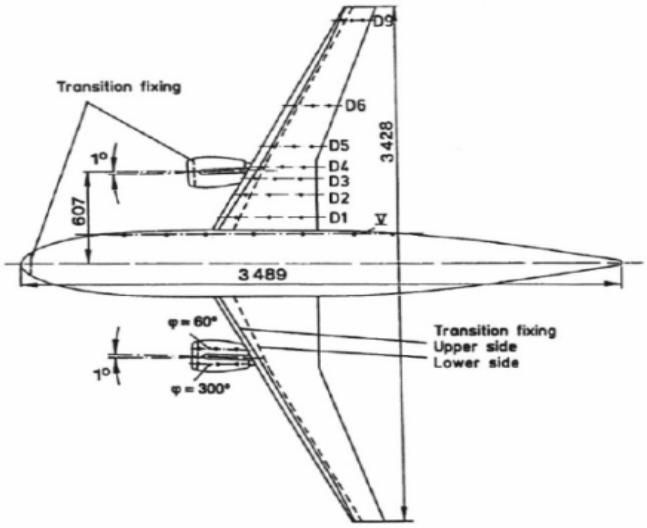

Figure 2.52 Sketch of the ALVAST model [2].

Hoheisel et al. [73] evaluated the impact of the increase in the engine by-pass ratio over the range from 6.0 to 17, and the influence of engine thrust behaviour on the aerodynamic performance of the aircraft. The tests were carried out in the ONERA S1MA wind tunnel. The scaled model of A320 geometry (DLR-ALVAST) was used, (Figure 2.53) [73].

Figure 2.53 ALVAST model equipped with different engine simulators in the test section of the ONERA S1MA wind tunnel [73].

Comparison between three different test configurations showed there to be an increase in the nacelle drag with bypass ratio, (Figure 2.54). This comparison included the effect of jet interference with the wing for the installed engine case, (Figure 2.54). The effect of the jet interference was correlated with the difference between the drag values for a through-flow nacelle (TFN) and the

engine running at SOC (maximum thrust - the start of the cruise) conditions [73]. The increase in the drag coefficient (C_D) due to the jet's influence was ≈2.3% for the turbofan; this value rose for the UHBR engine to 3.9% [73].

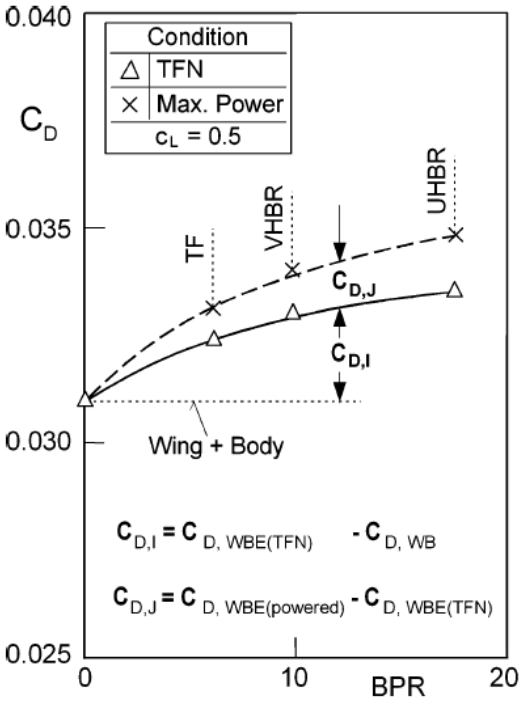

Figure 2.54 Variation in the drag coefficient (C_D) as a function of by-pass ratio and jet interaction for wing-body engine configuration WBPE at M_∞=0.75 [73].

DLR-F6 Model

The ***DLR-F6*** *model* is a transonic model of a transport aircraft designed by the German Aerospace Centre; it was derived from an older model, the DLR-F4 [74]. The model was designed for a transonic M_∞ of 0.75 and a corresponding lift coefficient of 0.5. It is a wing-body configuration of a scaled twin-engine aeroplane, (Figure 2.55). The model can be equipped with different engine configurations to quantify the interaction effect between the aeroplane and nacelle [74]. The aim of developing this model was to provide validation data for the AIAA Drag Prediction Workshop [74].

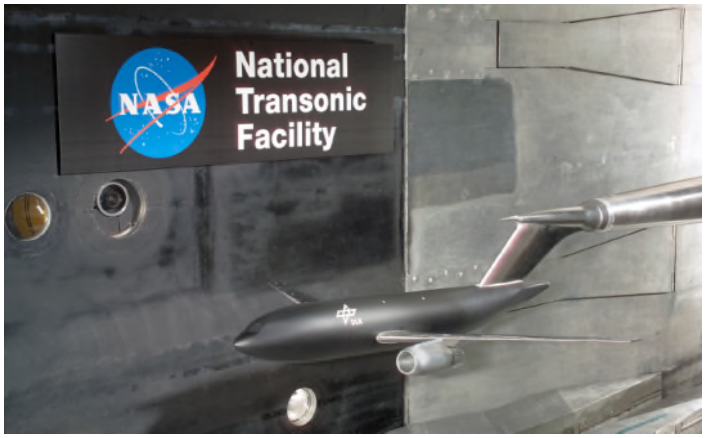

Figure 2.55 Photograph of the DLR-F6 model mounted in the test section of the NASA National Transonic Facility [74].

NASA Common Research Model (CRM)

The NASA Common Research Model (CRM) is the latest version of the scaled civil aircraft model, (Figure 2.56). The model was designed for M_∞ of 0.85 with corresponding C_L of 0.5 [75] but was used with M_∞ across a range from 0.7 to 0.87 [76]. The CRM was designed by NASA to validate current CFD codes and analyse the flow around modern aeroplane configurations [77]. The CRM model has been widely used in Drag Prediction Workshops and has high-quality and abundant experimental data with details of flow measurements, including force, momentum, pressure, and skin friction data in addition to experimental data on the unsteady flow features [77].

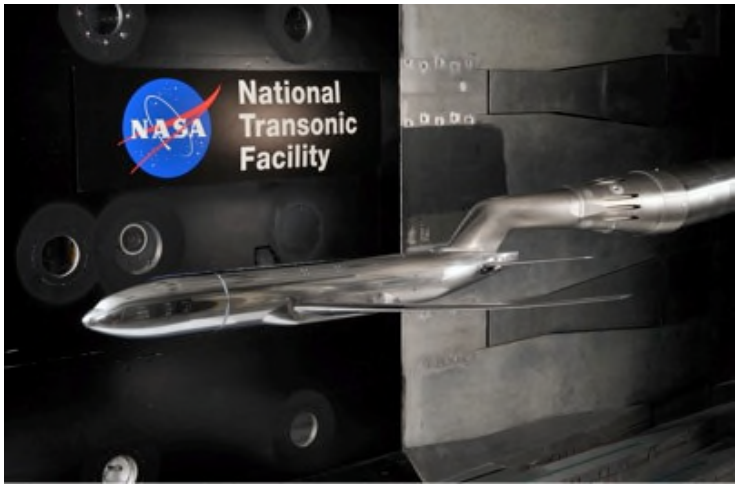

Figure 2.56 Photograph of the CRM model mounted in the test section of the National Transonic Facility [77].

2.2.2 Numerical studies of the assessment of installed engine aerodynamic interactions

Aeronautical ground test facilities can model more of the physical features of flow, but they require long lead times for testing a new configuration in addition to having very high costs [78]. Using such facilities, aircraft programmes have incurred high development costs and taken a long time to verify design modifications [79]. The replacement of the in-flight testing of flow behaviour around the aircraft was through the wind tunnel test. However, the use of a wind tunnel does not produce data at high flight Reynold's number (Re) values [80], which can lead to inaccuracies in measurements of the wing interference with really long cowl engines, (Figure 2.57) [15].

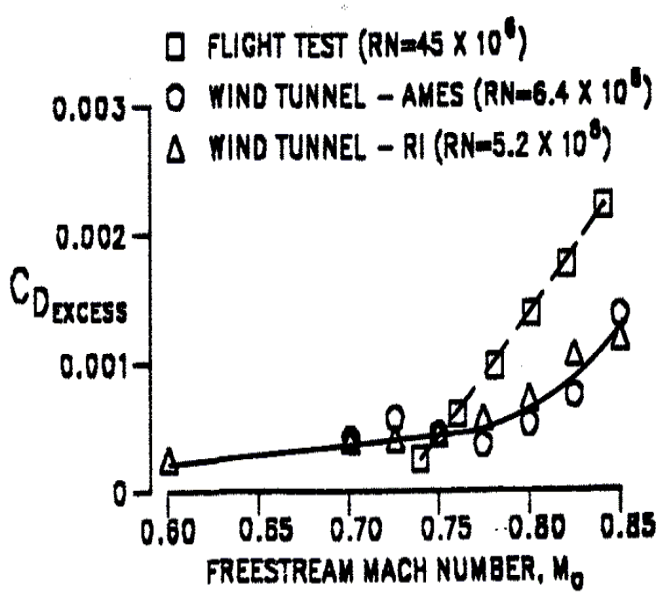

Figure 2.57 Flight test, wind tunnel and full-scale nacelle drag coefficient as a function of Re values of 45x10^8, 6.4 x10^8 and 6.4 x10^8 [15]

It became imperative to use another technique to overcome these drawbacks and implement the required corrections to the wind tunnel data. Computational Fluid Dynamics (CFD) methods are now widely used and play a central part in the development of all aerospace investment and research studies [80]. CFD can yield more details of a flow field than a wind tunnel because all aerodynamic parameters are computed at each grid point [79]. In addition, it has the capability

of determining and optimising parameter configurations before committing to model construction. In this respect, CFD calculations assist in making more efficient use of the ground test facilities. CFD not only provides a detailed study of the sources of the flow interactions but also enables a fast method to book-keep the forces and quantify interference effects. One of the primary CFD advantages over wind tunnel tests is its capability to explore the effect of the closed-coupled nacelle on the wing, (Figure 2.58). In sum, CFD and ground test facilities are complementary to one another, not competitors.

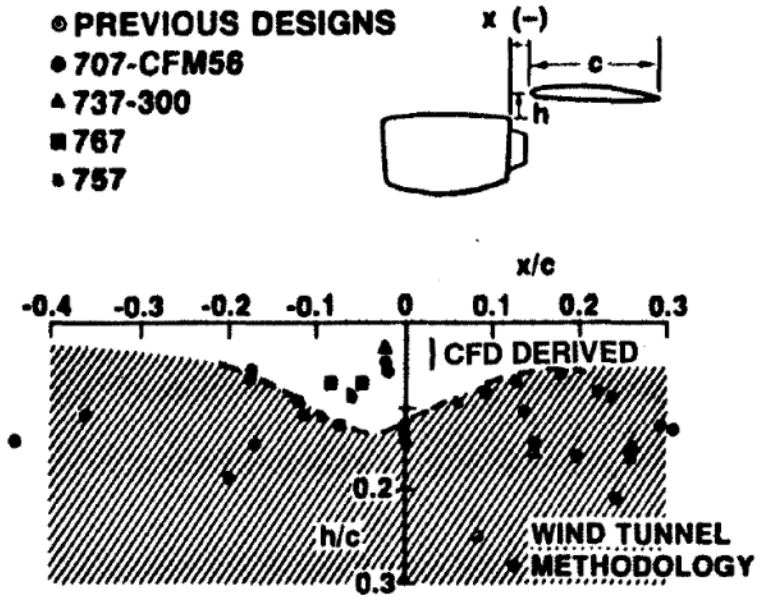

Figure 2.58 CFD derived close-coupled nacelle applied to design of Boeing KC-135R nacelle installation [15].

In this section, the discussion is on currently available CFD studies concerned with nacelle-wing interference. The focus is mainly on CFD studies that tackled the interference between the wing and exhaust system.

Reidel et al. [81] reported the interaction effect between the wing and nacelle installed over the wing using Euler calculations. The interaction was presented as a static pressure distribution at various stations over the nacelle with a change in the azimuthal angle. The installation results showed a reduction in the pressure at circumferential angles of 140˚ and 220˚, (Figure 2.59). Moreover, the pressure distribution on the inboard side indicated there to be a further reduction in comparison with the outboard side, (Figure 2.59). In general,

Euler's calculations results demonstrated agreement with the flight data except over the trailing edge of the nacelle [81].

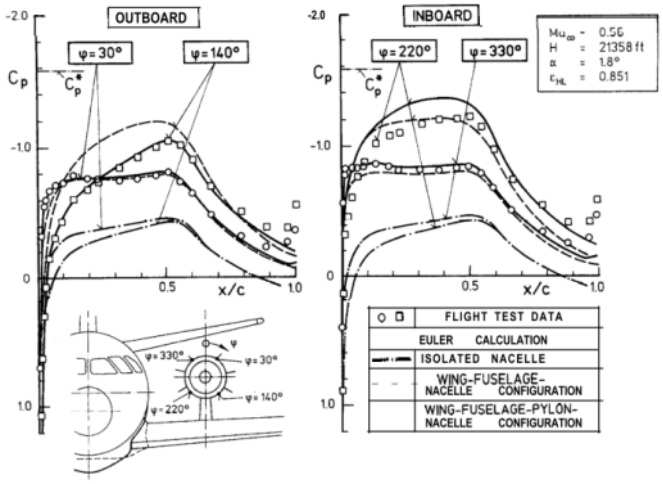

Figure 2.59 Comparison between the flight test data and Euler calculations for a static pressure of the external flow over the NLF nacelle fan cowl at cruise phase; the comparison includes a comparison between isolated and installed nacelles [81].

Rossow and Hoheisel [82] solved Euler's equations to simulate the flow around a nacelle-wing configuration for three different engine BPRs (HBR, VHBR and UHBR). The simulations were conducted with DLR-code CEVCATS [82]. The engine position was changed with respect to the wing leading edge and, as was expected, the UHBR exhibited the greatest interaction with the wing [82]. This interaction became significant when the nacelle was located very close to the wing [82]. Rudnik and Rossow [1] also drew the same conclusions after carrying out a numerical analysis for different engine sizes installed on the ALVAST aeroplane model. They found the interference effect increased with engine size. There was no significant flow interaction owing to the vertical distance change, whereas in the horizontal direction, the engine movement produced a significant effect [1]. Rudnik and Rossow [1] also compared different CFD approaches, including Euler's, Euler's with viscosity corrections and RANS equations. The CFD results for the Euler solution with the viscosity corrections were in line with the experimental data regarding pressure distribution over the wing surfaces and comparable results with the RANS solutions, (Figure 2.60) [1].

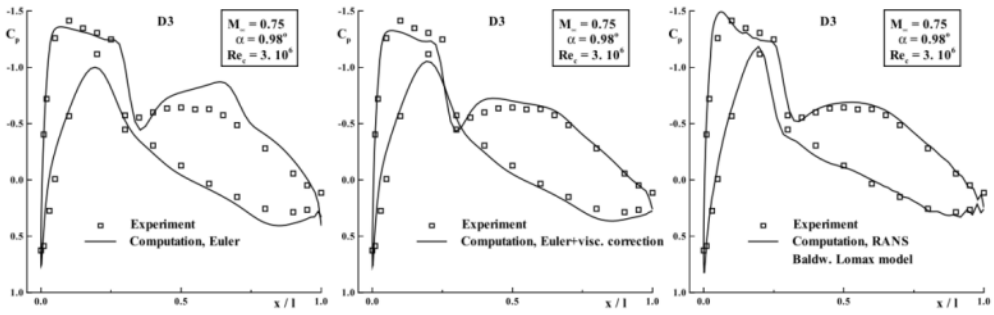

Figure 2.60 Comparison between CFD approach capabilities for simulating pressure distribution over the wing [1]

Brodersen and Stumer [83], Devine et al. [84] and Souza et al. [85] employed Navier-Stokes equations to perform a validation study for a CFD model with open-domain experimental data for different configurations of engines installed under the wing of DLR-F6 aircraft. Devine et al. [84] and Brodersen and Stumer [83] employed prismatic mesh elements to simulate the viscous sub-layer and Souza et al. [85] utilised hexahedral mesh to discretise the CFD domain. The results showed the ability of CFD and the mesh to predict the pressure distribution within an acceptable range of accuracy. Brodersen [86] along with Brodersen and Stumer [83] performed a sensitivity study varying engine positions and type. Two types of TFN long-nacelle engines (CFM56 and VHBR) were investigated. The positions of the engines were changed to simulate the engines' effect on nacelle drag and aircraft performance [83].

Burgsmuller [2] reported, using CFD simulations, there was an increase in the drag coefficient of the aircraft owing to the installation of a TFN on wing-body configuration. This increase was accompanied by a loss in lift coefficient when the simulations were carried out under take-off operating conditions with the angle of attack in the range of zero to 8.0°. Yet, the integration of TPS increased the interference drag in comparison with TFN. The wing lift distribution was affected by the jet interference through the region up to 60% of the wingspan [2].

Although there is supersonic flow in the channel between the long-nacelle and the wing, no wave drag or boundary-layer separation was determined in this

region. Generally, for this type of nacelle, the wing interference has little impact on nozzle performance.

Hoheisel et al. [87] evaluated the impact of the wing on nacelle surface pressure numerically. The configuration combined a TPS and scaled geometry of an A320 aeroplane. The numerical model consisted of solving Euler's equations. The pressure distribution over the nacelle circumferential surface was in agreement with experimental data except for the trailing edge of the nacelle, (Figure 2.61). The presence of the wing caused a decrease in pressure at the forebody of the nacelle and increased at its trailing edge, (Figure 2.61).

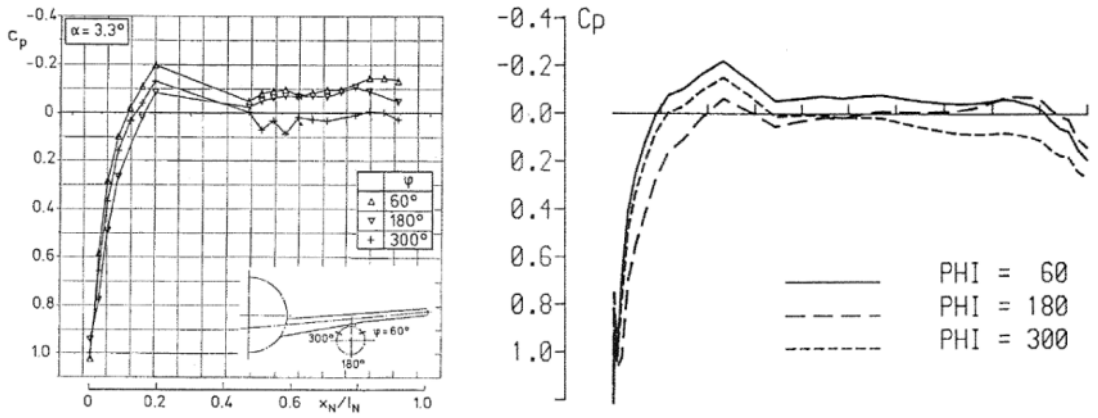

Figure 2.61 Comparison between the calculated and experimental data of the nacelle circumferential surface pressure distribution [87].

Hoheisel et al. [60] pointed out that the local high-speed flow under the wing that was accelerated because of the wing nacelle virtual channel is one of the reasons for the losses in the nozzle and the distortion of the fan exit flow. The high-speed flow in the region between the wing and the nacelle owing to the presence of the pylon will alter the flow field at the fan nozzle exit, (Figure 2.62). The high-pressure region under the wing zone will deflect the thrust vector downward as this is considered one of the thrust-loss sources [60]. The high-speed region under the wing reduces the static pressure over the external upper surface of the nacelle on the inboard side of the nacelle.

On the other hand, the presence of the jet will elevate the interaction between the wing and jet plume [88]. This interference effect is accentuated whenever the engine is installed closer to the wing [89].

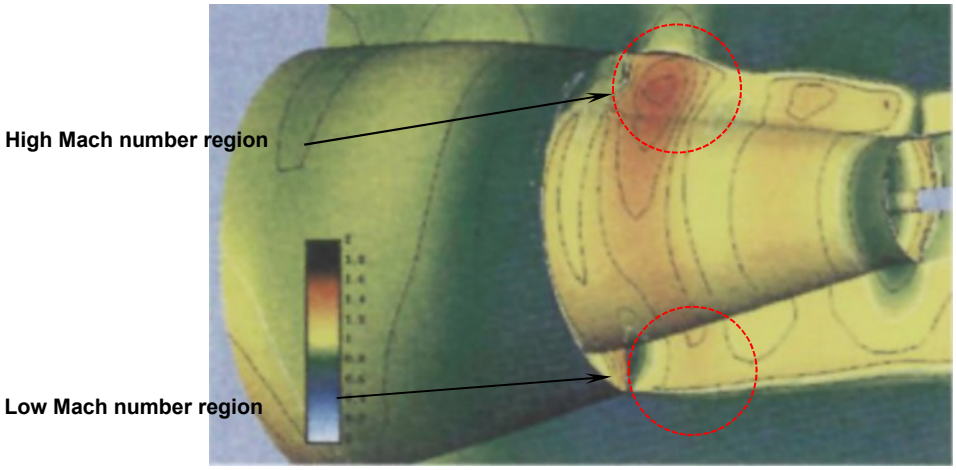

Figure 2.62 Mach number contour is showing the distorted and undistorted exit [60].

The effect of M_∞ was studied by Geyer et al. [3]. The numerical calculations were performed on TF and VHBR engines. A range of M_∞ was employed while retaining the power settings of the engine constant. The results revealed a reduction in the nacelle surface pressure as the M_∞ increased from 0.0 to 0.75. However, this behaviour was reversed at the trailing edge of the nacelle, (Figure 2.63). This was attributed to the effect of the exhaust jet plume which, with the decrease in M_∞, the rate of separation of the jet increased, and this altered the recompression region at the nacelle trailing edge [3].

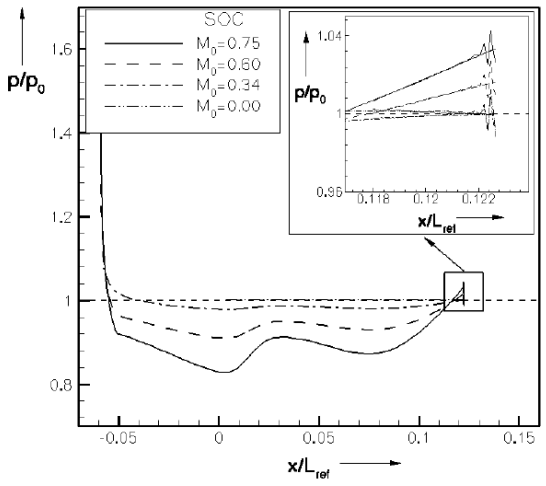

Figure 2.63 Variation of the pressure distribution on the nacelle at SOC power settings as a function of the M_∞ [3].

However, the effect of the external flow on the fan exhaust nozzle was insignificant because of the choked running condition of the nozzle. However, the nozzle rim region was sensitive to the free-stream flow owing to the

presence of a subsonic boundary layer, (Figure 2.64) [3]. Moreover, the external flow altered the jet structure along the core-cowl surface, and the external flow increased the pressure inside the jet, (Figure 2.65) [3].

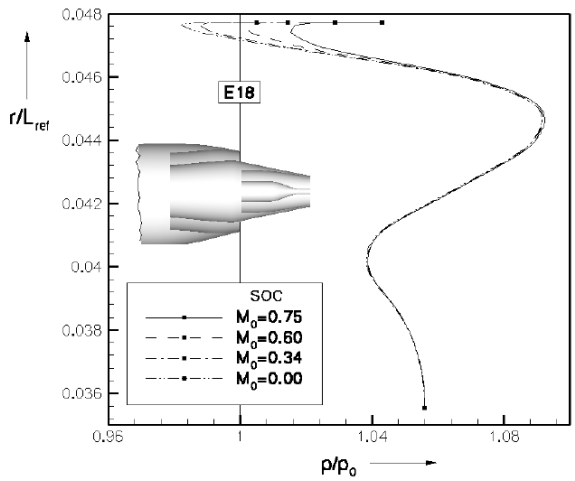

Figure 2.64 Pressure profile at the fan nozzle exit plane as a function of M_∞ [33].

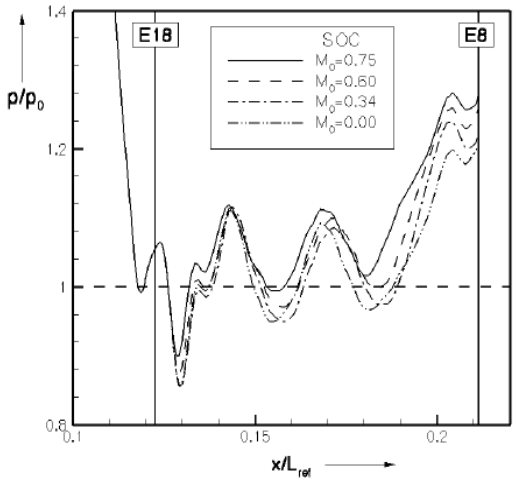

Figure 2.65 Pressure distribution over the upper surface core-cowl as a function of M_∞ [33].

After presenting the available methods that can be used in evaluating the aerodynamic interaction, the following section describes the influence of this interaction on overall engine performance and the approaches that have been applied to model it into an engine performance model.

2.3 Modelling the aerodynamics of the nacelle components

Here, a review of the previous studies that dealt with the nacelle components' aerodynamics and the approaches that have been used to model their effect on the engine and aircraft performance is presented. Gas turbine performance can be evaluated via different predictive tools, such as Turbo-Match [90]. These tools are based on one-dimensional isentropic thermodynamic equations. However, the multi-dimensional behaviour of the flow, internally and externally, has a great impact on predicted engine performance. In other words, the aerodynamic interaction between the nacelle components themselves and the wing has a significant effect on the performance, as established before. Therefore, it became crucial to use a high-fidelity model to predict the exterior and interior flow interactions of the aero-engine precisely. Mund et al. [7] developed, by using

CFD, a two-dimensional representation of the intake, bypass duct and nozzle, to estimate the flow losses of these components. The results were employed in correcting a zero-dimensional performance model. Mund et al. [7] highlighted that it was worthwhile of including the two-dimensional flow interaction effect, through a CFD model, to predict engine performance. Meanwhile, the engine installation effect on the performance of the aircraft and engine was examined by Sibilli [4]. Sibilli [4] combined the engine and aircraft performance model by taking into consideration aspects of the gas turbine installation within the range of installation positions. This method is based on generating engine performance correlations to evaluate the installation impact. The correlations are represented by the ratio of the net propulsive force (NPF) (the net force of the engine transfer to the airframe [4]) to the engine net thrust as a function of the engine position for two different types of engine, (Figure 2.66). It was observed that there was a minor effect of the variation in the vertical position of the nacelle on the aerodynamic performance of the aircraft and NPF, whereas the horizontal positioning of the engine significantly affected the value of NPF. The change in fuel consumed based on the variation in the axial position of the engine was estimated to be 4.2% [4].

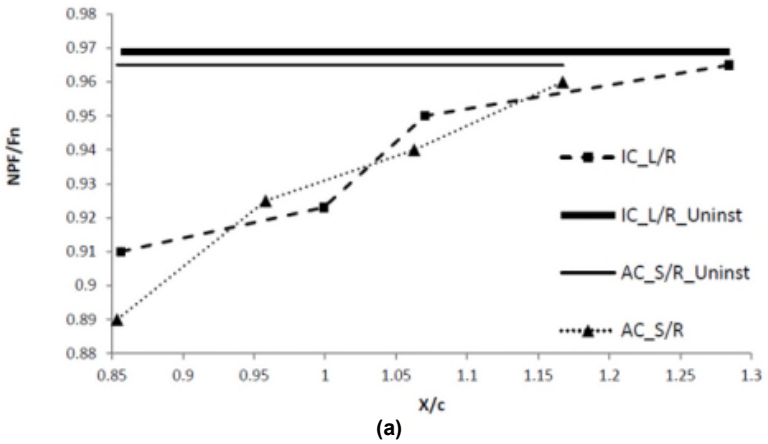

(a)

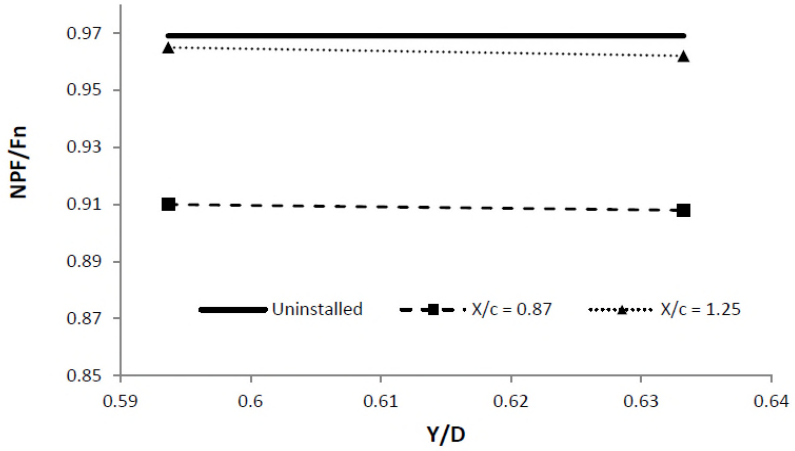

(b)

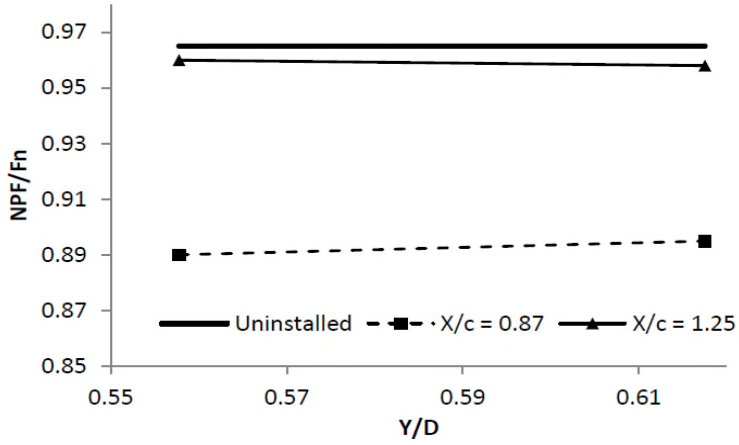

(c)

Figure 2.66 (a) (NPF/F_n) as a function of the horizontal position for the IC L/R and AC S/R engine, (b) (NPF/F_n) as a function of vertical position for the IC L/R engine, (c) (NPF/F_n) as a function of vertical position for the AC L/R engine [4].

The nacelle shape, free-stream Reynold's number (Re), free-stream Mach number (M_∞) and mass flow capture ratio (MFCR) effects were quantified by Christie [5], who also corrected the isolated engine and aircraft performance by assessing the impact of the up-flow angle. All these effects have been modelled using the empirical models from ESDU 81024 [91] combined with a CFD approach. These models were integrated into an aircraft performance in-house tool (Hermes). The model results showed there to be an increase in the amount of fuel burnt and reduction in the flight range throughout the flight trajectory because of the effect of the installation and the impact of the flow around the nacelle [91]. He also showed the importance of modelling the installation interference between the wing and the engine.

2.4 Summary

Nozzle aerodynamics was discussed in detail herein. The previous studies that dealt with the assessment methods of the nozzle performance were described. Moreover, the state-of-the-art studies in modelling nacelle aerodynamics were also reviewed.

This section concludes main information that was taken from the previous studies and main outcomes as well as deficiencies:

a) The exhaust nozzle at cruise conditions runs at choked conditions (NPR_{crit}=1.89 (Air γ=1.4)). However, the choking condition changes such that, sometimes, it occurs at higher or lower NPR than the NPR_{crit}, depending on the back pressure values around the nozzle exit [11, 17].
b) The flow downstream the civil engine nozzle exit, for the over- or under-expanded nozzle conditions, is complex and includes various flow features. These flow features encompass the boundary layer and various types of shock waves and contribute to the nozzle performance.
c) The main parameters that affect the performance of the nozzle are the NPR and boat-tail angle for the single-stream nozzle [19, 22, 27]. Moreover, core-cowl angle, plug length influences the plug-nozzle and the dual-stream nozzle performance [6, 33, 32, 56], respectively.
d) The curvature of the internal geometrical profile of the nozzle has a significant impact on nozzle performance [50].
e) The jet stream affects the pressure forces over the boat-tail. Furthermore, the temperature of the exhaust jet has an impact on the boat-tail drag at a high nozzle charging temperature, NPR and boat-tail angle [24, 25].
f) The boat-tail drag is not greatly affected by the angle of attack of the aeroplane. The effect becomes significant at high M_∞ [22].
g) The performance metrics of the nozzle are the non-dimensional parameters of discharge, velocity and thrust coefficient. The thrust coefficient is calculated based on several control volumes. Some of them include the exterior parts (plug and boat-tail) as a contributor to the engine thrust [43].

h) The installation of the nacelle under the wing has an impact on the aerodynamic performance of the engine [63, 70, 77, 90].
i) Performing an experimental investigation with a parametric analysis is an expensive task in terms of time and cost.
j) The analytical models do not provide a full description of the physical behaviour of the flow. There are always assumptions that oversimplify the case study. The calculations of C_d and C_{fg} using the boundary-layer theory are not sufficient for the dual-stream nozzle. Moreover, they do not have the flexibility to perform parameterisation. Furthermore, employing incompressible flat-plate theory overestimated the boundary-layer thickness; as a result, the theory will under-predict the C_d.
k) The numerical calculations were in strong agreement with the experimental data. They also provided freedom in terms of performing the parametric analysis.
l) The current engine performance codes do not consider the multi-dimensional impact of the flow interaction on the nozzle performance. The one-dimensional thermodynamic theory is the only description of nozzle performance currently available, besides old experimental performance data for a single-stream nozzle.

2.5 Gaps in the knowledge

The gaps in the topic that are of concern in this project are:

a) lack in the multi-degree of freedom nozzle performance maps in the open literature, maps that can predict the combined impact of the aerodynamic and geometric parameters of the nozzle across a wider range;

b) Little information regarding the core nozzle's characteristic behaviour with the variation of the fan nozzle pressure ratio;

c) No correlation that predicts the effect of the wing flow field on the nozzle performance as a function of the local static pressure; and

d) Current engine performance models do not consider the multi-dimensional impact of the flow interaction on nozzle performance.

3 Methodology and scope

3.1 Overview

This chapter presents the methodology that is employed to analyse the performance of the nozzle of the civil aero engine in isolated and installed situations, as well as the development of performance maps. After evaluating the existing literature, it was observed that Computational Fluid Dynamics (CFD) analysis contributed extensively to the studies reported and provided results of acceptable accuracy. Therefore, it was decided to employ a CFD model in this project to perform the analysis and establish the corrections and the performance maps. However, before start using the CFD method, the initial geometry had to be built. Therefore, a baseline engine was designed with the aid of a CAD (Computer-Aided Design) tool. The CAD model was kept as simple as possible while guaranteeing the accurate generation of the geometric curves. The dimensions of the initial engine nozzles were derived from performance analysis of aero-engines based on the available engine performance data. On another aspect, for the installed engine cases, the engine was installed on an infinite two-dimensional swept wing (SW) and the NASA Common Research Model (CRM) Wing body (WB) aircraft configuration.

The CFD domain needed to be discretised so that the system of linear equations in CFD code could be solved at each node. Therefore, a mesh that filled the flow domain had to be generated. An axisymmetric and three-dimensional CFD analysis was performed in the current work. The axisymmetric domain was used to produce the isolated nozzle performance data, and the three-dimensional cases were employed to predict the flow interaction because of the installation. The extracted data were then manipulated to determine the required exhaust system characteristics, with the appropriate thrust definitions to assess the nacelle and exhaust system aerodynamic performance. The maps were fed into a low-order performance model to provide an improved engine performance prediction tool. The methodology is described in details in the following sections.

3.2 Non-dimensional engine performance model

The lead parameters of the initial geometry were required to design the baseline nacelle for the CFD analysis. The full set of the geometrical lead parameters of the aero-engine nacelle were not available in the open literature. Therefore, to design a nacelle that is adequate for the current work, a number of assumptions were made, and correlations used. The nacelle chosen for the ongoing work is for a dual-stream nozzle engine. This type of engine nacelle is the modern design nacelles employed for current high bypass turbofans, was used because of its lighter weight than long-duct nacelles.

3.2.1 Engine selection and performance analysis

Two types of engines were used with bypass ratios of 5.3 and 8.1 under cruise conditions. The performance information of these engines was selected based on the available data of the GE CF6-80E1 and GE90-B85 engine models [92,93]. A nondimensional thermodynamic performance model (Turbo-Match[9,90]) was utilised to match the engine thrust and specific fuel consumption (SFC). This engine performance model is based on iterative procedure and components performance maps.

Data regarding GE CF6-80E1 and GE90-B85 fan diameters are available in the open domain [92]. The available information together with the performance model data could be employed to design the nacelle based on the assumptions and correlation that advocated by Williams, (2015) [63]. For more details, see Chapter 4 and its associated Appendixes, which present a full description of the nacelle design procedure. The primary information extracted from the performance model is the nozzles area.

The performance model inputs regarding the available gas–turbine characteristic are the overall pressure ratio (OPR), bypass ratio (BPR), inlet mass flow rate and turbine entry temperature (TET). The target was to achieve the engine thrust (50.24 kN for CF6-80E1 [93] and 69.1 kN for the GE90-B85[94]) by matching the open domain performance parameters of the engine and making appropriate assumptions for the others. Afterwards, the fan pressure

ratio (FPR) was optimised to achieve the highest net thrust and lowest SFC, (Figure Ap.A 2 and Figure Ap.A 3). The engines' design point was at mid-cruise conditions M_∞= 0.82, for the CF6 engine and M_∞= 0.85 for the GE90, both with Alt. = 36,000 ft (11,000 m). The reason for selecting mid-cruise as the engine design point is because it is the longest running period of the aero-engine [95]. Table 3-1 presents the performance data and engine characteristics. The CF6-80E1 engine nacelle model was used at the early stages of the project to produce the performance maps for the isolated exhaust system.

The GE90-B85 engine nacelle was used to determine the installation effect on the nacelle and nozzle aerodynamic performance. The reason behind the selection of the GE90-B85 for this purpose is because this type of engine is more representative of the modern engine than the CF6-80E1 class. For the same reason, the GE90-B85 nacelle was used to produce the core nozzle performance corrections.

Table 3-1 Performance data of the utilised engine models.

GE CF6-80E1			GE90-B85		
Parameters	**Value**	**Comments**	**Parameters**	**Value**	**Comments**
$\dot{m_{in}}$ [kg/s]	363	Calculated	$\dot{m_{in}}$ [kg/s]	544.42	Janes [94]
Thrust [kN]	50.24	Matched with (50.28 kN[36])	Thrust [kN]	68.24	Matched with (69.1 kN[94])
FPR [-]	1.64	Optimised	FPR [-]	1.58	Optimised
TET [°K]	1350	Guessed	TET [°K]	1380	Janes [94]
BPR [-]	5.3	Janes [92]	BPR [-]	8.1	Janes [94]
sfc [mg/ N sec]	17.03	Matched with (16 [mg/ N sec])	sfc [mg/ N sec]	15.20	Matched with (15.6 mg/N. sec [94])

3.3 Overview of geometry generation

This section presents a general view of the methods that were used to generate the nacelle and initial geometry of the three-dimensional exhaust system. Full descriptions of the methods are presented in the associated Chapters.

The front part of the civil engine nacelle up to the maximum diameter location is composed of an intake, fore-body, mid-body and after-body, (Figure 3.1). These parts contribute to nacelle performance, as they are located in the thrust and drag domain of the propulsion system. The design of the engine fore-body was conceived with a systematical method presented by Williams (2015) [63]. This method is based on a number of assumptions and correlations that were derived from previous parametrical analysis of nacelle geometry.

Another essential component of the nacelle is the exhaust system. The civil engine exhaust system encompasses the core cowl and plug, (Figure 3.1). The core-cowl was designed using the configurations advocated by ESDU (2001) [96]. It is a circular arc starting from the nozzle exit plane and continues as a conical after-body. A similar concept was followed for the design of the plug.

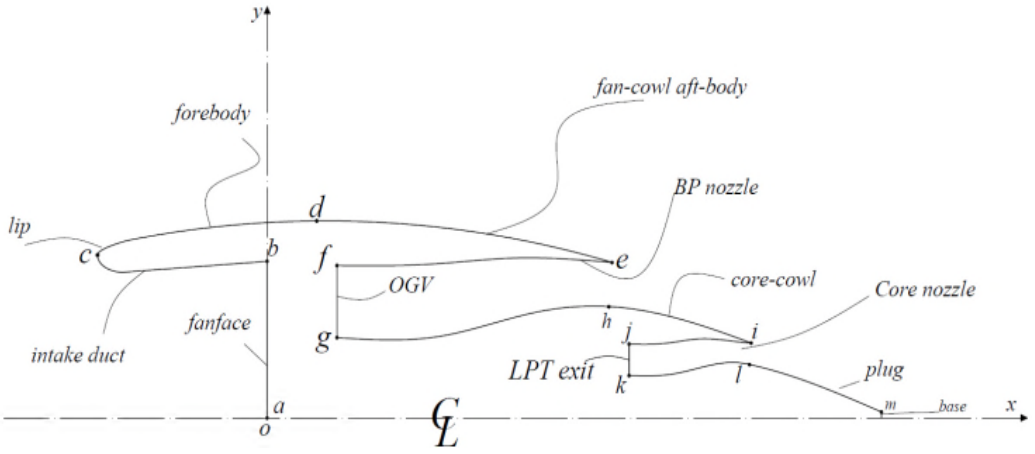

Figure 3.1 Nacelle: simplified sketch illustrating the main parts.

The internal walls of the nacelle were designed using nth-order polynomials to generate the required geometrical curves, based on the available dimensions. The reason behind using a polynomial is the ability to produce very smooth curves that would not affect the flow features. Any disturbance in the curve of the surface walls could produce a disruption in the flow with consequent unknown effects on the performance.

Part of the current project had the target of studying engine exhaust-system performance for the installed engine utilising a proposed infinite swept-wing design. In addition, the NASA Common Research Model for a simplified

aeroplane was also used. These geometry generation procedures are presented in Chapter 6.

3.4 Gridding methods

For the axisymmetric cases, a structured mesh topology was used. The mesh consists of parallelogram elements. It was generated by dividing the flow field into a number of regions that make it easy to be mesh know as blocks. The main configuration region was mesh by using O-grid mesh topology to discretise the boundary layer. The drawback of this type of the mesh is it needs to be generated manually. However, since the mesh elements have a regular shape the interpolation procedures that occur during the numerical calculations will be more efficient. Therefore, the numerical error will be less. Because of that, the structured mesh provides high flow resolution and the solver convergences faster.

For all the three-dimensional simulations, a hybrid mesh has been used. The hybrid mesh is a combination of unstructured mesh elements and prismatic layers that are placed on the solid surfaces of the geometry. The unstructured mesh has tetrahedral elements that fill the external domain and internal paths of the nacelle (intake and nozzle). The selection of this type of mesh is based on the flexibility of this mesh to fill the complicated geometry regions, its automated generation and fewer computer resources that required in generating the mesh.

The procedure of mesh generation is constructed as follows. Robust Octree (Octant Tree) mesh was generated first. It is known as Octree, as the generation of the elements depends on the spatial decomposing process of the first large elements into smaller elements [97]. To generate the mesh, a meshing tool (ICEM CFD), which uses a bottom-up approach [98], has been utilised. The bottom-up approach is a process of placing nodes over each curve of the main geometry. The two neighbouring nodes are joined with a straight line to generate the mesh elements edge. Every three edges will produce rectangular or the face of the element. The propagation of quadrilateral elements continues to fill the outer domain. After that, the mesh was made conformal to the geometry features. Therefore, the main concept of the Octree mesh is to

decompose the geometry into smaller rectangular elements according to the specified element size. The new geometry that is generated from the mesh formation has less complex geometrical features. The simplified geometry will be easier to mesh [97]. After generating the mesh, by the Octree approach, the volume mesh has been regenerated by using Delaunay triangulation method. The Delaunay mesh shows improved elements distribution. In which, this mesh generation method based on modifying the Delaunay triangulation by a series of face swaps processes until the geometry boundary achieved [99].

The Delaunay triangulation is the creation of triangles that connects a set of existing points in space. As such, it is necessary to provide a method for generating node locations over the geometry or the domain first. A typical approach is first to mesh the boundary of the geometry to provide an initial set of nodes using Octree gridding generation. The boundary nodes are then triangulated according to the Delaunay criterion.

After the unstructured mesh filled the flow-field domain, the time now is to generate the prismatic layers. The prism layers generation is based on the already generated triangle elements over the viscous surfaces. The generation process starts firstly by marching the node over the surface vertically and then generating the prism layer in the matching direction [99]. To do this, the marching direction should be identified, in which it is usually normal to the viscous walls, the edge of the prism will be formed, at last, the side faces of the prism are the created, (Figure 3.2). The prism layers height has been changed exponentially based on the total height of the prism layers and the initial height [98]. The mesh has been refined globally to ensure a homogenous refinement for the entire numerical domain.

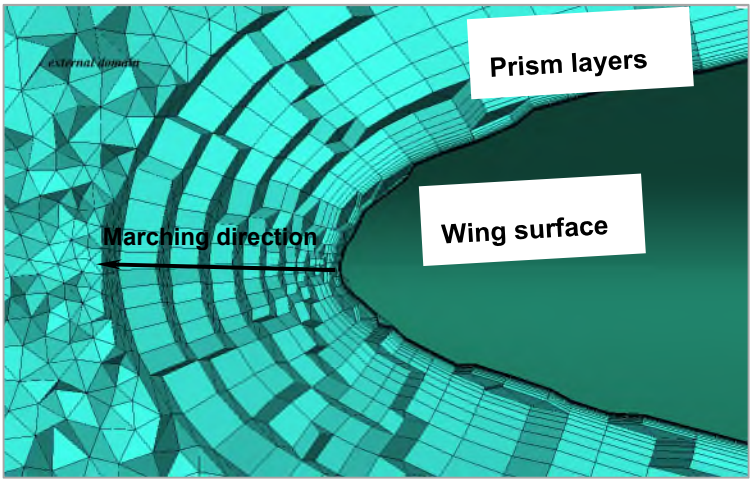

Figure 3.2 Close look to the prism layers over the wing surface.

The method of checking the asymptotic convergence of the mesh that is advocated by Roach [100] was used; a method based on the calculation of the **G**rid **C**onvergence **I**ndex (GCI) for the coarse and fine meshes. The GCI is an estimation of the discretisation error in the finest mesh compared with the current converged mesh results [100] and the likely level of the error; it is also an indication of the mesh convergence and the eliminated effect of the element number.

In general, all the meshes showed a monotonic convergence with the increase in the mesh size, as it is presented in the associated chapters. The discrepancy in the value of the physical properties of interest can be accepted. The selection of mesh sizes to perform the simulations was based on the available simulation power at the time of the beginning of the project and the time framework of the project.

3.5 Numerical scheme

The nature of the flow in the current simulation is a combination of low and high-speed flows. The high-speed flow is represented by a free-stream flow, which is a combination of subsonic, transonic and supersonic flow under cruise conditions, which means compressibility effects have to be considered. The low-speed flow occurs near the configuration's surfaces where the viscosity is dominant and plays a significant role in the dissipation of the flow kinetic

energy. The formulation of the Reynolds-Averaged Navier-Stokes (RANS) equations, including the shear stress and pressure gradient terms for turbulent flow, describes this type of the flow. The unknown Reynold's stress terms, which are generated owing to the averaging of the flow scalar quantities, needed to be modelled. Several transport equations were used to find a satisfactory representation of Reynold's stress. In the current work, the RANS equations were closed by k−ω Shear-Stress Transport (SST)[101] two-equation turbulence model to carry out all of the simulations. Although several sources advocated this turbulence model for aerospace flow analysis [102,103], a validation study was conducted, (see the next the Chapter), using a commercial flow solver, ANSYS Fluent [102].

The flow around the nozzle and the aircraft configuration were simulated in the steady-state conditions. An implicit and density-based solver was employed to solve the governing equations of continuity, momentum and energy. These equations are non-linear such that the density-based solver linearised the equations and converted them into a set of linear equations [102]. These equations were solved simultaneously [102]. As the density-based solver is coupled, the governing equations will be solved together, and the turbulence transport equation will be solved afterwards, at all cells at once [102]

The current solver is based on a finite-volume method. Therefore, it uses the control-volume-based technique to convert the transport equations to linear equations that can be solved numerically [102]. This control volume technique consists of integrating the conservation equations for each surface of the control volume, producing set discrete equations. The cell face encloses the control volume; therefore, the value of the scalar over the cell face is required. However, the solver stores the solution variables and their derivatives at the cell centres, so an interpolation to obtain the predicted values at the cell-face centres was required.

The Green-Gauss node-based method was utilised to compute the flow-field gradients. This method was recommended for the unstructured mesh, especially for triangular and tetrahedral elements [102]. This scheme constructs

the value of the linear functions at the node from the surrounding cell-centred values on the unstructured mesh cell. A second-order accurate upwind scheme was employed for the spatial discretisation of the flow field. The upwind scheme means that the face value and direction of the flow stream is derived from quantities in the cell located upstream. The reason for choosing second-order accuracy is that the interpolation techniques become complex when the geometry of the problem requires curvilinear or unstructured grids. For this reason, finite volume schemes of the second order remain the most widely applied [104]. The main difficulty is that the line connecting neighbouring grid points does not pass through the face midpoint as a result of the triangulation of the elements. This can be overcome by increasing the element density at the region of interest to provide higher accuracy of the solution.

The CFD calculations have to be initialised with appropriate values of the flow field properties, to avoid delays in convergence. For the current calculations, it was found that initialising the flow by applying the far-field conditions was appropriate. The boundary conditions and the convergence technique are presented individually in the associated Chapters.

3.6 Aerodynamic performance calculating method

3.6.1 Nozzle performance metrics extraction

Exhaust system performance was evaluated by estimating non-dimensional quantities of the discharge (C_d) and the gross thrust (C_{fg}) coefficient. Farokhi [105] postulated a criterion for evaluating the C_d, based on addressing the effect of boundary-layer creation over the walls of the nozzle and its blockage impact on the geometric discharge area. However, the static pressure variation of the external flow field has a noticeable effect on the value of the nozzle pressure ratio (NPR), especially for subcritical nozzle-running conditions [106]. Therefore it will affect the performance of the nozzle.

The C_d is defined as the ratio of the actual mass flow rate, to the fully expanded nozzle mass flow rate,(refer to Equation (3-1)) [64,107,108]. In this context, the C_d is not a measure of the nozzle efficiency, rather a design parameter to produce

the required physical nozzle area to match the gas turbine thermodynamic cycle.

$$C_d = \frac{\dot{m_a}}{\dot{m_i}} \tag{3-1}$$

$$\dot{m_i} = Ae\, P_0 \left(\frac{1}{NPR_{crit}}\right)^{1/\gamma} \sqrt{\frac{2\gamma}{(\gamma-1)RT_0}\left(1-\left(\frac{1}{NPR_{crit}}\right)^{\frac{\gamma-1}{\gamma}}\right)} \tag{3-2}$$

where the subscript i, stands for the ideal conditions of a fully-expanded nozzle with exit Mach number of 1.0 and $crit$ is the referring to the critical NPR.

The gross-thrust coefficient represents the measure of the engine's thrust losses or, in other words, the nozzle efficiency. It is the ratio of the actual gross thrust to the ideal gross thrust assuming ideal mass flow rate [28,108]. Several definitions have been proposed to evaluate the thrust of the engine. This variety of definitions originates from the difference in the inclusion of the exhaust system components in the thrust control volume. These exhaust-system components contribute to the engine thrust due to either jet flow behaviour (such as the core-cowl or the plug) or the interaction with the external flow field (cowl after-body).

To define a proper formula for the gross thrust, it must include both the sources of loss and the gains in the thrust; the proper selection of the engine post-exit stream tube boundaries is necessary for correct book-keeping. It is vital to employ an appropriate Thrust-Drag Book-keeping (TDB) method to break down the sources of loss for each exhaust system component [109]. One of the most used definitions of the engine's gross thrust is Equation (3-3) [43,64].

$$(F_G)_a = F_{gBP} + F_{gcore} - \left(\int_{walls} (p - p_\infty) d\vec{A} + \int_{walls} \tau\, d\vec{A}\right) \tag{3-3}$$

where F_g represents the momentum flux (or stream thrust)[28] and the pressure thrust at the charging station. The gauge pressure and shear forces were integrated over the walls of the core-cowl, plug, and the nozzle's internal walls (red lines in Figure 3.3). The integration was implemented in the axial direction.

The subscript (CP) in Figure 3.3 denotes the charging plane at the location just after the fan and the LPT exit of the turbofan engine.

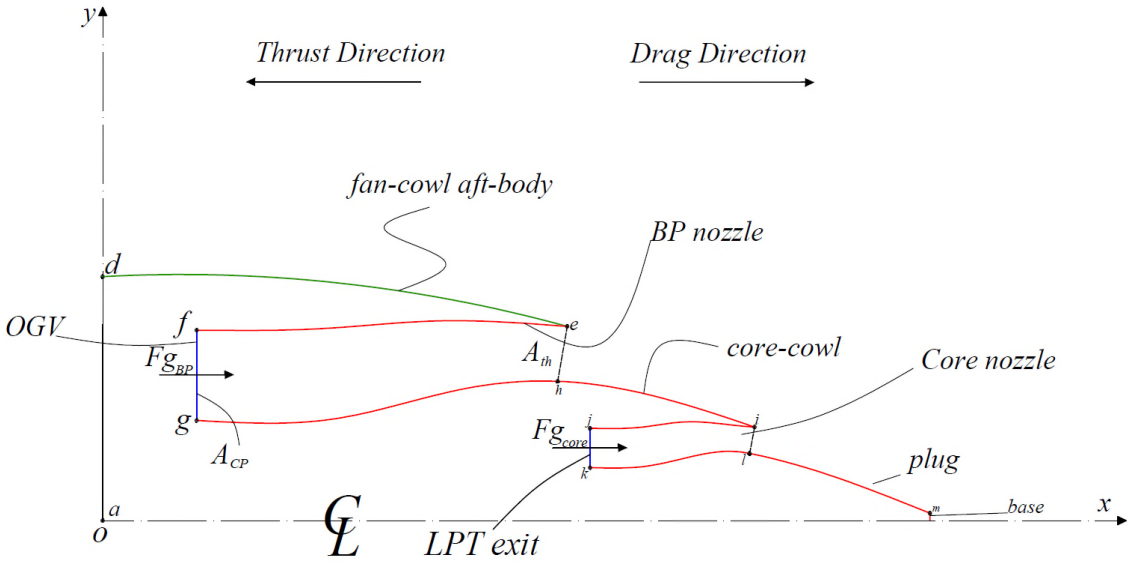

Figure 3.3 Meridional section view of the exhaust system showing the main civil engine exhaust-system components.

However, for the work herein, to distinguish between the impact of different components on the nozzle performance, the cowl after-body was excluded from the thrust definition proposed by [12]. In the current work, and for simplification in distinguishing between both definitions, the one excluding the fan-cowl afterbody is denoted as thrust definition (1). Therefore, thrust definitions (2) will be the one that includes the cowl after-body (green line in Figure 3.3) in the thrust control volume. Quantifying the effect of the installation on nozzle performance will provide the required correction to modify the isolated engine thrust calculations. Both definitions that are mentioned here will be used in the calculation of the installed engine thrust.

The gross thrust coefficient (C_{fg}) will then be calculated by the ratio of the modified actual gross thrust to the ideal gross thrust, Equation (3-4)[28,108]. The nozzle velocity coefficients are calculated using the same procedure above, except the actual thrust normalised to the actual mass flow rate rather than the ideal one, Equation (3-5).

$$C_{fg} = \frac{(F_G)_a}{\dot{m_i} V_s} \tag{3-4}$$

$$C_v = \frac{(F_G)_a}{\dot{m_a} V_s} \tag{3-5}$$

The isentropic fully-expanded velocity is given by Equation(3-6) [64,108].

$$V_s = \sqrt{\frac{2\gamma R T_0}{(\gamma-1)}\left(1 - \left(\frac{1}{NPR}\right)^{\frac{\gamma-1}{\gamma}}\right)} \tag{3-6}$$

where NPR = $\left(\frac{P_o}{p_{amb}}\right)$, R is the gas constant, and γ is the heat capacity ratio of air. The value of the NPR is equal to NPR_{crit} in the calculations of the ideal mass flow rate and V_s based on P_t and T_t [108].

The drag coefficient over the afterbody of the nozzle surface is calculated using Equation (3-7).

$$C_{D\ aft-body} = \frac{D_{aft-body}}{0.5 \rho U_\infty^2 A_{nac,max}} \tag{3-7}$$

It should be noted that the definition of the discharge coefficient is universal and can apply to any nozzle configuration. However, the gross thrust coefficient can be defined in several ways. In the current work, the utilised definition of the gross thrust coefficient considers the ideal thrust calculation based on the ideal mass flow rate. In this case, the flow losses are included in a single non-dimensional parameter, that is C_{fg} [108].

3.6.2 Installed aero-engine performance data extraction

The nacelle of the engine experiences aerodynamic forces in terms of drag and thrust forces as are portrayed in Figure 3.4. Therefore, to evaluate the engine performance in both the isolated and installed situations, accurate bookkeeping is required whereby there is no duplication of the calculation of any one of these forces. The drag assessment of the nacelle was accomplished by using a modified near-field method [12,62,110] based on the integration of the stream forces

on the outer boundaries of the pre-entry and post-exit stream tubes. This was in addition to the summation of the pressure and viscous forces over the external nacelle surface for the isolated engine (and the pylon, if it is considered).

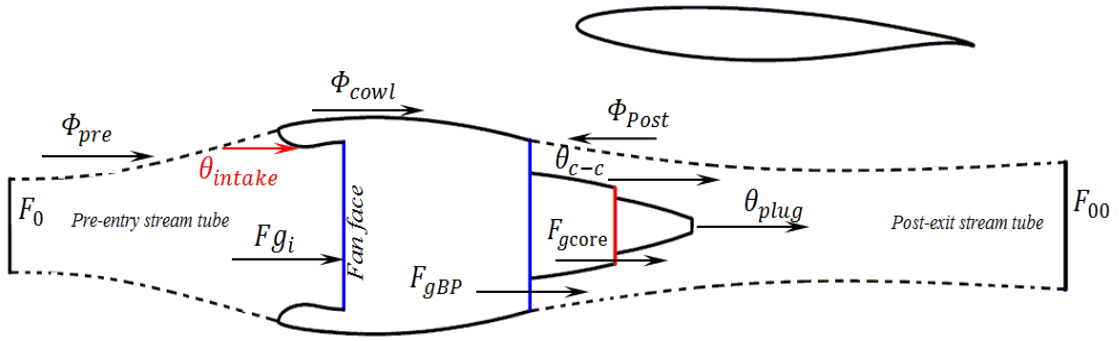

Figure 3.4 Schematic of the decomposition of the forces applied to the nacelle and its stream tubes [12,62,110].

Aero-engine net thrust represents the differences in momentum and pressure flux between the upstream stream-tube inlet (0) and the far downstream of the post-exit stream tube (00), taking into account the drag sources along this domain, Equations (3-8). The unknown terms, which are F_{00} and Φ_{post}, can be replaced by the engine flux at the nozzle exit and the forces over the downstream components, (Equation (3-9)) [62,64,109,110].

The nacelle drag (D_{nac}) is determined by the scalar summation of the rearward forces(relative to the free-stream flow direction) from the pre-stream tube (Φ_{pre}) and the nacelle surface from the fan face to the cowl after-body trailing edge (Φ_{cowl}),(Equation (3-10)) [5,111].

To evaluate the pre-entry force (Φ_{pre}) over the captured stream tube, the location of the stagnation point at the engine intake has to be identified. However, this task is quite difficult, especially for three-dimensional simulations. Therefore, to tackle this difficulty, a pre-entry force definition that was modified by Christie [5], was employed, (Equation (3-11)). As a result, the modified drag was calculated using Equation (3-12). The drag coefficient was computed as the ratio of the drag force to the dynamic pressure of the free-stream flow, Equation (3-13). The reference area is considered the nacelle maximum projected area ($A_{nac,max}$).

To assess the required power that must be produced by the engine to drive the aircraft and overcome drag forces, the net propulsive force (NPF) was estimated. The NPF represents the difference between the overall engine thrust and the drag forces. The modified net thrust and drag is used to estimate the NPF, (Equation (3-14))[111]. The lift coefficient is calculated as the ratio of the lift force over the wing and the fuselage for the CRM configuration to the free-stream dynamic pressure times the reference area, (Equation (3-15)).

$$\mathbf{F_N} = (\mathbf{F_{00}} - \mathbf{F_0}) - \mathbf{\Phi_{pre}} - \mathbf{\Phi_{cowl}} - \mathbf{\Phi_{post}} \quad (3\text{-}8)$$

$$\mathbf{F'_N} = (\mathbf{F_{gBP}} + \mathbf{F_{gcore}} - \mathbf{\theta_{plug}} - \mathbf{\theta_{c-c}}) - \mathbf{F_0} \quad (3\text{-}9)$$

$$\mathbf{D'_{nac}} = \mathbf{\Phi_{pre}} + \mathbf{\Phi_{cowl}} \quad (3\text{-}10)$$

$$\mathbf{\Phi_{pre}} = (\mathbf{F_{gi}} - \mathbf{F_0}) + \mathbf{\theta_{intake}} \quad (3\text{-}11)$$

$$\mathbf{D'_{nac}} = (\mathbf{F_{gi}} - \mathbf{F_0}) + \mathbf{\theta_{intake}} + \mathbf{\Phi_{cowl}} \quad (3\text{-}12)$$

$$\mathbf{C_{D\,nac}} = \frac{\mathbf{D'_{nac}}}{\mathbf{0.5\rho U_\infty^2 A_{nac,max}}} \quad (3\text{-}13)$$

$$\mathbf{NPF} = \mathbf{F'_N} - \mathbf{D'_{nac}} \quad (3\text{-}14)$$

$$\mathbf{C_L} = \frac{\mathbf{L_{A/C}}}{\mathbf{0.5\rho_\infty U_\infty^2 A_{ref}}} \quad (3\text{-}15)$$

3.7 Modifying a non-dimensional engine performance model calculations

The select gas-turbine performance evaluation code for the current research is Turbo-Match [9], which was developed to assess propulsion system performance under design (DP) and off-design (OD) conditions. The input to this software package is user-friendly, and it encompasses a set of engine performance parameters associated with the specific components of the gas turbine. The outputs from the simulation are the gross thrust, net thrust, SFC, bypass and exhaust nozzle areas as well as the thermodynamic properties at each stage within the engine.

The code is based on a number of “bricks”, where each brick consists of a set of thermodynamic equations. Most of the components have an accompanying set of

maps that provide empirical performance data for that particular component. The engine components that are represented in the Turbo-Match are [9]: compressor, combustor, turbine and nozzles. A brief description of the Turbo-Match working procedure is presented subsequently.

The current project focuses on modifying the nozzle brick. This code subroutine uses a nozzle thrust coefficient map, the calculated mass, velocity and static pressure at the nozzle exit to calculate the engine gross thrust. The current nozzle simulation is for two types of nozzles convergent and Convergent-Divergent. They can be distinguished by using a specific input identifier (brick data) in the input file.

New performance calculations have been added to the current nozzle brick that can capture the aerodynamic interference impact of the main non-dimensional nozzle parameters (NPR, CR and the cone (plug) half-angle, β). For the new multidimensional maps, a response surface method is used employing a cubic-spline interpolation and linear interpolation. This leads to an increase in the number of the code inputs so that it enables the parameterisation of the geometrical characteristics of the nozzle and captures its impact on the engine thrust under DP and OD conditions for installed and isolated cases. More details are presented in Chapter 7.

3.8 Methodology roadmaps

This section provides the methodology roadmaps that have been followed.

A- Nozzle maps generation

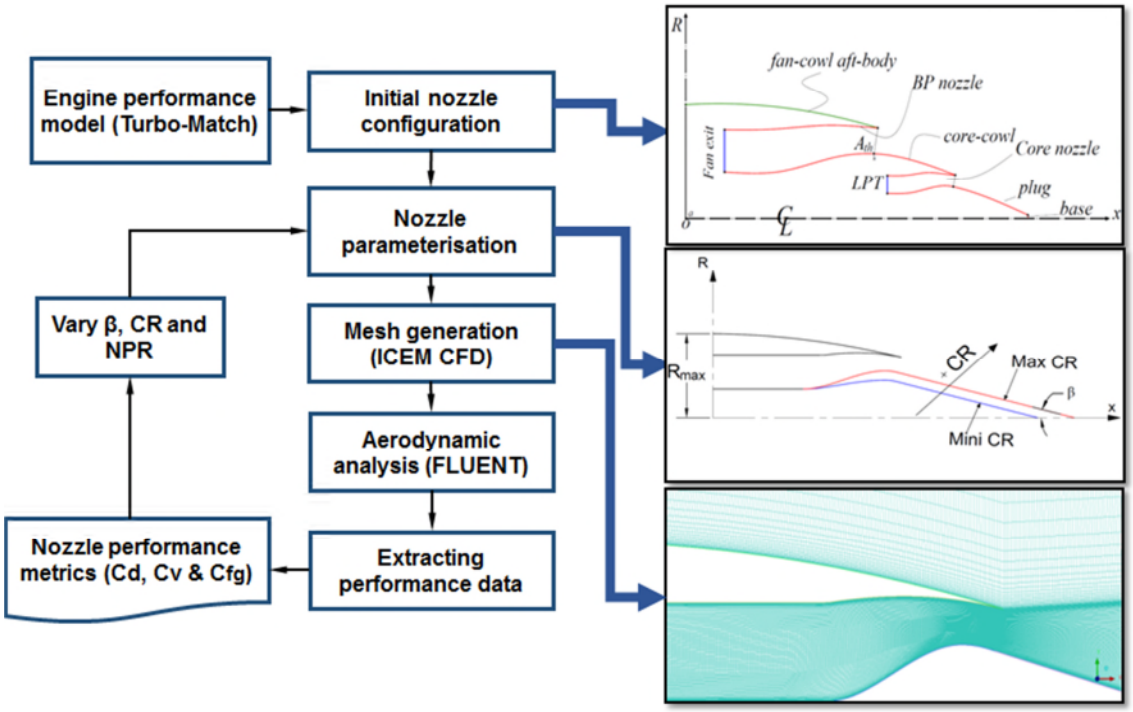

B- Evaluation of the installation interactions impact on the nozzle

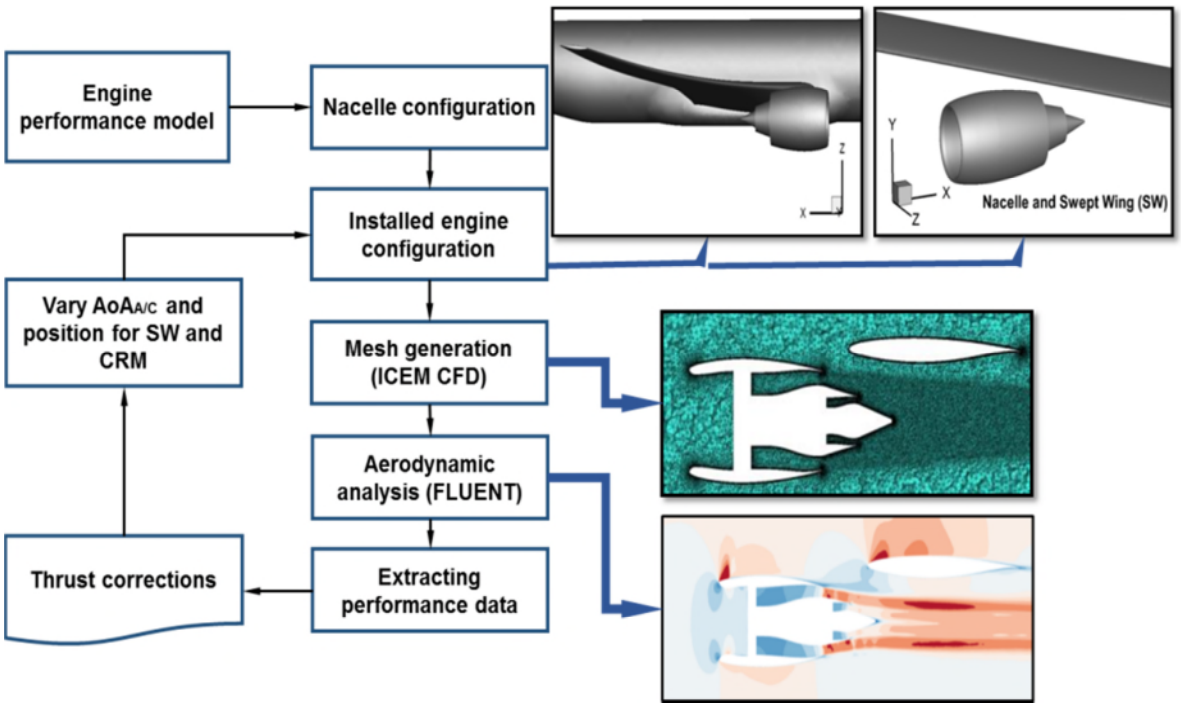

4 Numerical model validation cases

Despite the fact that numerical methods (i.e. CFD) are widely used in the design and optimisation of aero-engines, validation of the calculated results remains essential. This chapter contains the results of the validation tests for the engine exhaust system, the aircraft and the aircraft-nacelle configuration. The aim is to ensure that the used numerical model results are within acceptable range. Furthermore, is to report any discrepancy of the numerical results from the measured data due to “numerical errors” and the selection of the boundary conditions. Moreover, the tests are also used to evaluate the performance of the selected mesh topology.

4.1 Validation of nozzle configuration simulations

The selection of the appropriate numerical and turbulence model is important for the nozzle design process, to capture the flow characteristics downstream the nozzle exit accurately. The current validation aims to assess the performance of the numerical model that is used in the calculations of the nozzle’s aerodynamics and to investigate the effectiveness of the different turbulence models in capturing the complex flow features of a single stream and plug nozzle configurations. The CFD results are compared with the available experimental data in terms of the pressure coefficient distribution, local static pressure and nozzle efficiencies.

For the single-stream nozzle configuration, the validation simulations were carried out for free stream Mach numbers (M_∞) of 0.4, 0.8 and 1.3, to cover the three flight phases, subsonic, transonic and supersonic, and nozzle pressure ratios of NPR= 2.02, (Table 4-1). Three different single stream nozzle configurations were examined with different fineness ratios ($\frac{l_{bt}}{D_{max}}$), Figure 4.1, of 0.8, 1.0, 1.77. For the plug nozzle, M_∞ = 0.60 and 0.91 and NPR = 2.66, 3.12 and 3.71 were examined and single nozzle configuration, (Table 4-2).

Six turbulence models were examined in this validation. These turbulence models were the Spalart–Allmaras one-equation (SA)[112], standard k-ε (sk-ε)[113],

RNG k-ε, Realisable k-ε, Standard k-ω (sk-ω) and Shear Stress Transport k-ω model (SST). The SA model is known as a one-equation model as the modelling is of turbulent viscosity only [102]. The two-equation models include the turbulence kinetic energy (k) and its dissipation rate (ε or ω). It is vital to select and assess the turbulence model appropriate for the given turbulent flow parameters.

Table 4-1 CFD calculations geometrical and operational parameters of the single-stream nozzle.

Config. No.	$(\frac{l_{bt}}{D_{max}})$	β_c (°)	NPR [-]	M_∞	Turbulence Models
(1)	0.80	17.0	2.02	0.4, 0.8	SA, sk-ε, RNG k-ε, realizable k-ε, sk-ω and SST k-ω
(2)	1.00	13.7	2.02	0.4, 0.8	
(3)	1.77	7.9	2.02	0.4, 0.8	

Table 4-2 CFD calculations geometrical and operational parameters of the plug nozzle.

	M_∞ [-]	NPR [-]	Turbulence Models
Single configuration	0.60	3.12	SA, sk-ε, RNG k-ε, realizable k-ε, sk-ω and k-ω SST
	0.91	2.66	
	0.91	3.71	

4.1.1 Geometry description

The geometry details that were used in the experimental work that was taken from [21,29] and the current work are described in this section. Since the experiment was conducted at zero angle of attack [21], axisymmetric simulations are adequate, and three-dimensional flow features were ignored. The single-stream nozzle had a fixed closure ratio ($\frac{D_e}{D_{max}}$) of 0.50, the nozzle fineness ratio ($\frac{l_{bt}}{D_{max}}$) had values of $\frac{l_{bt}}{D_{max}}$=0.80, 1.00 and 1.77, (Figure 4.1). The generation of the computational geometry of the plug-nozzle was based on the work of Harrington [29], (Figure 4.2). The internal walls of the nozzle were generated using fifth order polynomial fitted curves.

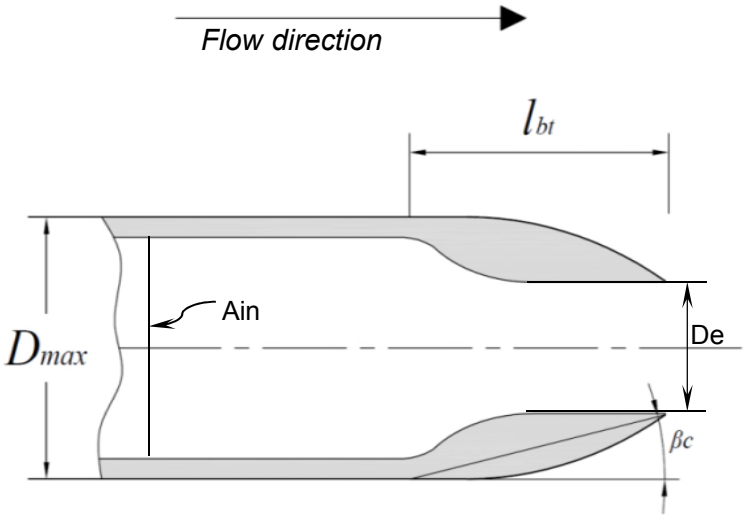

Figure 4.1 Sketch of the single-stream nozzle configuration.

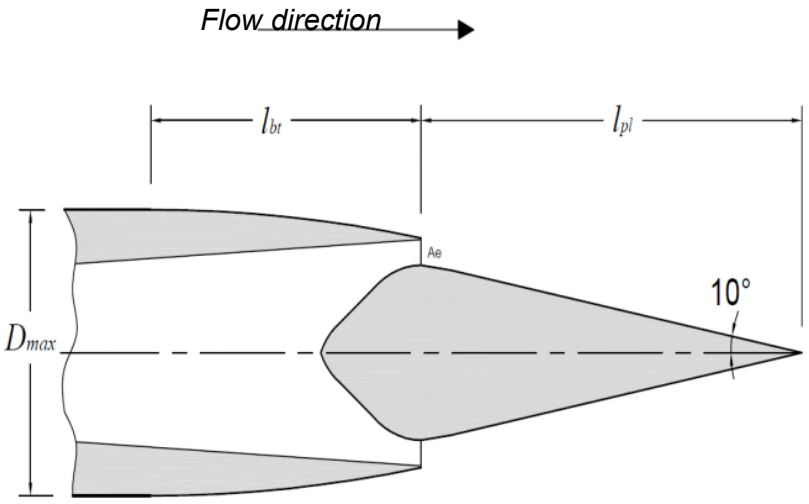

Figure 4.2 Sketch of the plug nozzle configuration.

4.1.2 CFD domain and meshing topology

To ensure that the computational boundaries do not affect the aerodynamic characteristics of the nozzle, a domain sensitivity study was conducted for different domain sizes. For the single-stream nozzle, four different domain sizes were identified by the width (W) and height (H), (Figure 4.3). The domain size changed from smallest domain of W=30D_{max} and H= 10D_{max} to the largest domain of W=120D_{max} and H= 40D_{max}. The domain width was increased by an interval of 30D_{max} and the height by 10D_{max}. Since the main objective of the current work is the evaluation of the pressure force, the value of the pressure

drag coefficient for various domain sizes was assessed. For the single stream nozzle, the results showed that as the domain size increased, the effect of the domain size on the drag coefficient reduced. The pressure drag coefficient over the boat-tail decreased by 0.0090% when increasing the domain width from W = $90D_{max}$ to $120D_{max}$, and height from H = $30D_{max}$ to $40D_{max}$; so W = $90D_{max}$ and H= $30D_{max}$ were the values chosen for the numerical domain of the current investigation.

For the plug nozzle, the smallest domain size was W/D_{max} = 25 and H/D_{max} = 10, and the maximum was W/D_{max} = 100 and H/D_{max} = 40. The pressure drag coefficient decreased by 0.0094% when increasing the domain width from W = $75D_{max}$ to $100D_{max}$, and height from H = $30D_{max}$ to $40D_{max}$, so W = $75D_{max}$ and H = $30D_{max}$ were the values chosen for the current investigation.

A multi-block structured mesh topology was used to create the required mesh for the axisymmetric numerical domain. The mesh was refined in a region where the significant changes in the flow features occurred, particularly through the exhaust jet region. The boundary layer was discretised to ensure that the value of the dimensionless wall distance (y^+) was less than or equal to one. For the single stream nozzle, the number of nodes that were distributed radially, perpendicular to the aero-lines, was 75, and 53 for the plug nozzle. The mesh growth ratio, for the single stream nozzle, in the radial direction was 1.3 for the boundary layer region and 1.2 for the external domain and 1.27 and 1.3, respectively for the plug nozzle.

Three meshes were generated to investigate the effect of the number of cells on the physical properties of interest. For the single stream nozzle, the number of mesh elements was increased from $1.6x10^5$ to $4.0x10^5$ with an average refinement ratio of 1.57, and for the plug nozzle, the number of mesh elements was increased from $2.7x10^5$ to $7.6x10^5$ with average refinement ratio of 1.68. The value of the drag coefficient of the boat-tail was assessed to check its dependence on the number of elements. The Grid Convergence Index (GCI) [100], was used to assess the numerical performance of the meshes. For the single stream nozzle, the value of the $GCI_{1,2}$ between the medium and fine

meshes was 0.00085% and 0.0264% for the plug nozzle. The mesh of $4.0x10^5$ elements has been chosen for the single-stream simulations, and the mesh of $5.0x10^5$ was chosen for the plug nozzle simulations.

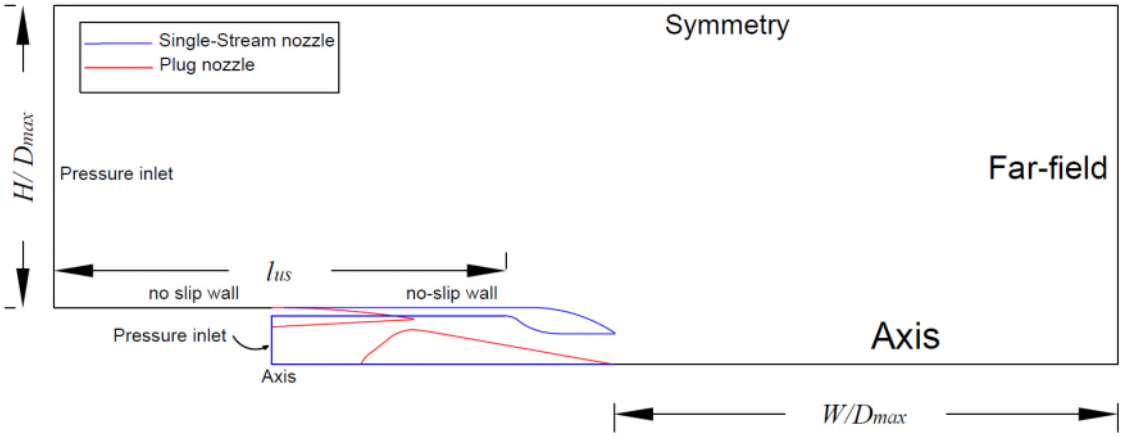

Figure 4.3 Schematic of the computational domain for single stream and plug nozzle, showing the boundary conditions used and the domain's geometrical features, (Not to scale).

4.1.3 Boundary conditions

The boundary conditions for the current model are the pressure–inlet at the nozzle inlet and the inlet plane of the CFD domain, (Figure 4.3). Uniform total pressure and temperature profiles were set pressure inlet boundary conditions. The values of the total pressure and temperature were taken from the original experimental work by Ruebush [21] and Harrington [29], Table 4-1 and Table 4-2, respectively. The no-slip wall conditions modified the internal walls of the nozzle, the plug and the boat-tail surfaces. The distance from the nozzle rim to the computational domain inlet (l_{us}), was selected based on the location of the boundary layer transition point from laminar to turbulent and the boundary layer thickness as provided by Ruebush [21] and Harrington [29]. For the single stream nozzle, the location of the upstream CFD domain inlet was selected to be $6.0D_{max}$, which is located at the beginning of the moving part of the experimental nozzle model.

For the plug-nozzle, the boundary-layer characteristics as given by Harrington [29], has the ratio of momentum thickness to the maximum diameter ($\frac{\theta}{Dmax}$) equals to 0.02 at the nozzle rim at M_∞ = 0.91. This value is constant across a

range of M_∞ from 0.70 to 1.19 [114]. Harrington [29] also found that the boundary velocity profile over the boat tail surface is similar to a 1/7th power law. Thus, the length of the upstream distance (l_{us}) from the nozzle rim was calculated based on flat-plate turbulent boundary layer theory to determine the appropriate boundary-layer thickness. This calculations produced an upstream length equals to $3.5D_{max}$. A turbulent velocity profile was then applied to the inlet of the numerical domain for both nozzle configurations. The pressure far-field boundary conditions were used to initialise the entire numerical domain properties.

4.1.4 Results and discussion

4.1.4.1 Nozzle aerodynamics

The computational results are presented for three nozzle fineness ratios ($\frac{l_{bt}}{D_{max}}$ = 0.80, 1.00 and 1.77), free stream Mach numbers (M_∞) of 0.40, 0.80, and 1.30 nozzle pressure ratios of 2.02. The k-ω SST two-equation turbulence model was utilised to examine the effect of the fineness ratio and the operational conditions on the nozzles' aerodynamics and the performance.

The pressure distribution over the boat-tail for the transonic case (M_∞=0.80), for all three nozzle configurations, show agreement with the experimental data throughout the region of flow expansion over the boat-tail, with a pressure coefficient difference (ΔCp) of -0.016 at x/l_{bt}=0.0, when the nozzle runs at NPR=2.02, for configuration (1) ($\frac{l_{bt}}{D_{max}}$=0.8, β_c=17.0°), (Figure 4.4). However, an over-prediction of Cp was noted for the separation region extending from x/l_{bt} = 0.65 to 1.0 with ΔCp of +0.083 at x/l_{bt} =1.0 for this configuration.

It can be seen that the measured Cp values, in Figure 4.4, in the region close to the nozzle trailing edge (x/l_{bt} > 0.65), level off due to the equalised axial pressure distribution along the separated boundary layer region. This behaviour is particularly noticeable for configuration (1), due to its low fineness ratio. The CFD results show that the pressure is still increasing for x/l_{bt} > 0.60, after passing through the separation point indicated by the experimental data. This

means that CFD simulation does not capture the separation of the flow efficiently, and the model predicts the separation further downstream than indicated by the measured data.

As the fineness ratio increases, from $\frac{l_{bt}}{D_{max}}$=0.80 to $\frac{l_{bt}}{D_{max}}$=1.77, the separation region decreases due to the reduction in the boat-tail chord angle (β_c) from 17.0° to 7.80° and lengthening of the boat tail. Therefore, there is a better agreement between computational results and experimental data as the fineness ratio increases. This can be seen with configuration. (2) ($\frac{l_{bt}}{D_{max}}$=1.0, β_c=13.75°), where the pressure coefficient difference between the measured and the calculated data is 0.065 at x/l_{bt}=0.96, which is significantly lower than configuration (1) results. As the fineness ratio increases further to $\frac{l_{bt}}{D_{max}}$=1.77(configuration (3), β_c=7.8°), the pressure coefficient difference (ΔCp) reduces further to 0.043 at x/l_{bt}= 0.96, (Figure 4.4).

The speed of the external flow has an impact on the predicted location of the separation point. With the increase in external flow velocity from subsonic speed (M_∞ =0.40) to transonic (M_∞ =0.80), the location of the separation point moves upstream for a given configuration, (Figure 4.5). For configuration (2) ($\frac{l_{bt}}{D_{max}}$ =1.0, β_c=13.75°) the separation over the boat-tail surface takes place at $\frac{x}{l_{bt}} = 0.8$ when M_∞= 0.40, whereas at M_∞= 0.80 the separation occurs at $\frac{x}{l_{bt}} \approx 0.65$, (Figure 4.5). This is attributed to the increase in the pressure gradient over the boat-tail at M_∞ =0.80 compared to the subsonic M_∞ across the same region of the boat tail from $\frac{x}{l_{bt}} = 0.43$ to $\frac{x}{l_{bt}} = 0.7$,(Figure 4.5). At M_∞= 1.3, different scenario the was observed. The pressure coefficient showed a continuous decrease along the boat-tail surface. This decrease caused the flow to shock at $\frac{x}{l_{bt}} = 0.65$,(Figure 4.5). The computed data compared very well with the experimental pressure coefficient at M_∞=1.3.

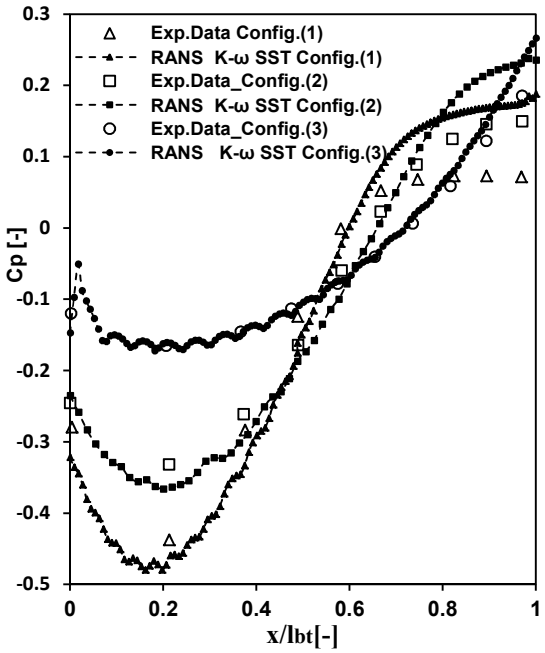

Figure 4.4 Experimental and computed pressure coefficient (Cp) distribution comparison, over the boat-tail surface, for three configurations of the single-stream nozzle, at a free stream (M_∞) of 0.80 and NPR of 2.02, the employed turbulence model is k-ω SST.

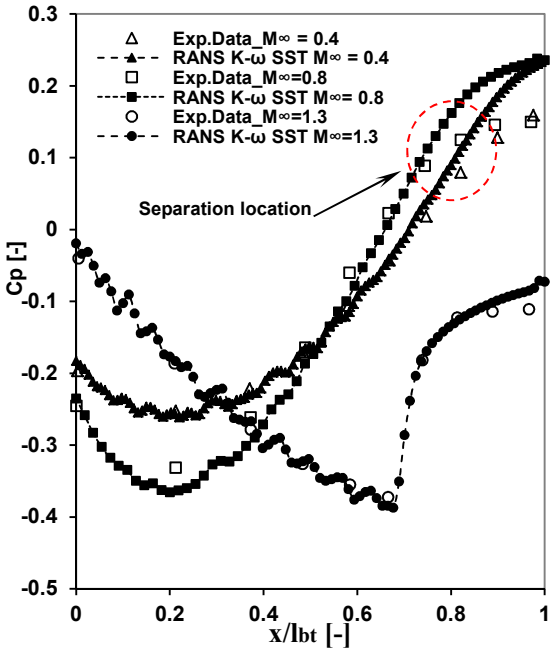

Figure 4.5 Experimental and computed pressure coefficient (Cp) distribution comparison over the boat-tail surface, for three different freestream Mach numbers of the single -stream nozzle, at NPR of 2.02, for Configuration.(2) (l_{bt}/D_{max} =1.0), the employed turbulence model is k-ω SST.

A comparison was made between the RANS k-ω SST and realizable k-ε model. The RANS k-ω SST model and the realizable k-ε model results show similar pressure distribution (Cp) over the boat-tail with a small deviation between them, across the region between $\frac{x}{l_{bt}} = 0.49$ to $\frac{x}{l_{bt}} = 0.72$, (Figure 4.6). Both of them showed an agreement with the experimental measurements. More specifically, the absolute difference of the average pressure coefficient (averaged along the boat tail length) from the experimental pressure coefficient ($\Delta \mathrm{Cp}_{\mathrm{ave}}$) is 0.050 for the realizable k-ε model, 0.049 for the RANS k-ω SST, (Figure 4.6). However, as the flow separates the RANS k-ω SST results showed better match with the experimental data, in terms of the location of the separation point than the realizable k-ε, which modelled the separation point at a location further down-stream. This behaviour also applies to the SA, sk-ε and RNG k-ε models.

Once the flow separated, an over-prediction of the pressure distribution over the boat-tail surface was observed along the separation region for the entire range of the turbulence models. The maximum difference was observed in the sk-ε model results, which have pressure coefficient difference of ≈2.0% at $\frac{\mathrm{x}}{\mathrm{l_{bt}}} = 1.0$. The standard k-ω and k-ω SST show better agreement with the measured data from the other models with pressure coefficient difference ($\Delta \mathrm{Cp}$) of 0.10 at $\frac{x}{l_{bt}} = 1.0$.

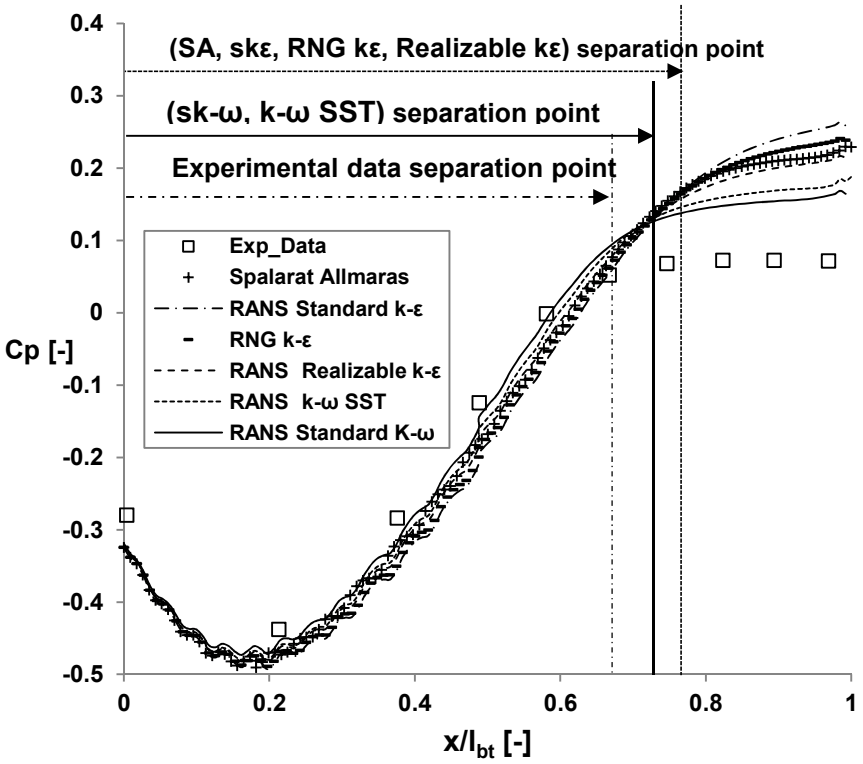

Figure 4.6 Pressure coefficient (Cp) comparison between different turbulent models and the measured data for the flow over the single stream nozzle of Configuration (1) ($\frac{l_{bt}}{\mathrm{D_{max}}}$=0.8, β_c=17°), at M_∞ = 0.8 and NPR = 2.02.

The aerodynamic results of the plug nozzle are expressed by the local static pressure distribution over the plug. The pressure values have been normalised by the nozzle inlet total pressure (P_7), to be comparable with the experimental data. The results of the RANS k-ω SST model show that, at M_∞=0.91 and NPR of 2.66, the static pressure ratio distribution ($\frac{p}{P_7}$) over the plug surface agrees with the experimental data, (Figure 4.7), and the average absolute difference between them in terms of the pressure ratio $\Delta(\frac{p}{P_7})_{ave}$ is 0.00127. At a higher

value of the NPR (3.71), except for the discrepancy between the numerical model and experimental data at one point located at x/l_{plug}=0.5, (Figure 4.7), the location and strength of the expansion and compression waves over the plug are predicted reasonably well.

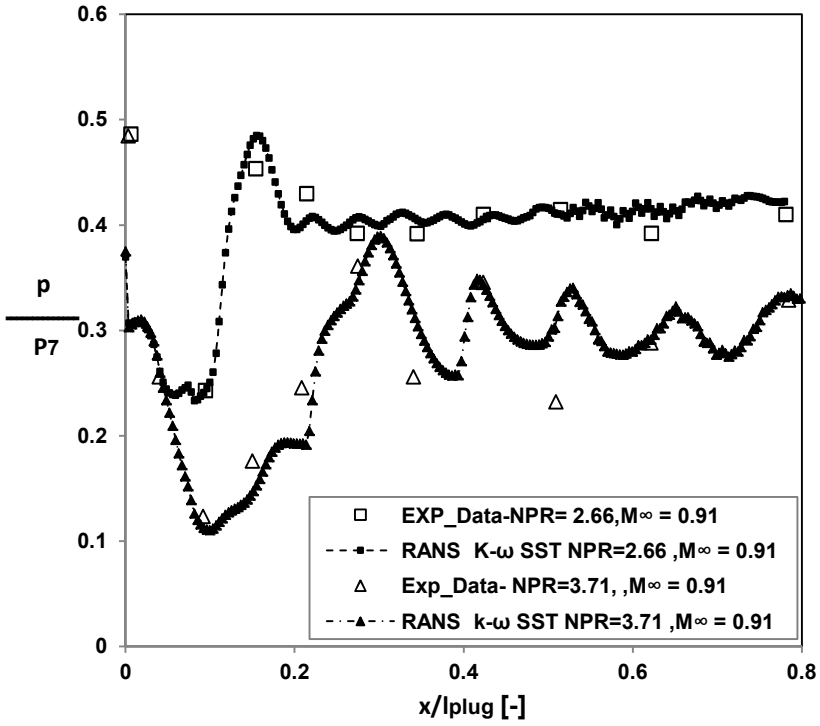

Figure 4.7 Comparison of the pressure coefficient (Cp) distribution over the plug surface between the computed and the measured data M_∞ of 0.91 and NPR of 2.66 and 3.71.

Most of the turbulence models show the same level of capability for capturing the shock wave's strength and location at the nozzle exit at NPR 2.66 and M_∞=0.91, (Figure 4.8). Downstream of the compression wave, the flow exhibits weak expansion and compression waves, and the models predicted the pressure distribution with only a small deviation from the experimental data.

At NPR = 3.12 and M_∞= 0.60, the k-ε family turbulence models showed completely different behaviour from the other models, (Figure 4.9). The turbulence model results over-predicted the compression wave strength at x/l_{plug} = 0.2 and then developed four shock cells which are in agreement with the experimental data, but the location of the waves is predicted to be further downstream than was indicated by the experimental data. This can be attributed to the ability of the k-ε models to predict the bulk flow with high accuracy. Apart

from the first expansion wave, the k-ω and SA turbulence model results did not predict the presence of four shock cells over the plug surface under this operational condition, (Figure 4.9).

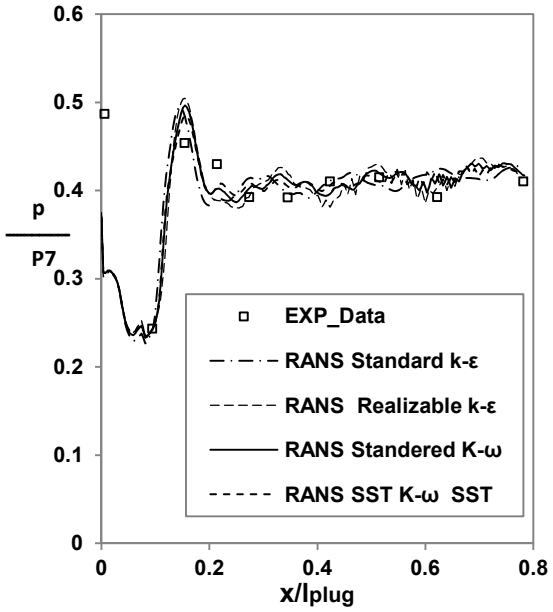

Figure 4.8 Comparison between of the local static pressure distribution over the plug surface between different turbulence models and the experimental data at free stream number (M_∞) of 0.91 and NPR of 2.66.

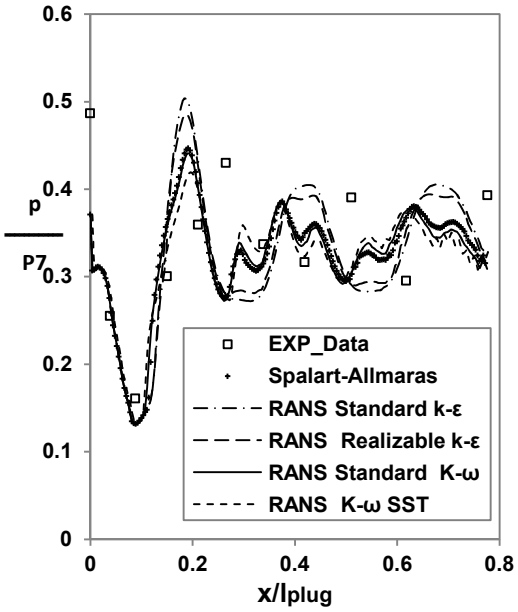

Figure 4.9 Comparison between of the local static pressure distribution over the plug surface between different turbulence models and the experimental data at free stream number (M_∞) of 0.6 and NPR of 3.12.

4.1.4.2 Nozzles' performance evaluation

The nozzle efficiency in the experimental data that are used for validation is represented by the ratio of the thrust-minus-drag (F-D) to the ideal nozzle thrust [21,29]. Reubush et al. [21] have calculated the F-D term, using an internal three-component strain-gauge balance adding to it the internal component pressure forces, while Harrington et al. [29] measured the F-D term by using a load cell. In the current CFD calculations, the nozzle efficiency was determined by using thrust definition (thrust definition (2)), Chapter 3. The actual mass flow rate was calculated at the nozzle inlet plane ($\dot{m_e}$). The ideal thrust was calculated using equation (4-1) in computed data reduction.

$$F_i = \dot{m_e} \sqrt{\frac{2\gamma RT_{tin}}{(\gamma-1)}\left(1-\left(\frac{1}{NPR}\right)^{\frac{\gamma-1}{\gamma}}\right)} \quad (4\text{-}1)$$

where: T_{tin} is the total temperature at the nozzle inlet.

The nozzle pressure ratio (NPR) range was extended from 1.83 to 3.88 for the single stream nozzle and from 2.60 to 6.33 in the case of the plug nozzle simulations. Three turbulence models were employed to assess their performance in computing the nozzle efficiency. The k-ω SST model, realizable k-ε and SA models results were assessed.

The results of the k-ω SST model showed that, for the single stream nozzle, it was noticed that the calculated performance results were lower than the experimental data by ≈ 3.29% at NPR = 1.83 and by 0.84% at NPR = 3.88, (Figure 4.10). Moreover, the numerical results for the plug nozzle predicted the nozzle efficiency with percentage difference from the measured data of -1.05% at NPR =2.64 and across a range from -0.46% to -0.68% between NPR =3.14 to 5.3. The utilised thrust definition results are comparable to the predicted nozzle efficiency of Malecki et al.[43], (Figure 4.11).

The realizable k-ε model result for the single stream nozzle predicted the nozzle performance better than the SA and k-ω SST model data. The worse was the SA results, (Figure 4.11). For the plug nozzle, k-ω SST model data showed the best prediction.

In general, the discrepancy between the numerical model results and the measured data is within the acceptable ranges that are computed in the other numerical models in the previous studies. Moreover, the selection of any one of the turbulence models is adequate. However, for the current work, the k-ω SST model is the most appropriate, as the aim of this activity is to simulate the flow around a nozzle configuration with a central body.

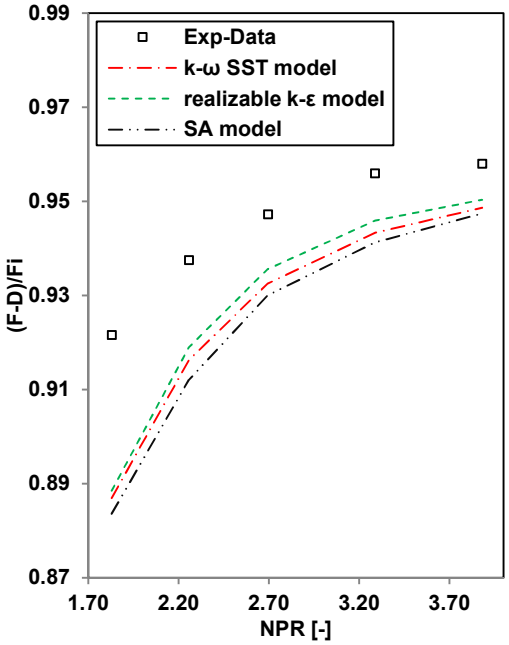

Figure 4.10 Comparison between the computed and the measured single stream nozzle efficiency (configuration 1) at M_∞ = 0.90 as a function of NPR, for the chosen turbulence model.

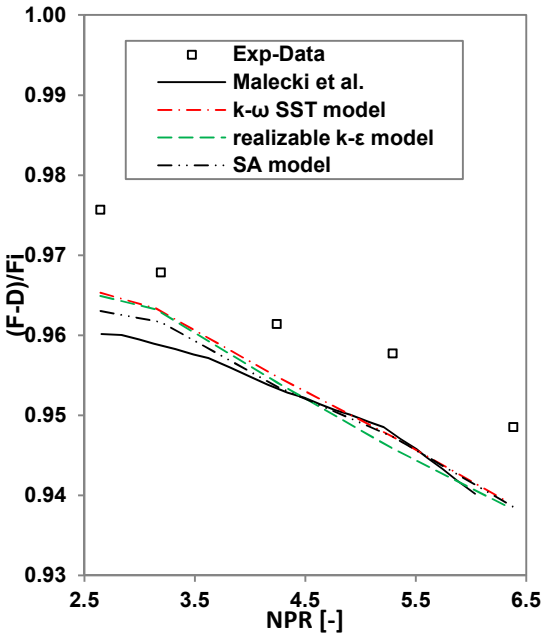

Figure 4.11 Comparison between the computed and the measured plug nozzle efficiency at M_∞ = 0.91 with NPR, for the chosen turbulence model.

4.2 Validation of clean WB and combined WBTFN simulations

A Common Research Model (CRM) of a 1/37 scaled aircraft wing–body with no tail (WB), (Figure 4.12), was used for the validation of the current project. Experimental data for the model, in terms of lift (C_L) and drag coefficients $C_{D(A/C)}$, and pressure coefficient (Cp) distribution over the wing area are available in the open domain [77]. The geometry file suitable for computational simulations was made available in the Fifth Drag Prediction Workshop (DPW-5) [76]. The CFD domain size has been examined and is provided by DPW-5 [76] as a hemispherical domain with a radius of 100 times the model reference chord length. The employed boundary conditions are the pressure far-field for the external domain boundaries with no-slip walls for the CRM aeroplane model surfaces.

For the wing-body pylon combined with a through flow nacelle (WBPTFN) configuration, was provided by DPW-5 [2] as well. Therefore, the same boundary conditions, domain shape and size were used. The purpose of using this

configuration was to evaluate the validity and performance of the numerical model and the meshes used for such simulations. Since the nacelle is a TFN, no boundary conditions were applied to the inlet and the exit of the nacelle, and the nacelle surfaces considered as no-slip walls.

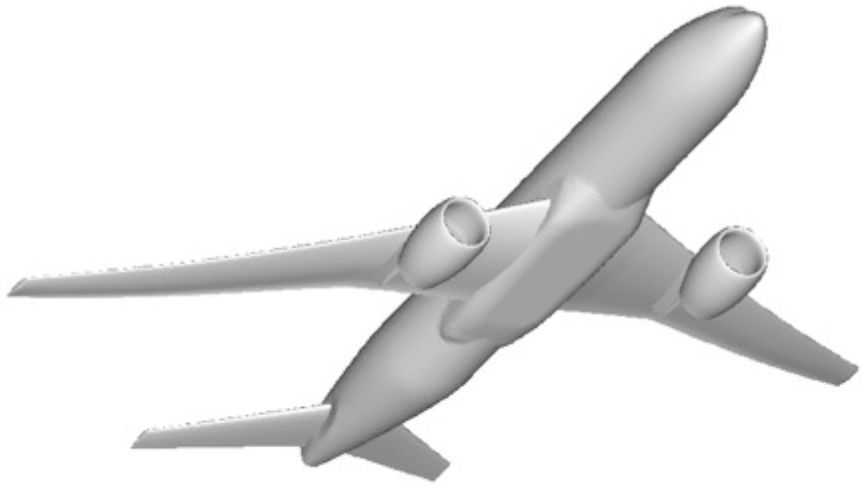

Figure 4.12 WBTFN-Tail CRM aircraft model [76].

4.2.1 Gridding methods

Since the CFD domain shape (hemispherical domain) and size were provided by the DPW-5 [76], the model was ready to be discretised. An unstructured hybrid mesh was generated to discretise the CFD domain. The hybrid mesh is a combination of unstructured mesh and prismatic layers that are placed on the solid surface of the geometry. The number of prism layers was set to be 27, with a growth ratio of 1.35; the total thickness prism layers are 0.0125 of the chord length. It was ensured that the non-dimensional wall distance (Y^+) was approximately one.

For the WB configuration, three meshes were generated as part of mesh sensitivity study, medium mesh with the number of elements ≈ 11 million, fine mesh with ≈19 million and extra-fine mesh with ≈ 27 million elements. For the WBPTFN configuration, the same mesh topology was used as for the clean wing, with the fine mesh selected for use. However, the number of mesh

elements had to be increased to 22 million due to the presence of the pylon and the nacelle surfaces, (Figure 4.13 and Figure 4.14).

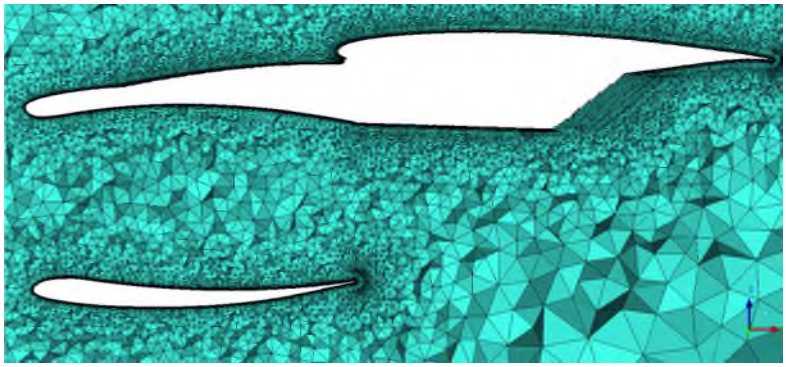

Figure 4.13 Z-X cut plane of the WBPTFN CRM mesh, the section shows the inboard region of pylon mesh and a cut section of the nacelle throughout its axis.

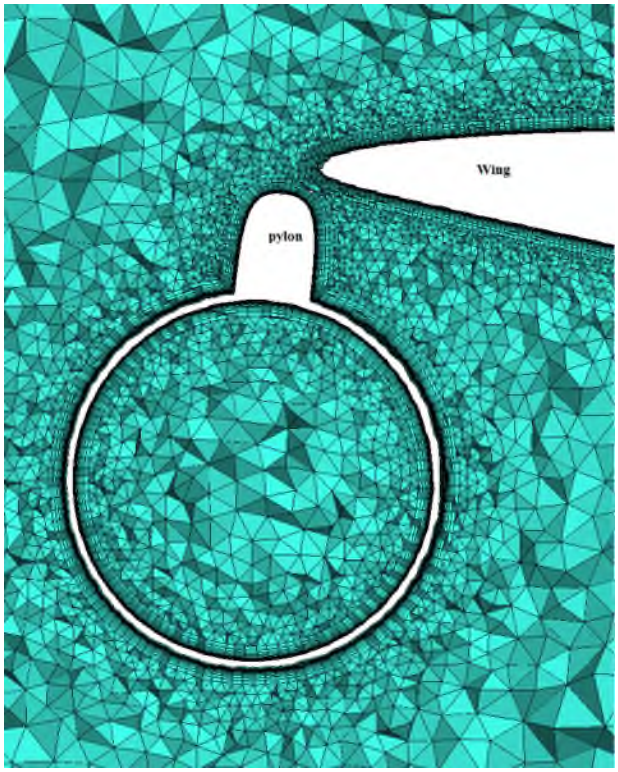

Figure 4.14 Y-Z cut plane of the WBPTFN CRM mesh, the section shows the mesh interaction region between the pylon and the lower surface of the wing.

4.2.2 Numerical scheme and operating conditions

The RANS numerical method coupled with the k−ω SST turbulence model was used. The numerical schemes used in the current simulations of the aircraft model are similar to those for nozzle validation. The only difference is in the convergence strategy used, in which the CFL number was changed from 1.0 for

the first 750 iterations and then increased to 25 with the step of 3.0 after every 750 iterations. After reaching 5000 iterations, the model was switched to a second order upwind discretisation scheme. The iterations continued until the residuals of the momentum, flow equations, energy equation and the turbulence kinetic and dissipation rate each achieved a value of 10^{-5}.

The operating conditions were Reynold's number of $5.0x10^6$ based on the reference chord length of 0.19m [76]. The free stream total pressure and temperature are 29.2 psi (201 kPa) and 100 ˚F (311 °K), have been extracted from DPW-5[76]. Two free stream Mach numbers (M_∞) investigated were: 0.83 and 0.85. The angle of attack of the aircraft ($AoA_{A/C}$) was changed from 0.0˚ to 6.0˚, in intervals of 0.5˚.

4.2.3 Results and discussion

The results are expressed in terms of the pressure coefficient (Cp) distribution at different stations along the wingspan and the aircraft performance in terms of the lift-drag polar for clean (Wing Body (WB)) and the Wing-Body Pylon Through Flow Nacelle) WBPTFN configurations.

Clean WB configuration

The pressure distribution was calculated at different span-wise stations over the wing surfaces. The station's location is denoted by the ratio of the span-wise distance, from the wing root to the local chord length and denoted by η, (Figure 4.15). Three stations (η = 0.201, 0.283 and 0.379) were selected to estimate the chord-wise pressure distribution (Cp). These stations represent the inboard and outboard regions from the pylon.

The computed Cp at the inboard station of η =0.201 shows an underprediction of the negative pressure along the upper surface of the wing, (Figure 4.16). This can be attributed to the experimental rig installation, in which the upcoming airflow twisted the aircraft configuration on the wing. As a result, the effective angle of attack was higher than expected which increased the negative pressure region over the wing. The computed results under predicted the pressure distribution from the wing leading edge up to an axial location over the

wing x/C (ratio of axial displacement over the wing to the local chord length) of 0.40, an overprediction was observed up to x/C =1.00. Apart from that, the calculated Cp over the pressure side surface of the wing agreed reasonably well with the experimental data of Reviers et al. [76]. The different mesh resolutions results showed very little difference, except at the Cp value at x/C =0.10, and x/C =0.40.

The computational results showed better agreement at η =0.283 and η =0.397 stations than at η =0.201, (Figure 4.17 and Figure 4.18). For η = 0.283 the data agreed very well with the measured values of Cp except for the region at the middle of the upper surface of x/C =0.49. The lower surface pressure data showed an agreement throughout the region from the wing tip to x/C =0.47, and the rear part of the wing lower surface. A small deviation was observed across the chord length from x/C =0.48 to 0.452.

At the station outboard from the pylon (η =0.397), the computed pressure coefficient matches the experimental one. However, there is a region where the experimental data were not provided. Therefore, it is difficult to predict the CFD model behaviour across this region. The meshes showed insignificant differences between the three sizes, which was taken, as a sign that mesh above a certain density does not significantly affect the calculated pressure values.

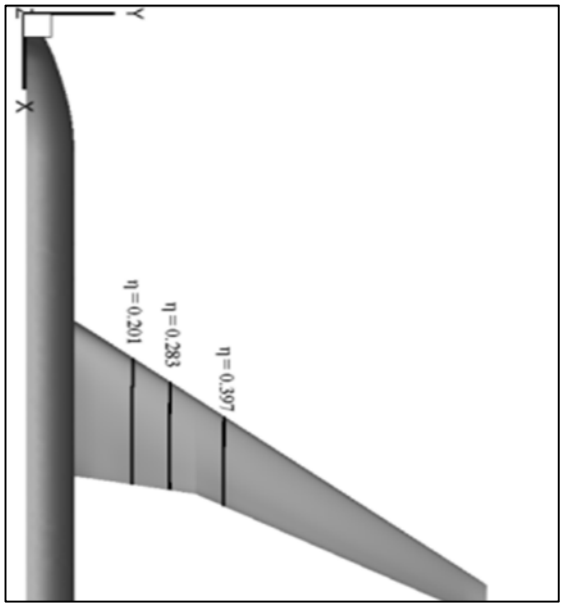

Figure 4.15 Top view of the WB configuration showing the pressure calculations stations.

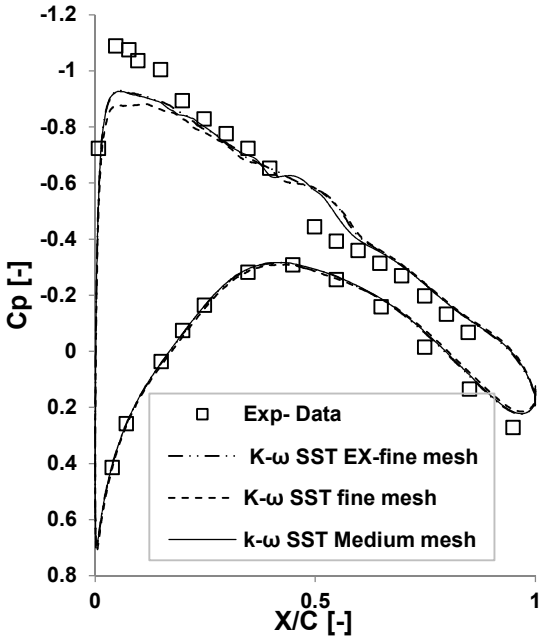

Figure 4.16 Computed results compared with experiments by Rivers et al [76] of the pressure coefficient distribution (Cp) for clean wing CRM (WB) at η =0.201, for three mesh resolutions: 'medium', 'fine' and 'extra fine' for $AoA_{A/C}$ =2.78˚, numerical C_L = 0.55 and experimental C_L = 0.50; All data at Re=5x10^6 and M_∞ = 0.83.

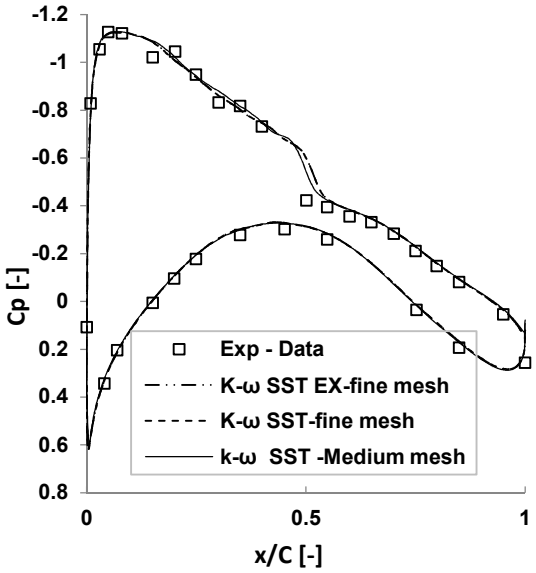

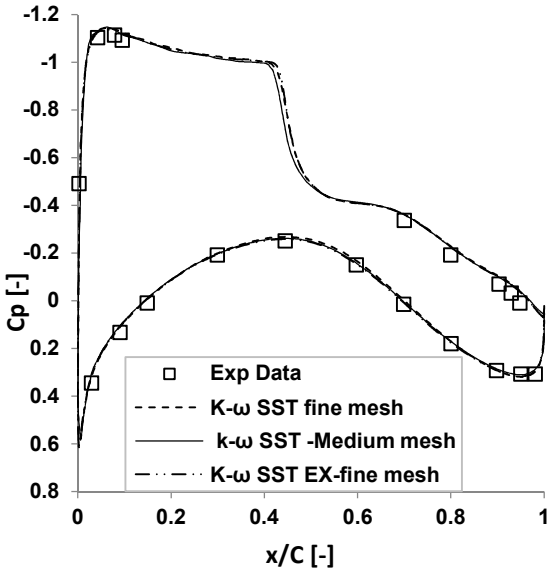

Figure 4.17 Computed results compared with experiments by Rivers et al [76]. Pressure distribution Cp for clean wing CRM (WB) at η =0.283, for three mesh resolutions: 'medium', 'fine' and 'extra fine' for $AoA_{A/C}$ =2.78˚, numerical C_L = 0.55 and experimental C_L = 0.50, All data at Re=5x10^6 and M_∞ = 0.83.

Figure 4.18 Computed results compared with experiments by Rivers et al [2]. Pressure distribution Cp for clean wing CRM (WB) at η =0.397, for three mesh resolutions: 'medium', 'fine' and 'extra fine' for $AoA_{A/C}$ =2.78˚, numerical C_L = 0.55 and experimental C_L = 0.50, All data at Re=5x10^6 and M_∞ = 0.83.

The aircraft aerodynamic performance is expressed in term of the lift-drag polar ($\frac{Cl}{C_{D(A/C)}}$). The results reveal that the computed aircraft drag is over-predicted by approximately $\Delta C_{D(A/C)} \approx 0.0046$ (46 drag count (dc)) for a range of lift coefficients (C_L) from 0.19 to 0.35, (Figure 4.19). With a further increase of C_L, the results for the fine mesh aligned well with the measured data, but the extra-fine mesh results over-predicted C_L. In general, calculations for all three sizes of mesh showed the best agreement with the measured data at high levels of C_L, with drag coefficient deviation of -0.0009 (-9.0 dc).

Realizable k-ε and Spalart-Allmaras (SA) performance were also assessed. The fine mesh was employed for this purpose. The results of SA model showed a close trend to the k-ω SST model results up to C_L = 0.62 where $C_{D(AC)}$ underpredicted. The realizable k-ε model result overpredicted the lift coefficient across the entire range of the aircraft angle of attack.

In general, all model results predicted C_D with the same discrepancy from the experimental data. However, the realizable k-ε and SA computed C_L higher than the calculated values using the k-ω SST model.

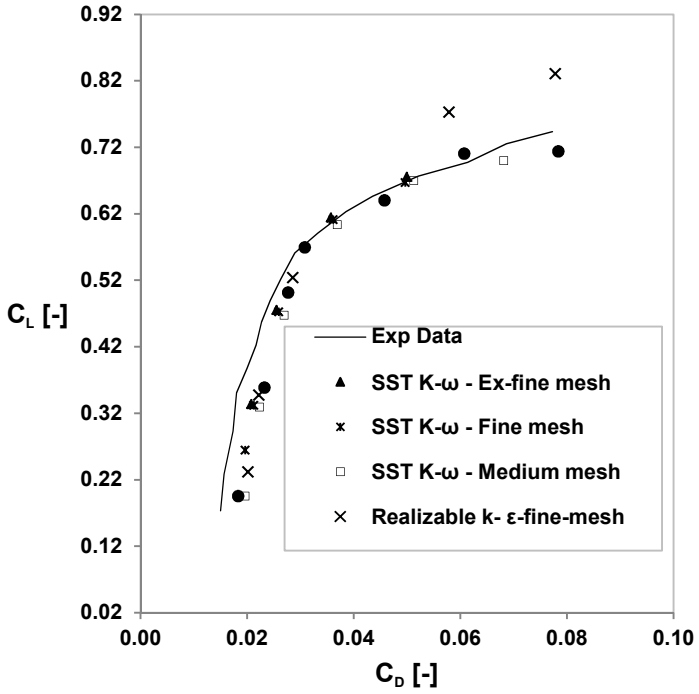

Figure 4.19 Lift-drag polar $(\frac{C_L}{C_{D(A/C)}})$ comparison between the experimental and the numerical results, the CRM configuration is WB, the operational conditions are Re = 5.0 x 10^6, M_∞=0.85 for the chosen $AoA_{A/C}$; medium mesh of 11 million, fine mesh of 19 million, and extra-fine of 27 million.

WBPTFN configuration

Same station locations of the pressure measurement were used for this configuration. The computed Cp data along the inboard stations at η =0.201 and η =0.283 showed an underprediction of the negative pressure over the suction surface of the wing, with ΔCp = 0.045 at x/C = 0.08, (Figure 4.20 and Figure 4.21). Apart from that, the computed results overpredicted the pressure distributions over the entire length and both surfaces. On the other hand, the location and strength of the shock wave were captured very well by the numerical model results for both stations. At η =0.397, the data agreed very well with the measured values of Cp over the pressure surface of the wing, (Figure 4.22). Despite the reasonable agreement over the pressure side of the wing, the negative pressure over the suction surface of the wing is underpredicted by the computed Cp, with a discrepancy of ΔCp = 0.0041 at x/C = 0.07.

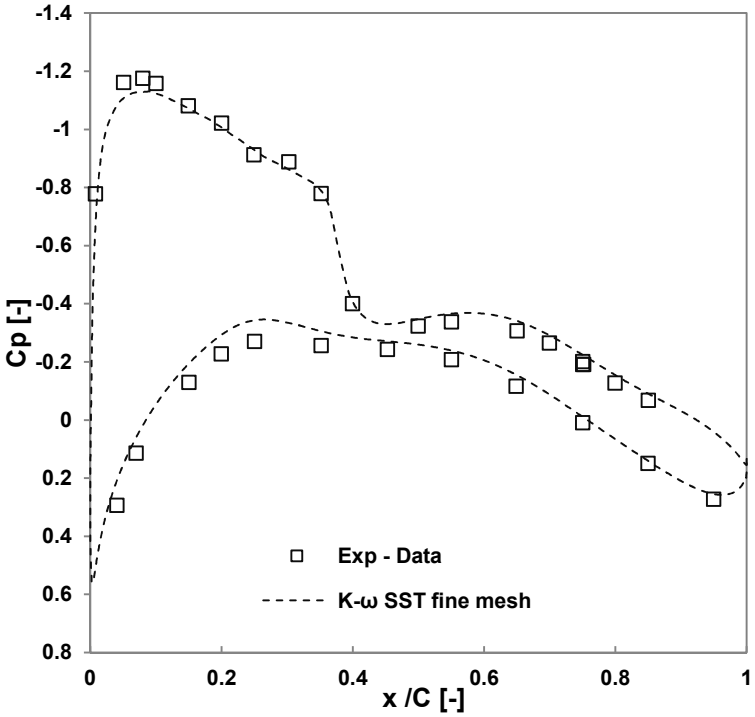

Figure 4.20 Pressure coefficient (Cp) distribution for combined CRM (WBPTFN) at η =0.201, for three mesh resolutions 'medium', 'fine' and 'extra fine' at $AoA_{A/C}$=2.78˚, numerical C_L = 0.55 and experimental C_L = 0.50, numerical results compared with experiments by Rivers et al. [76]. All data at Re=5x10^6 and M_∞ = 0.83, and numerical simulations $AoA_{A/C}$ = 2.5˚.

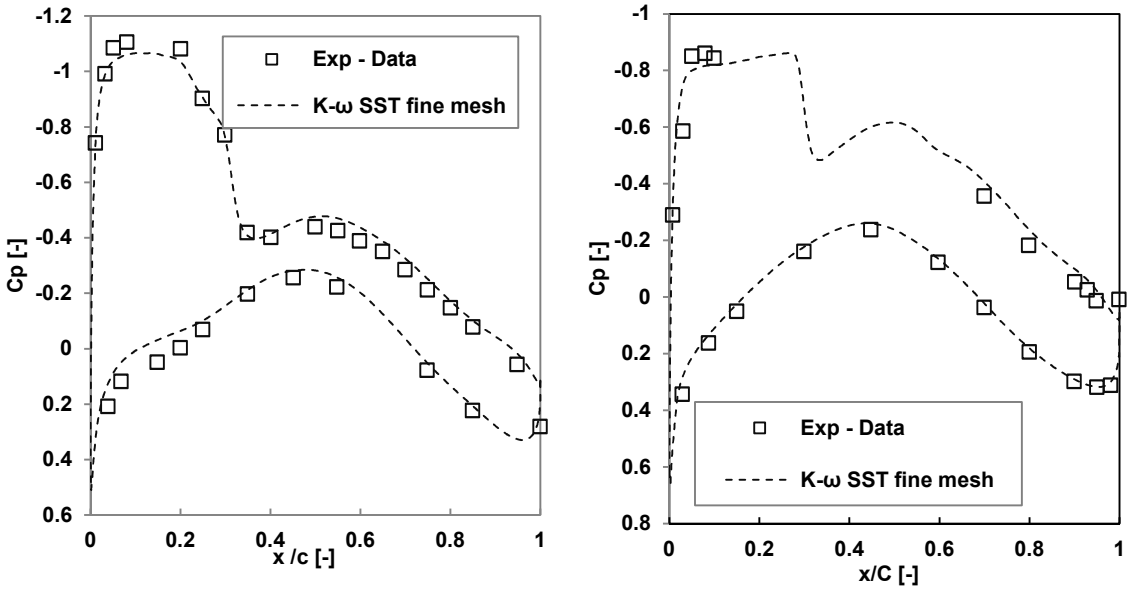

Figure 4.21 Pressure coefficient (Cp) distribution for the combined CRM (WBPTFN) at η =0.283, for three mesh resolutions 'medium', 'fine' and 'extra fine' at $AoA_{A/C}$ =2.78˚, numerical C_L = 0.50 and experimental C_L= 0.50, numerical results compared with experiments by Rivers et al. [76]. All data at Re=5x10^6 and M_∞ = 0.83, the numerical simulations $AoA_{A/C}$= 2.5˚.

Figure 4.22 Pressure distribution (Cp) for the combined CRM (WBPTFN) at η =0.397, for three mesh resolutions 'medium', 'fine' and 'extra fine' at $AoA_{A/C}$ =2.78˚, numerical C_L = 0.50 and experimental C_L = 0.50, numerical results compared with experiments by Rivers et al. [76]. All data at Re=5x10^6 and M_∞ = 0.83, the numerical simulations $AoA_{A/C}$ = 2.5˚.

The computed results for the lift-drag polar of the WBPTFN configuration demonstrated an underprediction for the aircraft drag coefficient across the range of C_L from 0.17 to 0.59, with $C_{D(A/C)}$ difference of 47dc at C_L =0.32, (Figure 4.23). Although $C_{D(A/C)}$ curve aligns with measured data at C_L = 0.67, with the further increase in C_L the computed $C_{D(A/C)}$ levels remain lower than the measured one with a discrepancy of -34 dc at C_L =0.6. A great underprediction in the C_L values was observed with the further increase in the angle of attack. The use of the realizable k-ε and SA models showed a better prediction to the $C_{D(A/C)}$ and C_L as compared with the k-ω SST model results, (Figure 4.23).

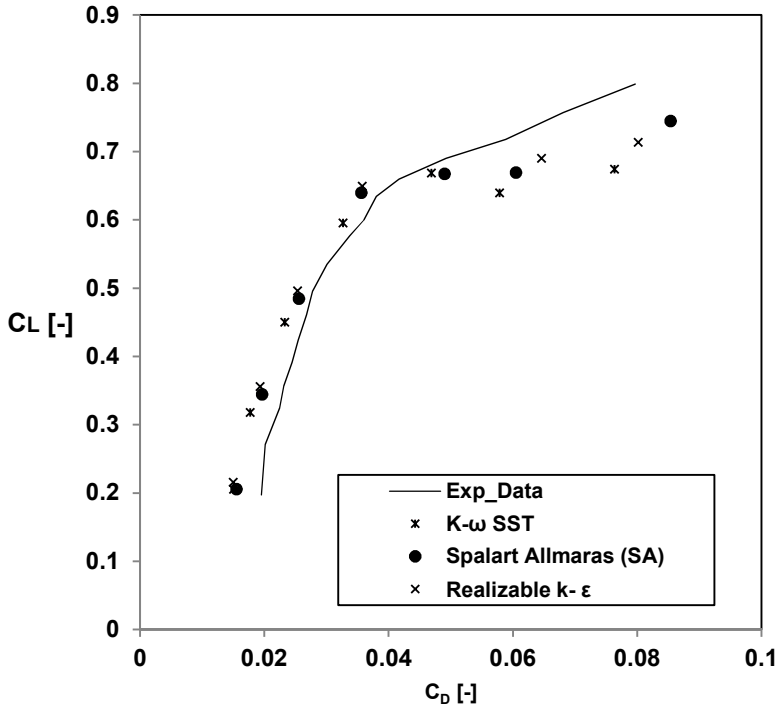

Figure 4.23 Lift-Drag polar ($\frac{C_L}{C_{D(A/C)}}$) comparison between the experimental and the numerical results, for CRM WBTFN configuration, the operational conditions are Re = 5.0 x 10^6, M_∞=0.85 for the chosen $AoA_{A/C}$; the mesh was extra-fine with 27 million.

4.3 Summary

a) Validation cases were performed for the exhaust system and the aircraft configurations, to assess the performance of the aerodynamics assessment model.

b) Two different nozzle configurations (single stream and plug nozzle) were chosen for the validation purpose.

c) The simulation results did not capture the separation region accurately. Moreover, the flow over the plug surface at NPR =3.12 and M_∞=0.6 show disagreement with the measured data. Despite that, at high fineness ratio of the single stream and low levels of the nozzle pressure ratio (NPR), the results agreed in a reasonable way, regarding the pressure distribution and the nozzle performance.

d) For the single stream nozzle, the calculated performance results were lower than the experimental data by ≈ 3.29% at NPR = 1.83 and by 0.84% at NPR = 3.88. On the other hand, the plug-nozzle efficiency results deviated from the measured data by -1.05% at NPR =2.64 and across a range from -0.46% to -0.68% between NPR =3.14 to 5.3.

e) Common Research Model (CRM) was used to validate the numerical model employed to assess the aerodynamic performance of the engine/aircraft configuration.

f) The pressure coefficient distributions along the wingspan showed agreement with the experimental data, except at the inboard station of the pylon, where there is an underprediction for the negative pressure region above the wing.

g) The k-ω SST turbulence model results showed the most acceptable deviation ranges from the measured data in comparison with the other models, for the nozzle and the aircraft configurations (WB and WBPTFN).

5 Isolated aero-engine exhaust-system performance analysis

5.1 Overview

The first part of the current work is to quantify the performance of the isolated exhaust system under different geometrical and operational conditions. A range of geometrical parameters has been varied to quantify their effect on the performance of the nozzle. Two nozzle configurations have been used in the current study, a basic nozzle with the central body (plug) and the dual-stream exhaust system. In this section, the nozzle configurations design, the domain, and the mesh study are presented. The aerodynamics and the generation of performance maps and the maps' aerodynamic behaviour are explained.

5.2 Rationale

The performance maps of the exhaust system should cover a wide range of the geometrical and operational conditions. Therefore, it will produce a more sophisticated performance prediction for several engine configurations and operational requirements. In this chapter, a parameterisation for an aero engine nozzle is performed, and performance characteristic maps are produced.

For the sake of covering a wide range of geometrical parameters, and separating the variables interference impact, the exhaust system of a civil engine was simplified. A basic nozzle with the central body (plug) was selected to perform the parameterisation at cruise Mach number.

To use these maps for the core nozzle, another set of simulations was performed using a dual-stream nozzle configuration. The simulations were carried out over the same selected geometrical and operational parameters of the basic nozzle configuration, but on the core nozzle only, in addition to the variation of the bypass nozzle pressure ratio.

5.3 Nozzle configuration design

The simulated basic nozzle configuration was extracted from the bypass nozzle of a civil aircraft engine (CF6-80E1). The reason behind that is to eliminate the

mutual effect of the geometrical modifications of the bypass nozzle on the core nozzle and vice-versa. The geometrical representation of the nozzle was defined using nth order polynomials. Moreover, an analytical method based on Classification-Shape-Transformation (CST) has been used for the parameterisation and to ensure a smoothed curve design. This method has been used to design the internal nozzle aero-lines. It eases the geometrical modification of the aero-line after changing the chosen parameters. The CST was proposed initially by Kulfan and Bussoletti [115]. It was derived from the basic equations that govern the geometrical aerofoil profile. This method was also used by Moritz and Dieter [116] to optimise the intake and cowl surfaces of a nacelle. Goulos et al.[64] used the CST methodology to optimise the civil aero-engine exhaust system. The authors exploited geometrical optimisation to achieve a correct nozzle exhausted flow, providing future engine designers with the optimum aerodynamic behaviour for exhaust systems[64].

This method mainly produces simple linear analytical equations that create smooth complex curves. The curves are connected by matching the spatial boundary conditions between the ends of the curve segments. Each curve segment has its unique system of linear equations depending on its spatial boundary conditions.

The CST method mainly consists of the class function $\left(\mathrm{C}(\psi)\right)$ to define the basic profile, and the shape function $(\mathrm{S}(\psi)\ )$ to create the specific shape within the particular geometry class. The final CST curve equation at the end of the combination of the class function and the shape function is:

$$\boldsymbol{\zeta}(\boldsymbol{\psi})_i = \boldsymbol{C}_{N2}^{N1}(\boldsymbol{\psi})_i \boldsymbol{S}(\boldsymbol{\psi})_i + \boldsymbol{\psi}.\Delta\boldsymbol{\zeta} \qquad \textbf{(5-1)}$$

where (ψ,ζ) are the vertical and the horizontal Cartesian coordinates in the non-dimensional coordinate design space, (i) is the curve segment identifier, and N1 and N2 are the exponents of the class function that gives the basic general class of geometrical shapes. The imposed value of the exponents for the current configuration is close to zero, which gives ($C_0^0(\psi)_i = 1$ for ψ=[0,1])[64].

The shape function $S(\psi)_i$is a Bernstein polynomial offering different behaviour at various orders of the polynomial in which the smoothness of the curve

increases with the polynomial orders (Equation (5-2)).

$$S(\psi)_i = \sum_{r=0}^{n} A_r \,.\, K_r^n \,.\, \psi^r \,.\, (1-\psi)^{n-r} \quad \textbf{(5-2)}$$

Where (A_r) is the weighting coefficient, controlling the curvature of the curves that form the nozzle aero-lines. The weighting coefficient, also, alter the curve shape when the configuration geometry constraints change. The Bernstein polynomial order (*n*) and the binomial coefficient (*K*) are defined in Equation (5-3). The distance offset (Δy) represents the distance between the curve end in the radial direction and the axial axis, which is represented by the inner-aero-line radius in the current configuration, (Figure 5.1).

$$\boldsymbol{K_r^n = \frac{n!}{r!(n-r)!}} \quad \textbf{(5-3)}$$

After applying the spatial boundary conditions, which were extracted from the imposed design dimensions of the exhaust system, a system of linear analytical equations was produced. This set of equations varies during the parametrisation process due to alteration of the spatial boundary conditions. For the current configuration, the nozzle was designed on the basis of non-dimensional performance analysis. The design variables for the current geometry are the slopes (the first derivative of the function) and the radius of the curvature, Equation (5-4). The effect of the variation of the design variables on the design space is translated as the spatial boundary conditions and weighting coefficients variation.

$$R_{ci} = \frac{\left[1 + \left(\frac{d\zeta}{d\psi}\right)^2\right]^{3/2}}{\frac{d^2\zeta}{d\psi^2}} \quad \textbf{(5-4)}$$

The order of the polynomials (*n*) controls the design space size, whereas the weighting coefficients $(A_{i,n})$ act as design parameters. Therefore, the order of the polynomials is different for each segment of the nozzle curves. The location of the point of origin (0,0) in the design space of the current geometries was assumed to be the start point of each segment. In other words, the zeros of the

x,y coordinates are moved to the beginning of each altered curve in the nozzle. This simplifies the modification of the curve analytical models. Therefore, the weighting coefficient ($A_{i,0}$) is equal to zero for all the curves. The other weighting coefficients are a function of the particular design variables, and they are sensitive to the spatial boundary conditions. The total number of the design variables depends on the order of Bernstein polynomial, which is n+1.

For segment (FG), in Figure 5.1, n is equal to 4.0; this will produce a design vector of P_{FG}= [$\alpha_1, \alpha_2, \frac{R_{c1}}{L_{nozzle}}, \frac{R_{c2}}{L_{nozzle}}$] and for segment DC n=3.0. Therefore, the design vectors are P_{DC}= [$\alpha_3, \alpha_4, \frac{R_{c4}}{L_{nozzle}}$]. Segment (GH) is a straight line; therefore, it has been designed based on straight-line equation with the design variables of a line slope (β), and $\frac{R_{c4}}{L_{nozzle}}$. The same geometrical representation has been used for the core nozzle in the dual-stream nozzle configuration.

It is worth to be mentioned that the flow area inclines inward; it represents the minimum distance that is connecting the nozzle rim and the hump aero-line of the nozzle[33].

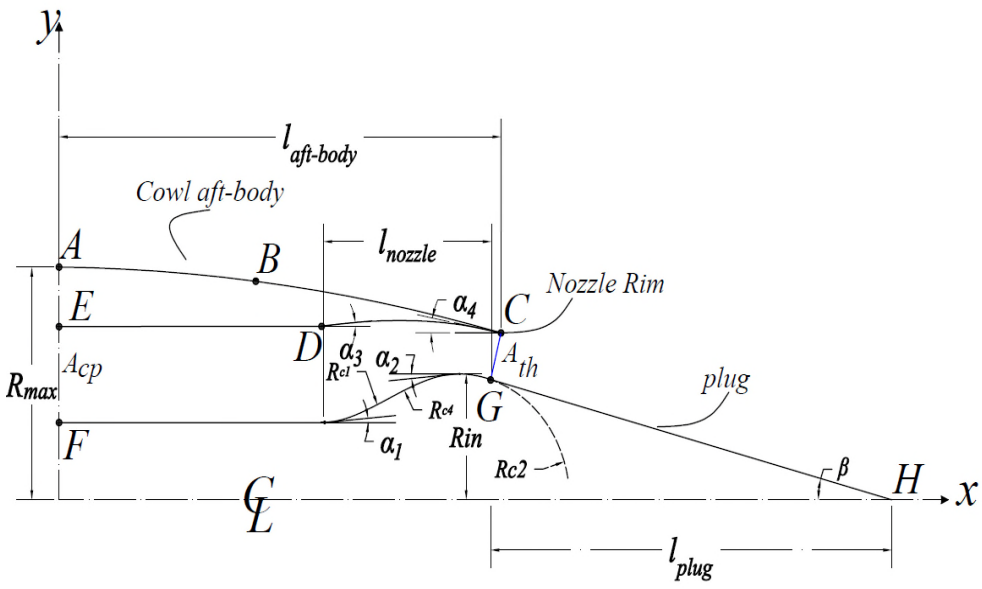

Figure 5.1 Section view of the basic exhaust system configuration with the main geometrical lead parameters.

5.4 Nozzle parameterisation

In the current project, a variation of a set of geometric and aerodynamic parameters was performed. These parameters include; the plug angle (β) accompanied with the variation of the nozzle pressure ratio (NPR) and the contraction ratio (CR) (the ratio of the inlet area to the throat area of the nozzle).

The variation in R_{in} changes the nozzle throat area and accordingly the contraction ratio ($\mathrm{CR} = \mathrm{A_{cp}}/\mathrm{A_{th}}$) within the range, which is presented in Table 5-1. and Table 5-2 for both, the basic nozzle and the dual stream nozzle, respectively. Full geometry details for the basic and the core nozzle configurations are presented in Table Ap.A 2, Table Ap.A 3 respectively, and Figure 5.2.

Because of the complexity of the turbofan exhaust-system design, the change in any of the design parameters alters some additional constraints of the neighbouring components. For instance, changing the angle of the core-cowl will be accompanied by a significant change in the core nozzle geometrical profile and the design shape. Therefore, to eliminate any mutual impact of a large number of design variables, some of the significant geometrical constraints were kept fixed.

The nozzle throat area ($\mathrm{A_{th}}$) change was achieved by the change in the inner aero-line radius of curvature of the nozzle. However, to keep β constant during the variation of CR, which has a significant impact on the nozzle performance, the length of the plug was changed to meet the increase in the value of lower aero-line radius (R_{in}), (Figure 5.1). However, the increase in the length of the plug (considering the plug with β =15˚ is the reference length) increased the gross thrust coefficient across a range from 0.2% to 0.3% from NPR =1.4 to 3.0, which is insignificant.

To explore the effect of the CR if it is changed in the other way around, in other words, by changing the inlet area of the nozzle rather than$\mathrm{A_{th}}$; two additional nozzle geometries were investigated. These geometries have different CR of 1.6 and 2.0, by varying the inlet area only, Figure Ap.A 4 and Figure Ap.A 5.

The nozzle discharge coefficient showed a negligible difference between the two configurations, with the maximum deviation (ΔC_d) of 0.0016 at NPR of 1.40. Furthermore, the maximum change in the nozzle thrust coefficient (ΔC_{fg}) is 0.0028 at the nozzle pressure ratio of 1.80 between the two configurations, (Figure Ap.A 6 and Figure Ap.A 7). Therefore, the variation of the CR by changing the inlet area is not of interest. Furthermore, another observation could be drawn from that, is the effect of the flow velocity (Mach number) inside the nozzle duct has a small influence on the overall nozzle performance.

The performance calculations were performed at mid-cruise operating conditions (Alt. = 36,000 ft, M_∞ = 0.82). The total temperature ratio of the nozzle inlet was kept constant at (T_{tcp}/T_∞) of (1.33) for the entire range of the nozzle pressure ratio (NPR). The effect of temperature was not considered in the current work. For the sake of reducing the variable variations and their impact, the gas was considered a real air without the inclusion of the engine combustion products.

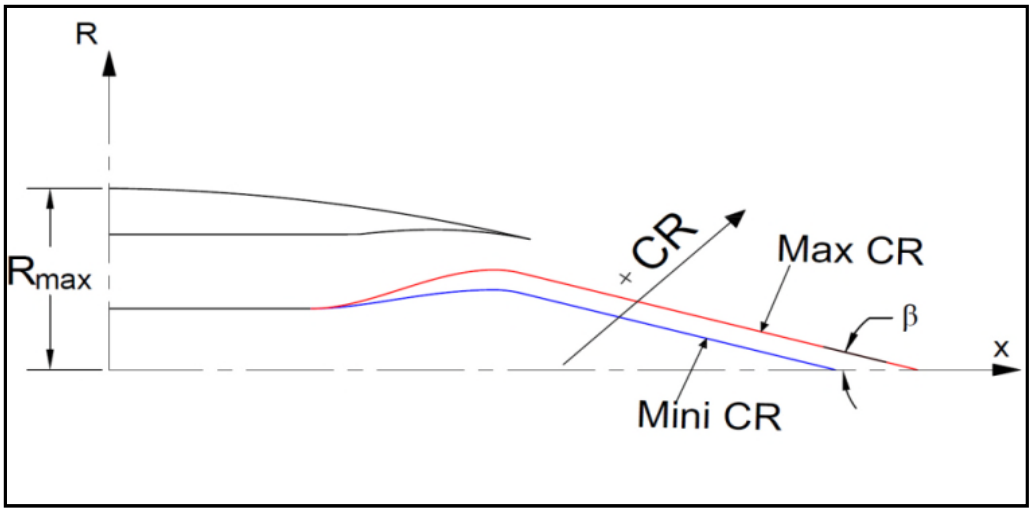

Figure 5.2 Schematic of the nozzle showing the main parameterisation parameters.

Table 5-1 Parameterisation cases of the basic-nozzle configuration.

Case#	$(CR = \frac{A_{cp}}{A_{th}})$	β Plug-half angle	NPR[-]	M_∞[-]
1	1.30	10°-20°	1.4-3.0	0.82
2	1.40	10°-20°	1.4-3.0	0.82
3	1.53	10°-20°	1.4-3.0	0.82
4	1.60	10°-20°	1.4-3.0	0.82

5	1.66	10°-20°	1.4-3.0	0.82
6	1.74	10°-20°	1.4-3.0	0.82

Table 5-2 Parameterisation cases of the core-nozzle configuration

Case#	$(CR = \frac{A_{cp}}{A_{th}})$	$(cCR = \frac{A_{cp}}{A_{th}})$	β Plug-half angle	FNPR[-]	Core NPR[-]	M_∞[-]
1	1.42	1.35	10°-20°	1.0 and 2.0-2.8	1.2-3.0	0.82
2	1.42	1.43	10°-20°	1.0 and 2.0-2.8	1.2-3.0	0.82
3	1.42	1.50	10°-20°	1.0 and 2.0-2.8	1.2-3.0	0.82
4	1.42	1.57	10°-20°	1.0 and 2.0-2.8	1.2-3.0	0.82
5	1.42	1.67	10°-20°	1.0 and 2.0-2.8	1.2-3.0	0.82
6	1.42	1.77	10°-20°	1.0 and 2.0-2.8	1.2-3.0	0.82

5.5 CFD solution

5.5.1 Domain sensitivity analysis and boundary conditions

The effect of the CFD domain size needs to be assessed. Since a rectangularly shaped domain is distinguished the employed numerical domain, the height and width of the domain were normalised to the maximum engine diameter (D_{max}). The radial and the axial domain size were identified by the ratio of H/D_{max} and W/D_{max}, respectively. Four ranges of H/Dmax and W/Dmax were examined; (Table 5-3). The increase in the domain size showed a negligible effect on the nozzle performance. It was found that, for the basic nozzle configuration, the C_d (discharge coefficient) variation between the third and the fourth domain is equal to +0.0027%, and C_{fg} (thrust coefficient) variation is +0.005964%. For the dual stream nozzle cases, the increase in the domain size showed that C_d variation between the third and the fourth domain is equal to +0.00007. The thrust coefficient (C_{fg}) variation is +0.00009 for the basic nozzle configuration and +0.00009 for dual-stream nozzle configuration. The third domain with H/D_{max}=30 and W/Dmax=90 was chosen to carry out the simulations for both configurations, (Figure 5.3).

Table 5-3 Domain sizes identifier.

Identifier	x	y
D1	30	10
D2	60	20
D3	90	30

D4	120	40

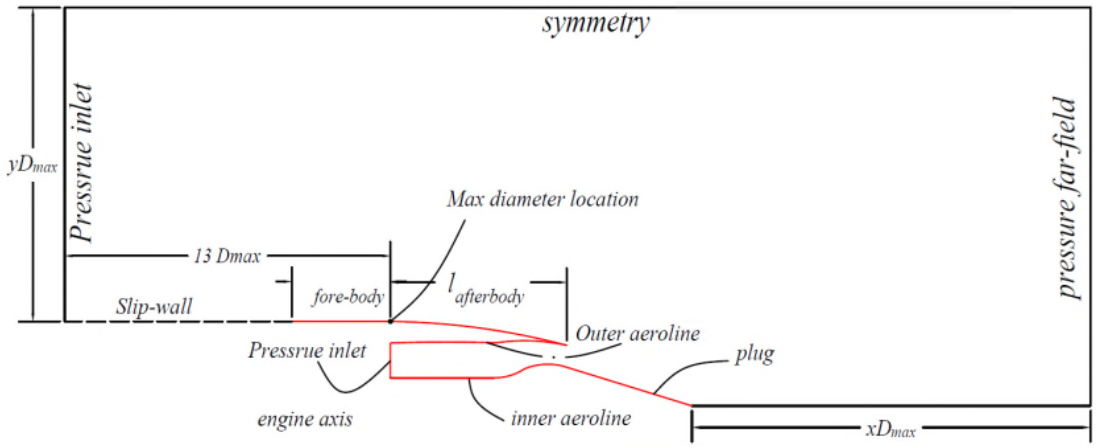

Figure 5.3 Domain and boundary conditions of the isolated basic exhaust system (Not to scale).

5.5.2 Gridding methods

The multi-block structure mesh topology was used to create the required mesh of the CFD domain. The flow surrounding the exhaust system was considered as being at 0.0° angle of attack; therefore, an axisymmetric domain was used for the current simulations. The mesh was refined sufficiently in the regions where there are significant changes in the flow features, particularly in the exhaust jet region. The boundary layer region was discretised to ensure that y^+ value was very close to one. The growing ratio of the mesh in the radial direction was 1.20 for the boundary-layer region and 1.22 for the external domain.

A grid sensitivity study for the mesh was carried out, to ensure the credibility of the utilised mesh. The mesh size has been increased to check the effect of the number of cells on the physical properties of interest. The mesh number of elements was increased from $8.6\text{x}10^4$ to $4.8\text{x}10^5$ with a refinement ratio of ≈1.45, for the basic nozzle configuration. For the dual-stream nozzle, the number of the mesh elements was increased by refinement ratio of 1.47 from $1.0\text{x}10^5$ to $2.3\text{x}10^5$. The value of discharge (C_d) and thrust coefficient (C_{fg}) was assessed to check their dependence on the number of elements. The last three meshes were chosen to report the Grid Convergence Index (GCI) as presented in Table 5-4 and Table 5-5.

Table 5-4 Grid sensitivity to the number of elements based on the evaluation of GCI for the basic-nozzle configuration at operational conditions of M_∞=0.82 and NPR =2.5, for configuration of CR=1.75 and β =15˚.

f	(p)	$GCI_{1,2}$	$GCI_{2,3}$	$\frac{GCI_{1,2}}{r^p GCI_{2,3}}$
C_d	2.08	0.007%	0.012%	1.0
C_{fg}	2.23	0.003%	0.006%	1.0

Table 5-5 Grid sensitivity to the number of elements based on the evaluation of GCI for the dual-stream nozzle configuration at operational conditions of M_∞=0.82 and NPR =2.5, for configuration of CR=1.4 and cCR=1.57 and βc-c =14º and β_{plug}=18˚.

f	(p)	$GCI_{1,2}$	$GCI_{2,3}$	$\frac{GCI_{1,2}}{r^p GCI_{2,3}}$
C_{dbp}	5.55	0.0006%	0.005%	1.0
C_{dcore}	6.0	0.004%	0.034%	1.0
C_{fg}	5.7	0.003%	0.03%	1.0

The medium mesh size with $3.25x10^5$ elements has been chosen to perform the simulations for the basic nozzle, and the fine mesh ($2.3x10^5$ elements) was used for the dual-stream nozzle simulations. The selection was based on considering the need for a strike balance between the accuracy of the results and the time required to carry out the calculations. The employed mesh for both configurations is presented in Figure 5.4 and Figure 5.5.

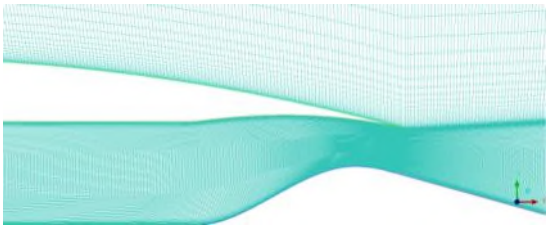

Figure 5.4 Close up of the mesh topology employed at the nozzle region, for the basic nozzle configuration.

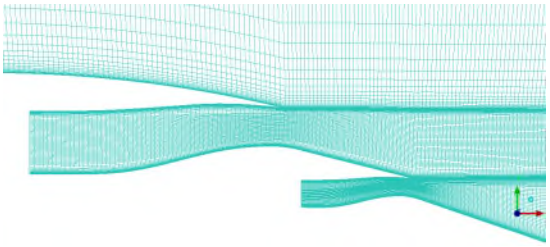

Figure 5.5 Close up of the mesh topology employed at the nozzle region, for the dual-stream nozzle configuration.

5.5.3 Numerical scheme and convergence criteria

Reynolds-Averaged Navier-Stokes (RANS) numerical methodology coupled with the k-ω Shear-Stress Transport (SST) turbulence model was employed. This approach was built in a commercial flow solver ANSYS™ Fluent [102]. A steady state, implicit, and density-based solver was set up to perform the simulations. The Green-Gauss node-based method was used to compute the flow field gradients. A second-order accurate upwind scheme was employed for

the spatial discretisation of the flow field. Sutherland's law was utilised for the calculations of dynamic viscosity [102].

A convergence strategy has been conducted to achieve fast iterative convergence. The calculations were initialised using uniform free-stream flow conditions, in association with Courant number (the time step) (CFL) of one, and the first-order upwind scheme. The value of the CFL was increased by 2.0 after every 500 iterations, up to CFL= 20. After achieving converged residuals of the first-order upwind scheme, the solver was switched to the second-order upwind scheme so that the divergence was avoided. The computations were continued to approximately 15,000 iterations, at which point the residuals of the flow equations reached the value of 10^{-7}, the momentum residuals achieved the value of 10^{-7}, and the turbulence and energy equations residuals were of the order of 10^{-5}.

5.6 Results and Discussion

In the current section, a discussion of the selected degree of freedom impact on the exhaust system of the aero-engine that has been covered in the current project is presented. This includes the nozzle pressure ratio (NPR), contraction ratio (CR), and the half angle of the plug (β); these parameters are applied to both types of the nozzle.

The results are presented in terms of the pressure coefficient over the surfaces, the pressure forces of the exhaust-system components, which normalised to the ideal thrust of the nozzle to enable a comparison between thrust and drag forces, and the nozzle performance metrics.

5.6.1 Nozzle system aerodynamics

Effect of the nozzle pressure ratio

The NPR has been changed from 1.4 to 3.0 to cover the range of an unchoked and choked nozzle operating conditions. The NPR value was increased by changing the total inlet pressure of the nozzle. Increasing the NPR will increase the value of the static pressure at the nozzle throat; consequently, the

expansion process of the exhaust flow to the free stream intensified. Because of that, the pressure over the plug surface increased with NPR, (Figure 5.6). It can be seen that the static pressure increases with the NPR at the nozzle exit plane (x/l_{plug} = 0.0), in which it reached to Cp = 1.9 at NPR = 3.0.

A shock structure occurred across a range of the NPR from 2.4 to 3.0, (Figure 5.6 and Figure 5.7). The shock structure increases the pressure forces over the plug. Since the plug surface is inclined backwards, the pressure forces contribute positively to the gross thrust of the engine, as the plug pressure force is added to the thrust values. Despite that, the presence of the shock produces a negative pressure over the plug expressed by a low-pressure area (shaded lines) that appeared at high NPR (2.6-3.0), (Figure 5.6). These negative occurs due to the strong expansion of the flow just behind the shock. The negative pressure regions contribute to the drag as they pull the engine backwards. However, the effect of these regions is insignificant, if it was compared with the size of the positive pressure regions. Even though there is an increase in the pressure forces of the plug, the ratio (Φ_{plug}/Fi) showed a decline in relation to the ideal thrust, (Figure 5.6), due to the expansion losses of the thrust with the increase in the NPR. Therefore, the contribution of the plug forces to the thrust with the NPR reduced. It should be noted that the positive sign of the forces stands for the forces directed downstream.

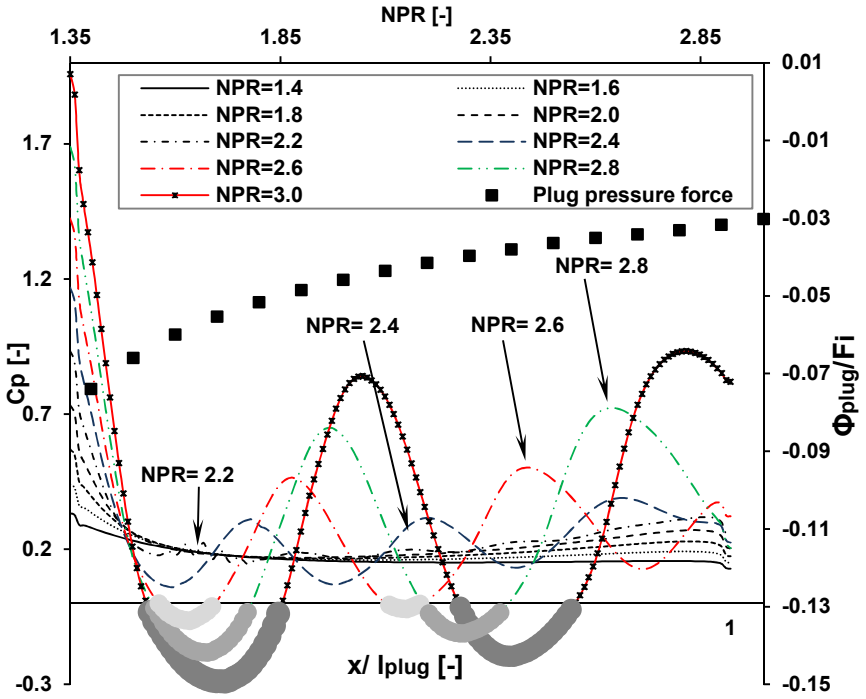

Figure 5.6 Pressure coefficient (Cp) and plug pressure forces (Φ_{plug}/F_i) distribution over the cone (plug) surface at different NPR, for the basic nozzle configuration of CR=1.4, and β =10˚.

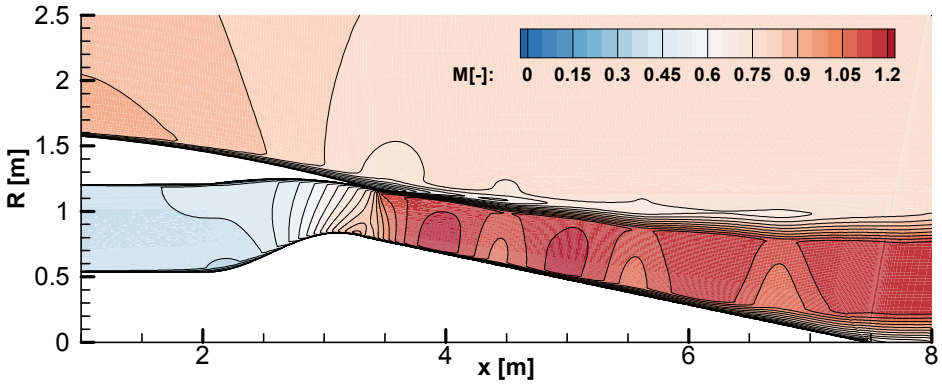

Figure 5.7 Mach number contour around the nozzle configuration of CR =1.60, M_∞ =0.82; for β =11˚; at running NPR of 2.5.

The pressure forces over the cowl after-body surface reduced with the increase in the NPR. This is attributed to the increase in the inclination angle of the jet stream tube with the NPR away from the engine axis. This indicates a reduction in the after-body drag component as the after-body surface inclined backwards. This reduction is balanced by the external free stream pressure forces that are exerted on the imaginary boundaries of the post-exit stream tube, which was considered as a thrust component [64,110].

As it can be seen in Figure 5.8, the averaged pressure coefficient, over the surface of the afterbody, predominantly increased with the NPR at the rear part of the afterbody (red line). This increase becomes noticeable at NPR higher than 2.2, as the difference in the cowl after-body averaged Cp is ≈0.020, from NPR of 2.2 to 3.0. The increase in the pressure forces reduced the cowl after-body drag component, especially across the range of NPR from 2.0 to 3.0, when the jet stream-tube starts to form.

The nozzle jet impact is insignificant along the region from the point B to A, (Figure 5.8), in which the average Cp shows a levelled off profile with the NPR. This indicates that the impact of the jet on the cowl after-body not necessarily extended from the nozzle rim to the maximum diameter location, as was pointed out previously.

The nozzle backpressure (at the nozzle rim (C)) shows a continuous increase with the increase in the NPR from low levels of 1.40 up to 3.0, (Figure 5.8). In other words, the backpressure of the nozzle has higher pressure levels than the free stream one, and this will change the nozzle operational condition at off-design engine run.

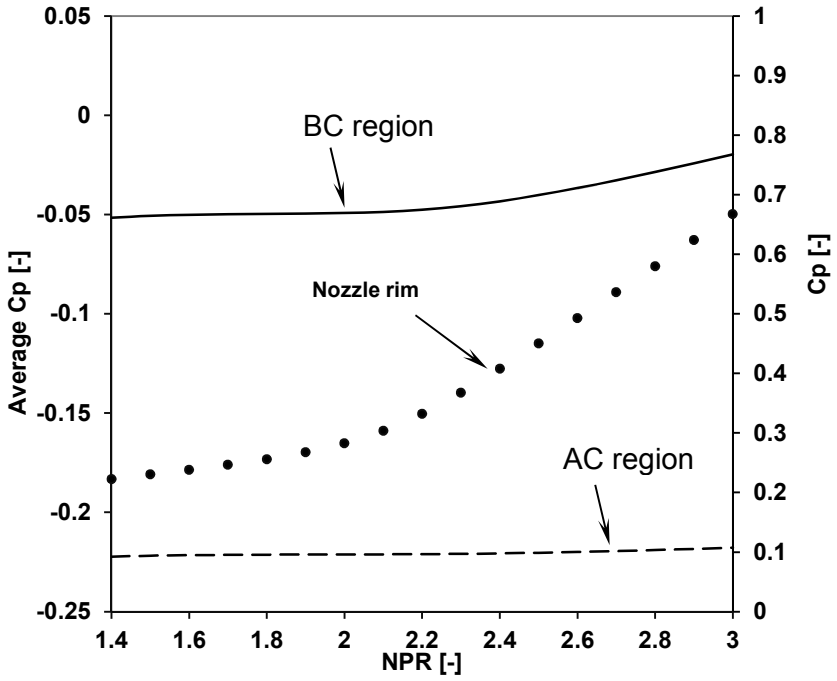

Figure 5.8 Pressure coefficient (Cp) distribution over the cowl afterbody as a function of the NPR, for the basic nozzle configuration of CR=1.54, and β =15˚.

Effect of the plug half-angle (β)

The increase in β affects the pressure distribution over the plug surface due to the increase in the area of the free stream tube downstream the nozzle exit plane. This can be seen in Figure 5.9, at low NPR (1.4), Cp increased by 0.0211 at the plug edge when β was increased from 10˚ to 20˚, with an increasing interval of ≈0.022 between every two following values of β. At high NPR (3.0), the strength of the wave structure slightly increases with β due to the increase in the stream tube area downstream the nozzle.

The normalised pressure forces over the plug surface increased towards the thrust direction, (Figure 5.10). The increase in the plug pressure forces is noticeable at low NPR, in which the plug force-ratio difference between the two extreme angles (β=10˚ and 20˚) is ≈ 0.040 at NPR =1.4. However, this difference reduces with the increase in the NPR, to $\Delta(\frac{\Phi_{plug}}{F_i})$ of 0.012 at NPR =3.0. The variation of the pressure force becomes insignificant between β =17˚ and β =20˚ across the range of NPR from 2.8 to 3.0. This behaviour can be attributed to the separation of the nozzle jet flow with the increase in β after experiences a strong shock.

The impact of changes in β on the cowl after-body is significant. The change in the plug angle produces a variation in the stream-tube shape. Furthermore, since the external flow is not static (M_∞= 0.0), the area of the oncoming stream tube will be altered, as well. Increasing the angle of plug pulls down the post-exit stream-tube; consequently, the area of the external stream-tube just over the after-body surface will increase. This increase raises the pressure forces that are directed backwards, causing an increase in the pressure drag, (Figure 5.11).

It was stated above that the pressure drag coefficient ($C_{Daft.body}$) over the afterbody reduces with the NPR. However, across the range of the NPR between 1.4 and 2.0 and across β range between 15˚ to 20˚, $C_{Daft.body}$

increased, (Figure 5.11). This behaviour is β value dependent, as it shows contradicting behaviour through the range of β from 10˚ to 14˚. This increase in $C_{Daft.body}$ in this ranges can be attributed to the increase in the inclination angle of the nozzle jet towards the plug surface, rather than axially. Therefore, the external free stream-tube directed towards the engine axis as well, causing a reduction in the pressure forces over the afterbody surface. Therefore, the effect of the forces that push the engine forward will reduce.

This behaviour is of importance, as across this range of NPR (1.4-2.0), the selection of β could be efficient for the engine running at low power settings; however, it produces a drastic increase in the afterbody drag. Therefore, it is essential to compromise between this trade-off in the aerodynamics of the exhaust system.

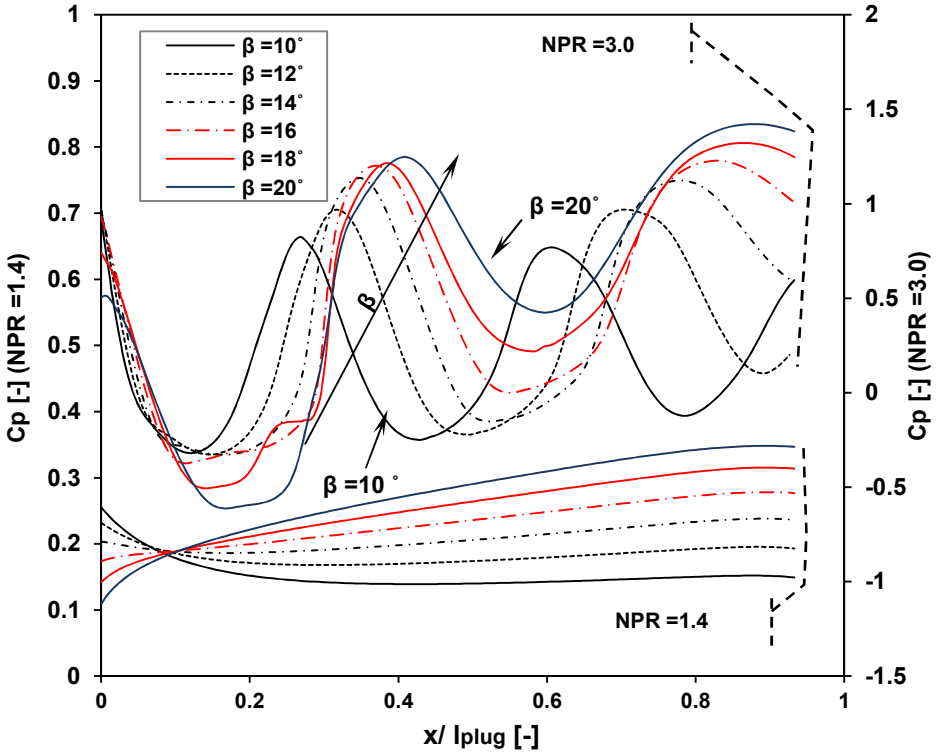

Figure 5.9 Pressure coefficient (Cp) distribution over the plug surface at NPR = 1.4 and 3.0, at the chosen cone half angle (β), at operational conditions of M_∞ = 0.82 and Alt. = 36,000 ft, for the configuration of CR = 1.75.

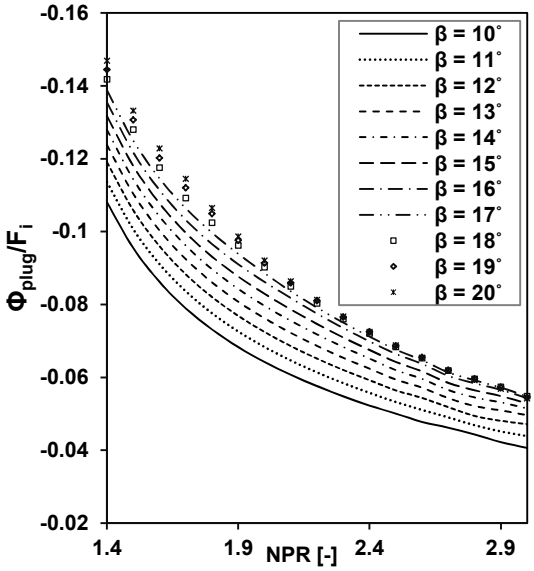

Figure 5.10 Pressure force of the plug as a function of the NPR for the chosen cone half-angle (β) at operational conditions of M_∞ = 0.82, for configuration of CR = 1.75.

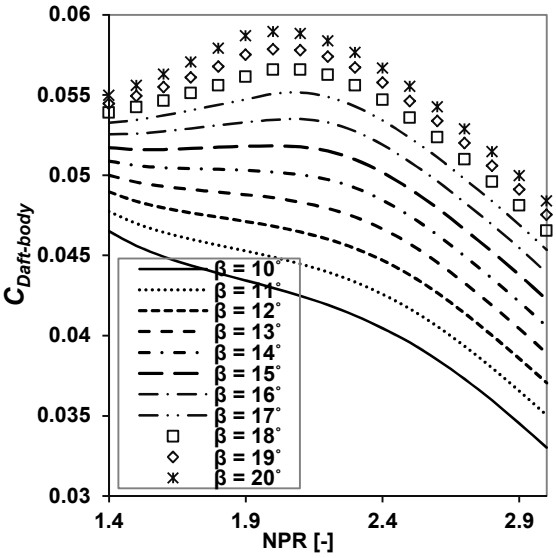

Figure 5.11 Drag coefficient of the cowl after-body as a function of the NPR for the chosen plug half-angle (β) at operational conditions of M_∞ = 0.82, for configuration of CR=1.75.

Effect of the contraction ratio (CR)

The increase in the CR has been achieved by reducing the throat area. The decrease in the throat area entails a decrease in the radius of curvature of the lower aero-line (R_{c4}) of the nozzle and an increase in R_{in}. This causes an increase in the pressure over the inner aero-line with the increase in the CR, (Figure 5.12). Therefore, the pressure inside the nozzle increases. Additionally, it was found that the pressure coefficient is in a proportional relationship with the increase in NPR, (Figure 5.12). However, as the flow passes the nozzle hump, the flow exhibits a contrary behaviour, in which the increase in the CR reduces Cp in the region between the nozzle hump and the nozzle exit plane. This is attributed to the increase in the flow velocity in this region, (Figure 5.13). This indicates a strong under-expanded flow behaviour at the nozzle exit with the increase in the CR and the NPR.

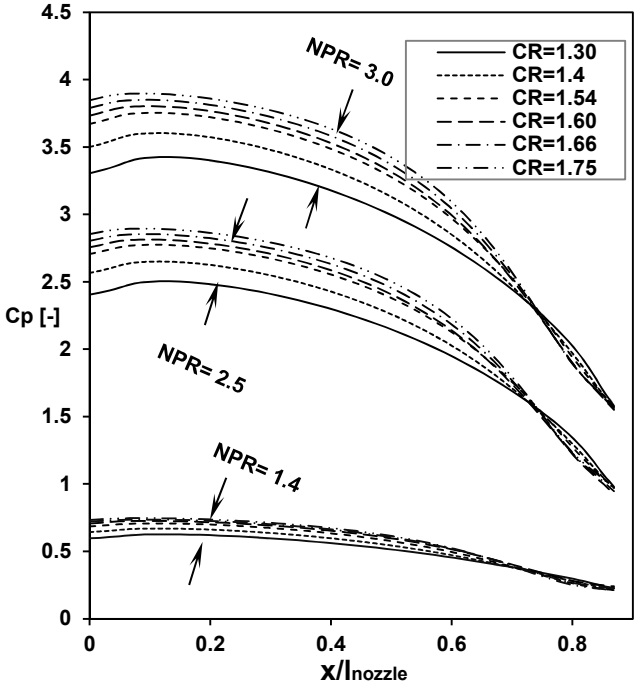

Figure 5.12 Pressure coefficient (Cp) distribution over the inner aero line of the nozzle, as a function of the CR for the chosen NPR for nozzle configuration of β =15˚.

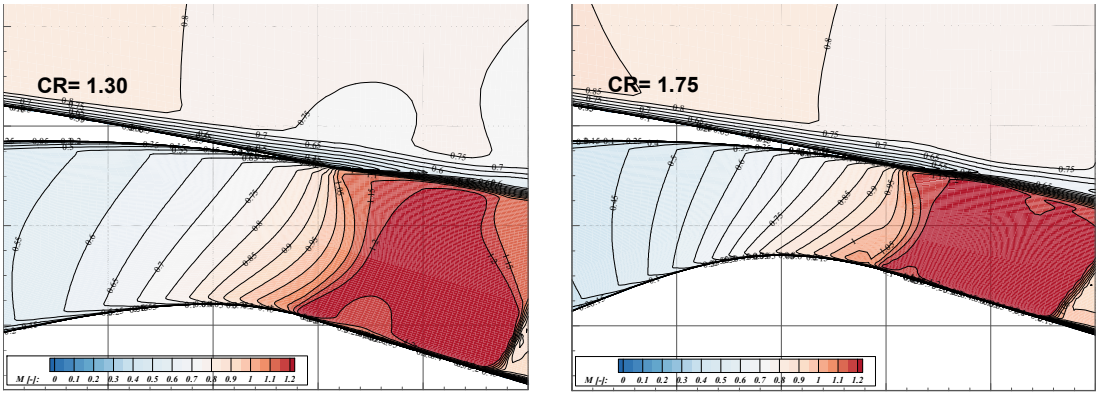

Figure 5.13 Mach number contour at the nozzle exit region of the basic nozzle for a configuration of CR=1.3 and CR-1.75 and β =20˚ at the operational condition of NPR =2.5 and M_∞=0.82.

The increase in CR intensified the pressure force over the plug surface, (Figure 5.14). The pressure force increased with the CR by 0.00257 as CR was changed from 1.66 to 1.75 at NPR = 3.0 and by 0.014 at NPR = 1.4, (Figure 5.14). This is attributed to the increase in the flow momentum flux exhausted from the nozzle with the reduction in the throat area that is associated with the increase in CR relative to the ideal thrust. This behaviour

will change the exhausted jet shape slightly and as a result the shape of the external stream tube.

Having different CR means the nozzle capacity and the power settings are different. Although the impact of the variation of the CR on the nozzle aerodynamics is small, it is still essential. The reason for this is the necessity to develop nozzle performance maps that apply to various engine thrust settings and capacities.

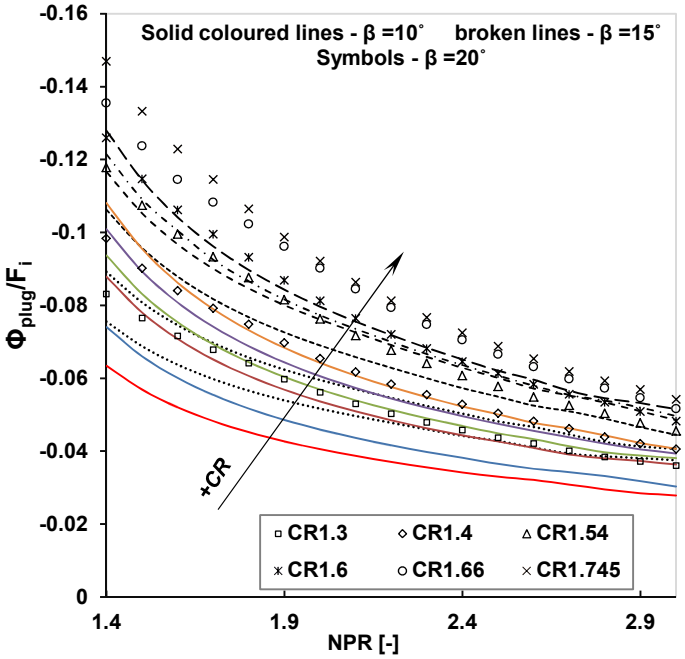

Figure 5.14 Plug pressure force as a function of NPR and CR.

5.6.2 Nozzle performance maps

After explaining the aerodynamic behaviour of the exhaust system components with the variation in the operational and geometrical parameters, it is clear now how the nozzle maps will behave. The nozzle maps were based on the calculation of the C_d (discharge coefficient), C_{fg} (gross thrust coefficient), and Cv (velocity coefficient).

Nozzle discharge coefficient (C_d)

The discharge coefficient (C_d) is affected by the backpressure surrounding the nozzle exit until its NPR passes the choking values (NPR_{ck}). After which no

noticeable change in C_d can be observed, (Figure 5.15). Despite that, the variation in the plug half angle showed an effect on the value of the C_d and the choking NPR (NPR_{ck}). The C_d data showed low levels at small values of β as compared to larger angles, (Figure 5.15). This is attributed to the reduction in the backpressure of the nozzle with the increase in plug half angle (β). The decrease in the backpressure with β is credited to the inclination of the post-exit stream tube towards the nozzle axis. This will reduce the pressure over the cowl after body rim, (Figure 5.16). It can be observed, from the backpressure data, that at low NPR values, the effect of the variation in β is moderate, as the nozzle jet has not formed yet; therefore, the interaction between jet plume and the external flow is small. This behaviour was also observed at high NPR (NPR>2.2) but when β exceeded 15˚, (Figure 5.16). Moreover, having the backpressure small, the choking NPR (NPR_{ck}) becomes lower than the typical values with the change in β, (Figure 5.17). It can be seen it goes smaller than the critical NPR of the nozzle, which is 1.89 when β =20˚. The variation of the backpressure could affect the stability of the engine running conditions. The discharge coefficient was calculated for each CR; the maps are presented in Figure Ap.A 8.

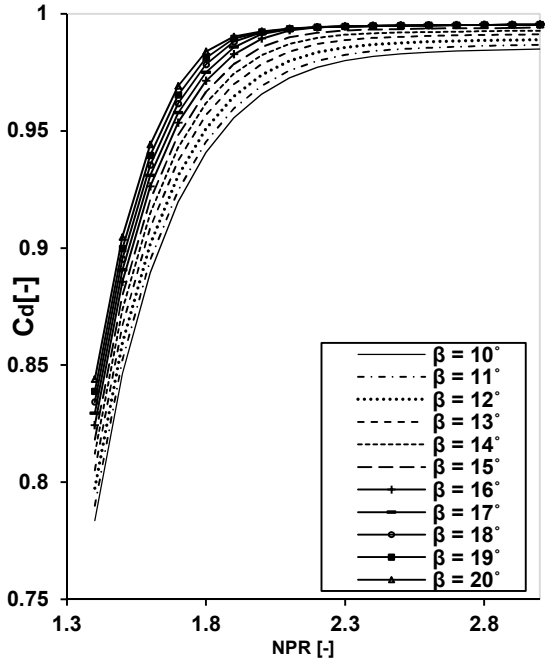

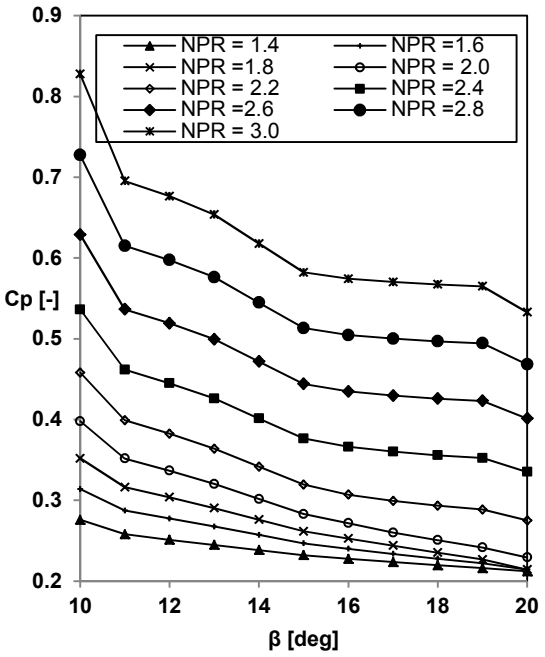

Figure 5.15 Nozzle discharge coefficient maps as a function of the NPR and β for the chosen CR at mid-cruise operational conditions.

Figure 5.16 Local pressure coefficient at the nozzle rim as a function of the β for the chosen NPR, at M_∞= 0.82.

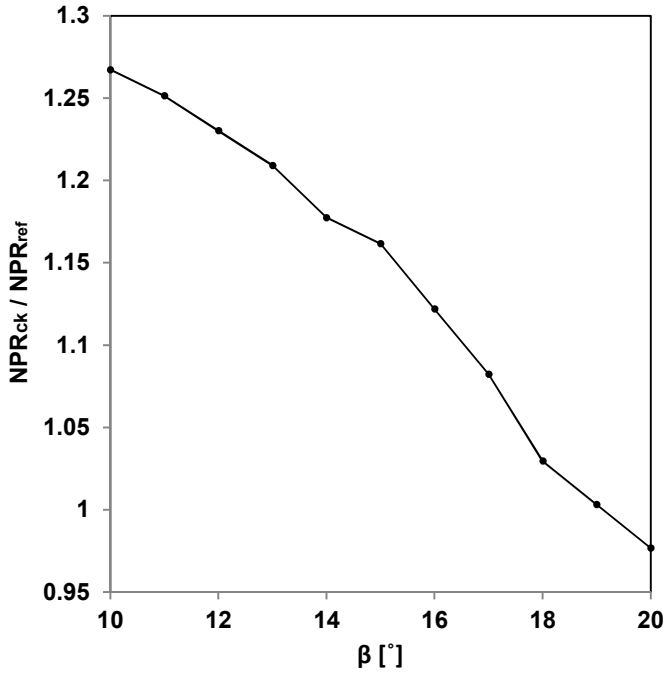

Figure 5.17 Ratio of the choking nozzle pressure ratio (NPR_{ck})to the reference choking nozzle pressure ratio (NPR_{ref}) as a function of β, for configuration of CR = 1.4.

Gross thrust coefficient (C_{fg})

Two modified definitions of the nozzle's gross thrust were used; the reason for that is to quantify the aerodynamic interference impact of the cowl after-body and the plug on the engine performance. The maps of C_{fg} are presented for a CR of 1.60 as a function of the NPR and plug half-angle (β), for the mid-cruise conditions (Alt = 36,000ft and M_∞ = 0.82), (Figure 5.18). The other maps of C_{fg} associated with every value of CR are presented in Appendix A.2.

The C_{fg} curves show a sharp increase with the variation of the NPR, across the range from 1.40 to 1.85, after that the performance data starts to decline. This decline is attributed to the decrease in the contribution of the plug pressure force to the engine thrust relative to the ideal thrust. Moreover, since the plug pressure forces increase with the CR, the C_{fg} shows an increase with the CR,

with a maximum value of the C_{fg} was achieved at NPR of 2.0 for nozzle configuration with CR = 1.30 with a value of 1.020, whereas for the CR = 1.75, C_{fg} = 1.059 at NPR = 1.80. The latter is the maximum value of C_{fg} for all sets of the maps as a function of NPR and β.

The increase in β improves the performance across a range of the NPR from 1.40-1.90. The deviation between the C_{fg} levels of two β values starts to reduce with the NPR across a range of β from 15˚ to 20˚. Where the deviation between β = 17˚ and 18˚ is 0.0002 for CR=1.66 and NPR =3.0, whereas this difference is equal to 0.0014 of the same β and the same CR but at NPR = 2.1.

The use of thrust definition (2) (including the cowl afterbody in the calculation of the gross thrust) reduced the performance significantly. Thrust definition (1) produced a value of C_{fg} higher than one at high values of β and NPR; however, all the values of C_{fg} that were derived from thrust definition (2) are less than 1.0, (Figure 5.18). This indicates that the cowl afterbody is contributing as a drag to the performance. However, as stated before, since the cowl afterbody drag reduces with the NPR, the performance showed an improvement with the NPR. The decrease in the pressure drag of the afterbody with the NPR caused the performance curves to level off with the NPR, (Figure 5.18). This behaviour made the difference in the performance between thrust definition (1) results and thrust definition (2) to reduce when the NPR values exceed 1.90. It was noticed that the difference between the two thrust definitions is -0.020 at β =20˚ and NPR = 3.0, whereas, at NPR 1.7, the difference is -0.082 for the same values of β.

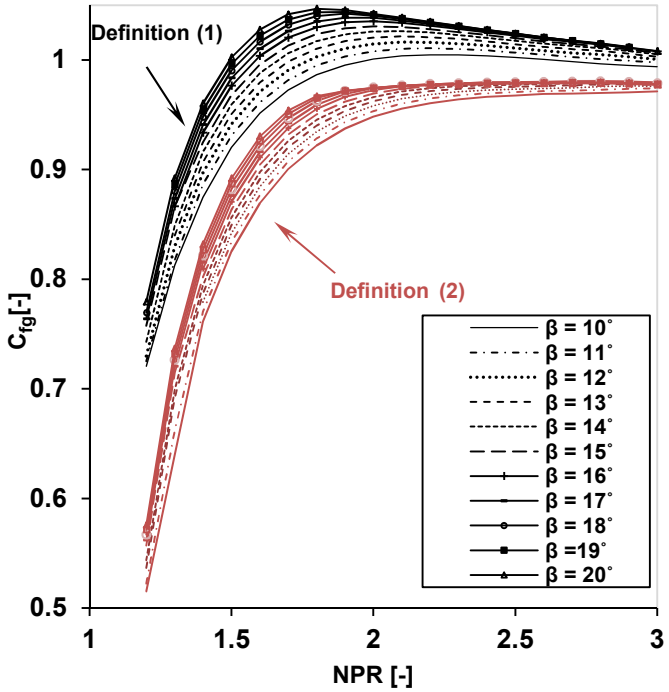

Figure 5.18 Nozzle gross thrust coefficient maps as a function of the NPR and β for the chosen CR at mid-cruise operational conditions.

Velocity coefficient (C_v)

The velocity coefficient of the nozzle was calculated by normalising the gross thrust to the actual mass flow rate exhausted from the nozzle. Similar to C_{fg} the cowl after-body forces were excluded and included in the thrust definition. The velocity coefficient results that excluded the cowl afterbody forces are referred as $C_{v|wo}$ and $C_{v|w}$ stands for the velocity coefficient with the cowl after-body forces considered.

The velocity coefficient (without the after-body forces) ($C_{v|wo}$) results decreased with the increase in the NPR, (Figure 5.19). This is attributed to the reduction in the plug forces relative to the ideal thrust with the NPR. The variation in plug half angle (β) improved $C_{v|wo}$. With high NPR and the further increase in β, the results showed a slight increase in $C_{v|wo}$.

The inclusion of the cowl afterbody forces changed the trend of Cv data, (Figure 5.20). The increase in the NPR values enhanced the computed $C_{v|w}$. In other words, the reduction in the drag forces of the cowl after body with the

NPR recovered the loss in the plug forces contribution to the nozzle thrust. The variation of β, on the other hand, showed a slight increase in $C_{v|w}$ more specifically at low levels of NPR (1.4 to 2.0).

At high values of β (β>15˚) and across the range of NPR from 1.4 to 2.0, the results showed insignificant improvement in the levels of $C_{v|w}$. This behaviour along with the reduction in the contribution of the plug forces to the thrust produced a drastic reduction in the performance at high values of β from 15˚ to 20˚.This is attributed to the increase in the boattail drag with β for particular thrust rating and mass flow.

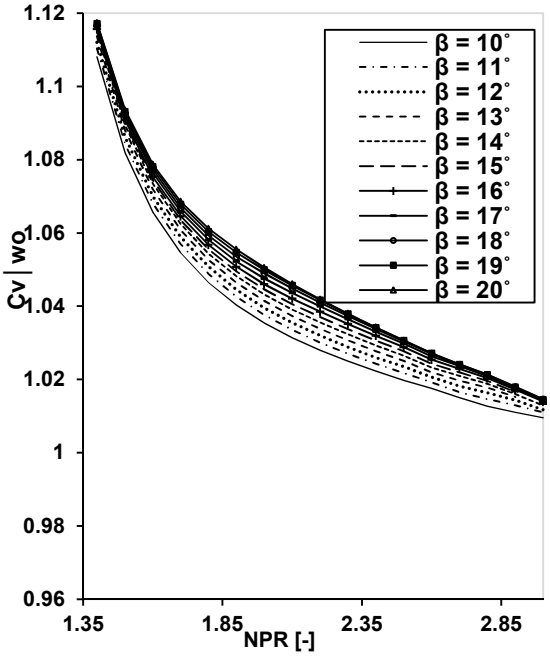

Figure 5.19 Nozzle velocity coefficient ($C_{v|wo}$) maps as a function of the NPR and β for the chosen CR at mid-cruise operational conditions.

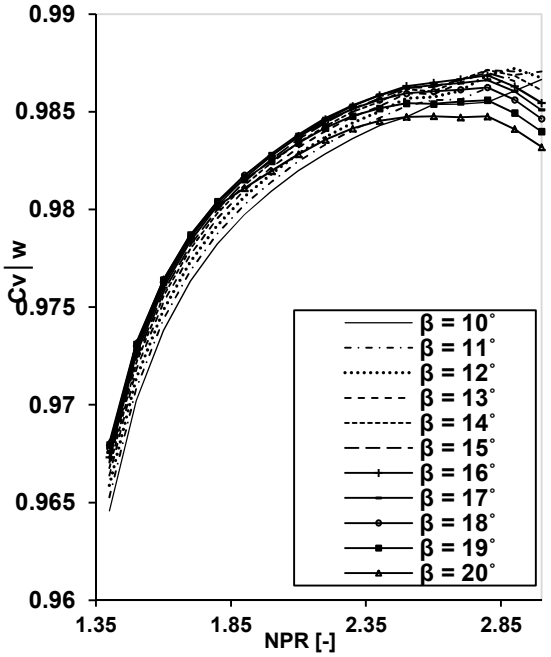

Figure 5.20 Nozzle velocity coefficient (calculated with the inclusion of the cowl after-body) ($C_{v|w}$) maps as a function of the NPR and β for the chosen CR at mid-cruise operational conditions.

In general, the new performance maps provide a modified and improved estimation that captures the effect of various degrees of freedom that affect the nozzle performance. Therefore, instead of the current one-dimensional maps that illustrate the NPR impact only, the multidimensional effect of the aerodynamic interaction was quantified in the new maps. The aim of including the cowl after body in the calculations of the nozzle performance is to capture

the effect of the external flow over the nacelle and in the same manner the pressure signature of the wing for the installed engine cases. Therefore, for the case when the engine is tested under static conditions, the inclusion of the cowl afterbody is unnecessary.

5.6.3 Core nozzle performance corrections

The effects of some geometrical and operational parameters on the nozzle performance were presented in the previous section. A set of performance maps were generated based on these parameters for the basic nozzle. These maps simulate a nozzle that is exposed to the free-stream flow. Therefore, the performance data of the core nozzle will differ from the basic nozzle one. The reason behind that is the core nozzle sees the stream tube of the bypass nozzle rather than the external flow. Therefore, it was suggested to produce corrections to the core nozzle thrust data. These corrections relate the thrust coefficient of the core nozzle at a specific pressure ratio of the fan nozzle (FNPR) and the core-nozzle performance data with FNPR 1.0. As a result, the corrections will assess the impact of the flow interaction between the bypass and the core nozzle. Therefore, additional series of simulations were performed to extract these corrections.

These corrections were created by simulating a dual-stream nozzle configuration across a range of the FNPR from 2.0 to 2.8 and core nozzle pressure ratio (CNPR) from 1.2 to 3.0. The contraction ratio of the core nozzle (cCR) was changed in the same manner that was conducted on the basic nozzle parameterisation, Section (5.4). Then the extracted values of the core nozzle $\mathrm{Cfg}_{\mathrm{core}\,|\,\mathrm{FNPR}}$ were normalised to $\mathrm{Cfg}_{\mathrm{core}\,|\,\mathrm{FNPR=1.0}}$. The applied FNPR was set to be 1.01, because of the simulations' stability requirements and to avoid the issues of reverse flow and convergence delay.

These derived corrections ($\frac{\mathrm{Cfg}_{\mathrm{core}\,|\,\mathrm{FNPR}}}{\mathrm{Cfg}_{\mathrm{core}\,|\,\mathrm{FNPR=1.0}}}$) will capture the impact of the bypass stream tube on the core nozzle flow and components (plug), (Figure 5.21 and Figure 5.22). It can be seen that $\frac{\mathrm{Cfg}_{\mathrm{core}\,|\,\mathrm{FNPR}}}{\mathrm{Cfg}_{\mathrm{core}\,|\,\mathrm{FNPR=1.0}}}$ increased with β and with FNPR.

This is attributed to the increase in the pressure forces that act on the plug surface due to the presence of the fan nozzle flow. The behaviour with the variation of CNPR is different: the correction factors increase up to CNPR of 2.0 and decrease with a further increase of CNPR.

Having these corrections derived the thrust coefficient sets of the basic nozzle can be used as a core nozzle performance data but after correcting them. A set of the core nozzle and the overall dual stream nozzle thrust coefficient are presented in Figure Ap.A 13 and Figure Ap.A 14.

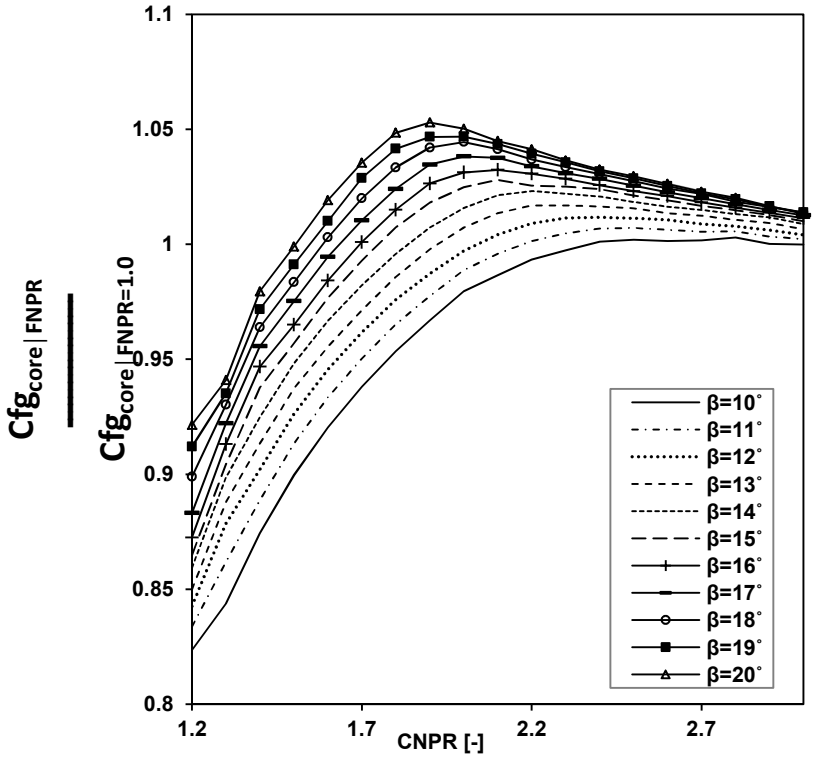

Figure 5.21 Extracted corrections of the core nozzle gross thrust coefficient, at FNPR, = 2.0 and cCR of 1.5, of a nozzle running at M_∞ = 0.82.

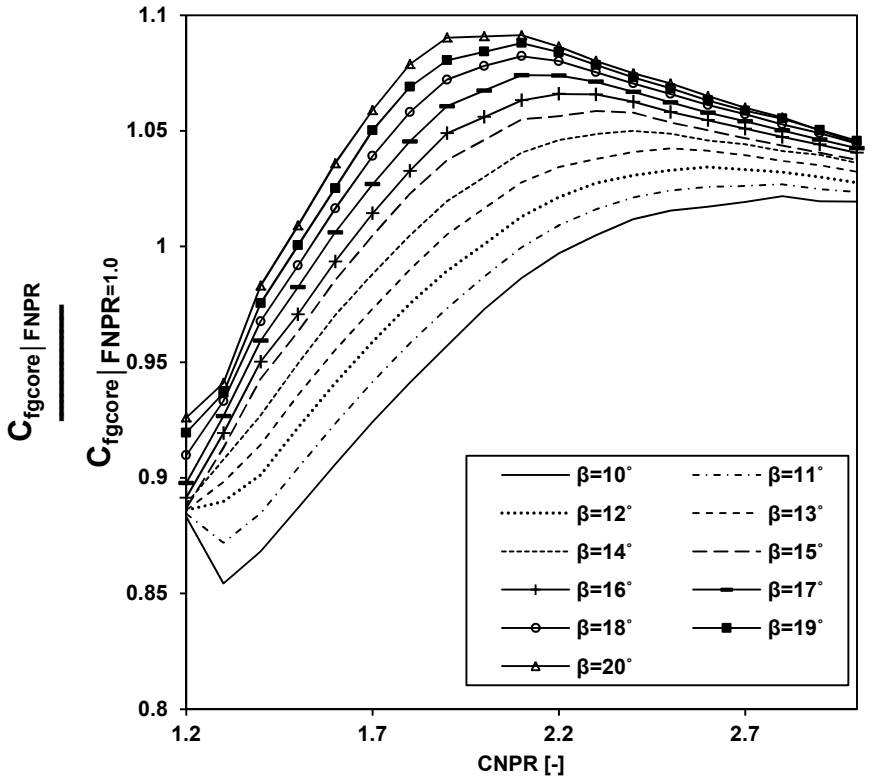

Figure 5.22 Extracted corrections of the core nozzle gross thrust coefficient, at FNPR = 2.8 and cCR = 1.5, of a nozzle running at M_∞ = 0.82.

To check the suitability of using the basic nozzle performance data as a representation of the core nozzle one, the flow behaviour around both configurations was tested. One of the main parameters that affect the nozzle performance is the surrounding pressure. To verify that the core nozzle sees the same pressure levels that the basic nozzle exposed to, at different free stream velocity, a comparison between the pressure values close the nozzle rim for both configurations was made. For the basic nozzle, the free stream Mach number was changed across a range of 0.07, 0.2, 0.5 and 0.82. For the dual stream nozzle, to achieve the same Mach number at the core nozzle rim the FNPR value was changed, and the Mach number was measured around at the nozzle rim. It was found the FNPR of 1.05, 1.09, 1.27 and 1.7 produce a local Mach number of 0.07, 0.2, 0.5 and 0.82, respectively, (Figure 5.23).

The results of the local static pressure for both configurations showed that the core nozzle is exposed to a pressure higher than the one surrounding the basic

nozzle configurations. The percentage difference between them is in a range from 4.3% to 5.0%, (Figure 5.24). Although this difference is high, it was believed that there would be no huge difference of their effect on the nozzle jet. As a result, from this comparison, the impact of the presence of the geometrical features of the bypass nozzle has an insignificant impact on the pressure behaviour that is surrounding the core-nozzle.

For more verification, the pressure distribution over the nozzle jet was calculated to check the difference in the pressure that the around the nozzle plume, (Figure 5.25). The comparison was made between the basic nozzle configuration running at NPR =2.50 and M_{∞} =0.82, and the dual stream nozzle configuration run under FNPR =1.0 and 1.7, and CNPR =2.50.

It was found that when the dual stream nozzle run at FNPR =1.70 (simulating the M_{local} ≈0.82), the pressure levels are higher than when the FNPR =1.0. At which the pressure levels are closes to the basic nozzle data. Therefore, it was decided to use the FNPR =1.0 as reference conditions that represent a nozzle exposed to free stream flow.

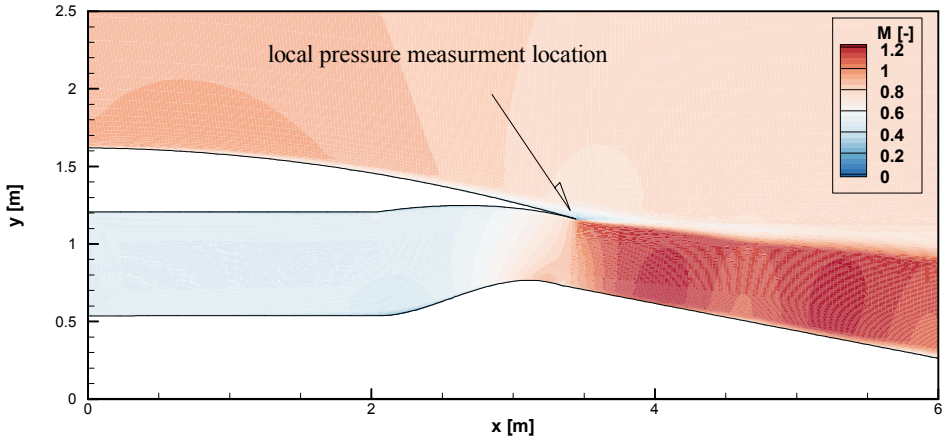

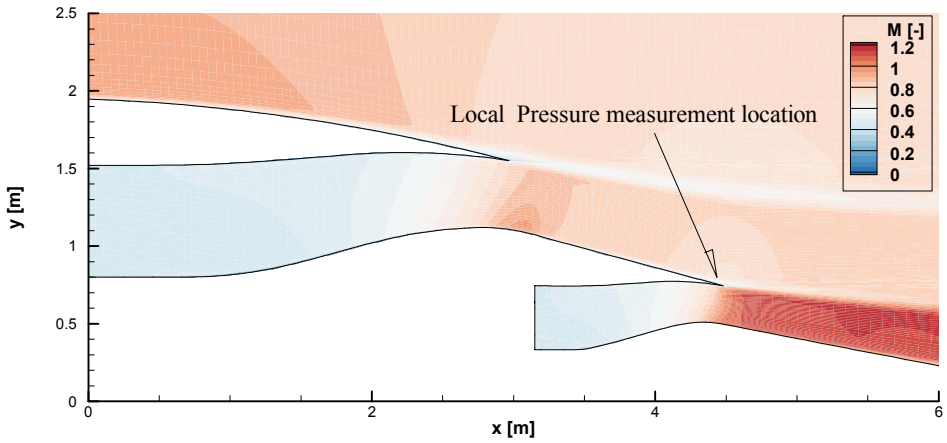

Figure 5.23 Mach number contour around the basic and the dual stream nozzle configuration, running at M_∞ of 0.82; the FNPR of the dual stream nozzle is 1.70.

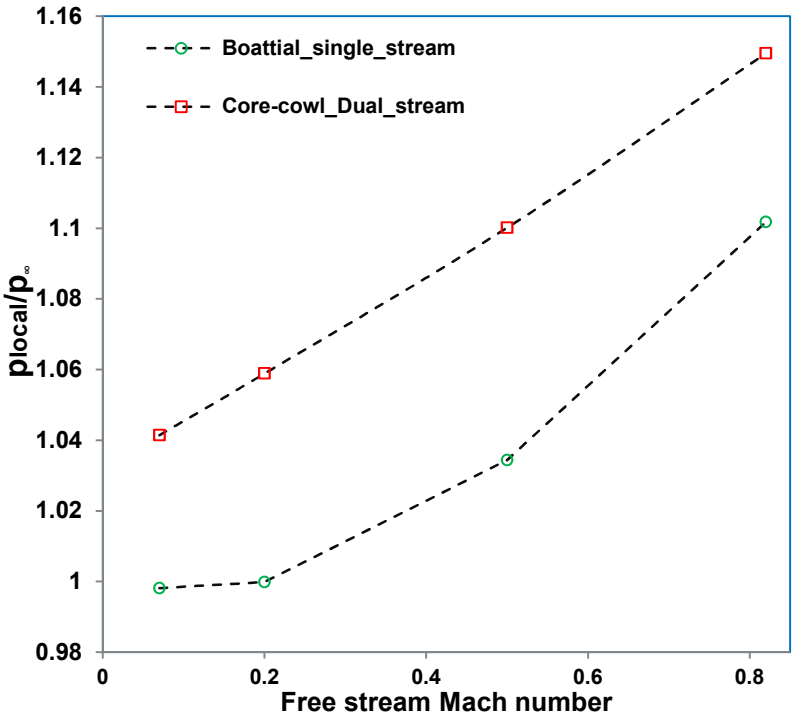

Figure 5.24 Comparison of the ratio of the local static pressure to the free stream pressure between the flow that surrounds the basic nozzle configuration and the dual stream nozzle, as a function of the free stream Mach number.

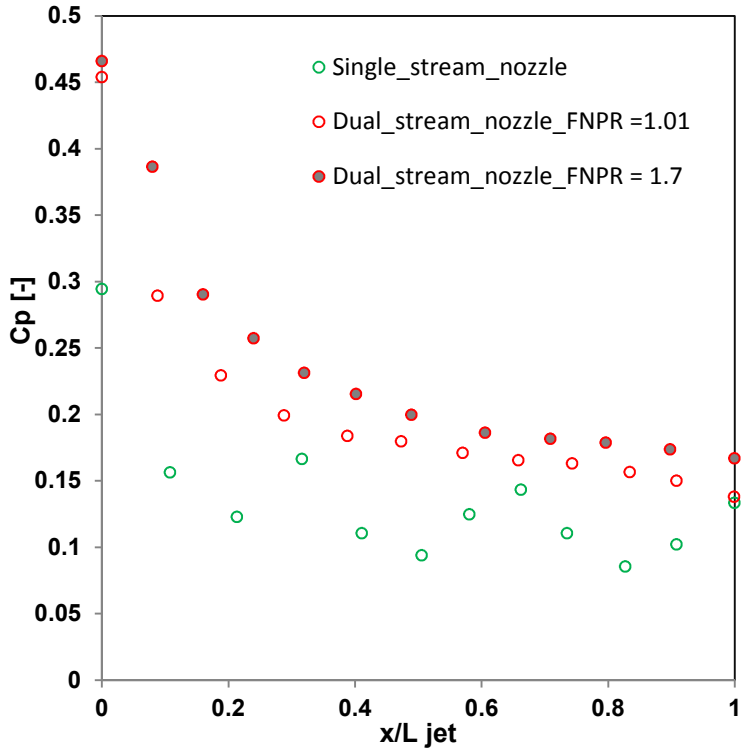

Figure 5.25 Comparison between the pressure coefficient (Cp) distribution over the nozzle jet of the basic and dual-stream nozzle configuration, for running NPR=2.5 and FNPR for the dual stream nozzle of 1.0 and 1.70; the L_{jet} refers to the length of the jet plume that is extended from the nozzle exit plane to the cone(plug) edge.

Effect of the bypass flow on the discharge coefficient of the core nozzle

It should be noted that the core nozzle discharge coefficient is extremely affected by the bypass nozzle flow, (Figure 5.26). When the FNPR =1.0, the bypass nozzle has no impact on the core nozzle, (Figure 5.26), in which insignificant variation in C_d was observed. However, at high FNPR, the bypass stream tube hugely affects the core nozzle C_d. As C_d decrease with the increase in FNPR, (Figure 5.28 and Figure 5.27). This is attributed to the increase in the static pressure levels that is surrounding the core nozzle with the presence of the fan nozzle jet. Furthermore, the variation of the plug half angle (β) is also affecting the performance of the core nozzle, (Figure 5.28). However, β variation effect is very small when there is no fan flow and increases with the increase in the FNPR,(Figure 5.26, Figure 5.28 and Figure 5.27).

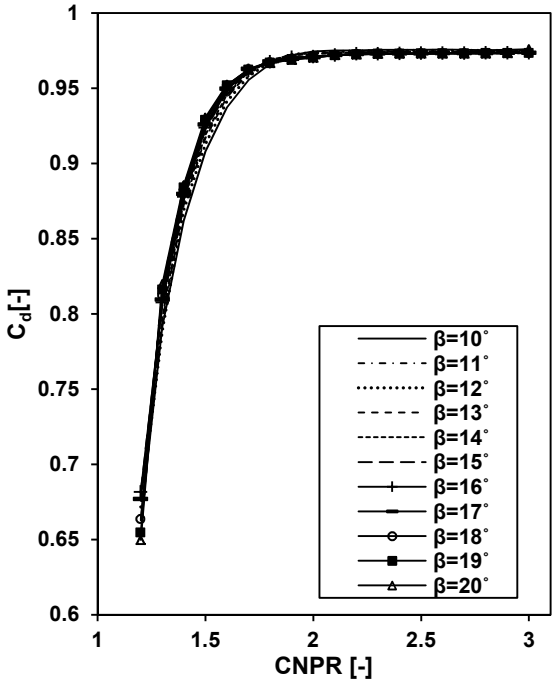

Figure 5.26 Discharge coefficient of the core nozzle, as a function of CNPR for the chosen β; for nozzle configuration of CR =1.50 at FNPR = 1.0.

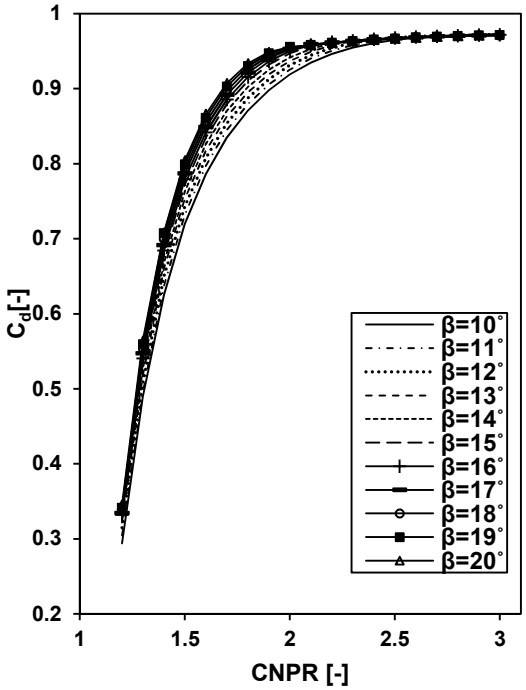

Figure 5.27 Discharge coefficient of the core nozzle, as a function of CNPR for the chosen β; for nozzle configuration of CR =1.50 at FNPR = 2.20.

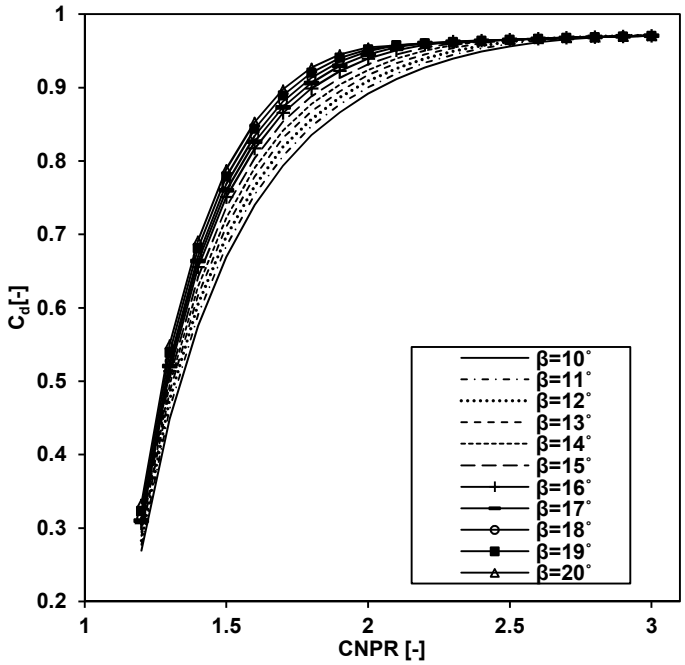

Figure 5.28 Discharge coefficient of the core nozzle, as a function of CNPR for the chosen β; for nozzle configuration of CR =1.50 at FNPR = 2.50.

5.7 Summary

The tasks and activities of this chapter can be summarised as follows:

a) Parameterisation of the basic nozzle geometric and aerodynamic characteristics has been performed to build nozzle performance maps.
b) Corrections for the core nozzle performance were derived, to capture the impact of the flow interaction with the bypass nozzle flow on it.
c) The examination of the effect of the nozzle parameterisation on the aerodynamic characteristics shows that:
    a) The pressure force over the plug surface increases with the nozzle pressure ratio (NPR), however, its contribution to the nozzle thrust is in reduction due to the expansion losses.
    b) The drag force of the cowl after-body reduces with the NPR due to the reduction in the inclination angle of the nozzle jet towards the engine axis. This reduction will recover part of the expansion losses in the nozzle performance with the increase in the NPR.
    c) The impact of the jet on the cowl afterbody is concentrated on the rear part only. No effect was observed over the region from the mid-point of the afterbody to the location of the maximum diameter of the nacelle.
    d) Increasing the contraction ratio (CR) intensifies the pressure forces over the lower nozzle aero-line. This behaviour is contrasted in the region behind the nozzle hump to the nozzle exit plane.
d) Performance maps of the nozzle that is established as a function of the CR, NPR and the cone (plug) half-angle and showed a high sensitivity to the variation of these parameters.
e) The increase in CR and the plug-half angle improved the performance of the nozzle.
f) The choking nozzle pressure ratio is highly affected by the change in the plug-half angle, in which it decreases with the increase in β.
g) The nozzle discharge coefficient is highly affected by the variation of the plug angle.

6 Installed aero-engine exhaust-system performance assessment

6.1 Overview

This chapter presents an assessment of the impact of the aerodynamic interference between the nacelle and the wing on the engine performance; with the focus on the exhaust system. A Computational Fluid Dynamics (CFD) module was built to approach this task. The CFD module consists of nacelle and wing configurations design, domain and mesh selection and extracting the performance data. The engine was combined with a swept-wing (SW) and the Common Research Model (CRM) configuration. A correction maps that are used to model the installed exhaust system performance are given at the end of the Chapter.

6.2 Rationale

The wing has a noticeable pressure signature on the engine's external and internal flows, in particular, exhaust nozzle flow. Therefore, attempting to evaluate exhaust system performance for an engine in the isolated situation is not practical. Moreover, the wing effect on the exhaust system varies with the position of the nacelle with respect to the wing leading edge. Therefore, the evaluation of the nozzle performance in installed engine case is important. An installed engine aerodynamic performance assessment module is built, and the corrections to the installation interaction impact are extracted.

6.3 Nacelle design

A separated nozzle engine configuration (3/4 nacelle) has been chosen. This type of nacelle consists of intake, fan cowl, core-cowl and plug. Internally it includes intake diffuser, by-pass and core ducts, and nozzles. Full and accurate detailed dimensions are not available; therefore, some assumptions had to be made to design the nacelle. The nacelle geometry was simplified, and the design concentrated on the exhaust system components, (internal duct, core-cowl and plug). The inlet spinner was removed for simplification, as the current work does not consider the intake performance assessment. Some dimensions

that were used to design the current nacelle have been taken from open domain manuals and Jane's [94].

The aero-engine nacelle was designed based on the open-domain performance data for the GE90-B85 engine [93,94]. Such as the fan diameter and total propulsion system length. The primary and secondary nozzle areas have been calculated using engine performance model results in the design point calculations. The performance model calculations have been performed using a non-dimensional in-house tool (Turbo-Match)[9]. Appendix A presents more details of the design procedure and the full nacelle geometrical data.

6.4 Infinite Swept-Wing (SW)

The swept-wing (SW) geometry was produced by extracting an aerofoil section from the CRM three-dimensional wing. The wing chord is 275.8 in (≈ 7.0 m), (Figure 6.1). The wing was considered had a swept angle of 35° with length equals to the semi-span length of the CRM aeroplane configuration. The SW was used to simulate the upwash and downwash pressure fields that the engine experiences.

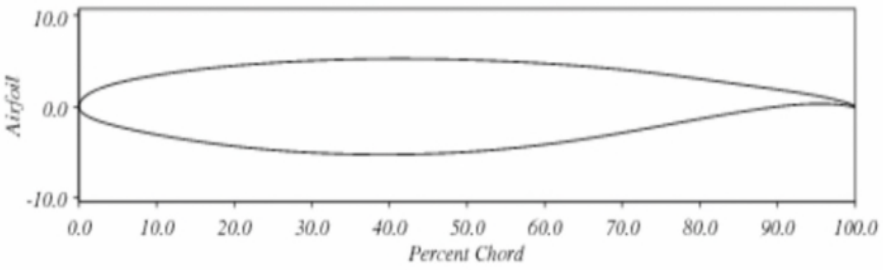

Figure 6.1 Airfoil geometrical characteristics of the CRM Wing [117].

6.5 Common Research Model wing-body (WB) configuration

The CRM geometry was taken from the open access NASA website [118], and the wing-body configuration was used to simulate the engine and the airframe configuration. The full description of the configuration and the sketch of the geometry were presented in Chapter 2 and Chapter4. The aim of using this type of configuration is to enable a comparison to be made between the pressure signatures for conventional aircraft and the SW, moreover, to produce the

required correlation between the local static pressure and the performance correction of the engine's exhaust system, for a wider range of the local pressure levels.

6.6 Parameterisation

Different engine and aircraft configurations mean different installation locations. The engine location on the aircraft is governed by the size of the engine and the height of the aircraft. It is expected that the civil aero-engine could be placed very close to the wing, as the size of the engine has increased as a result of the recent increases in bypass ratio and the fan diameter. Therefore, to calculate the impact of the installation aspects of the nozzle and engine performance, different engine locations were studied. The engine position was changed relative to the wing leading edge. Moreover, the aircraft angle of attack ($AoA_{A/C}$)was varied, in combination with the engine position variation. The variation in $AoA_{A/C}$ is important as the aircraft changes its incident during the flight journey.

6.6.1 Engine position variation

Engine installation positions are governed by the distance from the wing leading edge to the cowl trailing edge ∆x horizontally, and Δz vertically, (Figure 6.2). It has been reported [1,4,119] that the change in the vertical location does not have any noticeable effect on the aerodynamics of the nacelle. However, its impact on the exhaust-system performance was not reported. Therefore the vertical distance (Δz) was changed in two incremental steps.

The wing, simulations were carried out at seven engine positions as shown in Table 6-1.The positions from P01 to P03 have a fixed vertical distance from the wing leading edge of $\frac{\Delta z}{C}$ =-0.1, and positions from P04 to P07 are vertically closer to the wing with $\frac{\Delta z}{C}$ =-0.05.

To ensure that the selected locations were within the practical range of present and likely future engine locations, a comparison was made between current

engine location and available locations as discussed in open domain literature, (Figure 6.3).

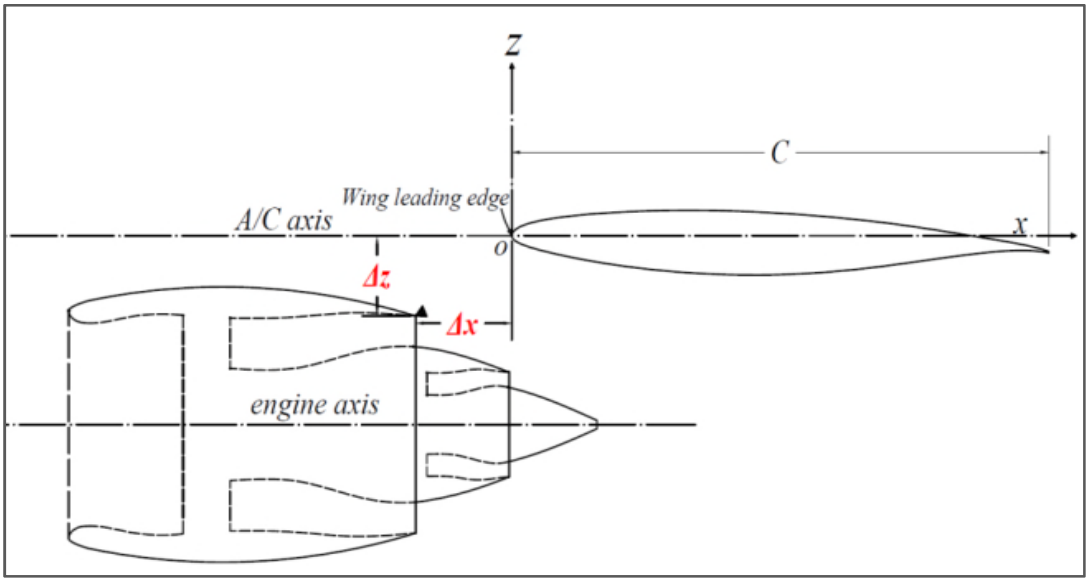

Figure 6.2 Schematic of the lead parameters of the engine location.

Table 6-1 Matrix of the engine locations.

	$\frac{\Delta x}{C}$	$\frac{\Delta z}{C}$
P01	-0.05	-0.10
P02	-0.15	-0.10
P03	-0.25	-0.10
P04	-0.05	-0.05
P05	-0.15	-0.05
P06	-0.25	-0.05
P07	-0.35	-0.05

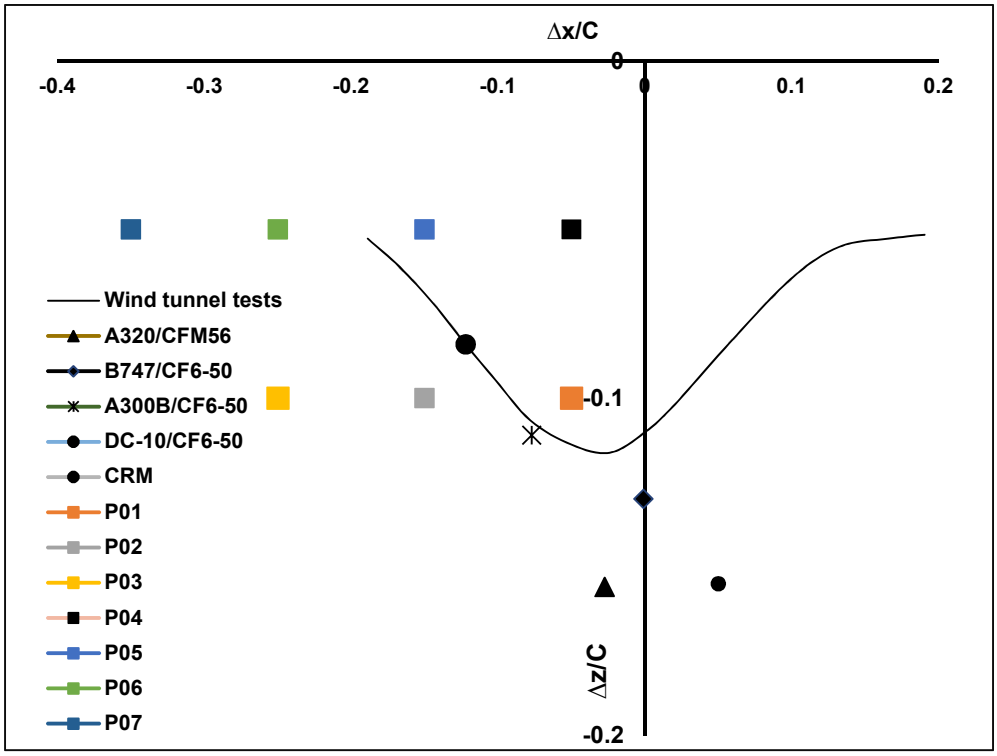

Figure 6.3 Comparison between the current engine and the commercial engine location;(the commercial engine positions were taken from [119]).

6.6.2 Angle of attack variation

The angle of attack was changed across a range of 0.0˚ to 3.5˚ in steps of 0.5˚.Moreover, to produce a fair comparison between the isolated and the installed engine data, the isolated engine was simulated at a different angle of attack as well. The isolated engine angle of attack was corrected by the value of the upwash angle due to the wing pressure field. The wing pressure has an impact on the streamline curvature of the upcoming air. The wing pressure deflects the flow streamlines in a manner that changes the upcoming flow angle. Thus, the effect of upwash flow has to be considered in the representation of the engine angle of incidence, for a correct resolution of the force components on the engine.

6.6.2.1 Angles definitions

Three different angles exist in the analysis of the forces of the installed engine configuration, (Figure 6.4). Aircraft angle of attack ($AoA_{A/C}$) is the angle between the aircraft axis and the upcoming flow. Installation angle it is the angle between the engine axis and the aircraft axis. This angle is specific to a given engine and

aircraft. Since the current engine is axisymmetric, the installation angle was not considered and was assumed to be zero. The up-wash flow angle (AoA_{upwash}), represents the deviation in the upcoming flow vector angle. The wing pressure field effect may increase or decrease the AoA_{upwash}. For the isolated engine, total upcoming flow angle (AoA_{local}) is the sum of all three angles, which is the actual flow angle to which the installed engine is exposed. AoA_{local} was used during the aerodynamic performance analysis of the isolated engine.

$$AoA_{local} = AoA_{upwash} + AoA_{A/C}$$

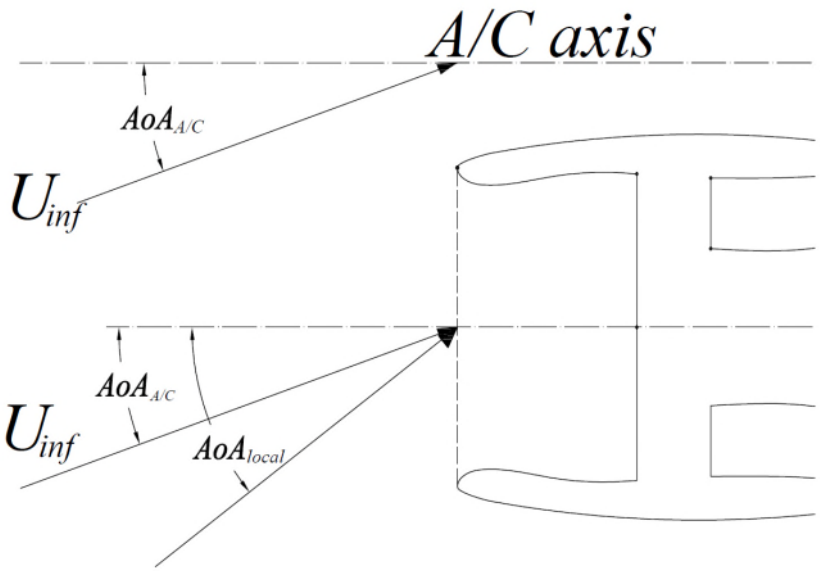

Figure 6.4 Illustration of the angle of attack of the aircraft ($AoA_{A/C}$), up-wash angle (AoA_{upwash}) and total upcoming flow angle (AoA_{local}).

Several CFD calculations have been performed to evaluate the up-wash angle of the current SW and the CRM. The calculations were based on varying $AoA_{A/C}$. After that, the radial and the horizontal velocity components were estimated, and the local relative speed angle was calculated. Different locations were chosen in front of the nacelle intake to measure the up-wash angle. The averaged value of the measured data was used as AoA_{local} during the simulations of the isolated nacelle, (Figure 6.5). These angles will produce a clear measure of the wing effect on the nacelle. It is clear that the SW produces a very large pressure field, which defects the flow stream tube noticeably.

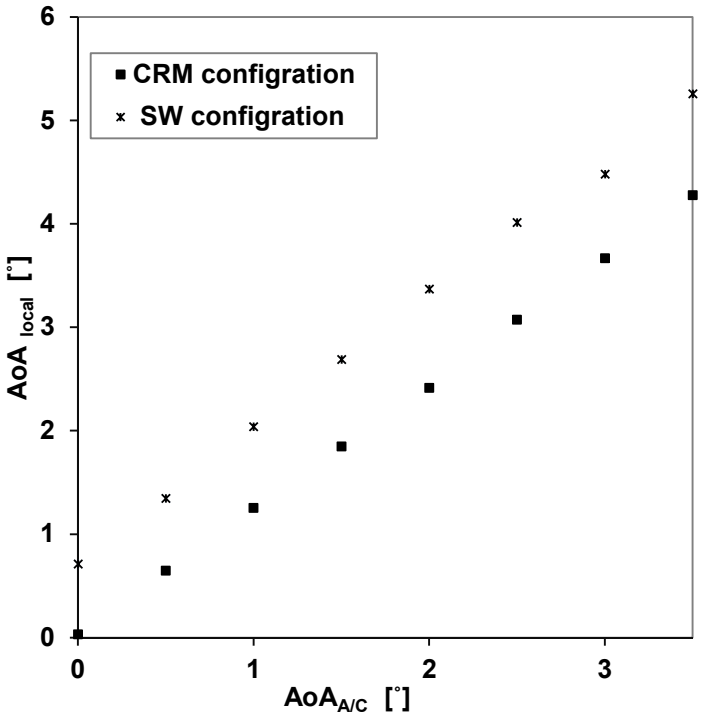

Figure 6.5 Engine local angle of attack for the swept wing and the CRM configurations as a function of the aircraft angle of attack.

6.7 CFD solution

6.7.1 Domain sensitivity analysis and boundary conditions

For the isolated nacelle and CRM installed engine configurations, a hemispherically shaped domain was chosen,(Figure 6.6). Whereas for the SW combined with the engine the domain features are presented in Figure 6.7. This domain is recognised by disk sides located at a distance equals to the CRM wing semi-span from the nacelle axis. The sides of the domain were set as periodic boundaries, to reduce the size of the domain and to ensure a two-dimensional flow nature around the wing.

The radius of the hemispherical domain was changed across a range of 30, 60 and 90 of the maximum nacelle diameter (D_{max}). The effect of the hemispherical domain size on the drag coefficient ΔC_{Dnac} of the nacelle was 0.234 dc (drag count) when the radius was changed from 60 to 90 of the D_{max}.The thrust and discharge coefficients, of the bypass and the core nozzle, increased by

0.0000253, 0.0000239 and 0.00004, respectively, because of the change in the domain radius.

For the SW-engine configuration, the domain radius was increased from $50D_{max}$ to 90 D_{max}.It was found that the drag coefficient decreased by 0.9 dc and the discharge coefficient variation of the bypass nozzle was +0.00004, and the core discharge coefficient increased by 0.00005. The thrust coefficient, on the other hand, increased by 0.00003. In conclusion, the domain diameter of $60D_{max}$ was chosen for the SW and the isolated nacelle configuration. The numerical domain size of the CRM configuration simulations was taken from [77] with a radius of $100C_{ref}$ (CRM wing reference chord).

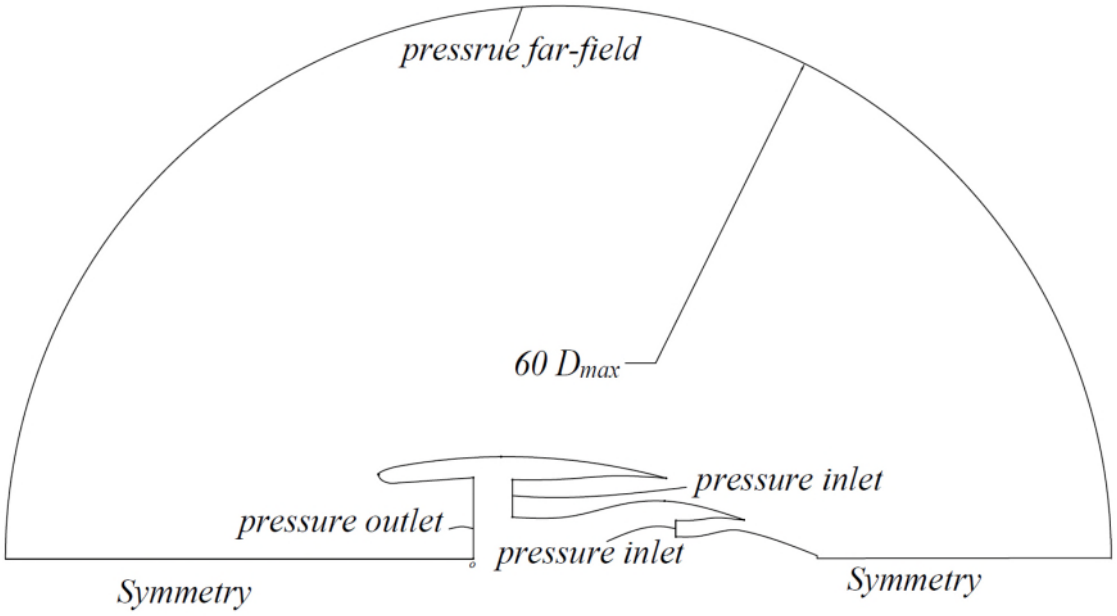

Figure 6.6 Hemispherical computational domain with the employed boundary conditions (Not to scale).

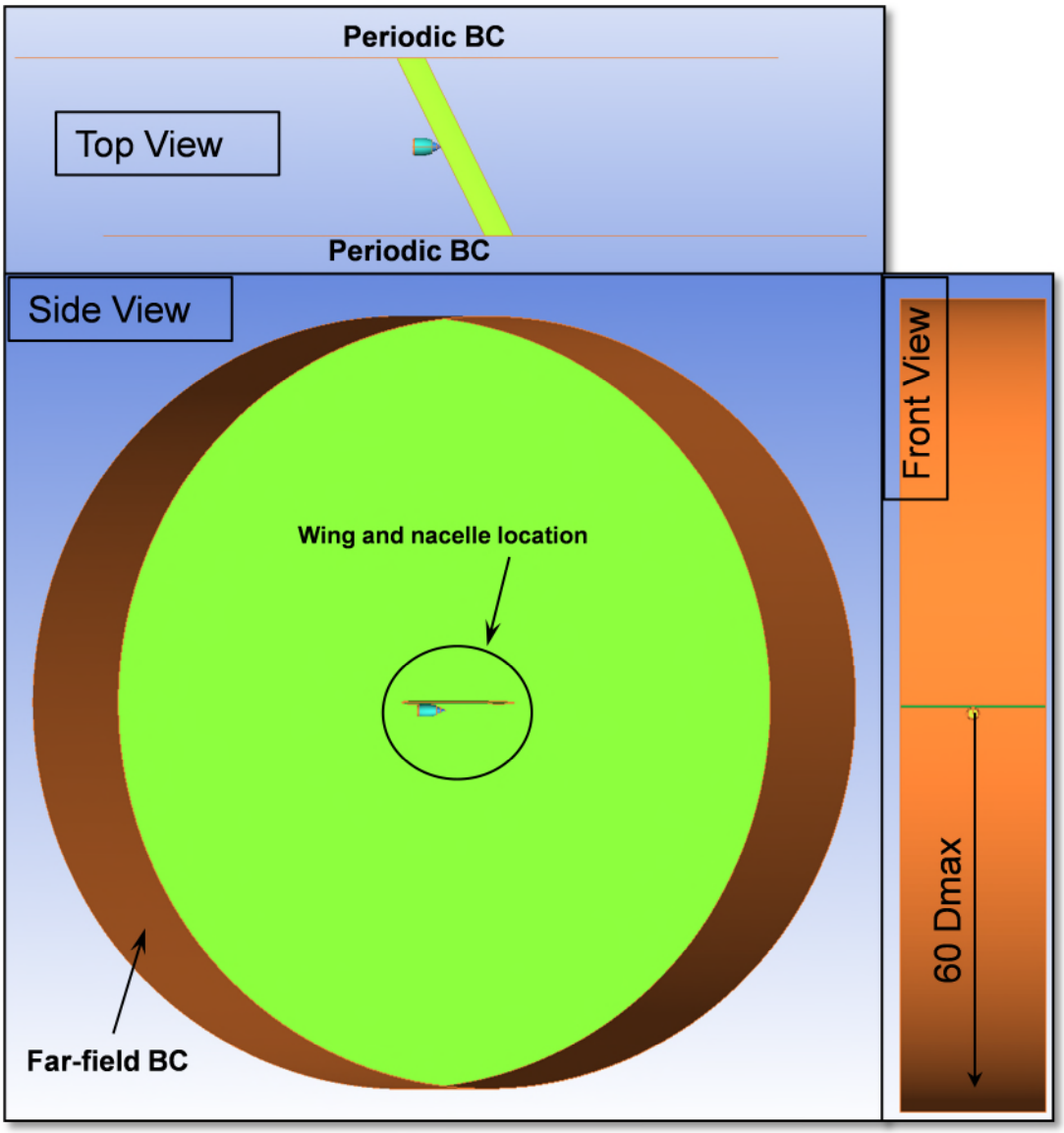

Figure 6.7 SW-nacelle configuration computational domain with the employed boundary conditions (Not to scale).

6.7.2 Gridding methods

Hybrid mesh topology was used to discretise the entire three-dimensional CFD cases. A twenty six prism layers with a growth ratio of 1.28 were generated to discretise the boundary layer regions. The value of dimensionless wall distance (Y^+) was kept close to unity for all meshes over the nacelle surfaces. However, in the installed engine results the Y^+ showed higher values ($1.0<Y^+<3.0$) over the wing surface, Figure Ap. B 1 and Figure Ap. B 2, which was consider acceptable as the number of the layer inside the boundary-layer region is sufficient to simulate it. According to the ANSYS guide [102] , the code depends

on the number of nodes inside the viscous layer with a minimum number of 20 nodes to simulate the sublayer in addition to the value of the Y^+.

The three-dimensional isolated nacelle computational domain was discretised using three mesh sizes. The number of mesh elements was increased from $3.7x10^6$ to $12.2x10^6$, the effective refinement ratio between fine and the medium mesh was 1.16, and between the coarse mesh and the medium mesh was 1.26. The mesh results show a monotonic convergence in terms of the nacelle drag difference equal to 23dc between the medium and fine meshes. The value of the fine mesh GCI_{12} is 0.0027 and for the coarse mesh (GCI_{23}) is 0.0078. The (gross thrust coefficient) C_{fg} shows little variation with the increase in the number of the elements, 0.000054 between the medium and the fine mesh.

To check whether the mesh is in the asymptotic convergence, the value of the GCI aspect ratio has to be close to one [100]. Isolated nacelle domain mesh results showed that the GCI aspect ratio is equal to 0.995. The fine mesh was used to perform the isolated engine simulations.

Three meshes were generated for the stand-alone SW. The mesh counts were $4.10x10^6$, $7.9x10^6$ and $12.2x10^6$, for coarse, medium and fine mesh, respectively. The effective refinement ratio is 1.2. The physical properties of interest are the lift coefficients (C_L). The lift coefficient showed a difference of $\Delta\, Cl = -0.0122\,\%$ between the coarse and medium mesh, and of $\Delta\, Cl = -0.0040$ between the medium and fine mesh. The mesh shows monotonic convergence. The GCI_{12} is 0.0073 and, the GCI_{23} gives a value of 0.023, this led to GCI aspect ratio of 0.99.

For the SW-nacelle combination, the mesh sensitivity analysis between four different meshes was performed. The mesh sizes were referred as coarse ($\approx 6.5x10^6$), medium ($\approx 10.55x10^6$), fine ($\approx 19x10^6$) and extra fine ($\approx 31.5x10^6$). The last three meshes were used to check the asymptotically of the meshes. The GCI aspect ratio of the mesh is 0.975 for the nacelle drag coefficient (C_{Dnac}). The fine mesh was used for the CFD parametric analyses. The thrust coefficient showed a variation of -0.0005 between the fine and the extra fine meshes with a GCI aspect ratio of 0.999.

The CRM and nacelle configuration meshes showed that the C_{Dnac} increase by 20dc when the number of the mesh elements increased from 19 million to 31 million. The aspect ratio was found to be 0.97. The nozzle thrust coefficient differs by 0.0005 as calculated using medium and fine mesh and a difference of 0.000033 between the fine and extra fine mesh. The calculated GCI aspect ratio had a value close to one.

Although the current mesh topologies showed some discrepancies in the prediction of the of the drag coefficient, the nozzle performance metrics were calculated within the acceptable range. Figure 6.8 and Figure 6.9 show the meshes used for the current analysis. For more details, Appendix B presents the results of the mesh study.

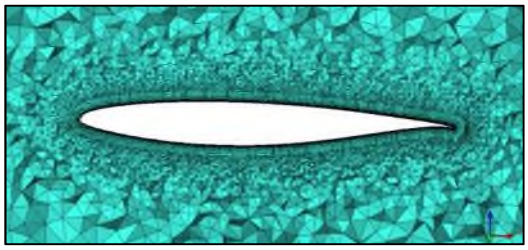

Figure 6.8 Close look for a sample mesh used for the computational analysis.

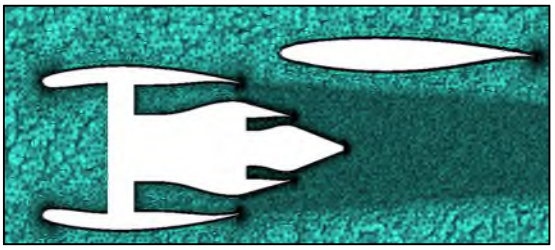

Figure 6.9 Close look for a sample mesh used the computational analysis.

6.7.3 Numerical scheme and boundary conditions

The numerical scheme and the solver setting are the same as the one used in the simulations of the isolated nozzle calculations. However, the current cases are three-dimensional, and boundary conditions and convergence strategy are different.

The calculations were initialised using uniform free-stream flow conditions, with Courant number (CFL) of unity, and the first order upwind numerical scheme. The value of the CFL was increased by two after every 1000 iterations, up to CFL=15. After achieving the targeted converged residuals in the first order upwind numerical scheme, the solver was switched to the second-order upwind numerical scheme. The computations were continued up to approximately 18,000 iterations, at which point the residuals of the continuity equation reached the value of 10^{-5}, the momentum residuals achieved the value of 10^{-6}, and the

turbulence equation residuals were of the order of 10^{-4}. The variation of the physical of interest (C_{Dnac}) with the iteration was equal to 0.00001, and the mass flow rate variation was null.

The boundary condition of the fan-face was set as a pressure-outlet, specified by an approximated static pressure and total temperature. The static pressure was provided to initiate the flow through the intake, after that, the CFD code switched to a targeted-mass flow rate boundary condition to achieve the requested mass flow capture ratio (MFCR) at specific operational conditions. The total pressure value was used to specify the nozzles inlet boundary conditions. All the engine boundary conditions were derived from the engine performance model (Turbo-Match). The external CFD domain boundary was set to the static pressure and temperature, and free stream Mach number (M_∞). The symmetry boundary conditions were applied to the isolated nacelle and the CRM configuration only to half the size of the CFD domain. The entire remaining solid surfaces are set to no-slip boundary conditions to model the viscous effect. The angle of incidence was changed automatically, and the code was run again to achieve convergence in about 4500 additional iterations.

6.8 Results and Discussion

This section discusses the impact of the aerodynamic interference between the nacelle and the wing with main concern on the exhaust system. SW-nacelle and the CRM-nacelle configurations aerodynamic interference is illustrated in this section. A comparison has been made between the effects of each of SW and the CRM on engine performance. Finally, corrections to the nozzle performance are presented at the end of the chapter. These corrections are used in the evaluation of installed engine performance.

6.8.1 Infinite SW-nacelle configuration aerodynamics interference

The purpose of this section is to present the evaluation of the interference mechanism of the installed nacelle under an infinite SW with a variation of engine location and angle of attack of the wing ($AoA_{A/C}$). To quantify this effect, a comparison has been made with results obtained from an isolated (stand-

alone) engine. Sixty-four swept-wing-engine CFD calculations have been carried out. These encompass varying the engine location, and at each location, the angle of attack was given eight different values, according to the matrix presented in Table 6.1, in Section (6.5).

Although the current project focuses on the impact of the aerodynamic interference due to the installation on the exhaust system, the effect of the wing pressure field on the nacelle aerodynamics is also presented due to the requirements of evaluating the nacelle aerodynamic performance. Because including the aerodynamic performance of the nacelle in the current work will highlight the importance of counting the interactions effect on the nozzle in the engine performance analysis. Furthermore, it enables a comparison with the previous studies, which have investigated the aircraft and nacelle up wash components aerodynamics only.

A substantial reduction in the drag coefficient (C_{Dnac}) with the presence of the SW wing was noted, (Figure 6.10). The C_{Dnac} reduced by about 0.005 at $AoA_{A/C}$= 0.0˚. Furthermore, as the angle of attack increases, C_{Dnac}, keeps decreasing moderately, which is contrasting the behaviour of the isolated engine C_{Dnac} data. The maximum decrease, ΔC_{Dnac}, was estimated is ≈-0.035, at AoA=3.5˚, for P01, (Figure 6.10).

As the engine is located closer to the wing (P01), the drag shows a higher reduction compared with P03 at $AoA_{A/C}$=3.5˚, (Figure 6.10). This reduction in C_{Dnac} is attributed to the increase in the pressure force over the fan-cowl after-body. This pressure force pushes the engine forward (towards the thrust direction). The force is directed upstream because the cowl after-body surface area is inclined backwards; therefore, the vector sum of the drag forces reduced.

In the situation where the engine was placed vertically closer to the wing ($\Delta z/C$ =0.05) (P04 to P07), the results show that C_{Dnac} decreases slightly. However, this variation is still not important. This can be seen when the evaluated smallest difference between the installed and isolated drag coefficient of the

nacelle (ΔC_{Dnac}) obtained for position P04 at $AoA_{A/C} \approx 2.5^{\circ}$, was -0.029 whereas at P01, ΔC_{Dnac} is -0.0277% for the same $AoA_{A/C}$.

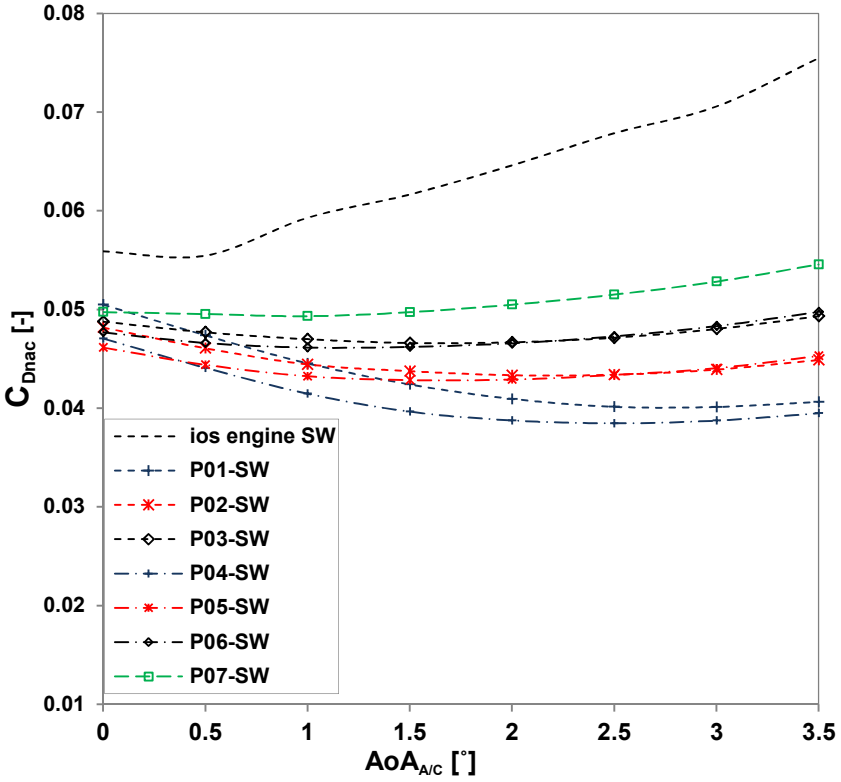

Figure 6.10 Installed nacelle drag coefficient variation with the engine position and the $AoA_{A/C}$, at M_{∞}=0.82 and Alt.=11000m.

The strength of the pressure field of the wing increases with the angle of attack and the region of high pressure increases over the lower surface of the wing, (Figure 6.11). It can be seen that the area of the high-pressure region, at the engine installation location, increased with the $AoA_{A/C}$. This produces a strong pressure effect on the nacelle. This explains the reduction in the values of C_{Dnac} with the variation of the $AoA_{A/C}$, especially when the engine installed close to the wing.

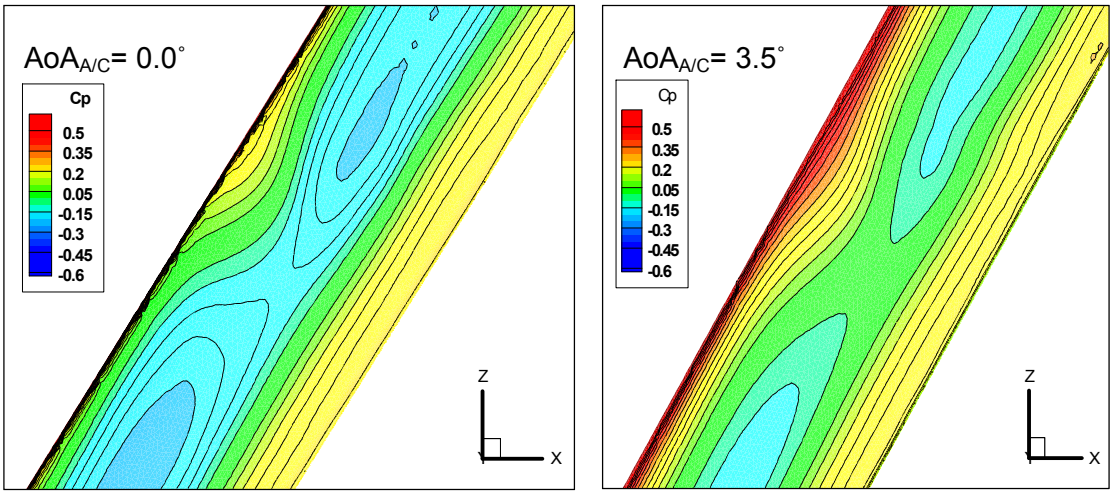

Figure 6.11 Pressure coefficient (Cp) contour over the pressure side of the SW, extracted from SW-nacelle configuration at installation position P03 and operating conditions M_∞ =0.82, Alt. 11000m.

The Net Propulsive Force (NPF) increased when the engine was installed on the wing, (Figure 6.12). This result was expected since there is a dramatic reduction in the drag of the nacelle because of the installation. The NPF_{inst} has been normalised to the net thrust of the engine $F_{n|ref}$ (68243 N) which was calculated using a non-dimensional performance model.

The NPF_{iso} of the isolated engine reduces with the $AoA_{A/C}$. The installation of the engine caused improvement in the NPF_{inst} of about 8.3% at $AoA_{A/C}$=0.0˚ and 11.7% at $AoA_{A/C}$ =3.5˚ for P03. As the engine was installed, further upstream, the NPF_{inst} reduced owing to the reduction of the effect of the wing pressure field.

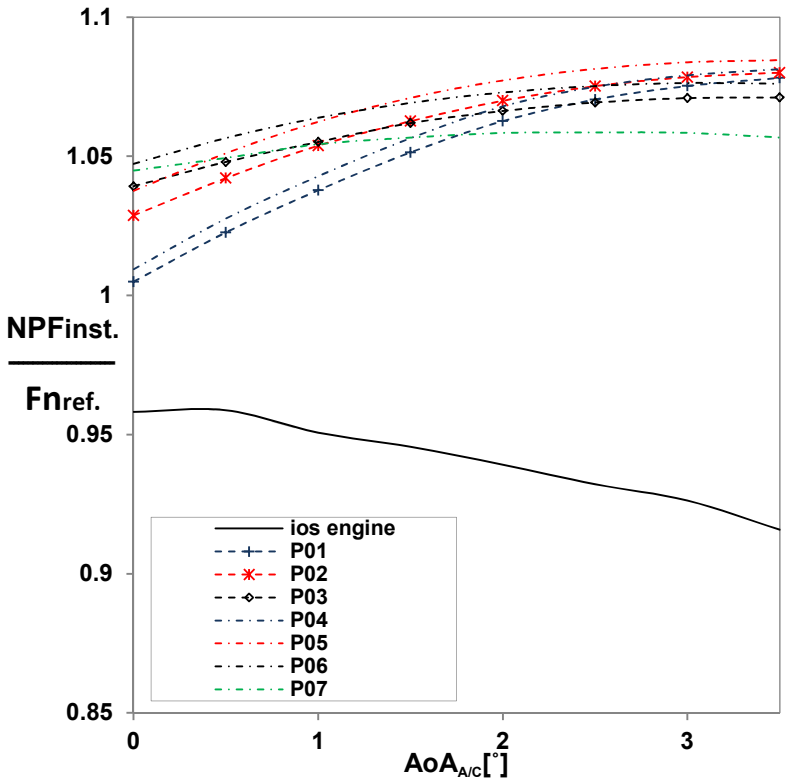

Figure 6.12 Ratio of the installed net propulsive force (NPF_{ins}) to the reference net thrust (Fn_{ref}) as a function of the $AoA_{A/C}$ for the chosen engine positions, at operating conditions of M_{∞}=0.82, Alt.= 11,000m.

Exhaust-system aerodynamic interference with the SW

Regardless the effect of combining the engine with the SW on the nacelle drag, the impact of the wing on the exhaust system is the primary purpose of the current project. The reason behind that is to seek the possibility of producing a generic model that can correlate the nozzle performance and the wing pressure field.

The impact of the installation aerodynamic interference on the exhaust-system components presents itself as the effect of the surrounding flow field on the core-cowl and the plug as well as the nozzle back pressure. The influence of the pressure field on the exhaust system components is pronounced, because of the high levels of the pressure field under the wing.

Since the thrust definition that has been used as a performance extraction method for the current project, includes the core-cowl and the plug pressure forces, the contribution of these parts to the thrust of the engine is presented in

Figure 6.13 and Figure 6.14. The results are presented in terms of the normalised pressure forces of the core-cowl and the plug to the ideal thrust of the engine. The values of the positive sign are the useful forces, which contribute to the engine thrust, and the negative sign is the drag penalty. It can be seen that there is an increase in the core-cowl forces ($\frac{\Phi_{c-c}}{F_i}$) towards the drag direction with the angle of attack of the isolated engine, (Figure 6.13). Conversely, when the engine is combined with the wing, $\frac{\Phi_{c-c}}{F_i}$ increased by 0.0072 at $AoA_{A/C}$=0.0˚ for P03. This means that this axial force contributes to the thrust of the engine. In other words, the integrated pressure force that is directed in the thrust direction will overcome the drag force components.

The results showed that the plug pressure forces ($\frac{\Phi_{plug}}{F_i}$) of the installed engine contributes to the engine thrust across all range of $AoA_{A/C}$, except for $AoA_{A/C}$ equals to 0.0˚ and 0.5˚ for installation positions P01 and P04. The variation of the engine location affects the pressure force over the plug with the presence of the wing, (Figure 6.14). As the engine was installed further upstream, ($\frac{\Phi_{plug}}{F_i}$) increased, as a result of the increase in the pressure field due to the presence of the wing. Installing the engine vertically very close to the wing increases $\frac{\Phi_{plug}}{F_i}$. This can be seen clearly in the comparison between the P03 and P06 results, (Figure 6.14). However, this effect reduces as the engine located axially close to the wing, (P02 and P05), (Figure 6.14). This is attributed to the increase in the flow velocity between the wing and the nacelle so that the pressure at this region will reduce.

Figure 6.15 shows the Mach number contours; it can be seen that jet Mach number increases with the reduction in the distance from the wing due to the increase in the velocity between the wing and the nacelle. Because of that, the jet velocity over the core-cowl or the plug increases, the pressure will reduce, causing a decrease in the net force pushing the engine forward.

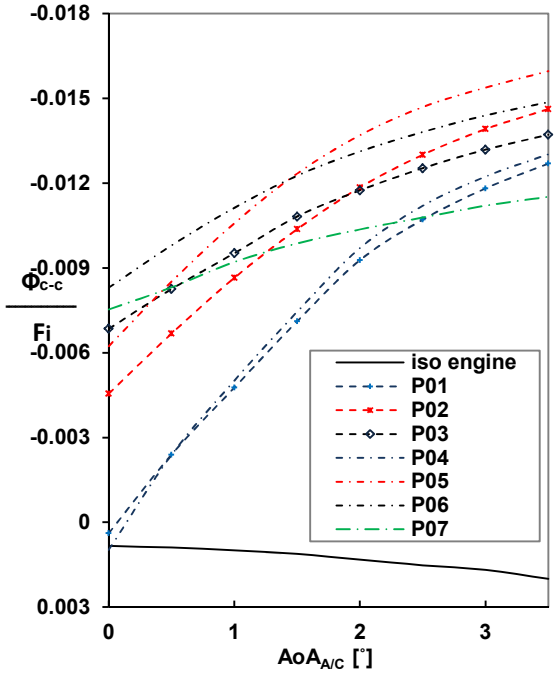

Figure 6.13 Variation of the normalised pressure force over the core-cowl ($\Phi_{c\text{-}c}/F_i$) as a function of the $AoA_{A/C}$ for the chosen position at operating conditions of M_∞=0.82, Alt. =11000m, FNPR=2.45, CNPR=1.92 and MFCR =0.73.

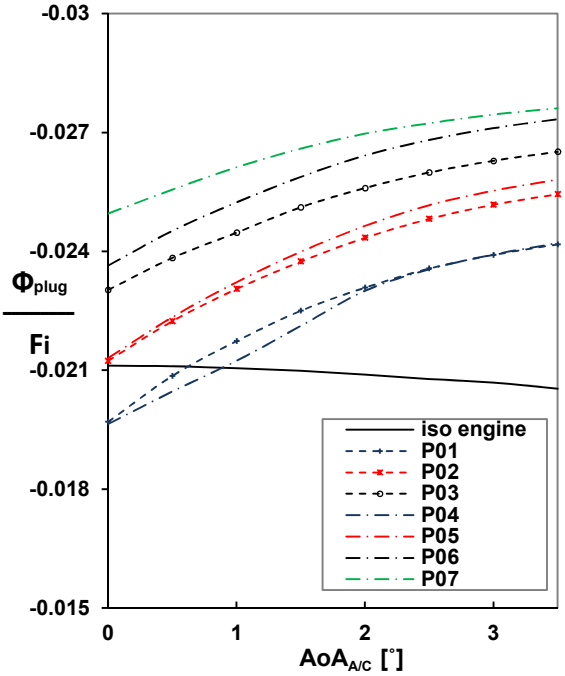

Figure 6.14 Variation of the normalised pressure force (Φ_{plug}/F_i) over the plug as a function of the $AoA_{A/C}$ for the chosen position at operating conditions of M_∞=0.82, Alt. =11000m, FNPR=2.45, CNPR=1.92 and MFCR =0.73.

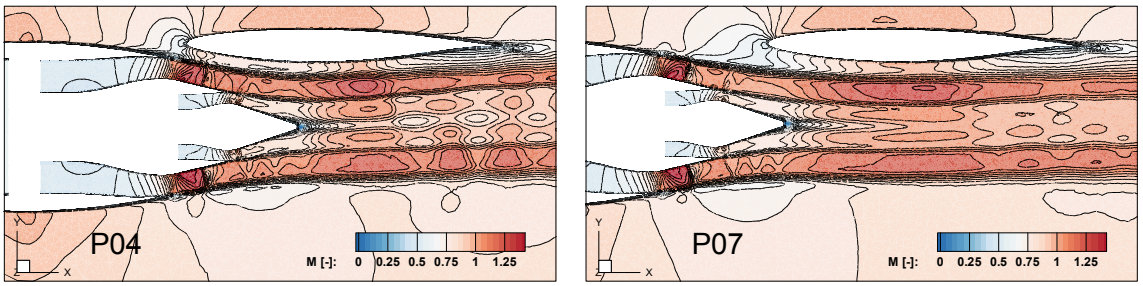

Figure 6.15 Mach number contour around the exhaust-system of an engine installed under the SW configuration for P04 and P07 showing the effect of the axial position variation.

6.8.1.1 Installed exhaust-system performance metrics

Exhaust system performance has been evaluated by calculating the discharge and thrust coefficients. To determine the impact of the installation aerodynamic interactions on these parameters, normalised coefficients $\left(\frac{C_{xinst.}}{C_{x\,iso.}}\right)$, were introduced, in which "*x*" stand for the type of coefficient, "inst" refers to the installed engine situation and "iso*",* refers to the isolated engine.

Impact on the discharge coefficient (C_d)

With the engine running under the mid-cruise conditions, the bypass (BP) nozzle is choked, and the flow inside the nozzle is unaffected by the external flow-field. Therefore, the variation in C_d remains small with the change in $AoA_{A/C}$ and engine position, (Figure 6.16). The maximum change between the isolated and installed engine bypass C_d was +0.0016 at $AoA_{A/C}$=0.0˚ at P07. This little variation in C_d means that the presence of the wing did not affect the choked conditions of the bypass nozzle. However, the presence of the wing increased the flow velocity in the channel flow. This high-velocity region has low-pressure levels. Therefore, the nozzle flow rate increases relative to the isolated nacelle engine data. In any case, since the nozzle is choked the variation in the C_d is not important.

The core nozzle, on the other hand, is greatly affected by the installation interference, the variation of the angle of attack and engine position. The flow coefficient, C_d, of the core improved when the engine was installed on the SW by 0.0080 at $AoA_{A/C}$ =0.0˚ for positions P01 and P04. However, C_d of the core nozzle decreases with the increase in the $AoA_{A/C}$ to a minimum value of C_d =0.944 for P06 at $AoA_{A/C}$=3.5˚. Furthermore, Changing the engine position vertically has an insignificant effect on the discharge coefficient. The maximum observed variation in C_d was less than -0.0020 between P06 and P03.

The core-nozzle flow rate was altered, due to the unchoked condition at which the core-nozzle was running and so any modification of external flow-field conditions will affect the flow rate of the exhaust gases. Therefore, the nozzle performance degrades due to the high-pressure field surrounding the exit plane of the nozzle, (Figure 6.17).

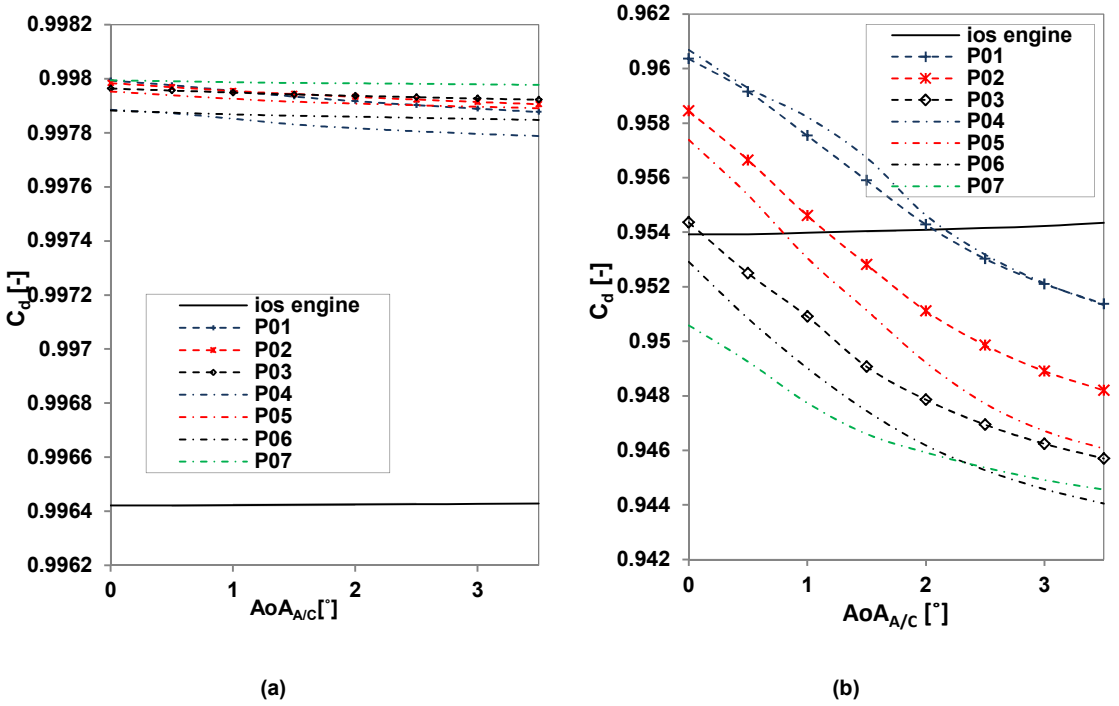

(a) (b)

Figure 6.16 Discharge coefficient (C_d) comparison between the isolated an installed nacelle on the SW configuration as a function of $AoA_{A/C}$ for the chosen position, at operating conditions of M_∞=0.82, Alt.= 11000m, MFCR =0.73, FNPR= 2.51 and CNPR =1.90, (a) By-pass nozzle,(b) Core nozzle.

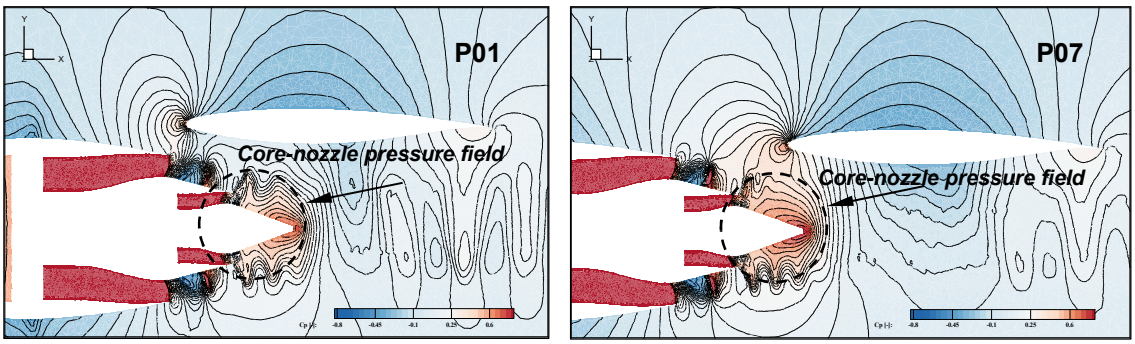

Figure 6.17 Close view of the pressure coefficient distribution around the exhaust-system of an engine installed under the SW configuration for two installation positions (P01) and (P07), at $AoA_{A/C}$of zero degrees and operating conditions of M_∞=0.82, Alt.= 11000m, FNPR= 2.45 and CNPR =1.92.

Interference impact on the thrust coefficient (C_{fg})

The modified thrust definition was used to calculate the exhaust system performance. Two main thrust definitions have been used in the current work. The difference between them is the inclusion and exclusion of the fan cowl after-body in the calculation, thrust definition (1) and thrust definition (2), respectively, as was presented in the previous chapter.

The gross thrust coefficient (C_{fg}) of the isolated engine is higher than one by ≈0.0047 after the inclusion of the core-cowl and the plug pressure forces in the thrust definition (thrust definition (1)), (Figure 6.18 a). The variation of the $AoA_{A/C}$ has a little impact on the C_{fg} (thrust definition 1) for the isolated engine, (Figure 6.18 a), in which the nozzle performance reduced slightly. On the other hand, the inclusion of the pressure forces of the cowl after-body (thrust definition 2) increased the gross thrust coefficient of the isolated nacelle with very small deviation, (Figure 6.18 b).

The main purpose of using thrust definition (2) is to capture the impact of the wing on the C_{fg} through the evaluation of its impact on the cowl after-body. The use of thrust definition (2) will increase the sensitivity of the C_{fg} to the installation and the influence of the angle of attack, (Figure 6.18).

Combining the engine with the SW increased the engine performance, as a result of the increase in the core-cowl and plug pressure forces, as stated above, (Figure 6.13). This also applies to increase in $AoA_{A/C}$. Increasing the axial distance (Δx/C) from the wing increases the thrust of the engine. The plug pressure forces increased when the engine had been installed for positions range of P01, P05 and P04 at $AoA_{A/C}$ of 0.0˚ and 0.5˚, therefore, the performance of the nozzle improved.

The variation of the vertical distance from the wing has a little impact on C_{fg}. The impact of the vertical distance from the wing increased when the engine installed axially away from the wing, C_{fg} varied by +0.068% between P01 and P04, and by +0.19% between P03 and P06 for $AoA_{A/C}$= 0.0˚, using thrust definition (1).

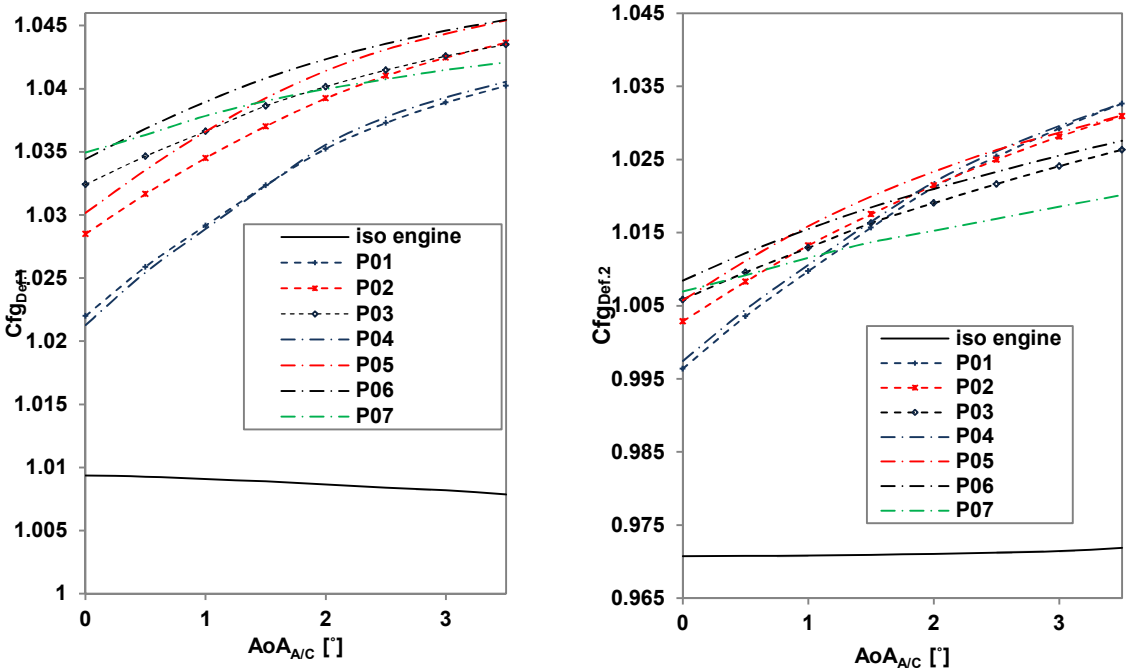

Figure 6.18 Gross thrust coefficient of the installed engine compared with the isolated engine as a function of the $AoA_{A/C}$ and engine position(a) thrust definition(1), (b) thrust definition (2).

The contribution of each component of the exhaust system, including the cowl after-body, on the nozzle performance, is presented in Figure 6.19, compared with the isolated engine data. The results show that the beneficial forces increase with the installation of the engine to the wing accompanied by a reduction in the cowl after-body drag. The upstream movement of the engine increases the pressure forces over the core-cowl and the plug, however, the variation between every two positions becomes insignificant at large $AoA_{A/C}$. The cowl after-body drag forces increased when engine placed at P03, P06 and P07, (Figure 6.19).

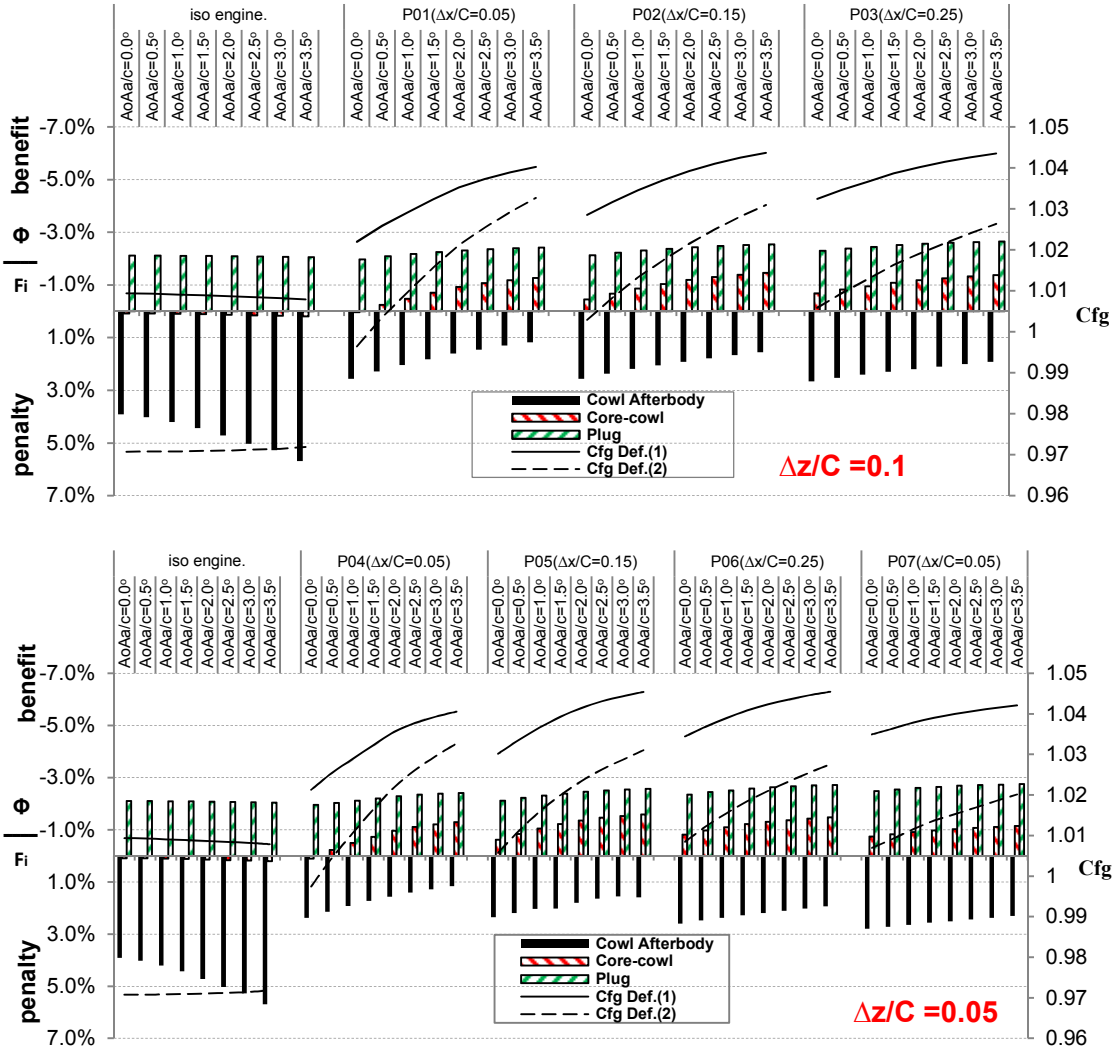

Figure 6.19 Comparison between the contribution of each exhaust-system components to the engine thrust as a function of the $AoA_{A/C}$ and the variation of the axial distance from the wing leading edge for the SW-nacelle configuration.

6.8.2 CRM-nacelle configuration aerodynamic interference

The aerodynamic performance analysis of the nacelle combined with the CRM configuration gave different results in terms of the drag coefficient (C_{Dnac}). The drag coefficient (C_{Dnac}) increased by 0.020 when the engine installed as compared with the isolated engine at $AoA_{A/C}$ =0.0°, (Figure 6.20), and decreased with the rise in $AoA_{A/C}$ and the change in horizontal engine location (Δx/C), (Figure 6.20).

Moreover, as the engine was located vertically closer to the wing C_{Dnac} decreases, as it can be seen in the comparison between P04 ($\frac{\Delta x}{c} = 0.05, \frac{\Delta z}{c} =$

0.05) and P01 ($\frac{\Delta x}{c} = 0.05, \frac{\Delta z}{c} = 0.1$), (Figure 6.20). However, this decrease is still insignificant where C_{Dnac} reduced by 40dc between P01 and P04 at $AoA_{A/C}$ =0.0° as the vertical distance was reduced. When the engine is installed axiallly close to the wing, the impact of the vertical position variation becomes more noticeable. This can be seen in the comparison between positions P04 to P06 and P01 to P03 results ,(Figure 6.20).

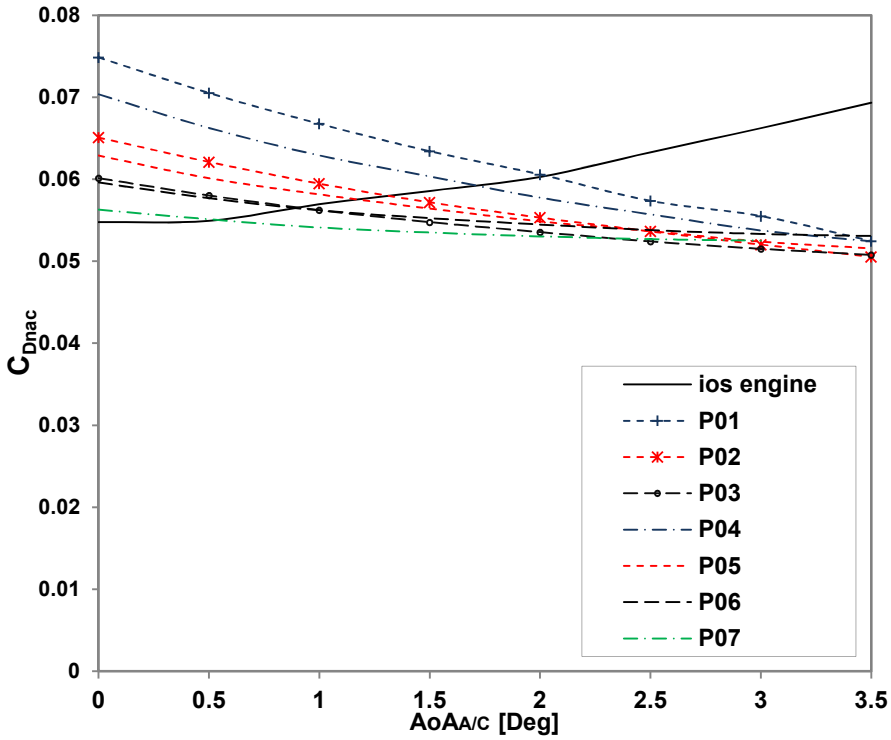

Figure 6.20 Drag coefficient variation with the engine position and the $AoA_{A/C}$, at M_∞=0.82 and Alt.=11000m. FNPR of 2.45 and CNPR of 1.92; for the Isolated and CRM-nacelle configuration.

The Net Propulsive Force (NPF) showed an expected behaviour. For the isolated engine, the NPF reduced because of the high nacelle drag levels, (Figure 6.21), which increases with the $AoA_{A/C}$. Installing the engine to the airframe of the aircraft reduced NPF significantly, when the engine installed close to the wing (P01, P02, P03 and P05), at low levels of $AoA_{A/C}$.

Despite there are some values of the NPF_{inst} higher than one, in general, the NPF for both isolated and installed situations is lower than the net thrust that is produced by the engine. This indicates that the engine thrust that is computed in the thermodynamic performance model is over-predicted. In other words, in

the CFD calculations, the net thrust was derived from the difference between the gross thrust and the momentum flux at the infinity upstream of the intake. This definition includes the effect of the nacelle drag and the flow interaction effect between the wing and the engine. These two effects were not taken into consideration in the thermodynamic model. Therefore, the calculation of the net thrust in the thermodynamic model is crude.

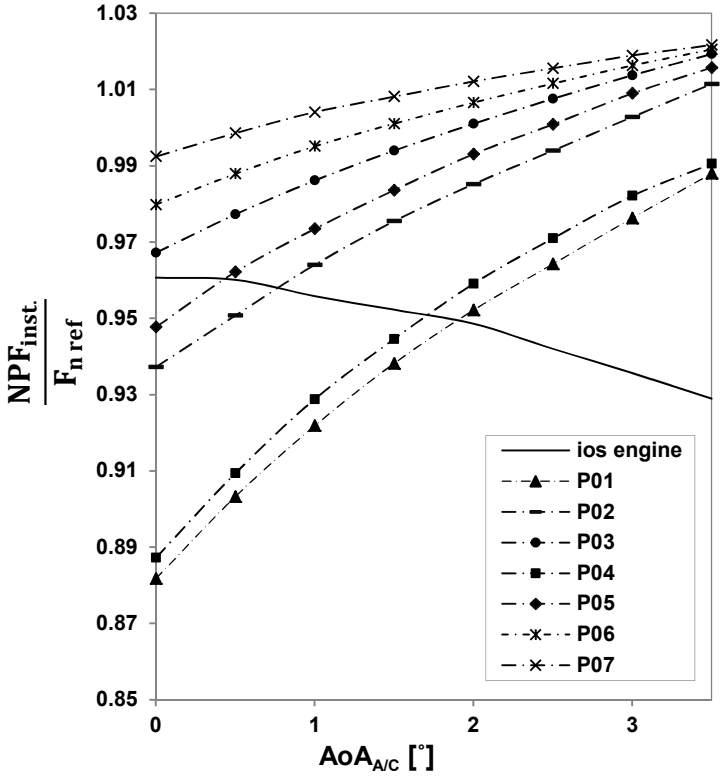

Figure 6.21 Ratio of the installed net propulsive force (NPF_{ins}) to the reference net thrust of the engine (Fn_{ref}) as a function of the $AoA_{A/C}$ for the chosen engine positions, at operational conditions of M_∞=0.82, Alt.= 11,000m, for the CRM-nacelle configuration.

Exhaust-system aerodynamic interference with the CRM configuration

The impact of the Common Research Model (CRM) wing on the exhaust system components is quantified by the calculation of the pressure forces over the core-cowl and the plug, (Figure 6.22). An increase in the pressure force over the core-cowl and the plug due to the installation interference was observed as compared with the stand-alone engine data, (Figure 6.22 and Figure 6.23). However, at a small angle of attack, the core-cowl pressure forces decrease with the installation, especially when the engine installed relatively close to the wing P01, P04, P02 and P05. This is regarded to the increase in

the exhaust jet velocity in the presence of the wing. The vertical movement of the engine increased the pressure force over the core cowl and the plug, (Figure 6.24). Moreover, with the increase in $AoA_{A/C,}$ the impact of the pressure due to the wing intensified, causing the pressure over the components of the exhaust system to increase, (Figure 6.24).

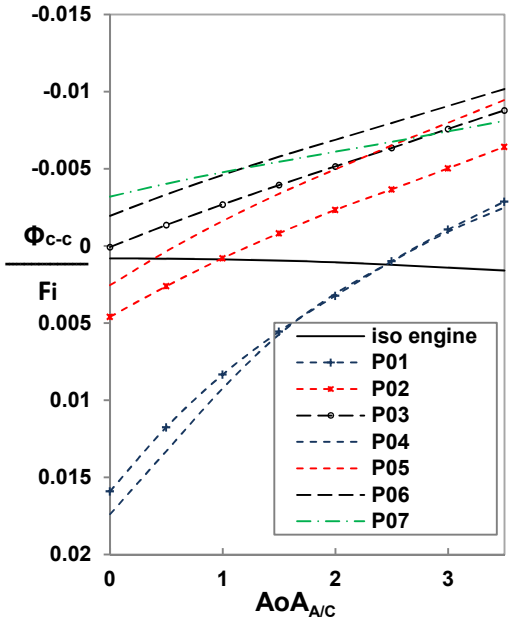

Figure 6.22 Variation of the normalised pressure force over the core-cowl ($\Phi_{c\text{-}c}/F_i$) as a function of the $AoA_{A/C}$ for the chosen position at operating conditions of M_∞=0.82, Alt. =11000m, FNPR=2.45, CNPR=1.92 and MFCR =0.73 CRM-nacelle configuration.

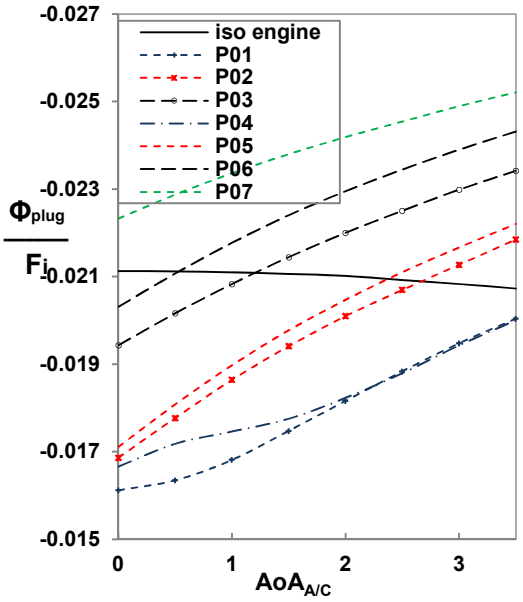

Figure 6.23 Variation of the normalised pressure force (Φ_{plug}/F_i) over the plug as a function of the $AoA_{A/C}$ for the chosen position at operating conditions of M_∞=0.82, Alt. =11000m, FNPR=2.45, CNPR=1.92 and MFCR =0.73, CRM-nacelle configuration.

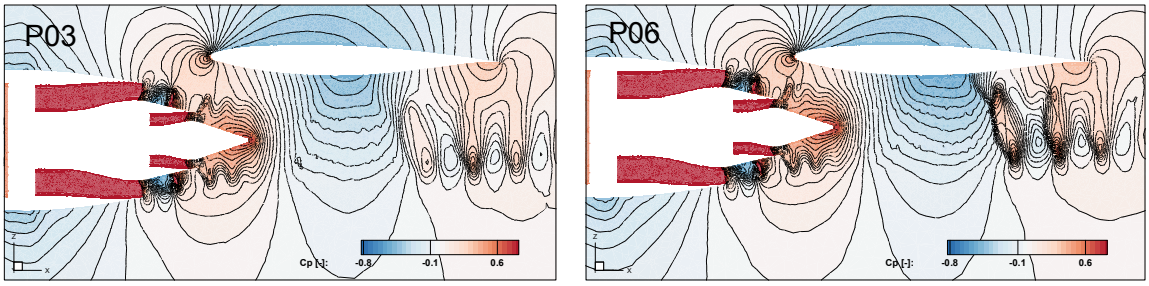

Figure 6.24 Pressure coefficient (Cp) contours around the CRM-nacelle configuration at $AoA_{A/C}$=0.5˚, and operating conditions of M_∞=0.82, Alt.= 11000m , MFCR =0.73, FNPR= 2.45 and CNPR =1.92.

6.8.2.1 Installed exhaust-system performance metrics

Interference impact on the discharge coefficient (C_d)

The variation of the discharge coefficient (C_d) of the bypass (BP) nozzle due to installation is very little, about 0.0012 at $AoA_{A/C}$ =0.0° for the installed engine at P06 as compared with the isolated engine C_d data. Moreover, the effect of the variation in engine location is not noticeable due to the choked running conditions of the BP nozzle, (Figure 6.25 a). However, the core nozzle C_d decreases with increase in $AoA_{A/C}$ for all engine positions, (Figure 6.25 b). The change in the vertical position of the engine has little impact on either nozzle.

The reduction in the core-nozzle discharge coefficient is attributed to the increase in the pressure field that surrounds the core nozzle. Since the pressure field of the wing increases with $AoA_{A/C,}$ the effective NPR will decrease, causing a reduction in C_d. This impact decreases with the reduction of the radial and axial distance from the wing.

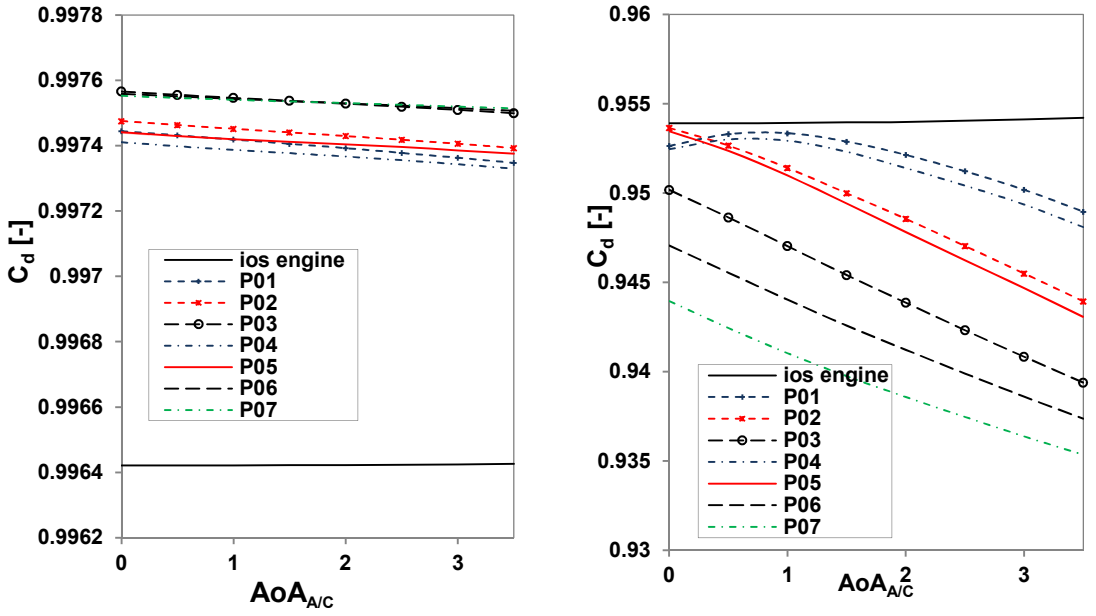

(a) (b)

Figure 6.25 Discharge coefficient (C_d) comparison between the isolated an installed nacelle on the CRM configuration as a function of $AoA_{A/C}$ for the chosen position, at operationg conditions of M_∞=0.82, Alt.= 11000m, MFCR =0.73, FNPR= 2.45 and CNPR =1.92, (a) By-pass nozzle,(b) core nozzle

For more clarification of the effect of the wing pressure field, the pressure that surrounding the nozzle is calculated, (Figure 6.26 and Figure 6.27), to highlights the effect of the presence of the wing and the engine position. The results showed that the pressure value around the rim of the bypass nozzle reduces

with the engine axial position, (Figure 6.27); this explains the increase in C_d of the bypass nozzle, (Figure 6.25 (a)). In other words, the NPR increases with the reduction in the backpressure and causes an increase in the mass flow that is discharging from the nozzle.

The core nozzle has stronger pressure field in comparison with the bypass nozzle, and increases when the engine location becomes further upstream from the wing, (Figure 6.27), causing the NPR to reduce and consequently the discharge coefficient. The increase in the $AoA_{A/C}$ shows little impact on the bypass nozzle environment; conversely, it is more noticeable around the core nozzle.

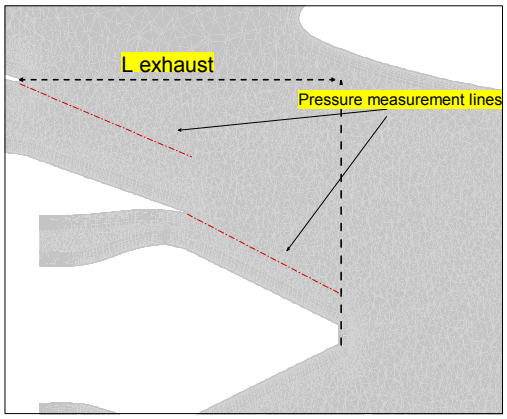

Figure 6.26 Close look to the nozzle exhaust region showing the location of the pressure calculations.

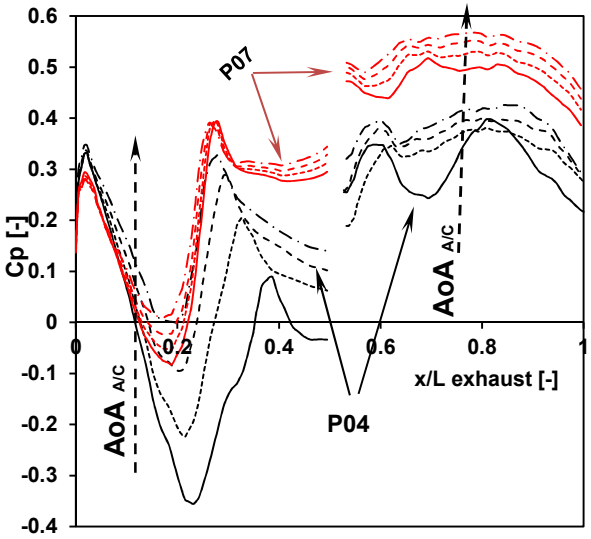

Figure 6.27 Pressure coefficient (Cp) distribution around the bypass and the core nozzle, for the chosen engine position and $AoA_{A/C}$.

Interference impact on the thrust coefficient **(C_{fg})**

The calculated values of C_{fg} according to the two definitions previously given are presented in Figure 6.28. Thrust definition (1) results showed an increase in the performance by 1.4% for the engine installed at P07 as compared with the isolated engine results at $AoA_{A/C}$=0.0˚. The further increase in the $AoA_{A/C}$ improved the performance of the nozzle, because of the increase in the wing lower-side pressure impact on the core-cowl and the plug. Moreover, at P01 and P04 and small values of $AoA_{A/C}$, the nozzle performance reduces less than

the isolated engine one by ≈1.2%. That means, installing the engine very close to the wing deteriorated the performance of the nozzle. Hence, placing the engine further upstream from the wing leading edge, increased C_{fg} by 1.4 % for P07 using thrust definition (1) relative to the isolated engine data at $AoA_{A/C}$ = 0.0˚. Installing the engine further upstream is the target of many aircraft design companies, due to the increase in the engine diameter.

It was noticed that including the cowl after-body increases the sensitivity of the performance data to the variation of the vertical displacement (Δz/C). For example, the results of P01 at $AoA_{A/C}$=0.0˚ deviates by-1.2% using thrust definition (1) as compared with the isolated nacelle results, whereas it became -1.43% after employing thrust definition (2). It should be noted that the C_{fg} of the isolated engine that is calculated by thrust definition (2) moderately increases all the way with the $AoA_{A/C}$. Conversely, thrust definition (1) results showed a decline in the performance of the nozzle at high ranges of $AoA_{A/C}$, (Figure 6.28).

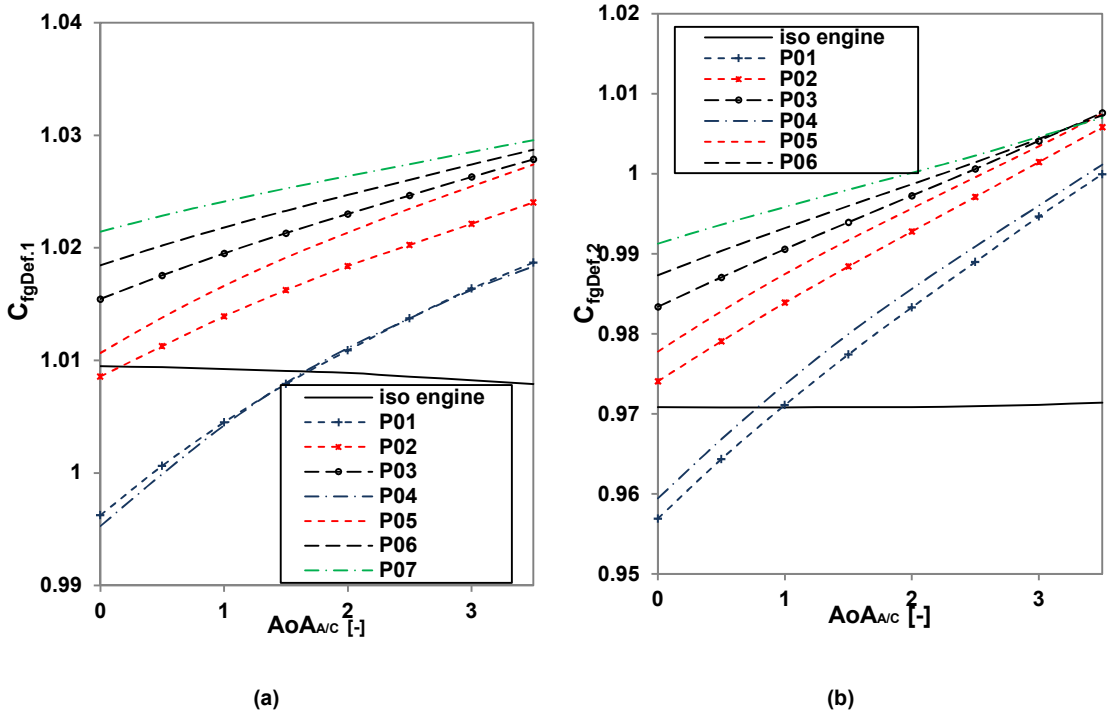

Figure 6.28 Gross thrust coefficient of the installed engine in comparison with the isolated engine as a function of the $AoA_{A/C}$ and engine position; (a) thrust definition(1), (b) thrust definition (2).

To compare the behaviour of the nozzle performance using both definitions for each engine position, a useful correlation is illustrated in Figure 6.29. The use of

thrust definition (2) increases the sensitivity of the nozzle performance to the installation position and the increase in the lift. The slope of the curves increased, and the effect of the vertical movement of the engine became slightly more pronounced than the data derived from thrust definition (2).

It can be seen that when the engine was installed axially very close to the wing (P01 and P04), there is the reduction in the nozzle performance at low lift levels (0.2-0.5). Placing the engine further away from the wing increased the performance, moderately as captured by thrust definition (1) and noticeably as captured by definition (2).

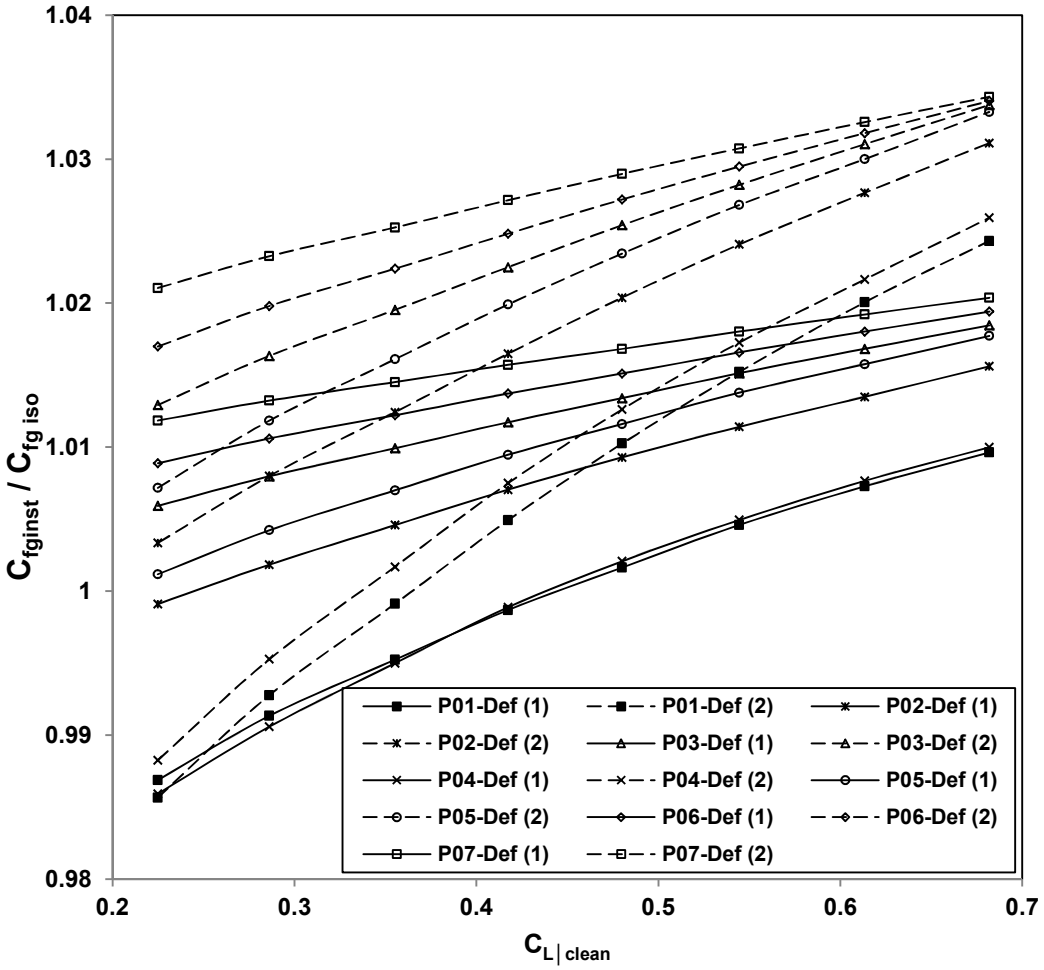

Figure 6.29 Ratio of the installed thrust coefficient (C_{fginst}) to the isolated thrust coefficient (C_{fgiso}) as a function for the lift coefficient for the chosen engine positions, according to both thrust definitions.

As in the swept wing case, the contribution of each component of the exhaust system and the cowl after-body, on the engine nozzles performance metrics, is

demonstrated in Figure 6.30, for the isolated and installed engine. It can be seen that there is a forced penalty over the cowl afterbody due to the installation. These penalties are greatly noticeable when the engine installed in position P01(very close to the wing). The drag forces of cowl afterbody decrease with the axial shifting from the wing leading edge. This behaviour applies to both vertical positions (Δz/C= 0.05 and Δz/C= 0.10). The latter explains the improvement in the performance of the nozzle when thrust definition (2) was employed to calculate C_{fg}.

The core-cowl pressure forces act as a drag force affecting the predicted level of the performance. However, the drag force reduces with the increase in the $AoA_{A/C}$ and the movement of the engine upstream. On the other hand, the plug pressure forces contribute to the thrust in each case; the isolated and the installed engine situations. This contribution of the plug forces increases with the installation and the axial movement of the engine upstream the wing leading edge as well as the increase in the $AoA_{A/C}$.

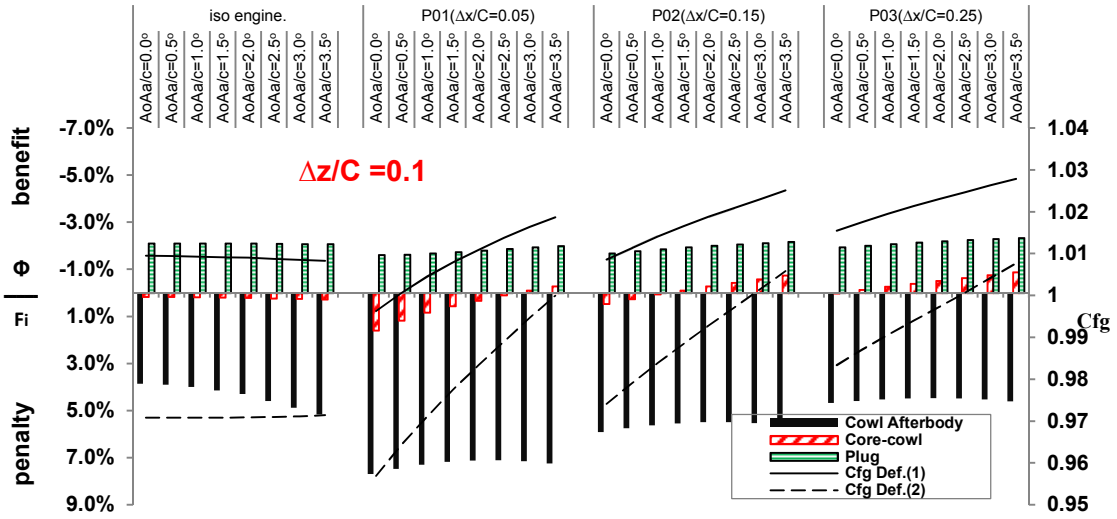

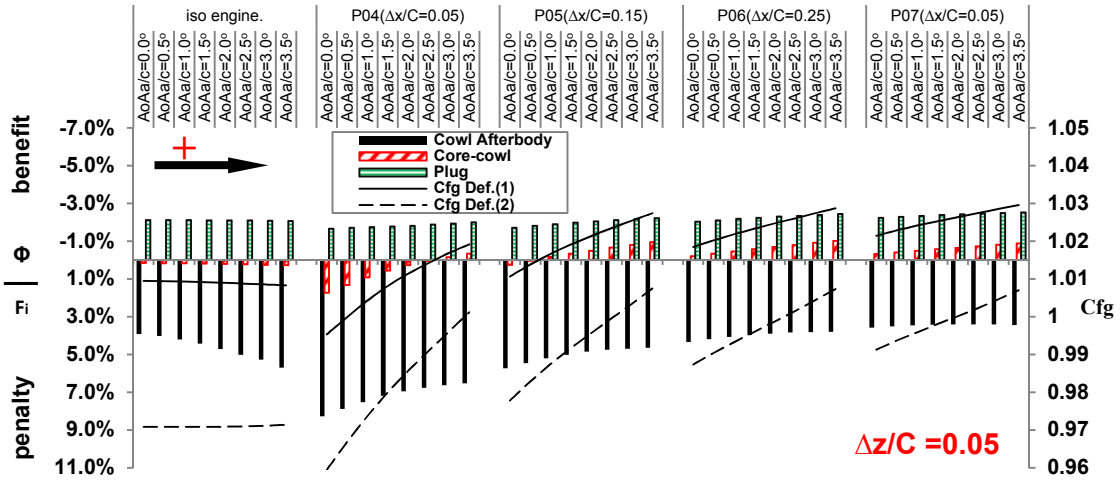

Figure 6.30 Comparison between the contribution of each exhaust-system components to the engine thrust as a function of the $AoA_{A/C}$ and the variation of the axial distance from the wing for the CRM-nacelle configuration.

6.8.3 Aircraft aerodynamic performance

Although there is an improvement in the engine aerodynamic performance at some engine installation location and angle of attack, the impact of the engine itself on the aircraft performance could be vital. The aircraft performance is represented by the ratio of the lift to drag forces of the aircraft or lift-drag polar $(\frac{L}{D})$.

The role of the engine is to produce the required thrust to drive the aircraft. This thrust is represented by the (Net Propulsive Force), NPF [110]. Although there are improvements in the engine performance because of the aerodynamic interference between the wing and the exhaust system, there is a trade-off between the aircraft and the engine aerodynamic performance. This trade-off came from the fact the aircraft aerodynamic performance is sensitive to the engine installation [4,5,82,119–121].

The aerodynamic characteristics of the aircraft are affected by the installation of the engine under the wing, (Figure 6.31). The drag coefficient of the aircraft ($C_{DA/C}$) is sensitive to the engine location. $C_{DA/C}$ decreases when the engine installed at P01, P02 and P04 at low lift levels, (Figure 6.32), and increases for all the other engine positions. The maximum aircraft drag increase that is

caused by the installation of the engine is 18dc when the engine combined with the airframe at P07 at C_L of 0.5, (Figure 6.32).

There is a continuous loss in the lift across the entire range of the angle of attacks, (Figure 6.33). The lift loss ($\Delta \boldsymbol{Cl}$) is varying from 0.018 at $AoA_{A/C}$ =0.0˚ to 0.041 at $AoA_{A/C}$=3.5˚, when the engine installed at P01, (Figure 6.33). It can be seen that the maximum loss was calculated when the engine was installed at P04 with $\Delta \boldsymbol{Cl}$ = 0.042 at $AoA_{A/C}$ of 3.5˚. Furthermore, It was noted that the vertical location variation (Δz/C), has an impact on C_L. Installing the engine further vertically away from the wing increased the loss in the lift coefficient,(Figure 6.33).

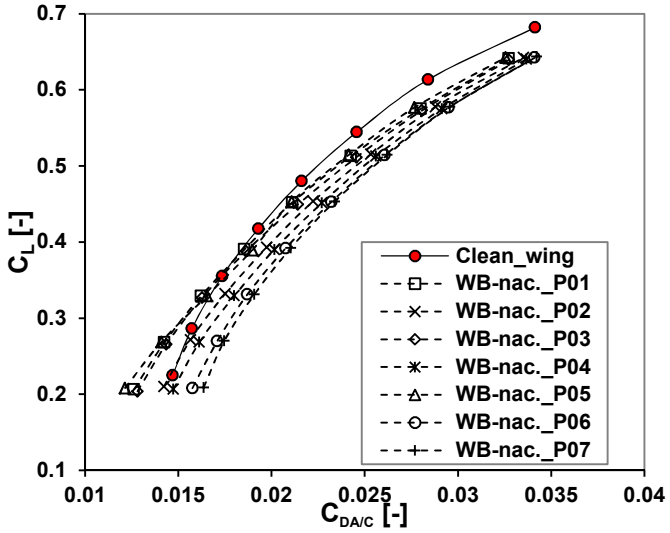

Figure 6.31 Comparison of the lift-drag polar between the combined nacelle and aircraft configuration and a clean wing configurations (without nacelle), as a function of the engine position; under operating conditions are M_∞ = 0.82 and Alt. 11000ft.

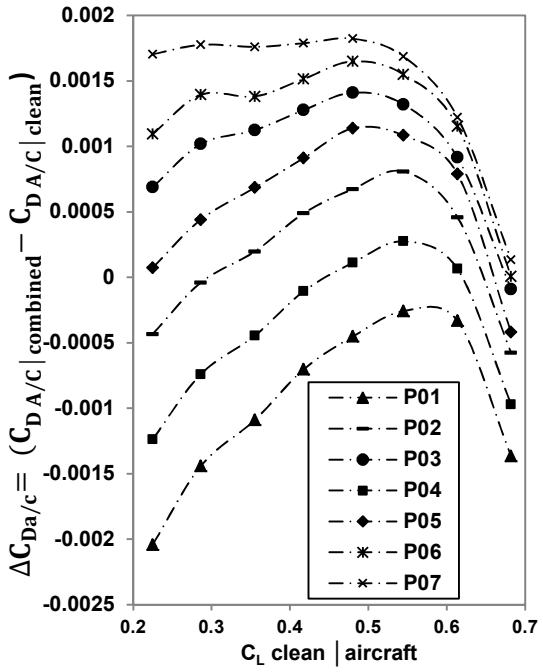

Figure 6.32 Aircraft drag variation $(\Delta C_{DA/C})$ between combined aircraft and nacelle configuration and the clean wing configuration, calculated at constant C_L; M_∞ =0.82 and Re = 35x10^6 (based on reference chord length), for the chosen engine positions.

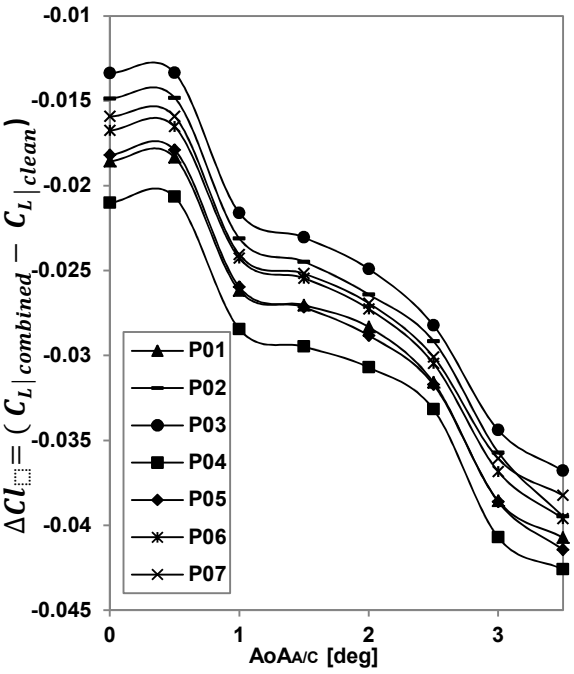

Figure 6.33 Loss of lift (ΔCl) between combined aircraft and nacelle configuration and the clean wing configuration, calculated at constant C_L; M_∞ =0.82 and Re = 35x10^6 (based on reference chord length), for the chosen engine positions.

The above results showed that the compromise impact between the airframe and the engine has to be considered in the calculations of the aircraft and engine performance. In other words, the clean aircraft drag values need to be correlated to the combined one to assess the impact of the presence of the engine on the aircraft aerodynamic characteristics. The results of this correlation show that the aircraft drag reduces due to the installation when the engine is mounted close to the wing and increase with the further axial movement relative to the wing leading edge as compared with the clean airframe, (Figure 6.34). The further increase in the lift of the aircraft (C_L >0.6) reduces the drag coefficient for the entire range of engine positions.

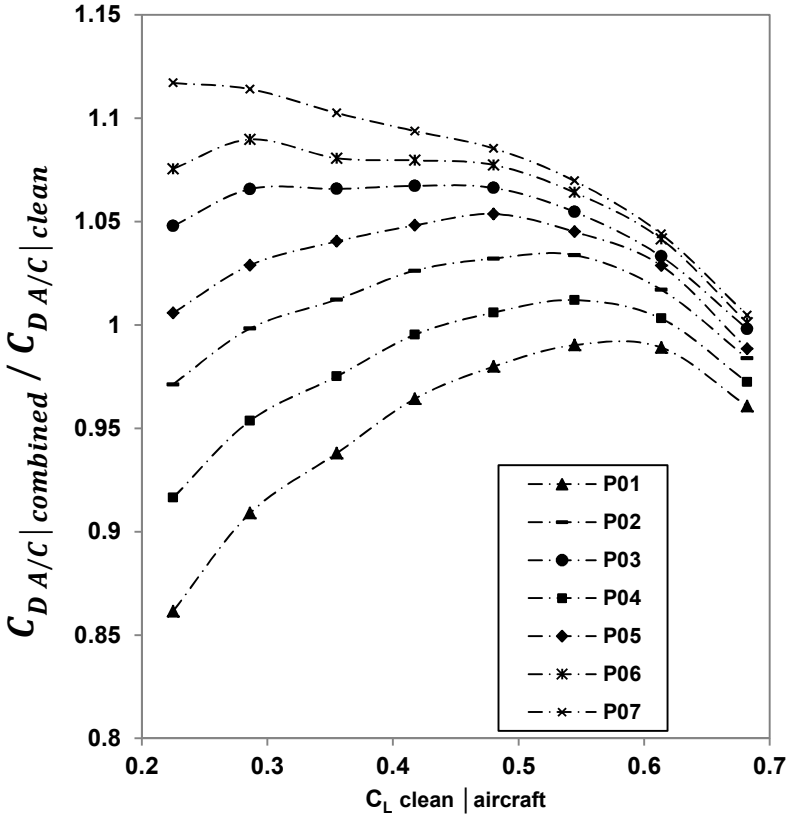

Figure 6.34 Ratio of the combined and nacelle configuration drag coefficient to the clean wing aircraft ($C_{D\,A/C}|_{combined} / C_{D\,A/C}|_{clean}$), at constant lift coefficient and for the chosen engine position; M_∞ =0.82 and Re = 35x10^6 (based on reference chord length).

The overall horizontal force that the engine thrust needs to overcome is the axial forces along the engine axis. This force is expressed by the difference between the engine net propulsive force (NPF) and airframe drag force ($D_{A/C}$), (Equation (6-1)) [110,120].

$$F_x^{'} = NPF - D_{A/C} \tag{6-1}$$

A correction factor that considers the effect of the installation on the axial forces of the engine referred as an axial force correction factor ($F_{x\mathrm{CF}}^{'}$), (Equation (6-2)), which is presented in Figure 6.35. The entire data in terms of the aircraft drag and the NPF derivation are extracted from the CFD module.

$$F_{x\mathrm{CF}}^{'} = (NPF_{inst.} - D_{A/C})_{|combined} / (NPF_{iso.} - D_{A/C})_{|clean} \tag{6-2}$$

The entire set of the correction factors show a moderate growth as the angle of attack increases until the aircraft lift coefficient reaches to values higher than

0.5 where a dramatic growth in the force ratio is captured. The dramatic rise in the $F'_{x\mathrm{CF}}$ values, as the lift coefficient is further increased, is attributed to the increase in the aircraft and the isolated nacelle drag.

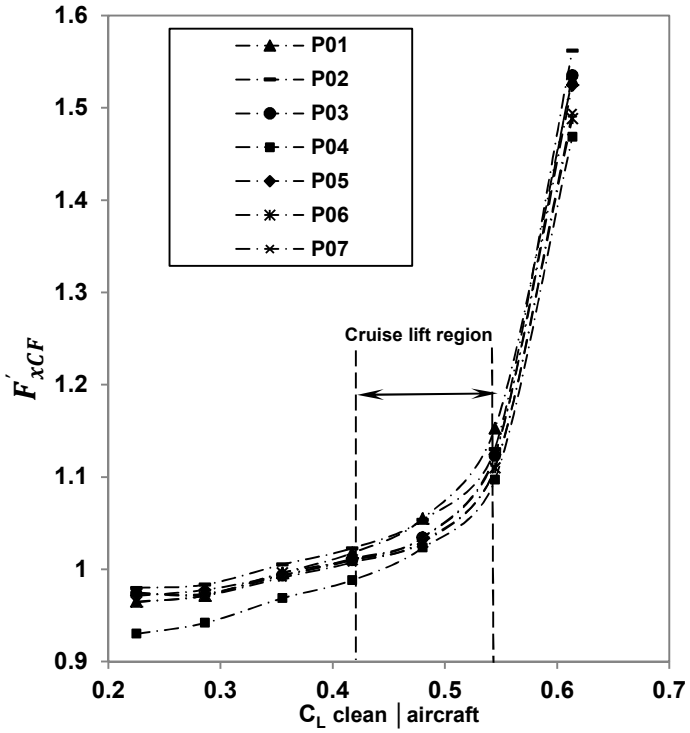

Figure 6.35 Ratio of the axial force along the engine aero-axis of the combined engine-aircraft configuration to the clean aircraft axial force; as a function of the lift coefficient of the clean wing, for the chosen engine position; M_∞ =0.82 and Re = $35x10^6$ (based on reference chord length).

6.8.4 SW and CRM configurations aerodynamic performance comparison

As observed before, the nacelle drag and the exhaust-system performance data behaviour differ when the engine was combined with SW and CRM configurations, owing to the difference in the pressure field of both configurations, (Figure 6.36). This pressure field difference will produce a different impact on the upcoming flow streamlines. As it was noticed before, Section 6.6.2.1, that the SW has a greater influence on the surrounding flow, which increases the local angle of attack (AoA_{local}) upstream of the wing leading edge, corresponding to the requested $AoA_{A/C}$.

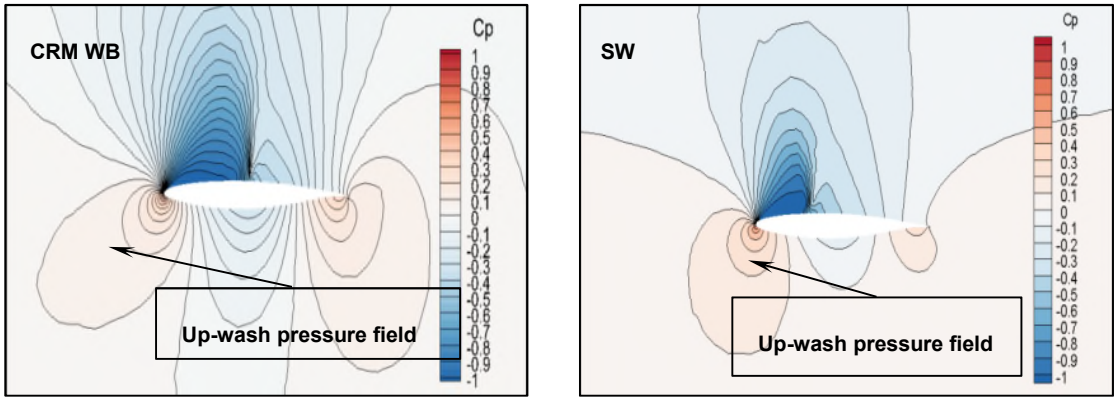

Figure 6.36 Pressure coefficient distribution around the wing (CRM and SW configurations) at M_{∞}=0.83, Re 5.0x10^{6} and $AoA_{A/C}$ =2.87˚.

On the other hand, the three-dimensional nature of the flow around the CRM wing also produces differences in the impact of the wing on the engine. This three-dimensional effect came from the twisted and bent geometry of the CRM wing. This impact of the CRM wing configuration is difficult to be produced by the two-dimensional SW configuration. This difference was expected. However, the aim of using this wing configuration (SW) was to produce a similar flow field behaviour to that of the CRM configuration, employing a simplified wing configuration.

The nacelle sees the front region of the pressure surface of the wing, which is represented by the pressure distribution over the wing lower surface. To find a correlation that relates the impact of the pressure field on the nozzle performance, the pressure distribution at a different location that is surrounding the clean-wing leading edge was calculated. This happened by proposing to main regions to compute the pressure around them. The first one is the region over the pressure surface of the wing that extends from the leading edge of the wing to midpoint of the wing chord length, (Figure 6.37). The pressure coefficient over this region was averaged along the length of the chord. It can be seen that the pressure at this region of the SW is stronger as compared with the CRM wing configuration data, (Figure 6.38).

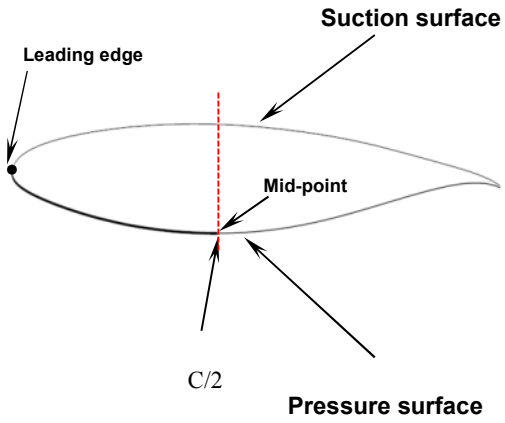

Figure 6.37 Sketch of a wing section showing the region of the pressure calculations; C stands for the wing chord.

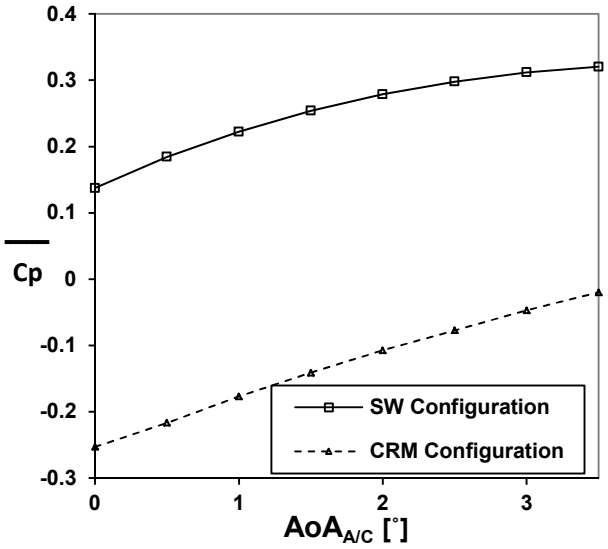

Figure 6.38 Comparison between the average pressure coefficient distribution over the region extended from the leading edge of the wing to the midpoint of the lower surface, at operational conditions of M_∞ =0.82.

For a clearer understanding of to what extent that the pressure field affects the aircraft combined with the engine aerodynamics interference, the local static pressure at the location of the cowl trailing edge, Figure 6.39, has been calculated with the variation of the $AoA_{A/C}$ and the engine position, and this is the second region. The pressure results show that as the axial distance (Δx) increases the difference between the SW and the CRM configuration pressure becomes smaller, (Figure 6.40). On the other hand, the pressure keeps in increase with the angle of attack for the CRM WB configuration; whereas for the SW configuration, the pressure curves distribution lose their linearity.

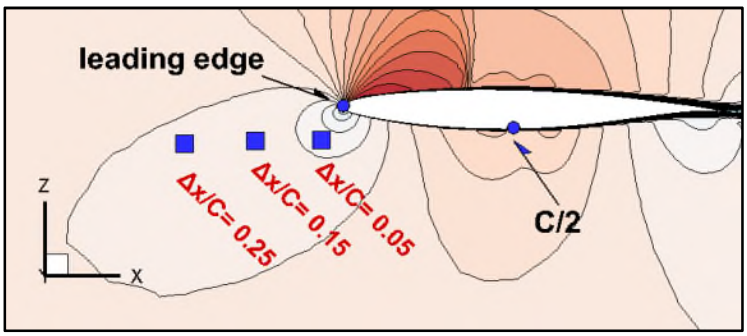

Figure 6.39 Proposed locations of the local static pressure measurement.

This dissimilar behaviour of the pressure that is surrounding the wing configurations (SW and CRM) produced the differences in the influence between each of them, as mentioned earlier in the prediction of the nacelle aerodynamics performance.

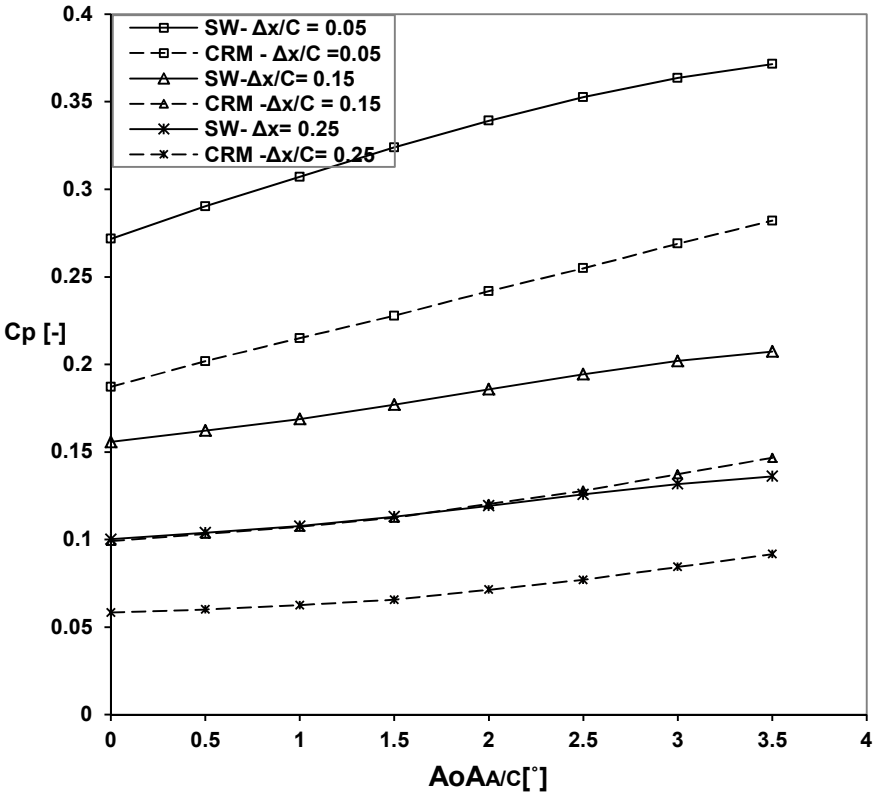

Figure 6.40 Comparison the local pressure coefficient around the wing of the SW and the CRM at various axial installation locations, Δx/C stands for the axial distance variation. All the pressure data were extracted at Δz/C (vertical distance deviation) of 0.1, and at operating conditions of M_∞ =0.82.

The drag coefficient variation ($\Delta C_{Dnac} = C_{Dnac\ inst} - C_{Dnac\ iso}$), as a function of the $AoA_{A/C}$ and engine position for both configurations, is presented in (Figure 6.41). It can be seen that the nacelle drag is reduced with installation for all positions and $AoA_{A/C}$ for the SW-nacelle configuration, whereas this is not the case for the CRM-nacelle configuration where the drag coefficient increases at low levels of $AoA_{A/C}$. As the engine moves away from the wing horizontally and vertically, the effect of the CRM on the nacelle increases and reduces the penalty of the drag due to the installation at low angles of attacks. This is not

the case for the SW-nacelle configuration, in which the drag increase with the axial distance when the engine is installed at the vertical location of Δz/C =0.05.

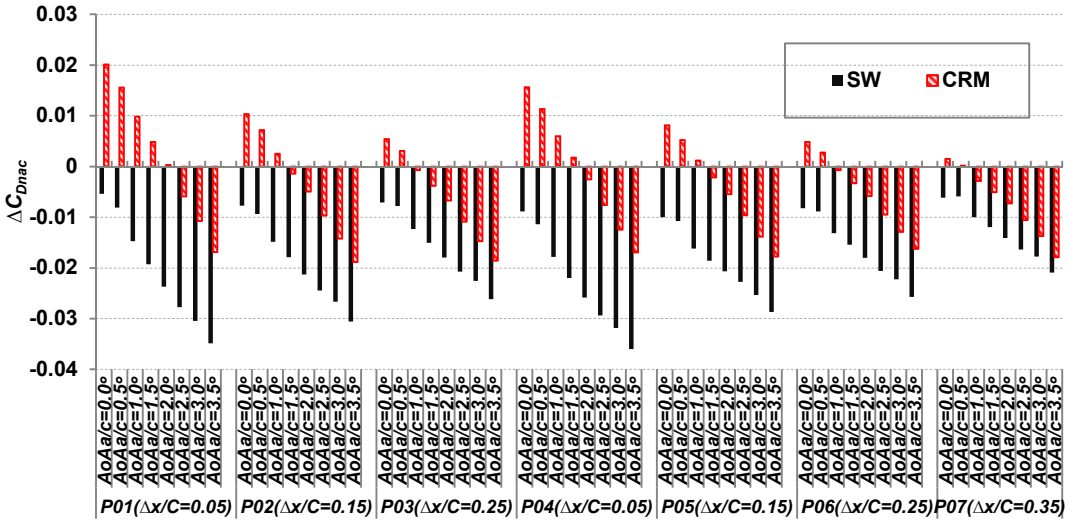

Figure 6.41 Comparison of the nacelle drag coefficient difference ($\Delta C_{Dnac} = C_{Dnac\ inst} - C_{Dnac\ iso}$) between the SW-nacelle and CRM-nacelle configurations.

The exhaust system performance, on the other hand, showed higher levels of improvement for the SW-nacelle configuration results than the CRM one for both definitions, (Figure 6.42 and Figure 6.43). This difference came from the effect of the wing pressure signature on the exhaust system components. When the engine was installed into the SW, the core-cowl contributed significantly to the engine thrust especially at a high value of $AoA_{A/C}$ (3.0˚). In contrast, the CRM-nacelle configuration results show that the core-cowl aerodynamic force gradually changes its direction from the drag side to the thrust side with the increase in the $AoA_{A/C}$, specifically when the engine is installed very close to the wing (P01, P04). This explains the reduction in C_{fg} at some low levels of $AoA_{A/C}$ and engine position as compared with isolated engine results.

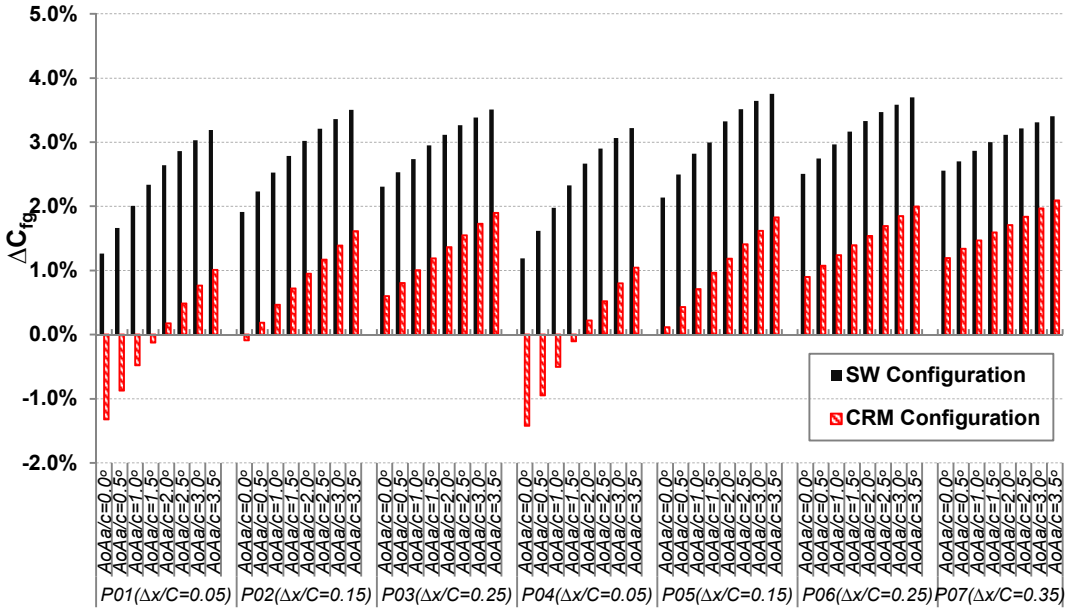

Figure 6.42 Comparison of the gross thrust coefficient difference ($\Delta C_{fg} = C_{fg\ inst} - C_{fg\ iso}$) between the SW-nacelle and CRM-nacelle configurations, using thrust definition (1).

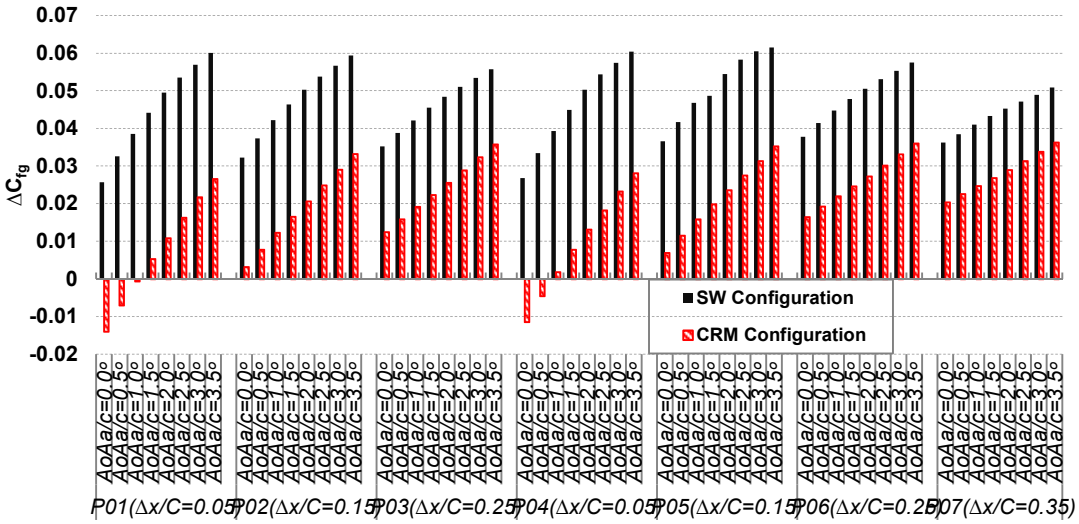

Figure 6.43 Comparison of the gross thrust coefficient difference ($\Delta C_{fg} = C_{fg\ inst} - C_{fg\ iso}$) between the SW-nacelle and CRM-nacelle configurations, using thrust definition (2).

6.8.5 Local pressure and thrust coefficient corrections correlations

The aim of producing such a correlation is to build a module can predict the nozzle performance as a function of the local static pressure of the wing. The employment of the SW aimed to produce a wider range of data that can cover high levels of the angle of incidence or angle of installation. To accomplish this aim, correlations between the nozzle performance data and the pressure coefficient were established.

The nozzle performance data were correlated in terms of the ratio of the installed to isolated thrust coefficient ($\frac{Cfg_{inst}}{Cfg_{iso}}$) with the average pressure coefficient over the region that is extended from the wing leading edge to about C/2 of the wing chord, (Figure 6.44). The results showed that the thrust coefficient improved with the intensity of the pressure for both configurations (SW and CRM), (Figure 6.44), in comparison with the isolated one. As it was expected, the comparison between the CRM and SW configurations shows that $\frac{Cfg_{inst}}{Cfg_{iso}}$ of the SW-nacelle configuration is much higher than the predicted data using the CRM-nacelle configuration.

For the CRM-nacelle configuration, when the engine was installed axially close to the wing (P01 and P04) the relation between the nozzle performance corrections and the pressure under the wing is linear. This behaviour was not observed for the SW-nacelle configuration results, in which for all engine positions and pressure levels the relation is not linear, (Figure 6.44). However, as the engine was installed axially away from the wing, the linearity in the CRM-nacelle configuration results disappeared.

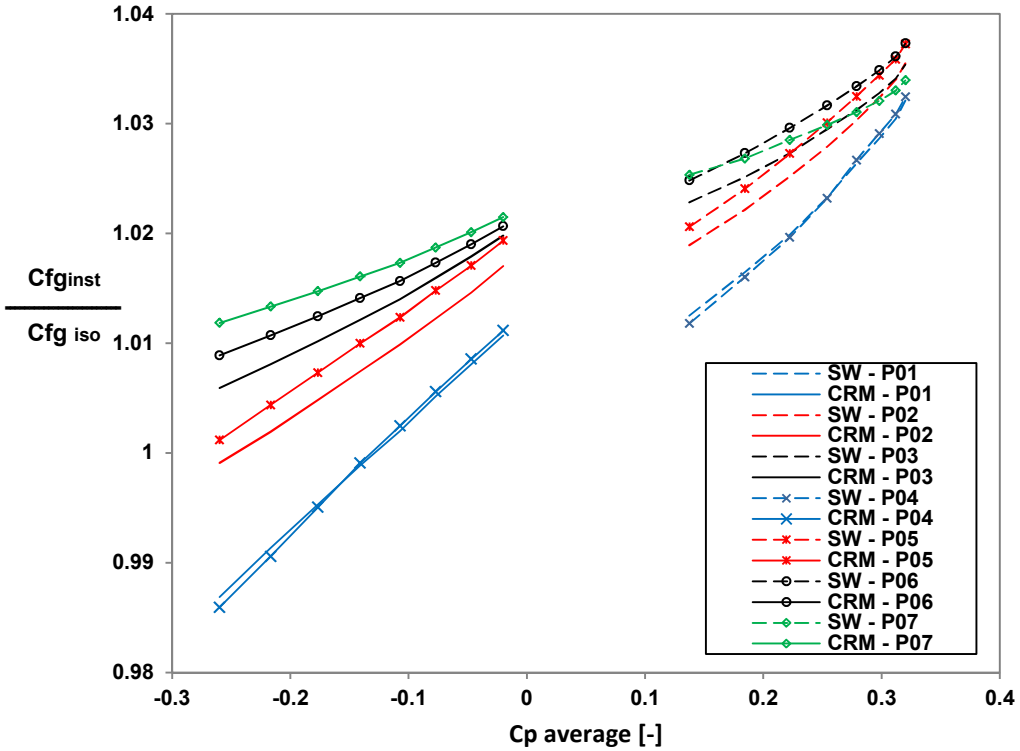

Figure 6.44 Correlation between the average pressure distribution along the pressure side of the wing and the ratio of the installed to isolated engine thrust coefficient, for the SW-nacelle and CRM–nacelle configurations, using thrust definition (1); for the chosen engine position.

The ratio of the installed to isolated C_{fg} was also correlated to the local pressure at the cowl trailing edge. The $\frac{Cfg_{inst}}{Cfg_{iso}}$ is correlated to different engine axial positions keeping the vertical distance constant. It was noted that there is an overlap between the $\frac{Cfg_{inst}}{Cfg_{iso}}$ of the CRM and the SW, when the pressure was calculated at the location of (Δx/C =0.05, Δz/C = 0.05), (Figure 6.45). This was expected, as the local static pressure in this region, of both configurations, is the same at a high value $AoA_{A/C}$, (Figure 6.40). Despite the overlap, the data of the SW-nacelle configuration are still higher than the CRM-nacelle configuration one.

Correlating the pressure data at the location (Δx/C =0.15, Δz/C = 0.05) with the performance data showed an improved trend between the SW-nacelle and the CRM-nacelle configuration in comparison with the previous correlations, (Figure 6.46). However, the results still show no match between both configurations. The highly nonlinear behaviour of the data was observed. It worth to be noted that placing the engine further upstream from the wing will not have a noticeable impact on the data, as it can be seen in Figure 6.47. Same trend was observed between the data that are derived from position (Δx/C =0.15, Δz/C = 0.05) and (Δx/C =0.25, Δz/C = 0.05).

Although the correlation between the simple two-dimensional infinite wing and the CRM WB configuration curves do not give the extended nozzle performance representation, the data are still useful. They can give an initial indication of the influence of the flow interaction due to the installation on the exhaust system performance. However, since the pressure distribution mainly depends on the shape of the wing, these correlations can be improved by handling the simplified wing profile. Therefore, the selection of the appropriate wing profile could enable the production of the extended performance interaction data.

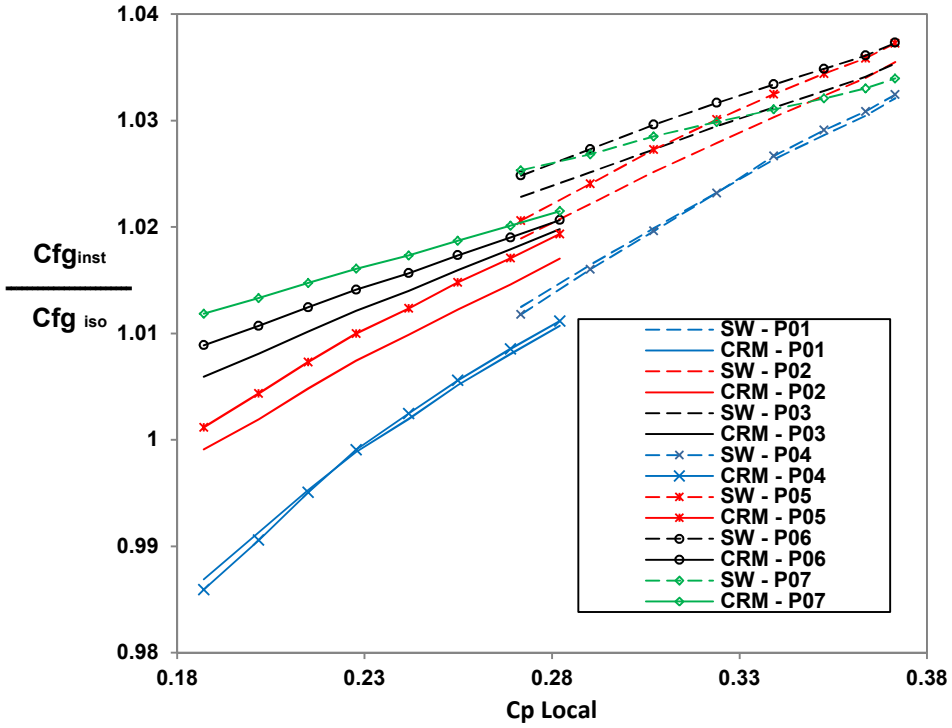

Figure 6.45 Correlation between the local pressure at the cowl trailing edge (Δx/C =0.05, Δz/C = 0.05) and the ratio of the installed to isolated engine thrust coefficient, for the SW-nacelle and CRM–nacelle configurations, using thrust definition (1); for the chosen engine position.

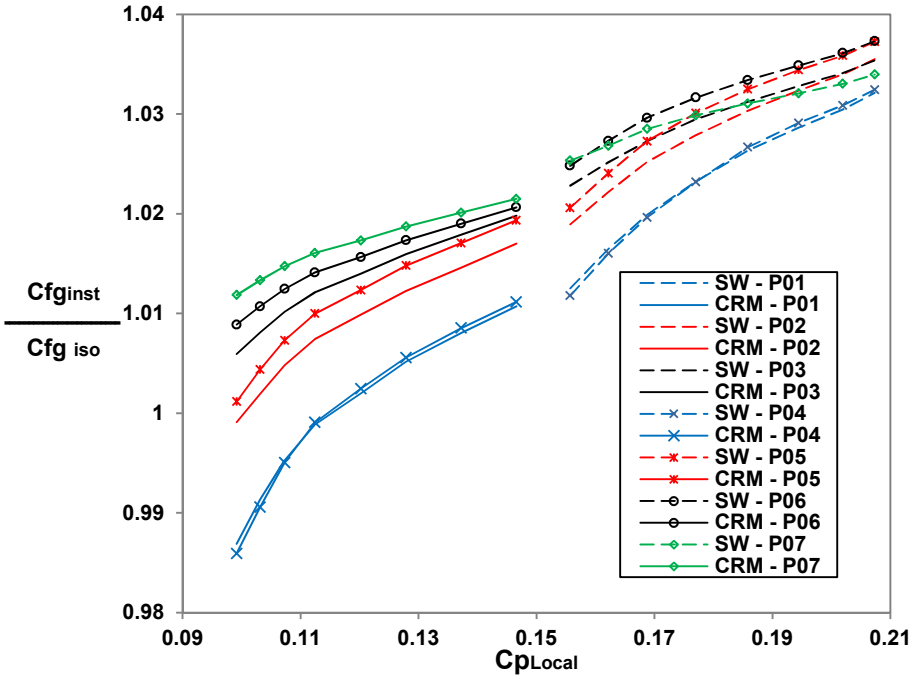

Figure 6.46 Correlation between the local pressure at the cowl trailing edge (Δx =0.15, Δz = 0.05) and the ratio of the installed to isolated engine thrust coefficient, for the SW-nacelle and CRM–nacelle configurations, using thrust definition (1); for the chosen engine position.

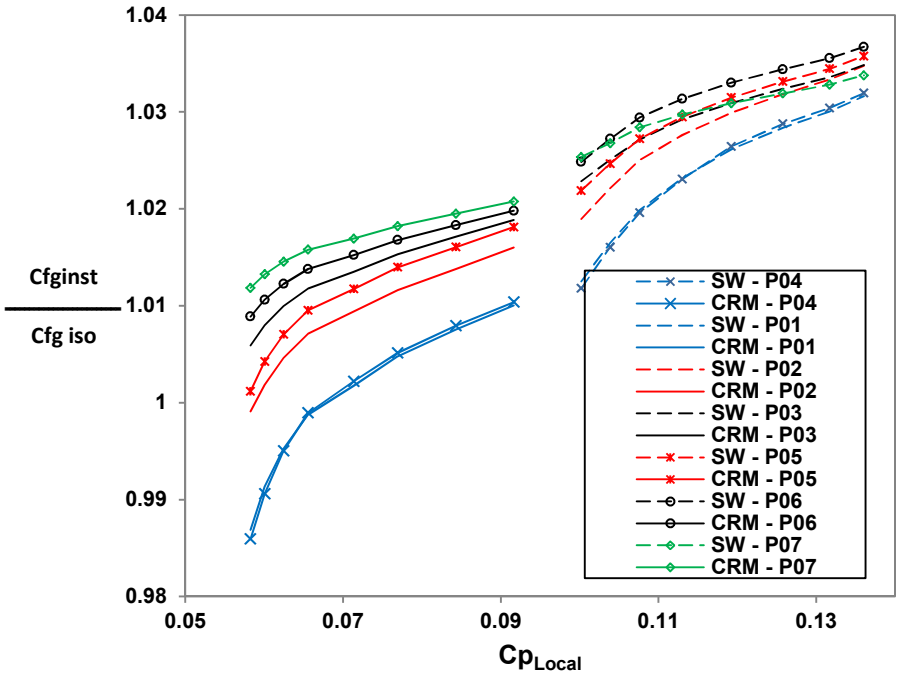

Figure 6.47 Correlation between the local pressure at the cowl trailing edge (Δx =0.25, Δz = 0.05) and the ratio of the installed to isolated engine thrust coefficient, for the SW-nacelle and CRM–nacelle configurations, using thrust definition (1); for the chosen engine position.

6.9 Summary

The tasks and activities of this chapter can be summarised as follows:

a. A computational fluid dynamic (CFD) model was used to calculate the aerodynamic interference impact because of the installation of the aero-engine exhaust-system performance. The numerical scheme was a RANS coupled with k-ω SST turbulence model. The simulations were conducted on SW-nacelle and CRM-nacelle configurations.

b. The result insensitivity to the domain and the mesh was confirmed.

c. The exhaust system performance was measured based on two main thrust definitions. The difference between the two definitions is the inclusion of the fan cowl after-body in the thrust calculations.

d. The drag coefficient decreased with the installation for both configurations, and with the increase in angle of attack, except at low values of $AoA_{A/C}$ for the CRM and nacelle configuration where the drag increases. Moving the engine axially upstream, decreased the drag coefficient, and as a result, the NPF increased.

e. The pressure field of the SW is much stronger than the CRM WB configuration, owing to the two-dimensional flow nature around the SW, as compared with three-dimensional one surrounding the CRM configuration.
f. Correlations between the local static pressure and correction factors of the installation influence show a simplified linear relationship. However, there is a gap between both sets of performance data of the SW and the CRM configurations.
g. These correlations are sufficient to give a rough prediction to the interference impact on the nozzle performance. The only information required is the local static pressure.

7 Enhanced engine performance modelling

The final objective of the research is to modify low-order performance model calculations with the focus on the exhaust system characteristics. The aim is to assess the impact of the primary nozzle geometrical and aerodynamic parameters, such as nozzle pressure ratio (NPR), core-cowl and plug angle (β) and the nozzle contraction ratio CR. Furthermore, to evaluate the impact of the engine installation interference on the engine performance at different engine location and angle of attack ($AoA_{A/C}$), by employing the nozzle performance corrections. A response surface method to produce a relationship between these parameters and the nozzle performance has been developed. This function has been coupled with Cranfield University in-house code (Turbo-Match)[9]. The development and the implementation of this modification are discussed in the current chapter.

7.1 Baseline nozzle performance calculation in Turbo-Match

The nozzle performance representation in Turbo-Match is based on a map of the velocity coefficient (C_v) as a function of the nozzle pressure and the area ratio of a Convergent-Divergent (Con-Div) nozzle, (Figure 7.1). The Con-Div nozzle is recognised by three areas inlet, throat and exit area ($\mathrm{AR} = {}^{\mathrm{A9}}/_{\mathrm{A8}}$). The area ratio of the Con-Div nozzle is the ratio of the exit area to the throat area. The map shows that the entire values of the nozzle coefficient are less than one, and it becomes close to one at small values of the AR (0.8 and 1.0) and nozzle pressure ratio (NPR) close to 3.0.

The utilised procedure of the engine thrust calculations in Turbo-Match is based on the selection of the required performance coefficient (C_v) as a function of the NPR and the AR of the nozzle. The value of C_v is then utilised in the gross thrust calculations, alongside with the ideal mass flow rate, the ideal velocity (calculated at NPR_{crit}) and the static pressure at the nozzle exit (in the off-design conditions).

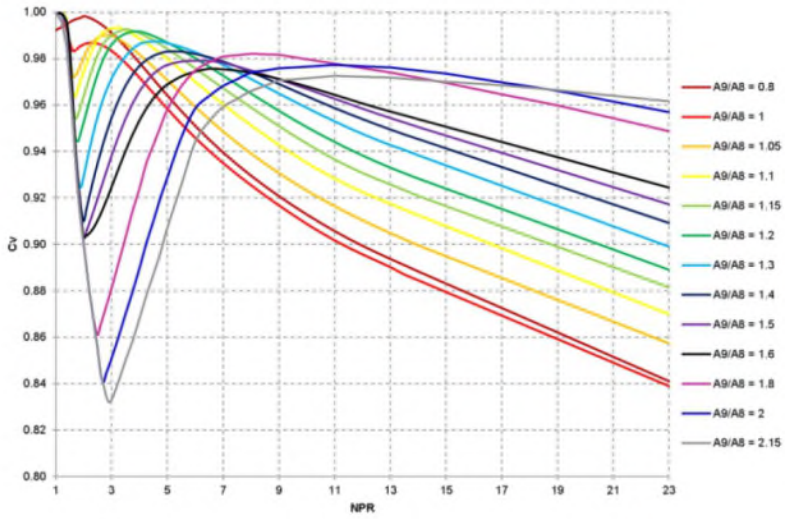

Figure 7.1 Current nozzle velocity coefficient maps as a function of the nozzle pressure ratio for the chosen area ratio; employed in Turbo-Match [9].

To select the required value of C_v, NPR and AR are required. The values of the NPR and AR are called from the main nozzle subroutine. A choosing procedure is then applied to select the value of C_v that corresponds to the imported NPR and AR. In case of lack of C_v data for specific value of the NPR and AR, parabolic and linear interpolations are used to calculate the missing data. The requested value of C_v is then utilised in the evaluation of the engine gross-thrust, (Equation (7-1)). The following roadmap presents the current engine thrust calculation, (Figure 7.2).

$$(F_g)_a = C_v \dot{m_e} V_e + (p_e - p_\infty) A_e \tag{7-1}$$

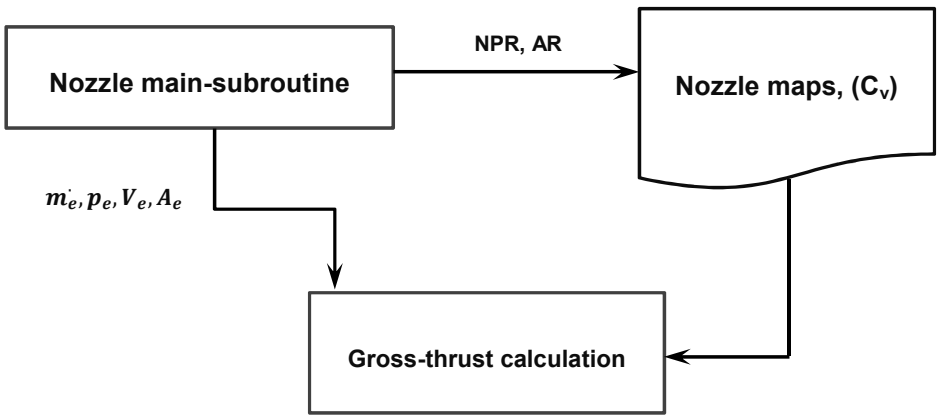

Figure 7.2 Baseline thrust calculation roadmap; performs inside the nozzle Brick (subroutine) in Turbo-Match [9].

7.1.1 Baseline code (Turbomatch) inputs for the nozzle subroutine

Current nozzle user input information is only the identification whether the nozzle exit is variable or a nozzle with the fixed area (convergent nozzle). Therefore, the value of -1.0 stands for the fixed area nozzle and 1.0 for floating exit area nozzle, (Figure 7.3), and the scaling factor.

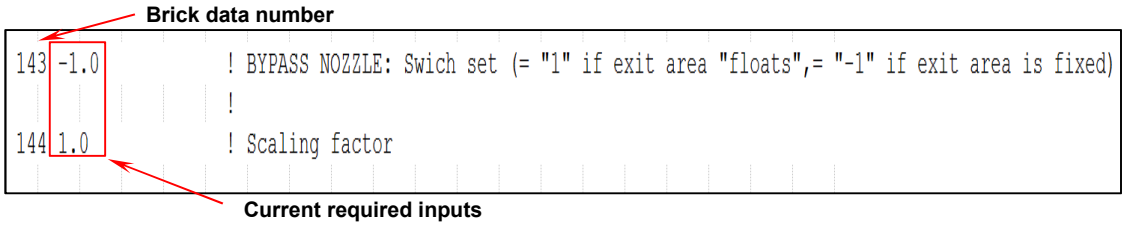

Figure 7.3 Nozzle subroutine inputs in the current performance model input-file.

7.1.2 Baseline code (Turbomatch) outputs from the nozzle subroutine

The main outputs from the nozzle brick are the nozzle area, the exit velocity, the gross thrust of the particular nozzle and the selected thrust coefficient, (Figure 7.4).

```
***** CONVERGENT NOZZLE  1 parameters *****
NCOSF =  0.10000E+01  DGNCOSF =  0.10000E+01
Area =  3.6982          Exit Velocity =  312.98  Gross Thrust = 184417.43
Nozzle Coeff. =  0.98655E+00
```

Figure 7.4 Nozzle subroutine outputs for the current performance model output file.

7.1.3 Limitations

A number of limitations in using the current map of the nozzle performance in the thrust calculations can be categorised as follows:

1. The current nozzle performance maps are based on old empirical data, which they were generated for a single stream nozzle with variable exit area. However, the civil engine has different geometrical features that would affect the nozzle performance significantly, therefore using the performance data of a single-stream nozzle are inconsistent.

2. Since the area ratio (the ratio of the exit area to the throat area) of the convergent nozzle is one, only one degree of freedom that affects the nozzle performance in the current calculations, which is the nozzle pressure ratio. Therefore, the current map is limited to a single nozzle configuration.
3. The current thrust calculation method is insensitive to the flow interaction between the nozzle and the external flow, especially at un-choked nozzle conditions.

7.2 Improved engine thrust evaluation (new nozzle maps implementation)

The new nozzle performance metric maps that are derived from the parameterisation of the nozzle geometric characteristics and the aerodynamic conditions are multidimensional. In other words, the value of the thrust coefficient depends on the contraction ratio (CR), plug half angle (β) and NPR. Because of that, the number of the inputs to the engine performance code had to be increased.

Two sets of maps (basic nozzle and core nozzle) have been generated to represent the nozzle performance calculation in Turbo-Match. The nozzle characteristics are called by selecting the coefficients and interpolating them based on the requested values of the nozzle parameters (geometrical and operational parameters). For the current new maps, two selection procedures and response surface methods (RSM) subroutines were needed to be developed for the bypass and the core nozzle.

The parameterisation of the core nozzle included the variation of the fan nozzle pressure ratio (FNPR). Therefore, the selection method is different from the bypass nozzle one; nevertheless, the RSM is the same. The selection technique of the performance data as a function of the NPR, β and the CR is presented in (Figure 7.5). This procedure is applicable for both nozzles, except for the core nozzle this process has to be repeated for each value of the FNPR, and then a linear RSM is applied to the results.

The parameters that are required to be imported from the main nozzle code is NPR (for each nozzle), β, CR and FNPR (for the core-nozzle maps use only), to extract the nozzle coefficient from the integrated maps in the interpolation subroutine. However, the old code provides NPR and the nozzles' exit area only. Therefore, the value of β was set as a user input to the code by introducing a new Brick data; furthermore, the CR was calculated internally in the main nozzle subroutine, by calculating the inlet area of the nozzle.

To calculate the inlet area, the static inlet conditions have to be available. Therefore, the nozzle inlet Mach number (M_{in}) has to be provided as input to the code by using an extra brick data. It was assumed that the inlet Mach number is within a range between 0.30 to 0.40 as it was advocated by Walsh [122]. However, since the purpose of using this range of M_{in} is to calculate the CR, it has been shifted to higher values (0.35 to 0.45) to match the investigated range of the CR in the current work.

It is worth to be mentioned that even this range of Mach number is flexible because the calculation of the nozzle inlet area is also dependent on the design point calculation of each engine. In other words, this range of M_{in} could be a user selection, depends on the selected design point of the engine.

After that, the nozzle inlet area is calculated by using one-dimensional mass flow rate equation as a function of Mach number and mass flow rate. The CR now is calculated. The FNPR should be taken from the bypass nozzle calculations, therefore; the use of the BP nozzle brick should be performed before the core nozzle during the performance calculations.

Rather than using the same old interpolation method, a Cubic-spline RSM has been employed. The employment of this interpolation method was based on the nature of the data, practically the variation of the nozzle performance coefficient with NPR. Nevertheless, interpolating the data as a function of the CR, β and the FNPR (for the core nozzle), was kept linear as it was found appropriate. Validations exercise will be performed later to assess the performance of the current response surface models.

The nozzle thrust calculations were modified to match the method that has been used to build the new maps. Therefore, a new thrust definition has been used, (Equation (7-2)). This definition includes the momentum flux term only. The pressure-thrust term is calculated during the extraction of the thrust data from the numerical calculations. Therefore, the value of C_{fg} encompasses the variation in the discharge coefficient, the internal losses of the nozzle in addition to the imperfect expansion of the nozzle. The roadmap of the modified thrust calculations is presented in (Figure 7.6).

$$(\mathrm{Fg})_a = \mathrm{C}_{fg}\, \dot{\mathrm{m}}_{\mathrm{i\ nozzle}} \mathrm{V_s} \quad \textbf{(7-2)}$$

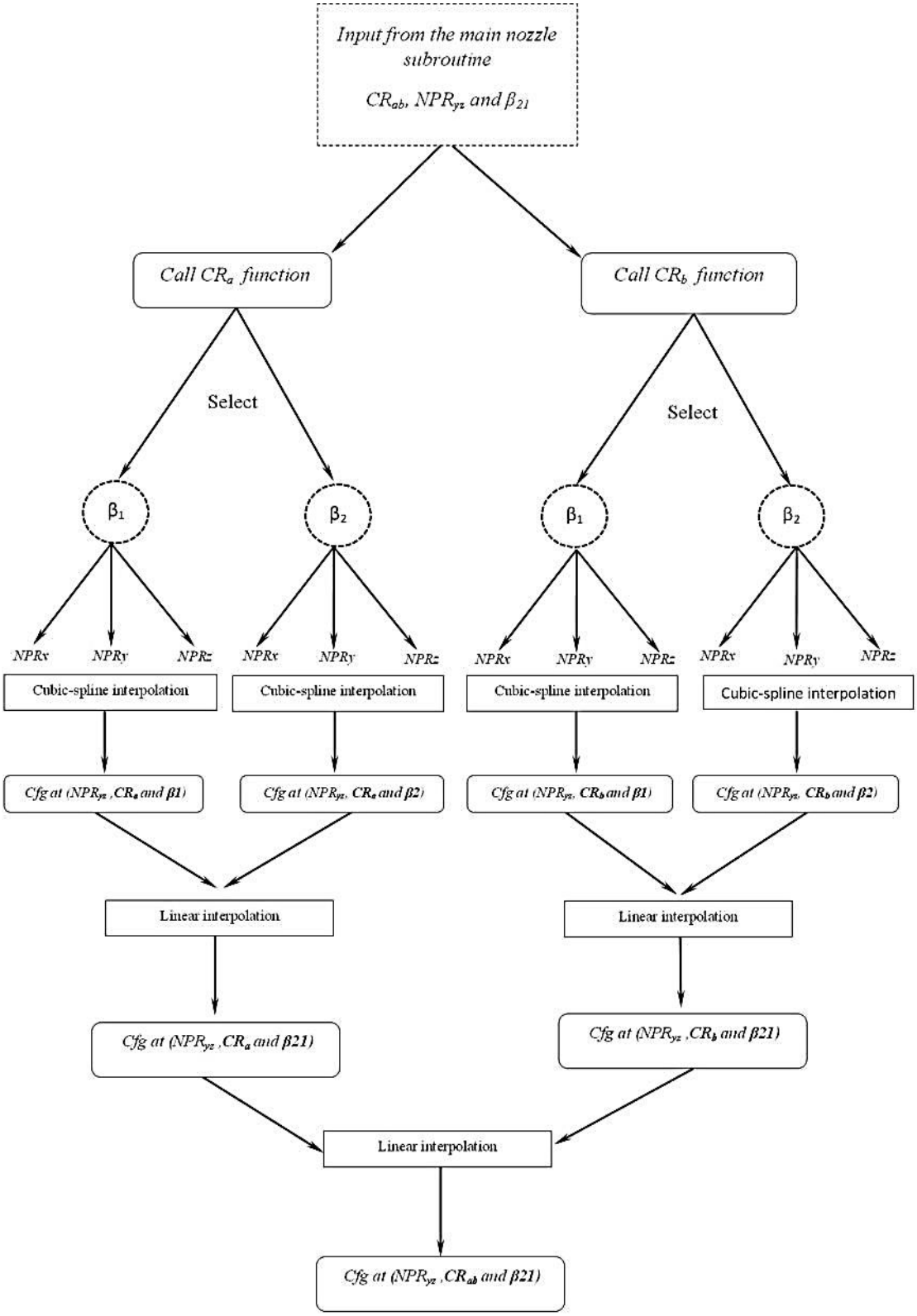

Figure 7.5 Selection procedure of the nozzle performance metric in the new maps as a function of the NPR, CR and β.

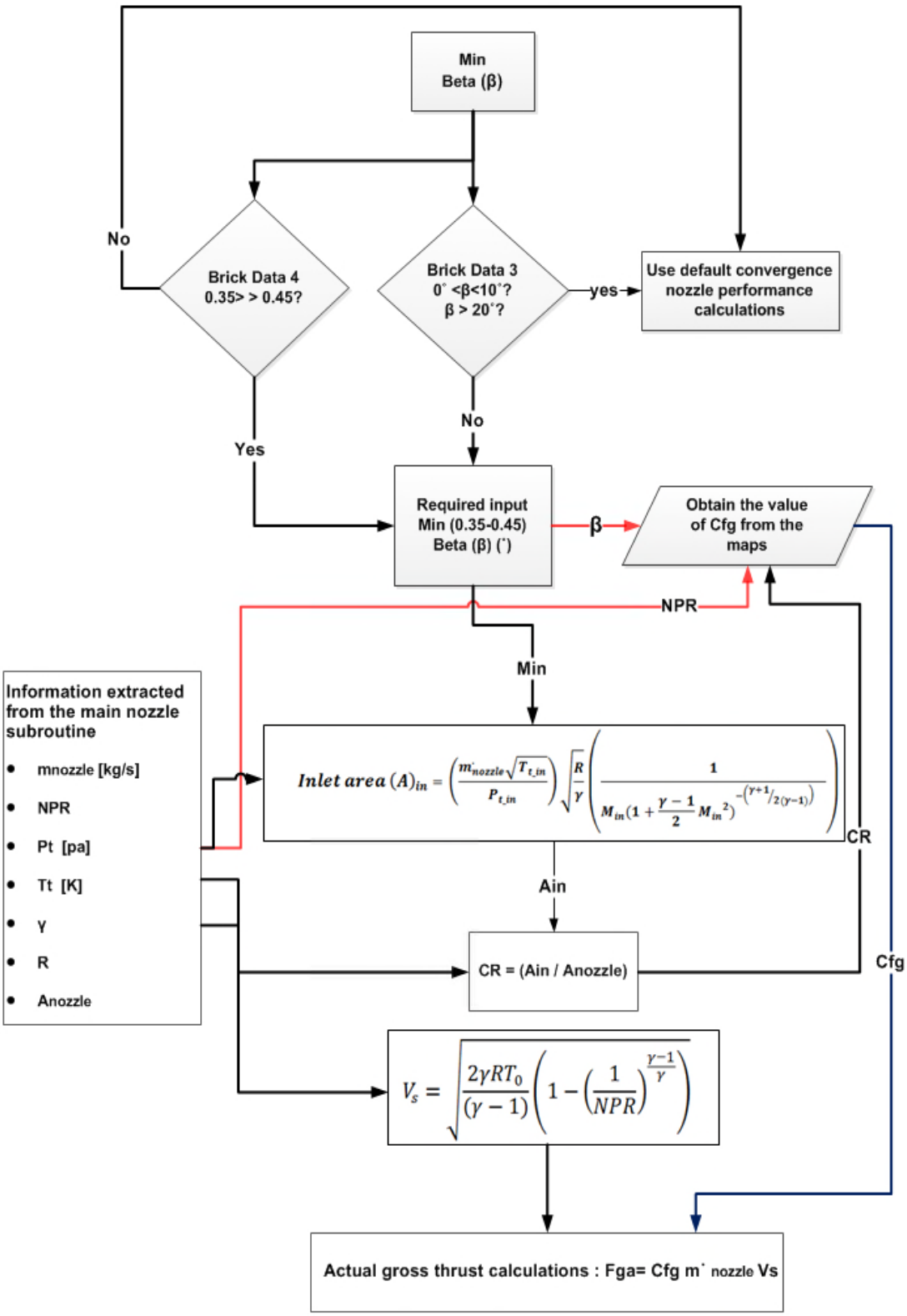

Figure 7.6 Roadmap of the improved thrust calculation.

7.2.1 Validating the response surface methods

The response surface methods (RSM) is used to predict the missing values of particular performance set of data. The performance of the selected RSM has to be assessed. Therefore, a cross-validation method (CV), in particular, Leave-One-Out approach (LOO), is employed, to estimate the test error associated with using a specific interpolation method on a set of observations (calculated nozzle performance data). This approach is performed by holding one data point (test data) out of the observed data (nozzle performance data), and rebuild the prediction model on the rest of the set of the data. Then re-predict the missing data point (test data). The error (or the difference between the predicted C_{fg} and the calculated one from the numerical(CFD) method), Equation(7-3), is then calculated from the original and the newly predict data value [123]. Then the LOOCV estimate is determined by the averaging the errors of all test data points (n), (Equation(7-4) [123].

$$\text{Error} = (y - \hat{y}) \tag{7-3}$$

$$CV_{(n)} = \frac{1}{n}\sum_{i=1}^{n}(y - \hat{y})^2 \tag{7-4}$$

For the current work, a single full column of the data was held out, and the prediction model was rebuilt again. The out taking data column is then re-predicted across each data point of the missing column values. This process is then repeated for each column. The value of the error and $CV_{(n)}$ of the basic-nozzle configuration performance, data and the core-nozzle corrections is presented in (Figure 7.7). The results of the basic nozzle data show that at low NPR (from the first column to the sixth) the error is high and decreases with the increase in the NPR. For the core nozzle corrections data, error values showed high scatter with the variation plug angle. The $CV_{(n)}$for the basic nozzle configuration is $1.7\text{x}10^{-3}$ and for core nozzle performance is $6.0\text{x}10^{-4}$ for the entire test points.

The linear interpolation relates the nozzle performance metrics with β. The results show accurate prediction at small values of β, for both nozzle configurations, (Figure 7.8). However, an increase in the error was observed at large values of β, as an indication of the nonlinear relationship between C_{fg} and β.

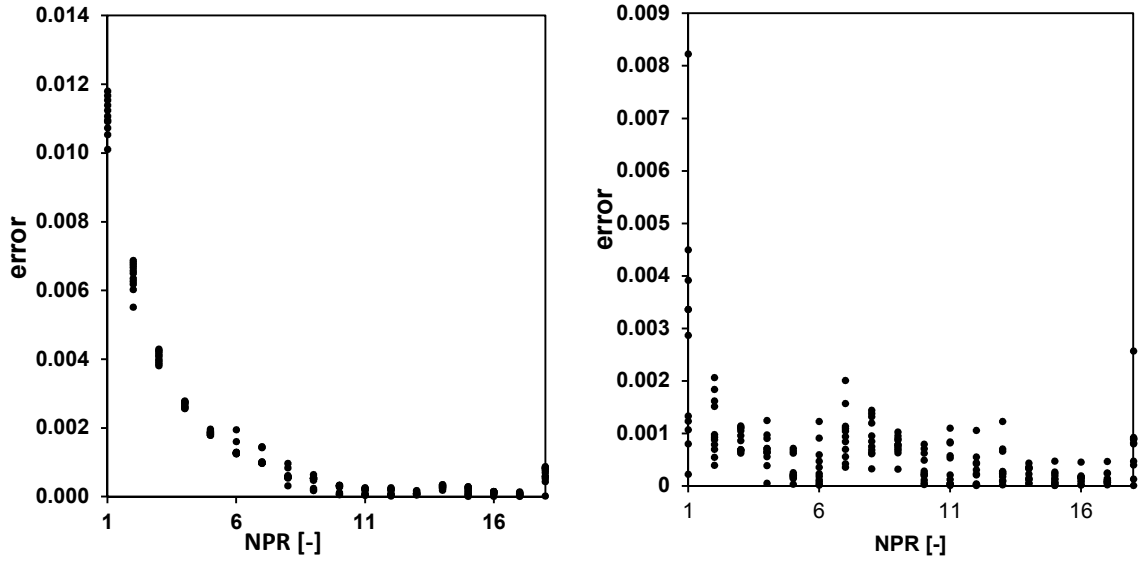

Figure 7.7 Cubic-Spline RSM discrepancy for each data point for the basic and the core-nozzle configuration performance data.

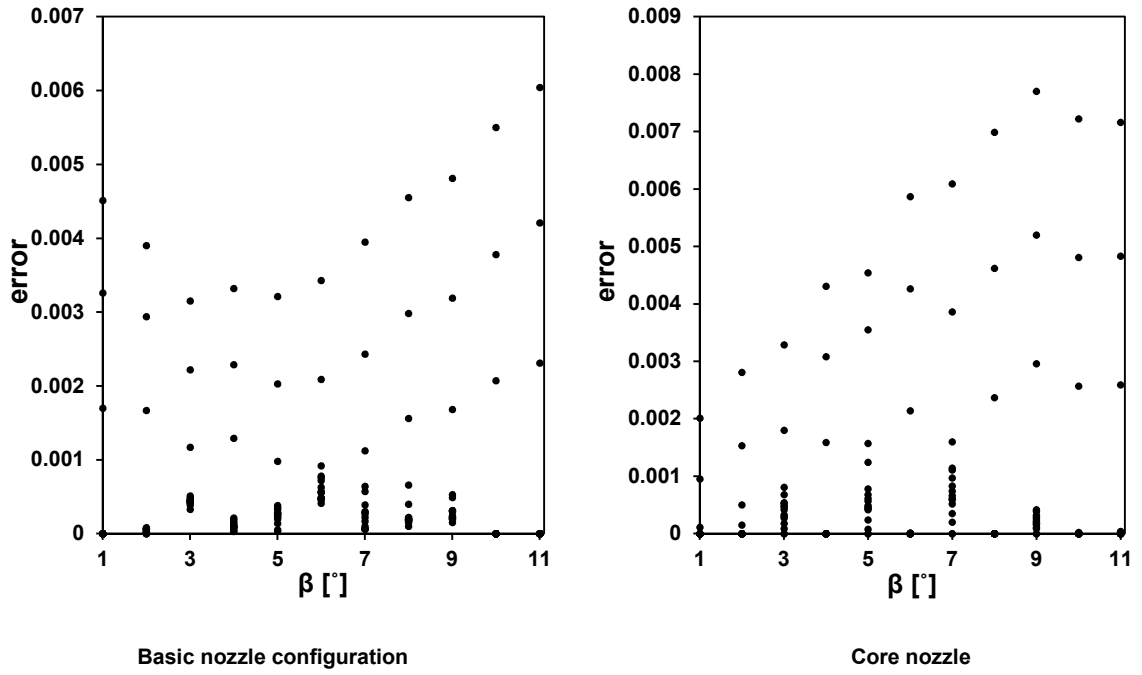

Figure 7.8 Linear RSM discrepancy for each data point for the basic and the core-nozzle configuration performance data.

A correlation between the CFD derived data, and the low order models (RSM) predicted data was built, (Figure 7.9). For the Cubic Spline RSM, it can be seen that the data are correlated very well specifically at high NPR. The Pearson correlation coefficient is one for both nozzle results. This means that they are correlated strongly. For the linear interpolation, the predicted data are very close the calculated one. A notable deviation from the data at large values of β and NPR was observed, (Figure 7.10).

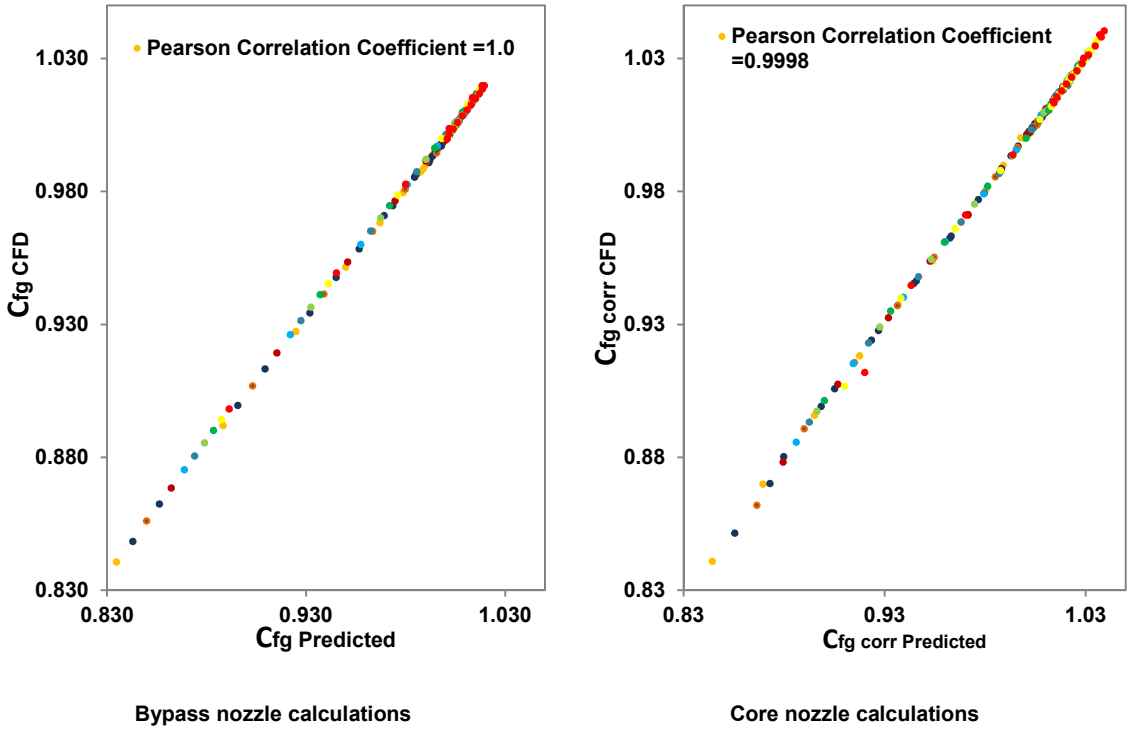

Bypass nozzle calculations

Core nozzle calculations

Figure 7.9 Correlation between the computed and the predicted gross thrust coefficient, using Cubic spline RSM.

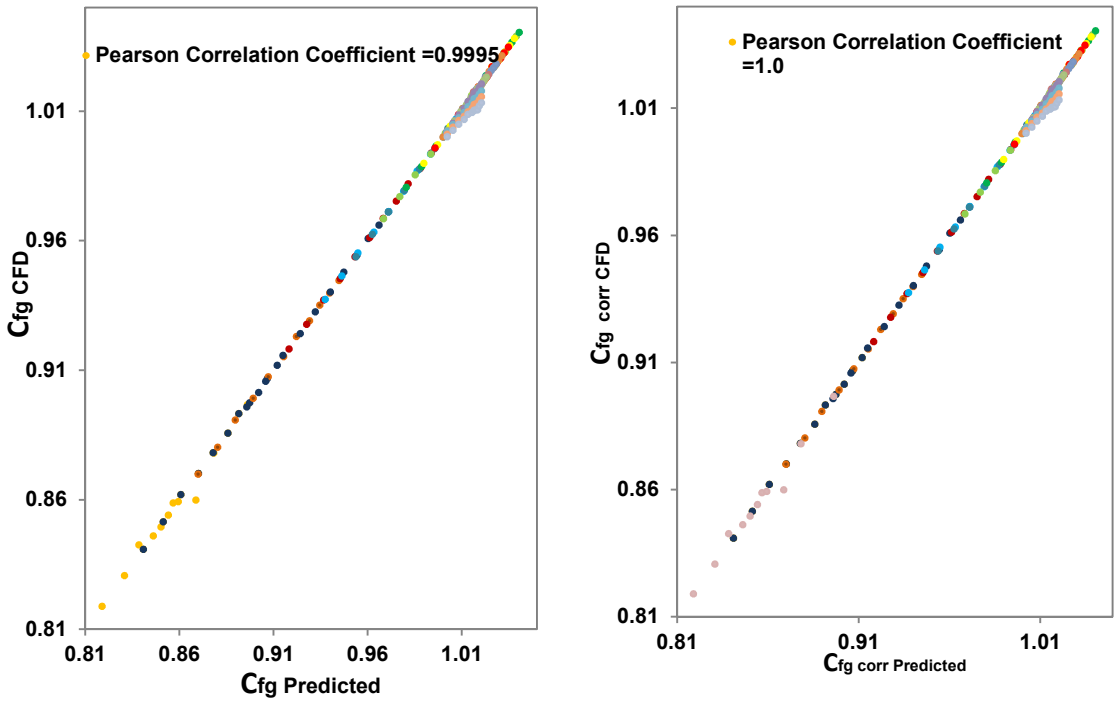

Basic nozzle calculations

Core nozzle calculations

Figure 7.10 Correlation between the computed and the predicted gross thrust coefficient, using linear RSM.

7.2.2 Test cases and results

Sensitivity of aero-engine performance to the exhaust system geometrical features

The new modified performance maps are sensitive to the variation of some of the geometrical and operational parameters of the nozzle. As a result of that, integrating these maps into the thrust calculations in the engine performance model enabled sensitivity of the engine to the nozzle geometrical characteristics. The aero-engine performance, in terms of the gross thrust, became sensitive to the variation of the NPR, β and the engine CR, (Figure 7.11).

Running different engine class across a range of OD (off-design) conditions produced engine performance data as a function of the FNPR and CNPR. The core-cowl angle ($\beta_{c\text{-}c}$) and the plug angle (β_{plug}) of the exhaust system have been varied through each off design point calculation.

The βc-c was changed across a range from 10˚ to 20˚ with an interval of 1.0˚; two β_{plug} levels was chosen and investigated for each $\beta_{c\text{-}c}$. Three different types engine performance were evaluated, Trent 1000, GE90-B85 and CF6-80E1. The reason behind the selection of different engine types is to cover various design point of different engines' bypass ratio.

To produce a range of operating condition for the engine, in other words, different NPR, the turbine entry temperature (TET) were changed. The contraction ratio (CR), on the other hand, was kept constant at its design point values. The CR is not changeable during the off-design calculations. The reason behind that, the nozzle inlet, exit area is sized during the engine DP calculations, and it is used for each off-design conditions. Although β (core-cowl or plug one), is a design parameter of the nozzle, it can be handled easily as it does not correspond to any engine performance parameter.

The implementation of the new performance maps of the nozzle showed that there is an improvement in the thrust at a high value of NPR for all engine types. At low NPR the effect is variable with the engine type, as it can be seen that from Trent 1000 results there is a reduction in the thrust across NPR range from 2.02 to 2.06 for the engine's nozzle configuration of $\beta_{c\text{-}c}$ =10˚ and β_{plug} = 15˚. The estimated difference for this case is about -0.2 kN at FNPR = 2.024 and reduces to -0.1 kN at 2.06. This behaviour is less intense in the GE90 and CF6 engine class as compared with the Trent 1000. This means that the performance model is sensitive to the nozzle aerodynamic and geometric parameters associated with each type of engine. It should be noted that the current results behaviour applies to the present DP calculations of the engines.

The maximum increase in the gross thrust is estimated to be 4.24% for the GE90-B85 engine class when it runs at FNPR 2.86 when both β values are 20˚. However, this is not a typical geometrical configuration for most turbofan engines. The CR, in this case, was kept fixed at values corresponded to M_{in} =0.4.

It should be noted that these curves, in particular, are affected by the behaviour of the code in calculating the engine performance during the OD simulations. In

other words, the iteration process that happens inside Turbo-match during the calculation of the OD performance data affects the value of the predicted gross thrust. It is difficult to avoid this possible error, as the current parameterisation requires OD simulations to handle TET and produces a range of FNPR and CNPR without altering the nozzles' area.

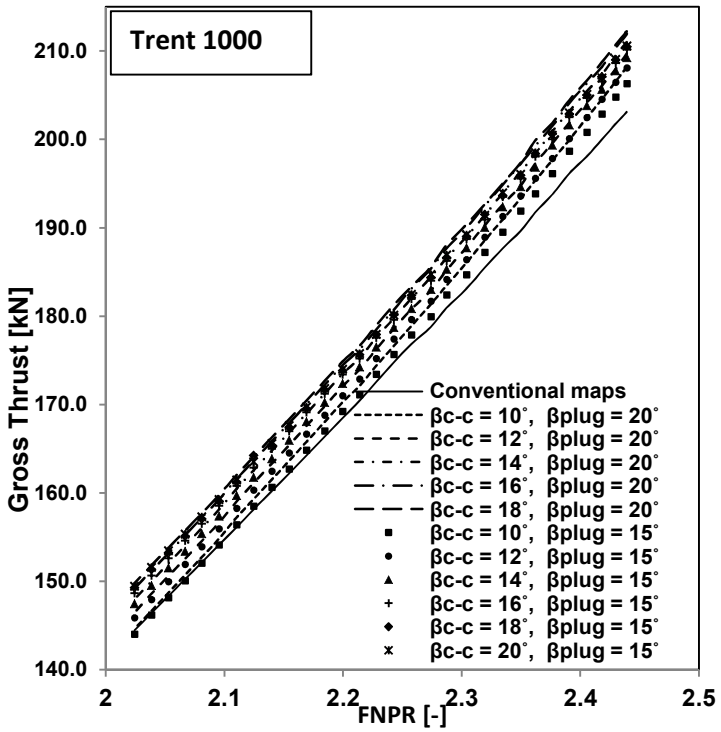

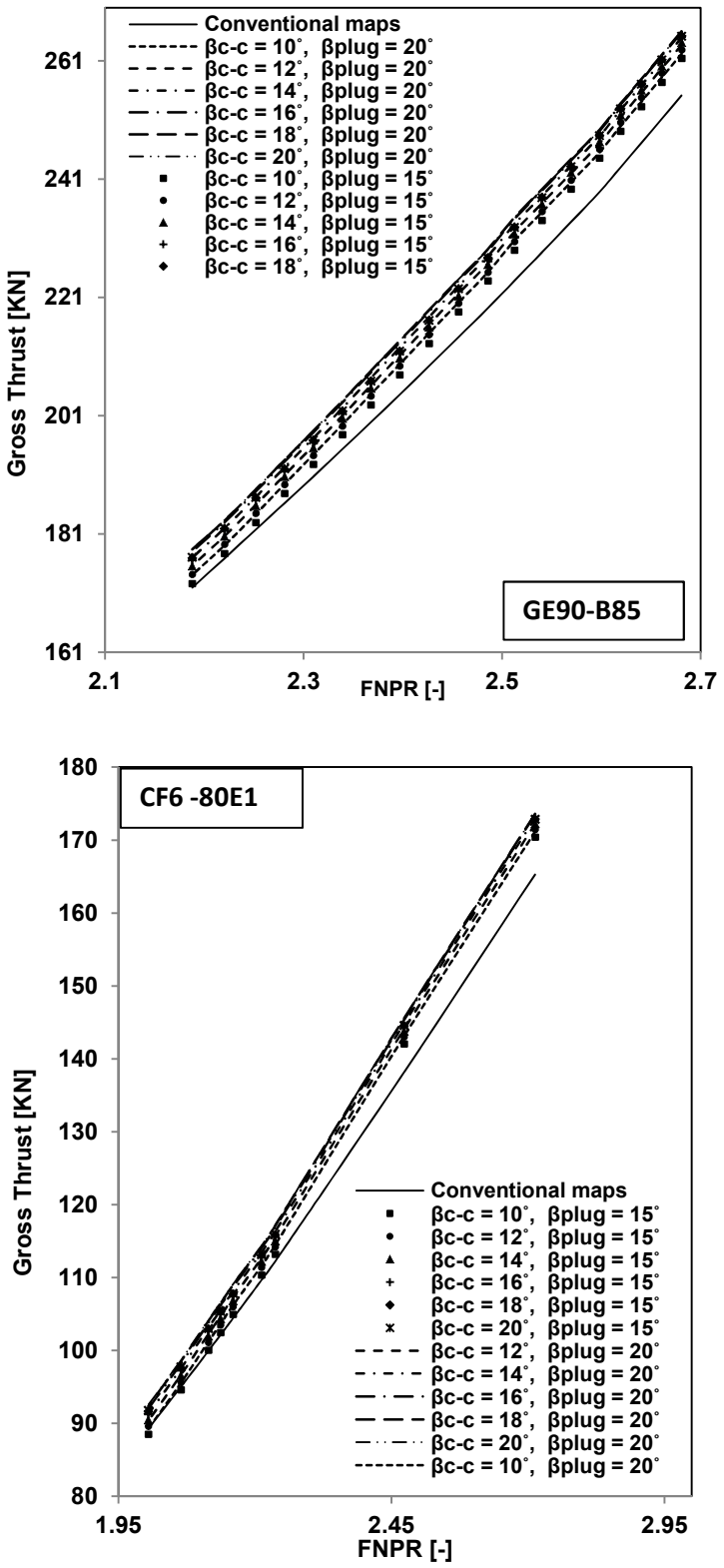

Figure 7.11 Sensitivity of the gross thrust to the variation of the engine power settings and the nozzle geometrical features; running at M_∞= 0.82 and Alt. = 11000 m for three different engine models.

Fortunately, this discrepancy can be avoided during the parameterisation of the nozzle contraction ratio (CR) and core-cowl and plug angle, during the design point calculations. The CR was changed by varying the inlet Mach number (M_{in}) of the nozzle. Three different values were selected to capture the effect of the CR on the engine gross thrust; they are 0.36, 0.4 and 0.45. These values produced a CR for the Trent 1000 of 1.73, 1.6 and 1.45 for the fan nozzle and 1.72, 1.57 and 1.44 for the core nozzle. For the GE90-B85 the CR values are 1.74, 1.6 and 1.44 for the fan nozzle and 1.75, 1.6 and 1.46 for the core nozzle. The CF6-80E1 engine, on the other hand, has a CR of 1.72, 1.6 and 1.45 for the fan nozzle and 1.74, 1.6 and 1.46 for the core nozzle. The gross thrust of the entire engine types increases with the angle of the core-cowl and the plug across the range from 10˚ to 16˚, after that they almost level off, (Figure 7.12). The results show that all the engine types have the same gross thrust behaviour with the variation of the core-cowl and plug angle, in addition to the CR. The gross thrust of the engine increased with the CR. The modified engine performance model shows the importance of considering the combined impact of varying different nozzle geometric and aerodynamic parameters on the intended engine thrust rating.

Since this modification aims to produce an improved nozzle thrust prediction, a comparison was made between three-dimensional CFD simulations results of an isolated nacelle as a representation of the GE90-B85 and the CF6-80E1 engine class and the calculated gross thrust from the improved Turbo-Match. It was found that the gross thrust that is predicted using the new performance maps is higher than the extracted thrust from the CFD calculations by 3.80% for the CF6-80E1 configuration and by 7.0% for the GE90-B85 engine configuration. Although this difference could be considered high if it was integrated to whole flight phase, however, this prediction is close enough to have a clue on the thrust values when the exhaust system components are considered in the calculations.

It should be noted that in addition to the difference in the geometries between the one that used to derive the maps, and the one that used in the three-

dimensional calculations, the effect of the boat-tail angle and internal nozzle profile has to be considered in the one-dimensional calculations. These factors would affect the predicted performance data in the improved Turbo-Match.

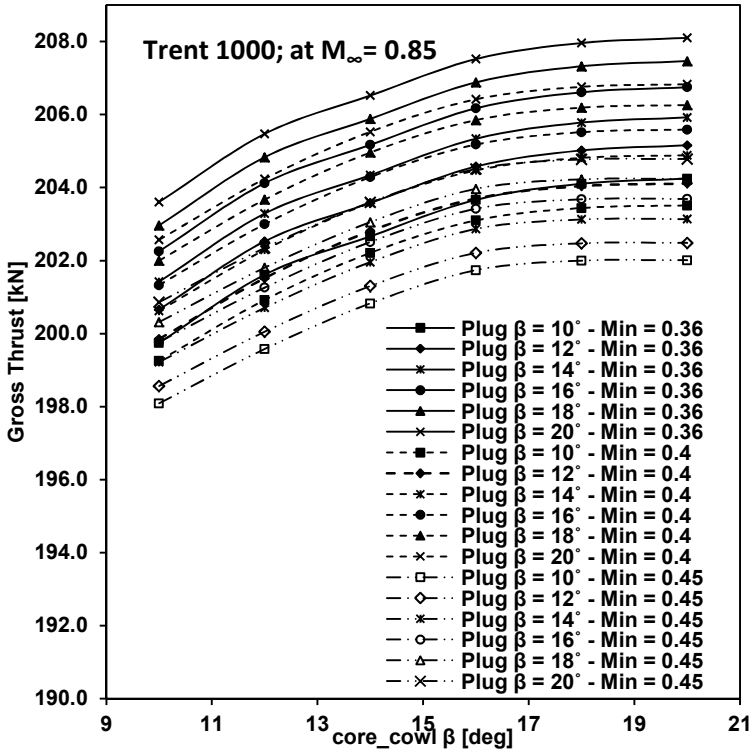

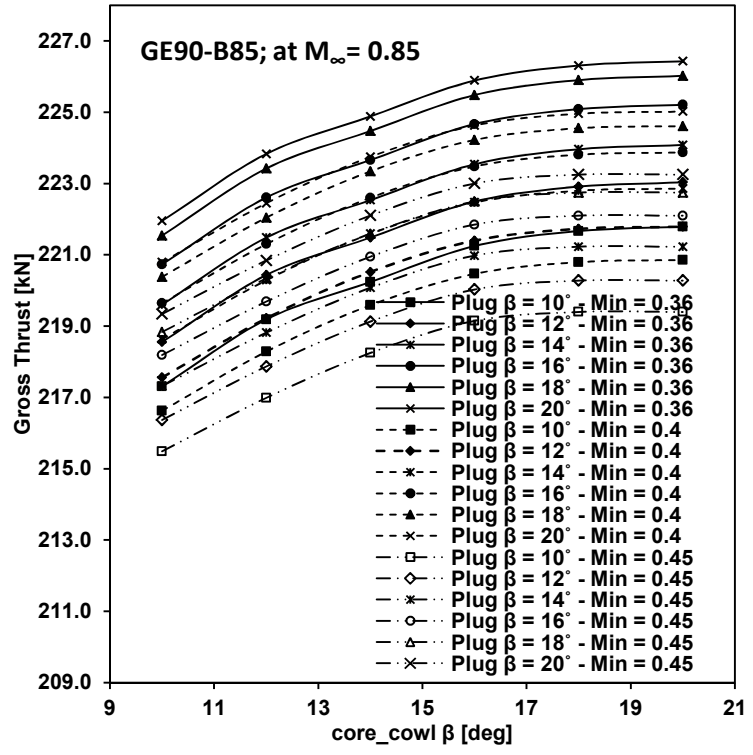

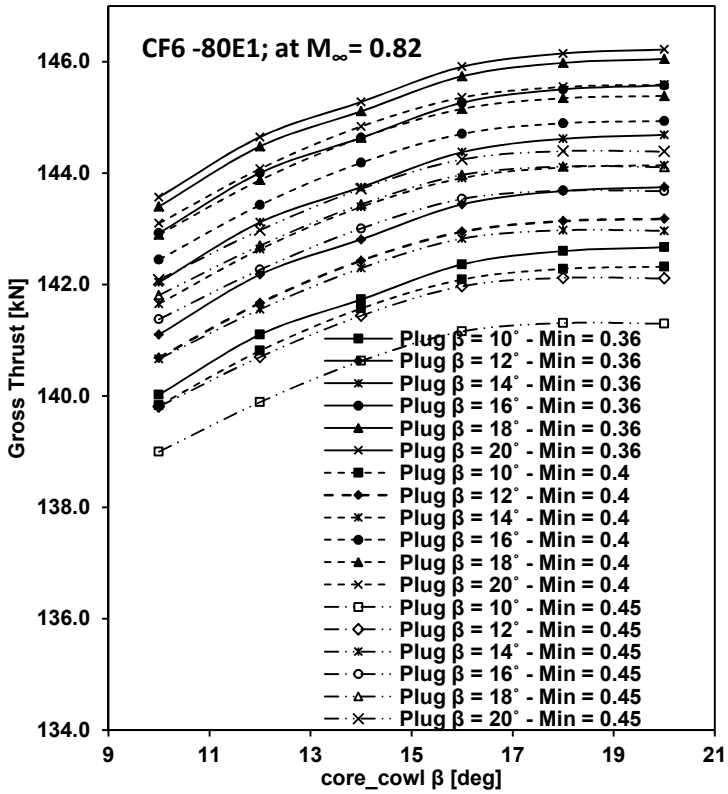

Figure 7.12 Sensitivity of the gross thrust to the variation of the engine power settings and the nozzle contraction ratio (CR); running at Alt. = 11000 m for three different engine models.

7.2.3 Implementation of the new nozzle thrust calculation to design the engine

Introducing the new thrust calculation module into the non-dimensional engine performance model has enabled a parameterisation to the exhaust system, throughout different operational conditions and geometrical features. Therefore, the designer now can simulate different nozzle configurations, for the conventional engine design, to capture the effect of the exhaust system components on the engine design. Because of that, more consistent evaluation of the engine performance is provided.

After the selection of the appropriate angles for the core-cowl and the plug, a redesign process can be done by requesting the required thrust from Turbo-match providing the angles as input. Two scenarios are possible; the first scenario is to run the engine at DP, in this case, the engine size will be changed, in terms of, the intake capacity and the nozzle areas. The second one

is to run the engine at OD, in this case, new throttle settings will be produced regarding the TET and consequently the inlet mass flow and the nozzle pressure ratio will be changed. These scenarios have been applied to the GE90-B85 engine as a case study; the results are presented in (Table 7-1). The angle of the core-cowl was chosen to be 14˚ and 18˚ for the plug nozzle.

Table 7-1 Test cases results of the GE90-B85 engine.

Engine parameters	Old DP	New DP run	New OD run
m_{in} [kg/s]	576	516.06	561.2
TET [K]	1380	1380	1336
FNPR	2.45	2.45	2.43
CNPR	1.91	1.91	1.788
Abp [m^2]	3.7	3.31	3.7
Acore [m^2]	0.8756	0.7845	0.8756

It can be seen that at the DP run, to produce the required thrust a new nozzle area is calculated. The new nozzle area is smaller the conventional one; this means that the new thrust is higher than the current one. Therefore the code scaled it down. This was expected as the new nozzle performance estimation includes the core cowl and the plug contribution to the engine performance. On the other hand, running the engine at OD conditions, requesting the new thrust and setting the TET as a variable, produced a new TET and nozzle operational conditions, keeping the nozzle's size fixed.

For both cases, new engine size is designed, to produce the corrected thrust of the engine. The engine performance was evaluated with the high sensitivity to the aerodynamic and the geometrical parameters of the exhaust system.

To capture the impact of the new calculations procedure on the engine fuel consumption, the nozzle thrust was kept constant, and the SFC of the engine was evaluated. These results are presented for different engine types and geometrical configuration, (Figure 7.13). It can be seen there is an improvement in the engine SFC because of the new thrust calculation method, where the

increase of the core cowl and the plug angles improved the performance of the engine. For the conventional design of the engine with $\beta_{c\text{-}c}$ =14˚ and β_{plug} =18˚, the SFC improved by 10%.

The results highlighted the combined influence of the aerodynamic and the geometric parameters on the predicted performance. Therefore, at some point, there will be degradation in the performance due to the interference impact between the NPR, CR and β. This can be seen clearly in Figure 7.14, in which there is a reduction in the SFC at small levels of β (for the core-cowl and the plug) at low power settings.

Both scenarios gave the same outcome, regarding the SFC, the selection between them is user chose. If resizing the engine is intended then the calculations at DP is appropriate. Retaining the nozzle size fixed and play with the combustion temperature is the objective, then the OD calculations are the one.

To conclude the use of a high degree of freedom nozzle performance maps is essential, to capture the gain and the loss in the thrust due to the flow interaction. The current modified performance module successfully predicted the impact of the investigated geometrical features of the exhaust system on the engine performance.

It should be noted that the baseline Trent 1000 Turbo-Match performance input file was taken from the code engine-library, which is available on the university network.

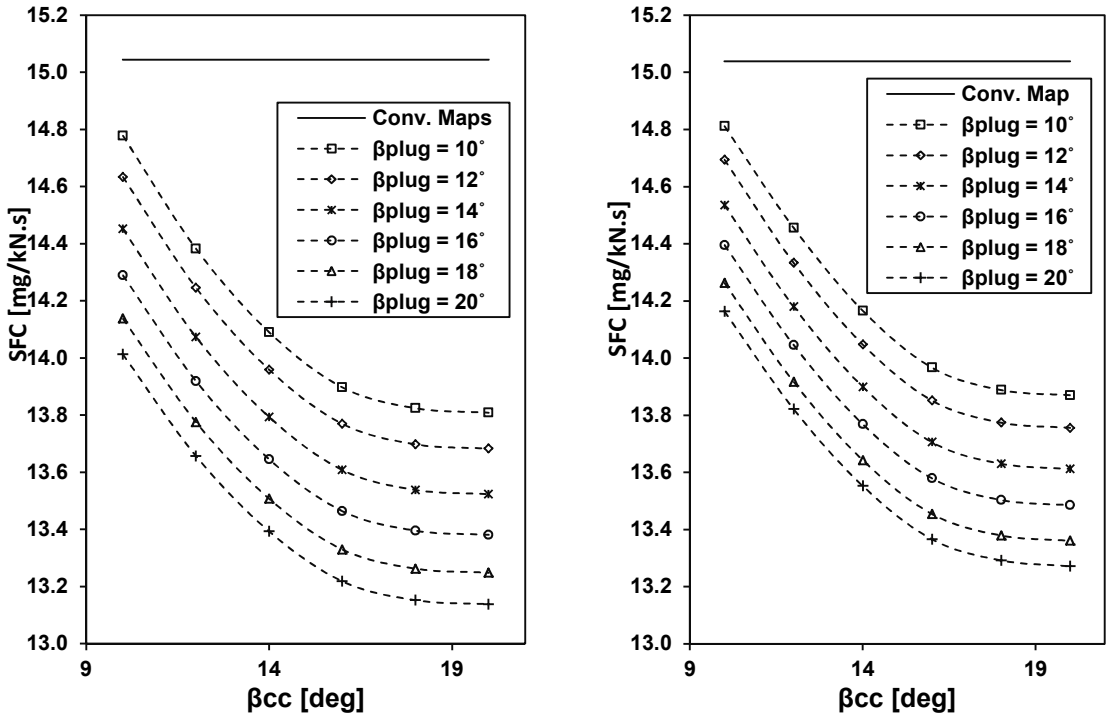

Figure 7.13 SFC comparison between the conventional and the improved thrust calculations as a function of the core-cowl and plug angles, for Trent 1000 engine performance data a thrust rating of 59.7kN; (Left)DP engine run, (Right) OD engine run.

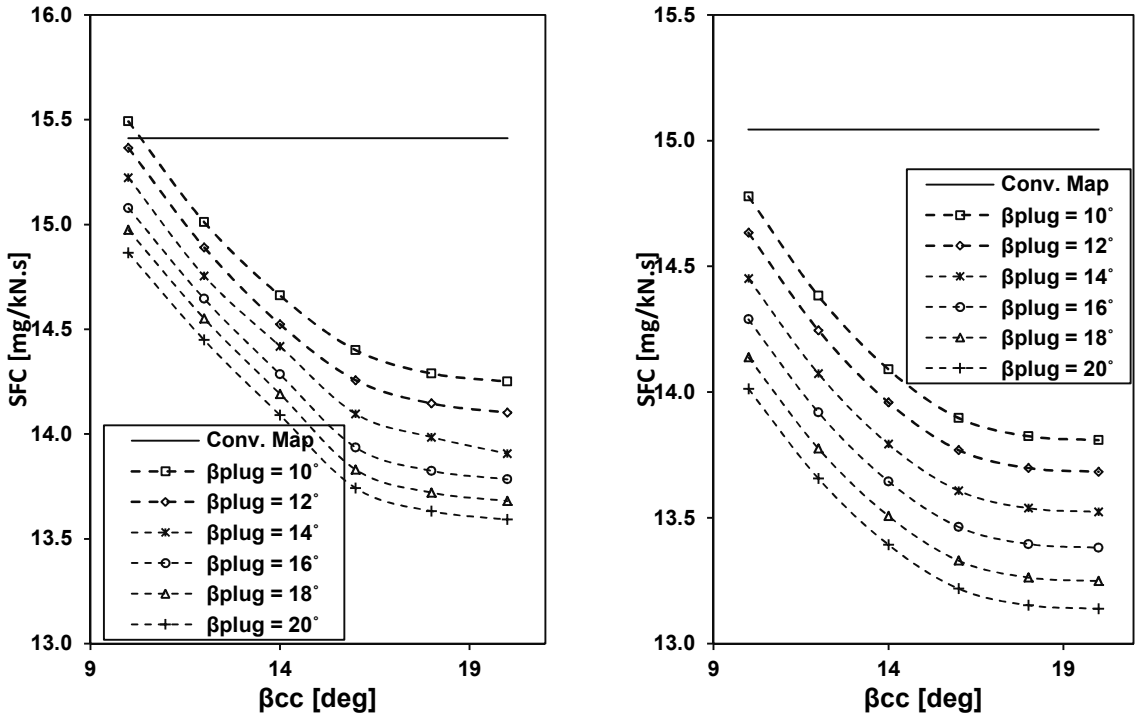

Figure 7.14 SFC comparison between the conventional and the improved thrust calculations as a function of the core-cowl and plug angles, for Trent 1000 engine performance data at thrust rating of 45.7kN; (Left)DP engine run, (Right) OD engine run.

7.3 Improved installed engine thrust evaluation using nozzle performance corrections

Corrections for the nozzle performance coefficients have been derived from the CFD module as a function of the engine location and the angle of attack ($AoA_{A/C}$). The utilised performance coefficients correction data were taken from the CRM-nacelle configuration simulation results. The corrections are represented by the ratio of the installed engine thrust coefficient to the isolated thrust coefficient ($\frac{Cfg_{inst}}{Cfg_{iso}}$) so that the effect of the aerodynamic interference due to the installation on the nozzle is assessed. The current CFD calculations covered the cruise trajectory only.

To have an indication on how the new corrections will affect the installed engine performance throughout all segments of the cruise phase, a low order performance model of an integrated engine aircraft (Hermes[124]) results, was used. This code calculates several aircraft performance parameters. It calculates mainly the installed engine net thrust (Fn) required for a specific aircraft configuration, and the specific fuel consumption (SFC), in addition to the fuel burnt per distance covered, the fuel required for each segment and the distance of each flight trajectory, (Figure 7.15). The most important performance data for the current work is the output values of the net thrust and the distance.

Thrust/engine (kN)	SFC (g/kNs)	segment fuel (kg)	distance (km)	Cum fuel (kg)	Cum distance (km)	LtoDrag ratio	DragCoeff	LiftCoeff	DragCoeffNac
20.4065	14.8330	1.8148	0.6914	1.8148	0.6914	17.6960	0.0340	0.6008	0.0018
20.4061	14.8330	3.6296	1.3829	5.4444	2.0743	17.6959	0.0340	0.6008	0.0018
20.4053	14.8330	3.6295	1.3829	9.0739	3.4572	17.6957	0.0340	0.6008	0.0018
20.4045	14.8329	3.6293	1.3829	12.7032	4.8401	17.6956	0.0339	0.6008	0.0018
20.4037	14.8329	3.6292	1.3829	16.3324	6.2230	17.6954	0.0339	0.6007	0.0018
20.4029	14.8329	3.6290	1.3829	19.9614	7.6059	17.6952	0.0339	0.6007	0.0018
20.4021	14.8329	3.6289	1.3829	23.5903	8.9888	17.6950	0.0339	0.6007	0.0018
20.4013	14.8329	3.6287	1.3829	27.2191	10.3717	17.6948	0.0339	0.6006	0.0018
20.4005	14.8329	3.6286	1.3829	30.8477	11.7546	17.6947	0.0339	0.6006	0.0018
20.3997	14.8329	3.6285	1.3829	34.4761	13.1375	17.6945	0.0339	0.6006	0.0018
20.3989	14.8329	3.6283	1.3829	38.1044	14.5204	17.6943	0.0339	0.6006	0.0018

Figure 7.15 Part of the results file from Hermes.

To modify the current low-order performance model results to capture the aerodynamic interference between the wing and the exhaust system, the ($\frac{Cfg_{inst.}}{Cfg_{iso}}$) correlation, was used. This correlation relates the average local pressure distribution along the front part of the pressure side of the wing ($\overline{Cp}$) and ($\frac{Cfg_{inst.}}{Cfg_{iso}}$).

The use of this correction factor should be performed on the gross thrust calculation so that the requested thrust from the aircraft performance model is corrected. Due to the time frame of the project this model was not integrated into Turbo-Match and Hermes. However, since the current work focuses on the cruise phase only, the calculation can be done simply outside these codes, and the integration of the methodology was left for future work. To do so, some information regarding the aircraft performance (lift-drag polar) and the pressure distributions around the wing are needed. These data were extracted from the CRM configuration CFD results. The aircraft/engine combination that was considered as a test case is the CRM configuration and the GE90-85B engine. However, it could be any engine and aircraft configurations. The method roadmap of the new calculation procedure is shown in Figure 7.16.

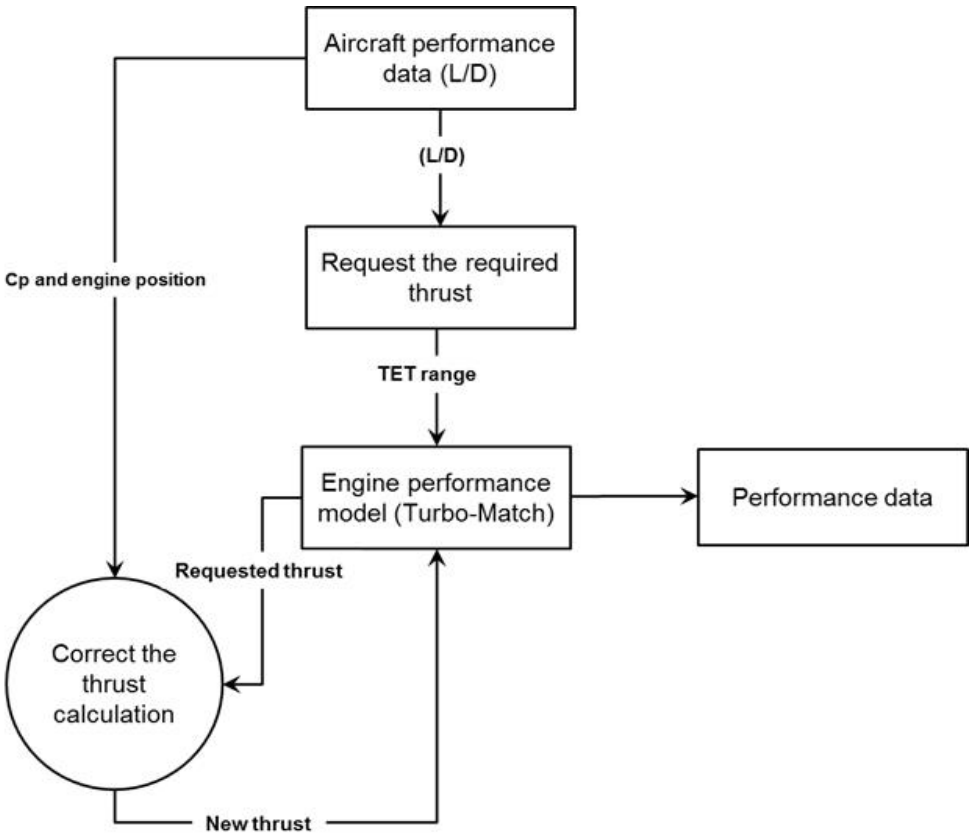

Figure 7.16 Roadmap of the implementation of the nozzle thrust coefficients corrections due to engine installation.

The CRM configuration performance data were determined at the typical cruise conditions of C_L = 0.51 and M_∞= 0.82. This will provide L/D = 21 and full aircraft drag of 99.2 kN. Therefore, each engine has to produce a thrust equivalent to

49.6 kN. To produce the required thrust, the engine was run in OD conditions across a range of TET. It was found that the engine produces the requested thrust at TET = 1254 ˚K and the corresponds to specific fuel consumption of 14.95 (m.g)/(N.s), and gross thrust of 171.765 kN. It should be noted that the altitude is constant at 36,000ft.

The value of $\frac{Cfg_{inst.}}{Cfg_{iso}}$ that corresponds to C_L of 0.51 and engine position at Δx/C =0.05 and Δz/C =0.10 is 1.0046. After correcting, the gross thrust and recalculate the net thrust; it was found that the engine has to produce less thrust by 0.80% than the requested one, because of the impact of the interaction between the exhaust system and the wing. This impact translated as a contribution of the exhaust system components to engine thrust that is represented by ($\frac{Cfg_{inst.}}{Cfg_{iso}}$). The TET was reduced to 1250.2K to achieve the required thrust. However, this is not the case all the time because the installed engine performance is dependent on the engine location and the pressure around the nozzle; therefore, it could be there is a degradation in the thrust due to the installation interference between the wing and the engine.

The inclusion of the thrust coefficient corrections in the thrust calculations, not the full story, the Net Propulsive Force (NPF) evaluation captures the impact of the installation interference on the overall nacelle aerodynamics. Therefore, the engine modified net thrust has to be replaced by the NPF to capture the installation interference effect. The ratio of the NPF to the engine net thrust that corresponds to the given value of the Cp and the engine position is 0.952.

After correcting the requested thrust, the NPF of the current installation aspect was 46.9kN, which represents the actual force that the engine transfers to the airframe. That means the engine loses from its thrust by 5.0% in consequence of the installation, despite the previous improvement in the performance. This value of the thrust that the engine produces is lower than the needed thrust to drive the aircraft. Therefore, the engine has to run at high power settings to recover the loss in the thrust. This value of the NPF should be fed to the engine

performance model to correct the provided thrust values to the aircraft. For this specific case, the engine was needed to be run at higher (TET = 1268.8K).

In conclusion, although at specific engine position and angle of attack there could be an improvement in the performance due to the aerodynamic interaction between the nozzle and wing, the impact of the wing on the nacelle (represented by NPF) could negate this improvement. At the same time, the consideration of the aerodynamic interaction impact on the exhaust system increases the NPF value in comparison with the case that neglects this impact. Therefore, in the previous studies, which they considered the NPF only in the calculation of the installed engine performance, the inclusion of the nozzle correction was necessary, and it would produce different results.

To extend the calculations to the full cruise phase, an analytical model represented by Hermes module was used. In Hermes, there is no information regarding the aircraft angle of attack ($AoA_{A/C}$) and the pressure distributions. Therefore, additional modifications were needed. This was achieved by calling the lift coefficient (C_L) that is calculated in Hermes and used to extract the required angle of attack ($AoA_{A/C}$) for each segment. The $AoA_{A/C}$ values were extracted by using C_L-$AoA_{A/C}$ correlation that can be calculated using a flow solver (in this case Fluent), (Figure 7.17). The extracted values of $AoA_{A/C}$are then used to find the associated value of $\overline{Cp}$ from the correlation in Figure 7.17. The value of $\frac{\mathrm{Cfg_{inst.}}}{\mathrm{Cfg_{iso}}}$ is requested by using the value of $\overline{\mathrm{Cp}}$, from the correlations that were presented in Chapter 6, Section 6.8.5.

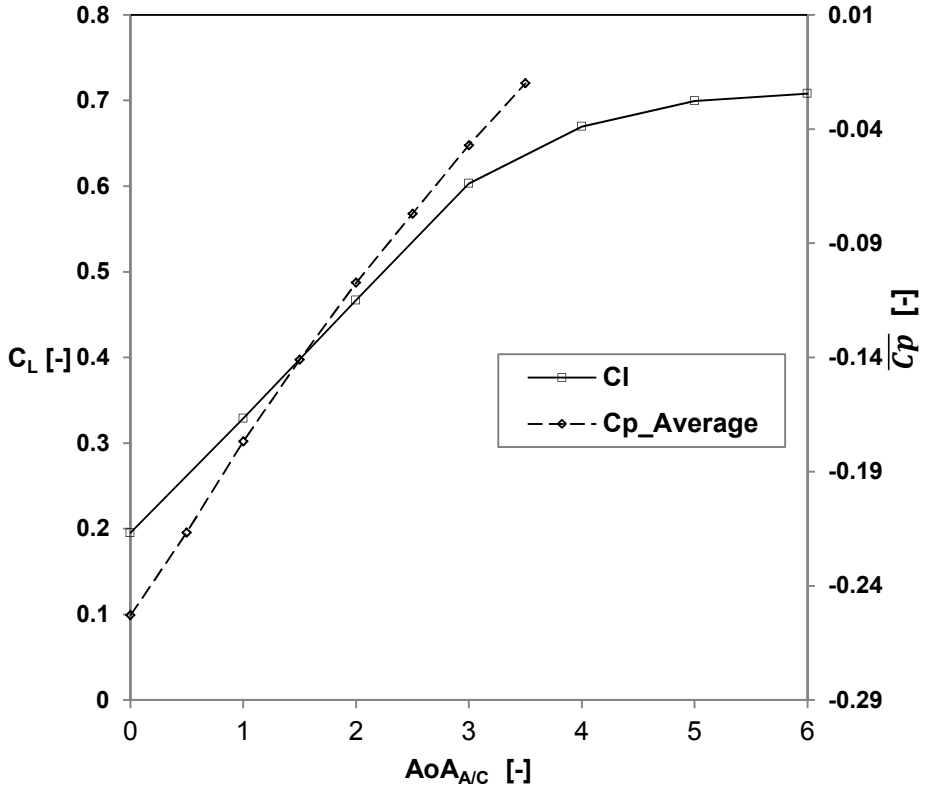

Figure 7.17 Correlation between the average pressure distribution under the wing and the lift coefficient and $AoA_{A/C}$.

Linear interpolation has been used, to determine the missing values of the of C_L, $AoA_{A/C}$, $\overline{Cp}$, and $(\frac{Cfg_{inst.}}{Cfg_{iso}})$. The use of the linear interpolation showed an acceptable prediction for the entire performance data, as that all the correlations are almost linear. Same procedure is followed for the replacement of the net thrust by the NPF. The procedure of the implementing nozzle performance corrections is presented in the roadmap in Figure 7.18.

The engine location had to be imported regarding the axial (Δx/C) and radial (Δz/C) distance between the cowl trailing edge and the wing leading edge. Because of that, the new engine performance results became a function of the$\overline{Cp}$, Δx and Δz.

It should be noted that the current project calculations were not integrated into Hermes main code. The performance data were extracted from the code output file. However, this procedure was found to sufficient for the current project requirements.

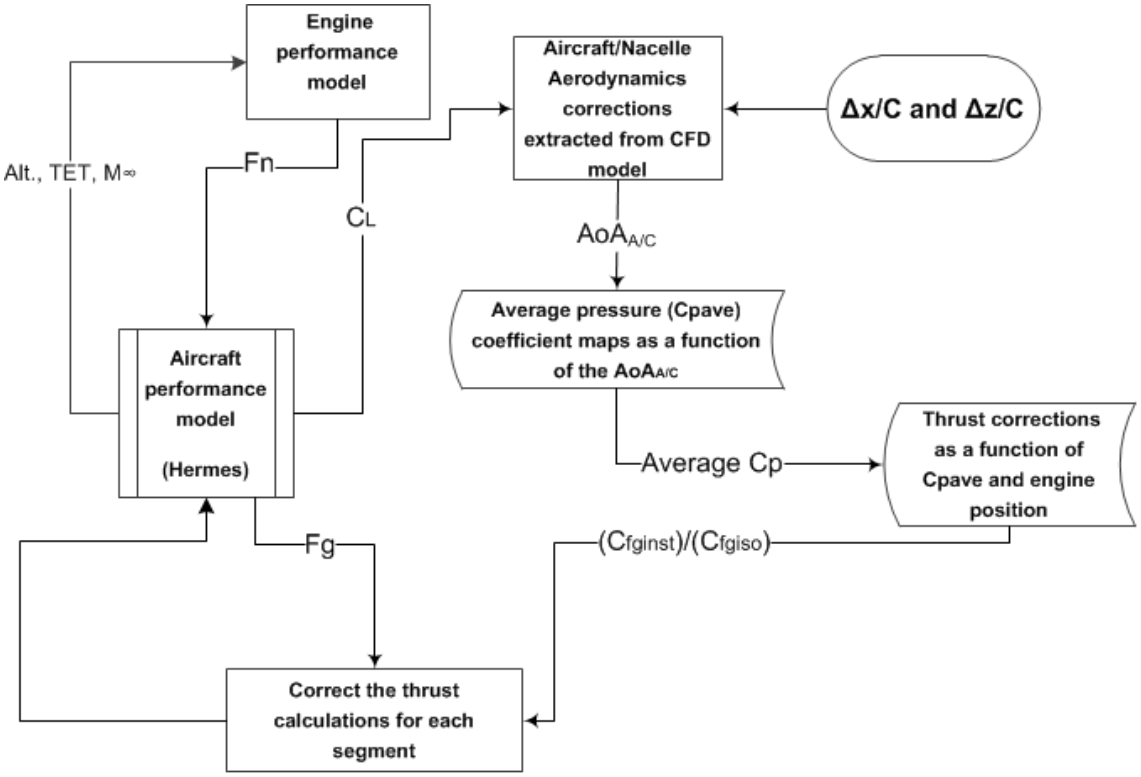

Figure 7.18 Roadmap of the implementation of the nozzle thrust coefficient corrections due to the engine installation interference; using the results of the aircraft performance model.

Test cases

The current modified engine/aircraft performance model was used to recalculate the engine performance after considering the impact of the installation interference on the nozzle performance. Two test cases were used to show the difference in the performance for different configurations, which they are CFM56 engine installed on A320 and B737 aircraft model. The baseline results were taken from [125].

Due to the positive impact of the installation interference on the nozzle performance at high $AoA_{A/C}$, there is an improvement in the engine performance in terms of the net thrust. The estimated improvement in the engine net thrust for the CFM56-A320 configuration is 2.3% at the start of the cruise (SOC) and 2.1% at the end of the cruise, (Figure 7.19).

For the CFM56-B737 configuration, the increase in the net thrust was found to be 2.5% at the SOC and reduces continually to 1.8% at the end of the cruise, (Figure 7.19). It can be seen that the engine performance behaviour is highly

dependent on the type of the engine and the installation aspect. It should be noted that the improvement in the net thrust of the installed engine means that there is an extra thrust generated because of the aerodynamic forces around the engine. This extra thrust means that the engine needs to run at lower power settings than before. As results, there will be an improvement in the engine performance in terms of the flight range.

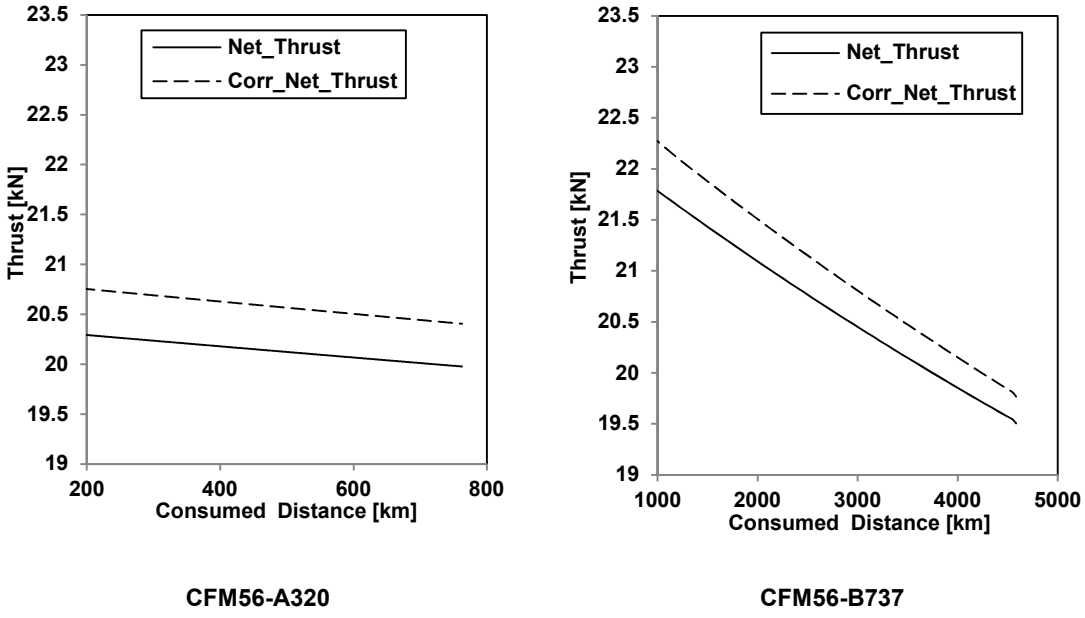

CFM56-A320 CFM56-B737

Figure 7.19 Comparison of the installed engine thrust rating between the conventional and modified engine/aircraft performance model, for two aircraft classes and an engine located at Δx/C= -0.05 and Δz/C = -0.10.

The inclusion of the NPF in the calculation of the engine performance has been modelled previously by [4]. This was performed by replacing the required net thrust by the Net Propulsive Forces (NPF). In this case, the engine/aircraft performance model becomes more sensitive to the engine installation and the size aspects.

The methodology roadmap that is presented in Figure 7.20 shows the current corrections applying procedure. It can be seen that the extracted performance data from the aircraft performance code (Hermes) are corrected by replacing the required net thrust by the NPF_{inst}, throughout the use of the correlation of the $\frac{NPF_{inst}}{F_n}$ that was presented in Figure 7.21. This correlation relates the NPF by the lift coefficient of the aircraft.

Since the aircraft performance code provides the lift coefficient of the aircraft at each flight segment, therefore the $\frac{NPF_{inst}}{F_{nref}}$ was called from the maps for each value of C_L and the engine axial and vertical distance relative to the wing leading edge.

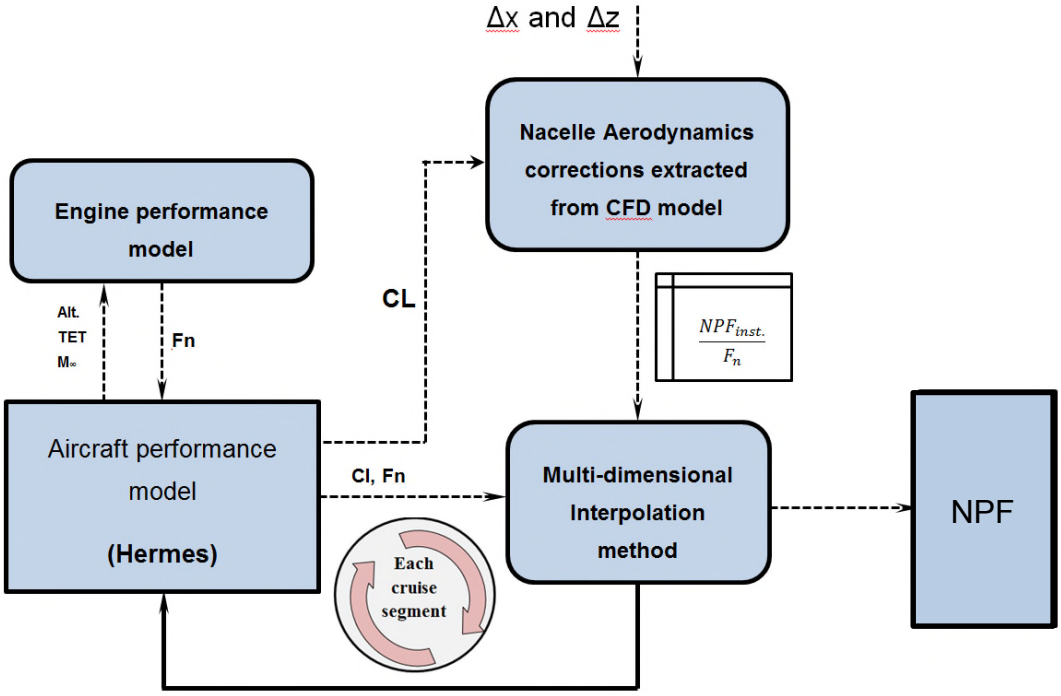

Figure 7.20 Roadmap of replacing the engine net thrust by the NPF for the isolated and installed engine cases.

The NPF_{inst} levels were lower than the net thrust by a range from 0.28% to 0.6%, between the SOC and the end of the cruise segment for CFM56-A320 combination, (Figure 7.21). Moreover, for the CFM56-B737 the results showed an increase in the NPF_{inst} by 0.4% in comparison with the net thrust for the first few cruise segments, (Figure 7.21). The difference between the two aircraft/engine combination results is attributed to the extracted values of $\frac{Cfg_{inst}}{Cfg_{iso}}$ which is highly depended on the operational conditions of the each engine, as it equals to 1.0095 for the CF56-B737 and 1.0075 for the CFM56-A320 configuration, at the SOC. However, CFM56-A320 combination has a higher value of $\frac{Cfg_{inst.}}{Cfg_{iso}}$ at the end of the cruise in comparison with the CF56-B737. That is why it has higher thrust in comparison with the net thrust of the engine at the cruise as it was shown above.

The comparison between the NPF_{inst} data before the inclusion of the nozzle interference corrections and after the consideration of the nozzle corrections highlighted the importance of considers the nozzle interaction with the external flow, (Figure 7.21). It was noted that the inclusion of the nozzle correction factors enhanced the performance. In other words, the use of the modified performance model showed the importance of calculating the aerodynamic interference impact on the nozzle characteristic and combined it with the NPF calculations. The calculation of only one of them (the installed nozzle characteristics or the NPF) will produce under or over prediction to the engine performance.

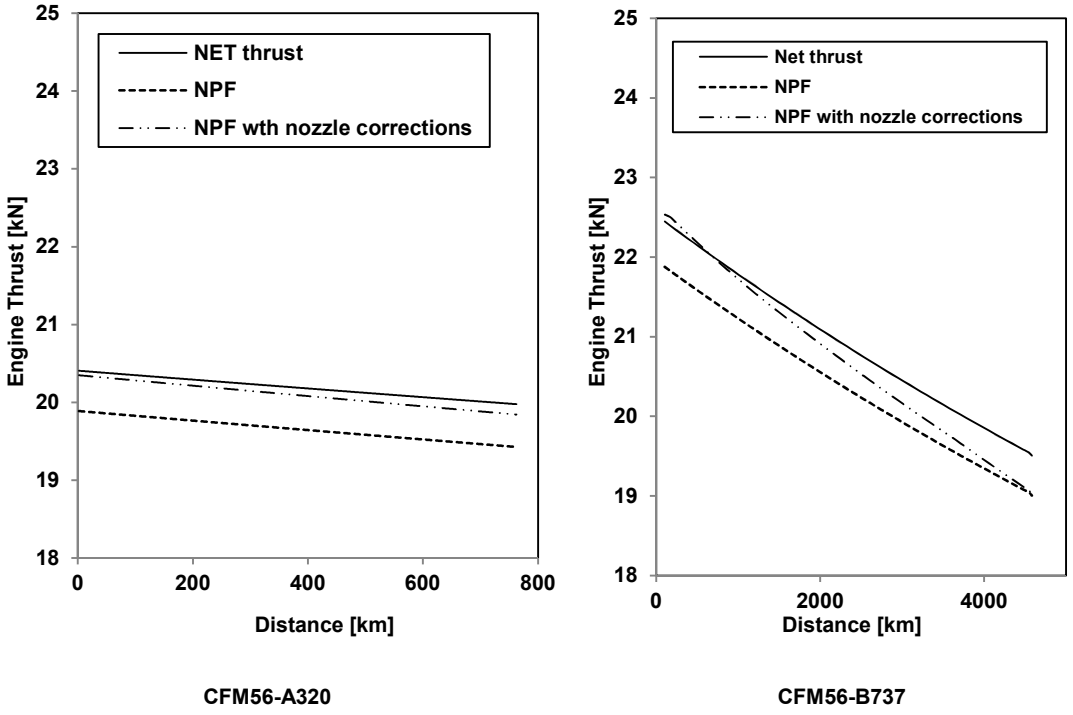

Figure 7.21 Comparison between two configurations performance, in terms of the net thrust and NPF, the engine located at Δx/C= -0.05 and Δz/C= -0.1; for two different aircraft classes.

7.4 Limitations of the new performance model

7.4.1 Engine performance model

1. The new model is applicable for civil engine simulations only.
2. This model is not applicable to the engine with a single stream nozzle and the mixed-nozzle engines.

3. For the bypass and the core nozzle simulations, the new model is limited to a range of NPR from 1.2 to 3.0, and core-cowl and plug-half angles from 10˚ to 20˚.
4. In the case of the core nozzle corrections, the pressure ratio of the bypass nozzle is limited within a range from 2.0 to 2.8.
5. The CR is constrained by the values that were presented in this work. Their values are controlled by changing the value of the inlet Mach number across a range from 0.35 to 0.45.
6. In the case of simulating a number of nozzles more than two, the use of this model is inaccurate, as there is no consideration of the mixing between streams flow of the nozzles.
7. The performance maps are restricted to the current nozzle internal profile and the fan-cowl afterbody angle. However, they still give a correct indication of the behaviour of the nozzle characteristics due to the flow interaction.
8. The performance data cover the cruise flying conditions only.

7.4.2 Engine/Aircraft performance model

1. The performance model is limited to the cruise phase only. The effect of the free stream Mach number and the altitude was not considered.
2. The range of the angle of attack variation is constrained by the range from 0.0˚ to 3.5˚. However, this range was found to be sufficient for the cruise phase.
3. The engine position variation is limited to the range that is presented in this project.

7.5 Summary

The tasks and activities of this chapter can be summarised as follows:

a) A conventional engine performance model was modified to take into consideration the impact of the aerodynamic interaction of the exhaust system components with the external flow.

b) The parameterisation of the nozzle components and their impact on the engine performance was tested and included the core-cowl angle and the plug half angle as well as the power settings.

c) Engine/aircraft performance model data were corrected to consider the installation impact on the nozzle performance as a function of the engine installation aspects and the angle of attack.

d) The use of the numerically derived data and the response surface methods (RSM) to predict the performance of the nozzle is one of the promising methods to modify the low-order model's calculations of the engine performance model.

e) There is an improvement in the engine SFC by 10% at constant thrust rating, when the new maps were utilised.

f) It is important to consider the installation aerodynamic interaction between the wing and the exhaust system of the engine; at the preliminary design stages of a turbofan.

8 Summary and conclusions

8.1 Main achievements

8.1.1 Multidimensional nozzle performance maps

This work provides a new set of performance metrics maps of the nozzle. These maps take into consideration the combined impact of the geometric features and the aerodynamic parameters variation on the performance of the engine. Low-order prediction models for the performance of the nozzle were then built on the architecture of these maps. The low-order model validation showed the suitability in predicting performance across a range of unknown operational and geometrical parameters.

The aerodynamic interference due to the installation between the exhaust system and the wing is now available as a set of corrections as a function of the local static pressure and engine position. These data can be fed into an aircraft performance model to capture the effect of the exhaust system interaction with the freestream flow.

8.1.2 Enhanced engine performance prediction model

Having the maps were developed, a non-dimensional engine performance model calculations can be improved. This model employs the new maps to construct a low-order response surface method (RSM). The RSM is integrative with any engine performance model to increase the sensitivity to the exhaust-system geometrical features. This new capability of the performance model provided a more accurate performance evaluation tool for the civil aircraft engines.

8.2 Conclusions

The use of the open literature nozzle performance characteristics could under-predicts the thrust levels. Furthermore, the newly predicted thrust levels could cause a resizing to the engine components to match the design-point thrust. Therefore, it is essential to consider the impact of the core-cowl and the plug, of

the dual-stream engine during calculations of engine's performance at the preliminary design stages.

To develop these maps, several Computational Fluid Dynamic simulations (CFD) were conducted to cover a range of operational conditions (nozzle pressure ratio) and geometrical features, including the plug angle and the Contraction Ratio of the nozzle. The CFD method has been validated against experimental data with typical discrepancies in the nozzle efficiency across a range from -1.05% at NPR =2.64 to-0.46% NPR =3.14.

The interaction between the pressure field of the wing and the exhaust system of the engine increased the thrust coefficient of the nozzle at high aircraft lift coefficient. This led to the average rise in the installed engine net thrust by 2.15% throughout the cruise phase.

A method of estimating the impact of the installation on the exhaust-system performance was developed. Correlation, which relates the effect of the pressure field of the wing on the exhaust system, was established using CFD model. This correlation can be used to adjust the net thrust of an installed aero engine, which was extracted from Aircraft/Engine performance model.

When the additional drag penalties of the nacelle of the engines were included in modelling the installed engine performance, the net thrust improvements were negated partially. This was captured by considering the impact of the installation interference on the engine performance by replacing the required net thrust of the engine with the Net Propulsive Force (NPF). The NPF, for some installation aspects, was less than the net thrust of the engine by 0.3%; this means that the engine has to run at high power settings to recover the loss in the thrust because of the drag penalty of the nacelle.

The nozzle performance correction and the NPF maps were generated by performing a number of numerical calculations across a range of angle of attack and engine locations. The simulations were conducted for the isolated and installed engine configurations. The numerical model and the mesh were validated against the available experimental data.

In sum, it is important to capture the interaction impact on the exhaust system during the engine design. The response surface methods showed the suitability in doing so. In particular, the cubic spline interpolation method showed validity in predicting the missing performance data that are associated with a specific plug angle and nozzle pressure ratio. Neglecting the installation aerodynamic interference impact on the exhaust system will produce under prediction to the engine performance.

8.3 General conclusion

a) The predicted behaviour of nozzle performance characteristics depends on the combined impact of CR, β and NPR.

b) The nozzle discharge coefficient is highly affected by the variation of the plug-half angle. The choking nozzle pressure ratio reduces with the increase in the cone-cowl half angle.

c) Nozzle backpressure is affected by the variation in the plug half angle.

d) The velocity coefficient reduces dramatically at high nozzle pressure ratio for configurations with plug half angle greater than 15˚.

e) Corrections to the nozzle performance data that consider the flow interaction between the bypass and the core nozzle are established.

f) The core-nozzle discharge coefficient is highly affected by the variation of the fan-nozzle pressure ratio.

g) The inclusion of the fan cowl after-body in the calculation of the nozzle thrust improved the performance at high nozzle pressure ratio.

h) For a particular type of engine/aircraft, C_{fg} was changed by 0.53% across the cruise flight phase owing to the installation.

i) The use of the swept wing configuration as a representation of the pressure impact of the conventional aircraft wing on the engine did not meet the expectation. However, the performance data are promising for future improvements.

j) As the engine is placed axially upstream, the impact of the pressure of the wing on the exhaust-system loses its linearity as a sign of the multi-dimensional effect of the pressure field.

k) The vertical movement of the engine has little impact as long as the engine is placed axially close to the wing, as this impact increases when the engine is located further upstream.

l) The inclusion of the cowl after-body forces in the calculation of the installed engine thrust increased the sensitivity of the nozzle performance to the engine location and angle of attack variation.

9 Suggestions for future work

This chapter includes three main sections as a recommendation for further work that can be carried out based on the findings of the current project. These are:

9.1 More advanced nozzle performance maps

A number of assumptions have been taken place in the current project for the reason of separating the variable that affects the performance and the need for a strike balance between the number of the cases and the timeframe of the project. Therefore, although the new nozzle maps and the installation corrections are considered sufficient, however, they are still limited to a specific range of configurations and operating conditions. Therefore, a number of suggestions can be used as next step to produce more advanced nozzle performance and installation corrections maps, inspired by the findings of the current work.

a) The nozzle parameterisation can be extended to produce high dimensionality maps that consider the impact of the variation of the boat-tail angle alongside with the pug half angle, on the nozzle performance metrics. It should be noted that this task could affect the capacity of the nozzle. Therefore, it should be guaranteed that the nozzle produces constant thrust rating.
b) In this work, the impact of the core nozzle geometrical characteristics on the fan nozzle was considered. However, the impact of the fan nozzle geometrical features on the core nozzle needs to be investigated.
c) A three-dimensional representation for the exhaust-system is required to take into the consideration the impact of the nozzle flow interaction with the pylon on the performance.
d) For the sake of separating the variables, the intake of the engine was eliminated from the proposed nozzle geometry; however, there could be an impact of the intake operating condition on the performance of the nozzle.

e) Although it has a little impact, the consideration of the inlet temperature variation in the calculations will improve the extracted performance data, in which it was assumed to be constant. Moreover, the exhaust gases contents can be represented to capture their effect on the nozzle maps.

9.2 Validation based on the current data

Due to the period of the current project and the lack of reliable experimental data to validate the modified performance model results of the engine, the validation was left for future work. Two procedures can be followed to perform the validation.

9.2.1 Validation based on experimental or in-flight test data

To achieve this task a full engine performance parameters need be available. These performance parameters will be used in the modified engine performance model to produce the performance data of the particular engine regarding the thrust rating and the SFC. The calculated thrust and SFC in addition to the engine nozzle size will be compared with the real-life engine performance data. It should be noted that this task should be performed into two stages; the first is for isolated engine and the second for the installed engine so that the accuracy correction due to the installation can be assessed as well.

9.2.2 Validation based on other numerical calculations or engine performance tools

Although in the current work the results were validated against the numerical calculation of the three-dimensional engine cases, it would be useful to validate the current data with external numerical (CFD) data to confirm the findings. To be sure other validate numerical results that were derived from different CFD tool produces the same data behaviour.

Another comparison can be made with other engine performance models. However, these models to be able to consider the nozzle characteristics into the performance calculations. It should be confirmed that these models use a high fidelity nozzle maps.

9.3 Further work

a) From the results of the current work the core flow is highly affected by the bypass nozzle jet, therefore, the free stream Mach number will have the same impact on the bypass nozzle characteristics. The current maps can be extended to consider a wider range of flight conditions in terms of the free stream Mach number.
b) A three-dimensional parameterisation of the nozzle component (the core-cowl and plug), while the engine is combined with the wing, will provide a highly detailed installed exhaust-system performance maps.
c) In the current project, it was found the impact of the installation on the exhaust system is essential. Therefore, the variation of the Mach number would be of extension for the current correction set.
d) Based on the current project findings, the variation of the vertical position of the engine has a significant impact on the nozzle performance. Therefore, the range of vertical engine position could be extended to cover a wider range.
e) The correlation between the installed nozzle performance corrections that were derived from the engine combined with the infinite swept wing configuration and from the engine and the conventional aircraft configuration can be improved by trying other wing profiles that would produce less pressure impact on the nacelle.
f) The current thrust coefficient correlations that correct the nozzle coefficient due to the installation interference can be integrated into an aircraft performance model to provide the amount of the fuel burnt during each flight phase.
g) The thrust calculation in the selected engine performance model can be improved by including the impact of the free stream Mach number and the angle of attack on the nozzle cha (in three-dimensional cases only).
h) Since the currently proposed response surface methods provided a good prediction to nozzle performance metrics, the new nozzle performance data can be used to build several different response surface methods, such as (kriging), to suit any parameterisation purposes.

REFERENCES

[1] Rudnik, R., Rossow, C., and Frhr, H., ‘Numerical Simulation of Engine/Airframe Integration for High-Bypass Engines’, *Aerospace Science and Technology*, vol. 6, 2002, pp. 31–42.

[2] Burgsmuller, Hoheisel, W.H. and Kooi, J. W., ‘Engine/Aircraft interference on transport aircraft with ducted propfans’, *ICAS*, 1994.

[3] Geyr, H., and Rossow, C., ‘A Correct Thrust Determination Method for Turbine Powered Simulators in Wind Tunnel Testing’, *41st AIAA/ASME/SAE/ASEE Joint Propulsion Conference & Exhibit*, American Institute of Aeronautics and Astronautics, 2005.

[4] Sibilli, T., ‘Modelling the Aerodynamics of Propulsive System Integration at Cruise and High-Lift Conditions’, Cranfield University, 2012.

[5] Christie, R., Ramirez, S., and Macmanus, D. G., ‘Aero-engine installation modelling and the impact on overall flight performance’, *Aerodynamics Specialist Group Conference*, BRISTOL: 2014.

[6] Zimmermann, H., Katheder, K. and, and Jula, A., ‘A numerical investigation into the nozzle flow of high by-pass turbofans’, *International Gas Turbine and Aeroengine Congress and Exposition Cologne*, Cologne, Germany: ASME, 1992.

[7] Mund, F. C., Doulgeris, G., and Pilidis, P., ‘Enhanced gas turbine performance simulation using CFD modules in a 2D representation of the low-pressure system for a high-bypass turbofan’, *Journal of Engineering for Gas Turbines and Power*, vol. 129, 2007, p. 761.

[8] Oates, G. C., ‘Variable Convergent-Divergent Exhaust Nozzle Aerodynamics’, *Aircraft Propulsion Systems Technology and Design*, American Institute of Aeronautics and Astronautics, 1989, pp. 299–336.

[9] MacMillan, W. L., ‘Development of a modular-type computer program for the calculation of gas turbine off-design performance’, Cranfield

University, 1974.

[10] Hunecke, K., *Jet engines : fundamentals of theory, design and operation*, Shrewsbury: Airlife, 1997.

[11] Zucrow, M. J., and Hoffman, J. D., *Gas dynamics*, New York: Wiley, 1976.

[12] ARC Technical Report, *Report of the Definitions Panel on the Definitions of the Thrust of a Jet Engine and of the Internal Drag of a Ducted Body*, C.P. No. 190, London: 1955.

[13] Presz, W. M., 'Computational Requirements for Efficient Engine Installation', *Numerical Methods for Engine-Airframe Integration*, American Institute of Aeronautics and Astronautics, 1986, pp. 169–191.

[14] Seed, A. R., 'Design Techniques for High By-pass Ratio Power Plant Nozzle Systems', *10th International Congress of the Aeronautical Sciences*, Ottawa, Ontario, Canada: National Research Council Canada, 1976.

[15] Lych F.T and Intemann G.A., 'The modern role of CFD in addressing Airframe/Engine integration issues for subsonic transports', *International Council of the Aeronautical Sciences,ICAS*, Spartan Books ; London, 1994.

[16] Minnikasma, B. and Jaarsma, F., 'Jet Interference of a Podded Engine Installation at Cruise Conditions', *Advisory Group for Aerospace Research and Development*, 1975, pp. 5–1.

[17] Salmi, R. J., and Cortright, E. M., 'Effects of external Stream flow and Afterbody Variations on the performance of a plug Nozzle at high subsonic speeds', *NACA Research Memorandum, NACA RM E56F11a*, 1956.

[18] James M. and Cubbage, J., 'Jet effects on the drag of conical afterbodies for Mach numbers of 0.6 to 1.28', *NACA Research Memorandum, NACA RM L57B21*, 1957.

[19] Putnam, W. K. A. and L. E., *Investigation of flow field surrounding circular arc boattail nozzles at subsonic speeds*, NASA Technical Paper 1633, 1980.

[20] Yajnik, K. S., and Mathur, N. B., 'Under expanded jet-free stream interactions on an axisymmetric afterbody configuration', *AIAA Journal*, vol. 28, 1990.

[21] Reubush, D. E, Runckel, J. F., *Effect of Fineness Ratio on Boattail Drag of Circular-Arc Afterbodies having Closure Ratios of 0.50 with Jet Exhaust at Mach Numbers up to 1.30*, NASA Technical Note(TN-7192), 1973.

[22] Wilcox, F. A., Chamberlin, R., Wilcox, F. A., and Chamberlin, R., 'Reynolds Number Effects on Boattail Drag of Exhaust Nozzles from Wind Tunnel and Flight Tests', *Technical Memorandum NASA TM X-71548*, 1974.

[23] William B. Compton III, *An Experimental Study of Jet Exhaust Simulation*, Washington, D.C. 20546: NASA Technical Memorandum, NASA TMX-71975, 1974.

[24] Mathur, N. B., 'Correlation for the Estimation of Afterbody Drag with Hot Jet Exhaust', *Journal of Aircraft*, vol. 35, Nov. 1998, pp. 981–984.

[25] Ashwood, P. F., 'A Review of the Performance of Exhaust Systems for Gas-Turbine Aero-Engines', *Proceedings of the Institution of Mechanical Engineers*, vol. 171, Jun. 1957, pp. 129–158.

[26] Thornock, R. L., and Brown, E. F., 'An experimental study of compressible flow through convergent-conical nozzles, including a comparison with theoretical results', *Journal of Basic Engineering*, vol. 94, Dec. 1972, pp. 926–930.

[27] Brown, E. F., *Compressible Flow Through Convergent Conical Nozzles with Emphasis on the Transonic Region*, University Microfilms, Incorporated, 1974.

[28] DeBonis, J. R., 'Gas Turbine Engines: Nozzles', *Encyclopedia of Aerospace Engineering*, John Wiley & Sons, Ltd, 2010.

[29] Harrington, D. E., *Performance of Convergent and Plug Nozzles at Mach Numbers from 0 to 1.97*, Washington, D. C.: NASA Technical Memorandum-NASA TM X-2112, 1970.

[30] Bergman, D., 'Effects of engine exhaust flow on boattail drag', *8th Aerospace Sciences Meeting*, 1970.

[31] Berrier, B., *Effect of Plug and Shroud Geometry Variables on Plug-Nozzle Performance at Transonic Speeds*, NASA Technical Note,TN D-5098, Washington,D. C: 1969.

[32] Welge, H. R., and Ongarato, J. R., 'Powered Engine Simulator Procedures and Experience of the DC -10 Wing Engine', *Journal of Aircraft*, vol. 8, 1971, pp. 523–529.

[33] Mikkelsen, K. L., Myren, D. J., Dahl, D. G., and Christiansen, M., 'Initial Subscale Performance Measurements of the AIAA Dual Separate Flow Reference (DSFR) Nozzle', *51st AIAA/SAE/ASEE Joint Propulsion Conference*, Orlando,USA: 2015, pp. 1–30.

[34] Hall, B. G. W., Eng, B. S., and Member, P. D. A., 'Application of Boundary Layer Theory to Explain Some Nozzle and Venturi Flow Peculiarities', *Proceedings of the Institution of Mechanical Engineers*, vol. 173, 1959.

[35] Mikkelsen, K. L., and Brasket, R. G., 'An Equation Set for ASME Nozzle Discharge and Thrust Coefficients', *49th AIAA Aerospace Sciences Meeting including the New Horizons Forum and Aerospace Exposition*, 2011.

[36] Olson, A. T., 'Nozzle Discharge Coefficients-Compressible Flow', *Journal of Fluids Engineering*, 1974.

[37] Beans, E. W., 'Relationships for nozzle performance relationships for nozzle performance coefficients', *ASME 79-GT-145*, New York, NY, USA:

1979, pp. 1–7.

[38] L'Ecuyer, M. R., Morrison, J. ., and Mallett, W. E., 'Correlation of Turbofan Engine Thrust Performance with Compound Nozzle Flow Theory', *Journal of Aircraft*, vol. 8, 1971.

[39] Swanson, R. C., *Numerical solutions of the Navier-Stokes equations for transonic afterbody flows*, National Aeronautics and Space Administration, Scientific and Technical Information Branch,Langley Research Center, 1980.

[40] Carlson, J. R., *Computational prediction of isolated performance of an axisymmetric nozzle at Mach number 0.90 [microform] / John R. Carlson*, Hampton, Va. : [Springfield, Va: National Aeronautics and Space Administration, Langley Research Center ; National Technical Information Service, distributor, 1994.

[41] DalBello, T., Georgiadis, N., Yoder, D., and Keith, T., 'Computational Study of Axisymmetric Off-Design Nozzle Flows', *42nd AIAA Aerospace Sciences Meeting and Exhibit*, American Institute of Aeronautics and Astronautics, 2004.

[42] Wehofer, S., and Moger, W. C., 'Transonic Flow in Conical Convergent and Convergent-Divergent Nozzles with Nonuniform Inlet Conditions', *AIAA Joint Specialist Conference*, San Diego, California: American Institute of Aeronautics and Astronautics, 1970.

[43] Malecki, R., and Lord, W., 'Aerodynamic performance of exhaust nozzles derived from CFD simulation', *31st AIAA/ASME/SAE/ASEEJoint Propulsion Conference and Exhibit*, San Antonio, CA: American Institute of Aeronautics and Astronautics, 1995.

[44] Malecki, R., and Lord, W., 'A 2D Duct / Nozzle Navier-Stokes Analysis System For Use By Designers', *31st AIAA/ASME/SAE/ASEEJoint Propulsion Conference and Exhibit*, San Antonio, CA: American Institute of Aeronautics and Astronautics, 1995.

[45] Peery, K., and Forester, C., 'Numerical simulation of multi-stream nozzle flows', *12th Fluid and Plasma Dynamics Conference*, Williamsburg, Virginia: AIAA, 1979.

[46] Forester C K Peery K, 'Numerical Simulation of Multistream Nozzle Flow', *AIAA Journal*, vol. 18, 1980, pp. 1088–1093.

[47] Keith, B. D., Uenishi, K., and Dietrich, D. A., 'CFD-based three-dimensional turbofan exhaust nozzle analysis system', *Journal of Propulsion and Power*, vol. 9, Nov. 1993, pp. 840–846.

[48] Abdol-Hamid, K. S., Uenishi, K., Keith, B. D., and Carlson, J. R., 'Commercial turbofan engine exhaust nozzle flow analyses', *Journal of Propulsion and Power*, vol. 9, May 1993, pp. 431–436.

[49] Ponsonby, L. J. H. and R. E., 'Applications of CFD technology to the design of aircraft propulsion systems', *International council of aeronautical sciences*, Stockholm: 1990.

[50] Lennard, D. J. and W. A. F., 'Performance Improvement Features of General Electric Turbofan Engines', *ASME*, 1982, pp. 1–7.

[51] Lahti, D. J., Dietrich, D. A., Stockman, N. O., and Faust, G. K., 'Application of Computational Methods to the Design of Large Turbofan Engine Nacelles', *AIAA 22nd Aerospace Sciences Meeting*, Reno, Nevada: 1984.

[52] Eltis, E. M. and Wilde, G. L., *The Rolls-Royce RB211 Turbofan Engine*, Lecture in Proceedings, Istitute of Mechanical Engineers, 1974.

[53] Zimmermann, H., Gumucio, R., Katheder, K., Jula, A., and Gmbh, T. M., 'CFD Study of Nozzle Configurations for Ultra-High Bypass Engines', *International Gas Turbine and Aeroengien Congress and Exposition,ASME 93-GT-389*, Cincinnati, Ohio: ASME, 1993.

[54] Dippold, V. F., *Computational simulations of convergent nozzles*, Technical Report, NASA Glenn Research Center, NASA/TM-2014-

218329; E-18926; GRC-E-DAA-TN14457, 2014.

[55] Spotts, N., and Guzik, S., ‘A CFD analysis of compressible Flow through convergent-conical nozzles’, *49th AIAA / ASME / SAE / ASEE Joint Propulsion Conference*, 2013, pp. 1–7.

[56] Zhang, Y., Chen, H., Zhang, M., Zhang, M., Li, Z., and Fu, S., ‘Performance Prediction of Conical Nozzle Using Navier–Stokes Computation’, *Journal of Propulsion and Power*, vol. 31, Apr. 2014, pp. 192–203.

[57] Domel, N. D., ‘Perspectives on Propulsion CFD for Nozzle Applications Relevant to the AIAA Propulsion Aerodynamics Workshop’, *51st AIAA/SAE/ASEE Joint Propulsion Conference*, American Institute of Aeronautics and Astronautics, 2015.

[58] Li, Z., Chen, H., and Zhang, Y., ‘NSAWET Results of the Dual Separate Flow Reference Nozzle from AIAA PAW02’, *51st AIAA/SAE/ASEE Joint Propulsion Conference*, American Institute of Aeronautics and Astronautics, 2015.

[59] Kuchemann, *The aerodynamic design of aircraft : a detailed introduction to the current aerodynamic knowledge and practical guide to the solution of aircraft design problems*, Oxford ; New York: Pergamon Press, 1978.

[60] Hoheisel, H., ‘Aerodynamic aspects of engine-aircraft integration of transport aircraft’, *Aerospace Science and Technology*, vol. 1, Oct. 1997, pp. 475–487.

[61] AGARD, *Engine-Airplane Interference and Wall Corrections in Transonic Wind Tunnel Tests*, London: Advisory Group for Aerospace Research and Development,AGARD-AR-36-71, 1971.

[62] Street, P. G., ‘Thrust Drag Analysis for a Front Fan Nacelle having Two Separate Coaxial Fan Nacelle having Two Separate Coaxial Exhaust Streams’, *Aeronautical Research Council Current Papers Report CP. No. 1311*, 1975.

[63] Williams, D., *Propulsion System Performance and Integration*, Lecture Notes, Cranfield University, 2013.

[64] Goulos, I., Stankowski, T., Otter, J., MacManus, D. G., Grech, N., and Sheaf, C., 'Aerodynamic design of separate-jet exhausts for future civil aero engines, Part 1: Parametric geometry definition and CFD approach', *Journal of Engineering for Gas Turbines and Power*, 2016.

[65] Raney, D. J, Kurn, A. G. and Bagley, J. A., 'Wind Tunnel investigation of Jet Interference for Underwing Installation of High Bypass Ratio Engines', *Aeronautical Research Council Current Papers Report CP. No. 13044*, 1969.

[66] James, C., Patterson, Jr., and Flechner, S. G., 'Jet-Wake Effect of a High-Bypass Engine on Wing-Nacelle Interference Drag', *NASA Technical Note, TN D-6067*, Washington, D. C.: 1970.

[67] CALLAGHAN, J. T., DONELSON, J. E., and MORELLI, J. P., *The Effects on Cruise Drag of Installing Long-Duct Refan-Engine Nacelles on the McDonnell–Douglas DC-8-50 and -61*, NASA CR-121218, 1973.

[68] Harris, A., and Paliwal, K., 'Civil turbofan propulsion system integration studies using powered testing techniques at ARA, Bedford', *13th Aerodynamic Testing Conference*, 1984.

[69] Hoheisel, H., Bütefisch, K.-A., Lehmann, B., Henke, R., and Roscher H.J. Seelhorst, U., '"THE JET BEHAVIOUR OF AN HIGH-BYPASS ENGINE AS DETERMINED BY LDA-MEASUREMENTS IN GROUND TESTS&quot';, *AGARD Conference Proceedings 498 Aerodynamic Engine/Airframe Integration for High Performance Aircraft and Missiles Fluid Dynamics Panel Symposium held in Fort Worth, Texas, US 7th - 10th October, 1991*, 1992.

[70] Smart, A. E., and Mooret, C. J., 'Aero-Engine Applications of Laser Anemometry', *AIAA Journal*, vol. 14, 1976, pp. 363–370.

[71] Bousquet, J., 'Survey of Engine Integration Testing in ONERA Wind

Tunnels', *Reston: AIAA; 2005 Report No.: AIAA-2005-3705.*, pp. 1–12.

[72] Donelson, J E, S. . P., 'Investigation of the Interference Effects of Mixed-Flow Long-Duct Nacelles on a DC-Wing', *NASA Technical Report NASA-CR-159202*, Hampton, Virginia: 1980.

[73] Hoheisel, H., Frhr, H., and Geyr, V., 'The influence of engine thrust behaviour on the aerodynamics of engine airframe integration', *CEAS Aeronautical Journal*, vol. 3, 2014, pp. 79–92.

[74] Gatlin, G., Rivers, M., Goodliff, S., Rudnik, R., and Sitzmann, M., 'Experimental Investigation of the DLR-F6 Transport Configuration in the National Transonic Facility (Invited)', *26th AIAA Applied Aerodynamics Conference*, American Institute of Aeronautics and Astronautics, 2008.

[75] Rivers, M. B., and Dittberner, A., 'Experimental Investigations of the NASA Common Research Model', *Journal of Aircraft*, vol. 51, Jul. 2014, pp. 1183–1193.

[76] Melissa B. Rivers, 'NASA Common Research Model Data' Available: https://aiaa-dpw.larc.nasa.gov/Workshop6/presentations/1_03_Rivers_CRM_DPW6_DC_June2016_v4.pdf.

[77] Rivers, M. B., and Dittberner, A., 'Experimental Investigations of the NASA Common Research Model', *Journal of Aircraft*, vol. 51, 2014, pp. 1183–1193.

[78] National Research Council, *The Influence of Computations Fluid Dynamics on Experimental Aerospace Facilities*, Washington,D. C: 1983.

[79] Korkegi, R. H., 'Impact of computational fluid dynamics on development test facilities', *Journal of Aircraft*, vol. 22, 1985, pp. 182–187.

[80] Johnson, F. T., Tinoco, E. N., and Yu, N. J., 'Thirty Years of Development and Application of CFD at Boeing Commercial Airplanes, Seattle', *16th AIAA Computational Fluid Dynamics Conference*, Orlando,USA: AIAA,

2003.

[81] Riedel, H., Ronzheimer, A., and Sitzmann, M., ‘Analysis of the static pressure distribution on a laminar flow nacelle based on euler calculations and flight measurements’, *Aerospace Science and Technology*, vol. 2, 1998, pp. 129–143.

[82] Rossow, C.-C. and Hoheisel, H., ‘Numerical Study of Interference effects of Wing-Mounted Advanced Engine concepts’, *International Council of the Aeronautical Sciences,ICAS-94-6.4.1*, Anaheim: 1994.

[83] Brodersen, O., and Stuermer, A., ‘Drag prediction of engine-airframe interference effects using unstructured Navier-Stokes calculations’, *19th AIAA Applied Aerodynamics Conference*, 2001, p. 10.

[84] Devine, R., Crawford, B., Benard, E., Cooper, R., and Raghunathan, S., ‘A Computational Investigation of Propulsion Integration’, *AIAA 4th Aviation Technology, Integration and Operations (ATIO) Forum*, Chicago, Illinois: 2004.

[85] Souza, F. J. De, ‘Engine Airframe Integration Studies Using the CFD++ Code’, *18th International Congress of Mechanical Engineering*, Ouro Preto, MG: 2005.

[86] Brodersen, O., ‘Drag Prediction of Engine -Airframe Interference Effects Using Unstructured Navier-Stokes Calculations’, *Journal of Aircraft*, vol. 39, 2002.

[87] Hoheisel, H., Kiock, R., Rossow, C. ., Rozheimer, A., Baumert, W., and Capdevila, H., ‘Aspects of Theortical and Experimental Investigations on Airframe/Engine Integration problems’, *ICAS*, Stockholm: 1990.

[88] Laban, M., ‘AIRcraft Drag And Thrust Analysis (AIRDATA)’, *National Aerospace Laboratory NLR, NLR-TP-2000-473*, National Aerospace Laboratory NLR, 2001.

[89] Oliveira, G. L., and Puppin-macedo, A., ‘Integration Methodology for

Regional Jet Aircraft with Underwing Engines', *41st Aerospace Sciences Meeting and Exhibit, AIAA 2003-934*, Reno, Nevada: 2003.

[90] Palmer, J. R., 'The TURBOMATCH scheme for Gas-Turbine Performance Calculations: Users Guide', 1983.

[91] ESDU 81024, *Drag of Axisymmetric Cowls at Zero Incidence for Subsonic Mach Numbers*, 1981.

[92] Gunston, B., and Group, J. I., *Jane's Aero-engines*, Jane's Information Group, 2011.

[93] Ahmed F. El-Sayed, *Aircraft Propulsion and Gas Turbine*, CRC Press, 2008.

[94] Daly, M., *Jane's Aero-engines*, Jane's Information Group, 2015.

[95] Cumpsty, N. A., *Jet propulsion: A simple guide to the aerodynamic and theormodynamic design and performance of jet engines*, Cambridge: 1997.

[96] ESDU 01012, *Subsonic pressure drag of boat-tails with negligible annular base area in the presence of a central propulsive jet*, 2001.

[97] Schroeder, W. J., and Shephard, M. S., 'A combined octree/delaunay method for fully automatic 3-D mesh generation', *International Journal for Numerical Methods in Engineering*, vol. 29, 1990, pp. 37–55.

[98] ANSYS Inc. (US), 'ANSYS ICEM CFD User Manual', *ANSYS, Inc.*, vol. 15.0, 2013.

[99] Nigel P . Weatherill , Bharat K . Soni, and J. F. . T., *Handbook of Grid Generation*, CRC Press, 1999.

[100] Roache, P. J., 'Quantification of uncertainty in computational fluid dynamics', *Annual Review Fluid Mechanics*, 1997.

[101] Menter, F. R., 'Two-equation eddy-viscosity turbulence models for engineering applications', *AIAA Journal*, vol. 32, Aug. 1994, pp. 1598–

1605.

[102] ANSYS Inc. (US), ‘ANSYS Fluent Theory Guide’, vol. 14.0, 2013.

[103] Versteeg, H. K., and Malalasekera, W. ., *Introduction to Computational Fluid Dynamics*, Edinburgh: Pearson Education Limited, 2007.

[104] Zikanov, O., *Essential computational fluid dynamics*, John Wiley & Sons, INC., 2010.

[105] Farokhi, S., *Aircraft propulsion*, Wiley, 2014.

[106] Greitzer, E. M., Tan, C. S., and Graf, M. B., *Internal Flow: Concepts and Applications*, Cambridge: Cambridge University Press, 2004.

[107] Mattingly, J. D., and Ohain, H. Von, *Elements of propulsion : Gas turbines and rockets*, American Institute of Aeronautics and Astronautics, 2006.

[108] Mattingly, J. D., Heiser, W. H., and Pratt, D. T., *Aircraft Engine Design*, American Institute of Aeronautics and Astronautics, 2002.

[109] Covert, E., *Thrust and Drag: Its Prediction and Verification*, UK: Cambridge University Press, 1985.

[110] MIDAP Study Group, ‘Guide to In-Flight Thrust Measurement of Turbojet and Fan Engines’, *Advisory Group for Aerospace Research and Development, AGARD-AG-237*, London: 1979.

[111] Stankowski, Tomasz P., MacManus, David G., Sheaf, Christopher T. and Grech, N., ‘Aerodynamics of aero-engine installation’, *54th AIAA Aerospace SciencesMeeting*, San Diego, California, USA: 2016, pp. 2673–2692.

[112] Spalart, P., and Allmaras, S., ‘A one-equation turbulence model for aerodynamic flows’, *30th Aerospace Sciences Meeting and Exhibit*, American Institute of Aeronautics and Astronautics, 1992.

[113] Launder, B. E. and Spalding, D. B., *Lectures in Mathematical Models of Turbulence*, . Academic Press, London, England, 1972.

[114] Harrington, D. E., ‘Jet effects on boattail pressure drag of isolated ejector nozzles at Mach numbers from 0.60 to 1.47’, *NASA TECHNICAL MEMORANDUM ,TM X-1785*, 1969.

[115] Kulfan, B., and Bussoletti, J., ‘“Fundamental” parametric geometry representations for aircraft component shapes’, *11th AIAA/ISSMO Multidisciplinary Analysis and Optimization Conference*, Seattle, Washington: American Institute of Aeronautics and Astronautics, 2006, pp. 547–591.

[116] Albert, M., and Bestle, D., ‘Aerodynamic design optimization of nacelle and intake’, *ASME Turbo Expo 2013: Turbine Technical Conference and Exposition GT2013*, San Antonio, Texas, USA: 2016, pp. 1–8.

[117] Ramakrishnan, K., and Ragothaman, S., ‘Development of a Common Research Model for Applied CFD Validation Studies’, *26th AIAA Applied Aerodynamics Conference*, Hawaii: 2008, pp. 216–228.

[118] Melissa Rivers, ‘NASA Common Research Model’ Available: https://commonresearchmodel.larc.nasa.gov/.

[119] Oliveira, G., Trapp, L. G., and Puppin-Macedo, A., ‘Engine-Airframe Integration Methodology for Regional Jet Aircrafts with Underwing Engines’, *41st Aerospace Sciences Meeting and Exhibit*, 2003.

[120] Tomasz P. Stankowski David G. MacManus, C. T. S. and N. G., ‘Aerodynamic Interference for Aero-Engine Installations’, *54th AIAA Aerospace Sciences Meeting*, 2016.

[121] Stańkowski, T. P., Macmanus, D. G., and Kolovos, I., ‘Engine installation module development for an aircraft mission analysis framework’, *RAeS*.

[122] Philip P. Walsh, P. F., *Gas Turbine Performance*, John Wiley & Sons, Ltd, 2008.

[123] Casella, G., Fienberg, S., and Olkin, I., *An Introduction to statistical learning*, Springer New York Heidelberg Dordrecht London, 2013.

[124] Laskaridis, P., and Pilidis, P., ‘An Integrated Engine - Aircraft Perfomance Platform for Assessing New Technologies in Aeronautics’, *ISABE 2005*, 2005, pp. 1–13.

[125] Novelo, D. alejandro B., ‘Nine Months Progress Report’, 2017.

[126] Mclelland, G., ‘Aerodynamics of vortex ingestion for aero-engines’, Cranfield University, 2013.

[127] Seddon, J., G. E. L., *Intake Aerodynamics*, Blackwell Science, 1999.

[128] ESDU, *NACA-1 series geometry representation for computational fluid dynamics*, 1994.

[129] Mehta, J. H. B. and R. D., *Contraction Design for Small Low-Speed Wind Tunnels*, NASA Technical Report, NASA-CR-182747, 1988.

APPENDICES

Appendix A Geometries generation

A.1 Aero-engine nacelle design

The fan diameter, engine length and additional available geometrical lead parameters of the GE CF6-80E1 and GE90-B85 engines are presented in (Table Ap.A 1) [92,94]. The throat area was calculated based on the provided mass flow rate of the engine and an assumed Mach number at the throat of the 0.75. Having the throat diameter identified the highlight D1 diameter can be estimated by using the contraction ratio $(\mathrm{D_1/D_{th}})$=1.22 [63]. The distance from the highlight plane to the fan face assumed to be 0.5 of the fan diameter [126].

The length of the fore-body was designed based on the value of the critical drag-rise Mach number $(\mathrm{M_D})$ correlation with the maximum diameter and the fore-body length, (Equation Ap.A 1).[63]. It has not to exceed the critical limits that would produce a strong shock over fan cowl. The value of the $\mathrm{M_D}$ was assumed equal to 0.9 ($\mathrm{M_\infty}$ +0.08) for the CF6-80E1 engine and 0.88 for the GE90-B85 engine [7]. To calculate the fore-body length $(\mathrm{l_f})$ the value of the diameter ratio (the highlight diameter to the maximum diameter) has been assumed 0.85 for CF6-80E1 and 0.84 for the GE90 engine. These values are within the proposed range of 0.8 to 0.9 for high bypass ratio engines [127].

$$M_D = 1 - \frac{1}{8}\frac{\sqrt{1-(\frac{D_1}{D_{max}})^2}}{\frac{l_f}{D_{max}}} \quad \text{.....} \qquad \textbf{Equation Ap.A 1}$$

The subsonic intakes entry lip represents the connection between the highlight with the throat plane. A superellipse curve was chosen with an aspect ratio (a/b) of 2.0 and an elliptic exponent of 2.0 [63] for both engines. The fore-body profile was decided to be designed based on the NACA 1-series cowl-fore body profiles[128]. It based on the calculated fore-body length and the highlight and maximum diameters ratio, (Equation Ap.A 2)[63].

$$\frac{y}{Y} = c\left(\frac{x}{X}\right)^{1/2}\left[\left[\frac{x}{X} - \left(\frac{x}{X}-1\right)\right] + \left[\left(1-\frac{1.5}{c}\right)\left(\frac{x}{X}-1\right)^2\right]\right] + \left[\sum_{n=0}^{7}(-1)^{n+1}A_n\left(\frac{x}{X}\right)^n\right]\left[\frac{\left(\frac{x}{X}\right)^{3/2}\left(1-\frac{x}{X}\right)^2}{\left(b+\frac{x}{X}\right)^2}\right]. \qquad \textbf{Equation Ap.A 2}$$

Where b = 0.05, c = 1.045 [63], x/X and y/Y are the cowl non-dimensional longitudinal and radial coordinates where X is the length of the fore-body L_f and Y = (D_{max}-D_1) /2.

A circular arc profile was used, with low curvature to avoided drag rise and flow separation. The boat-tail angle was 14.0° for GE CF6-80E1 engine and 13° for the GE90-B85 engine, were chosen such that the flow separation avoided [63]. The after-body length was chosen based on the equations reported in Williams [63].

The core-cowl angle was chosen to be 14˚. The external core-cowl length was extracted using the fineness ratio of the core-cowl from [96] equals to 0.65. Therefore, the inner diameter of the core nozzle was calculated based on the core nozzle exit area together with the core-cowl geometrical information.

For the CF6, the plug length was calculated considering the full propulsion length reduced by the fore-body components. In the GE90-B85 configuration, the plug length was chosen to satisfying the plug angle and the core-inner radius, as a result of the missing length in the open domain. The plug angle was assumed 29 °, for and 32° for the GE90-B85.

The by-pass inlet area was sized based on the ratio of the fan tip reduce to the bypass duct outer radius (r_2/r_{tip} =0.98) [7] along with the inlet mass flow rate that was estimated by the non-dimensional performance model and assumed inlet Mach number of 0.4. The bypass and core nozzle internal contours was designed based polynomials with different degrees to achieve the provided engine geometrical constrains. The initial GE CF6-80E1 exhaust system internal profile was design based on the fifth order polynomial (Equation Ap.A 3) that proposed by Metha [129]. In the case of GE90-B85 Bernstein polynomial based analytical model of CST [115] was used to design the ducts and nozzle profiles. All the geometrical lead dimensions and sketch are presented in the following figures and tables.

$$Y(X) = H_i - (H_i - H_o)[6(X)^5 - 15(X)^4 + 10(X)^3] \quad \textbf{Equation Ap.A 3}$$

where H_i : Inlet duct height; H_o : Outlet duct height ; X : non-dimensional duct length

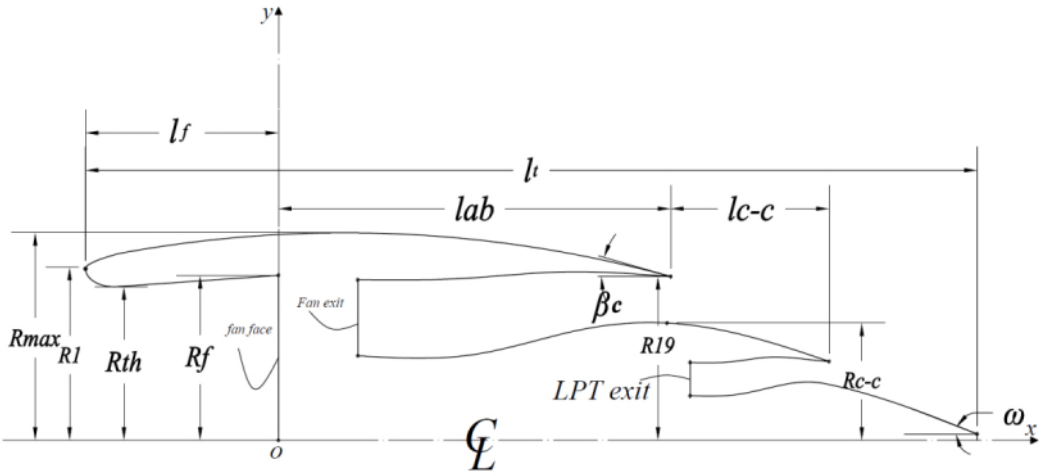

Figure Ap.A 1 Main nacelle geometrical lead parameters

Table Ap.A 1 Main normalised geometrical dimensions of the selected engine nacelles.

Similar to GE CF6-80E1 engine (D_f = *2.443 m)*											
R_{max}/R_f	R_{th}/R_f	R_1/R_f	R_{19}/R_f	$R_{c\text{-}c}/R_f$	R_{cn}/R_f	l_f/R_f	L_{ab}/R_f	$L_{c\text{-}c}/R_f$	L_t/R_f	βc	ω
1.33	0.926	1.1223	0.975	0.623	0.5	1.72	1.99	1.024	6.09	7.5˚	14.0˚
Similar to GE90-B85 engine (D_f = *3.124 m)*											
R_{max}/R_f	R_{th}/R_f	R_1/R_f	R_{19}/R_f	$R_{c\text{-}c}/R_f$	R_{cn}/R_f	L_f/R_f	L_{ab}/R_f	$L_{c\text{-}c}/R_f$	L_t/R_f	βc	ω
1.23	0.93	1.04	1	0.72	0.5	1.46	1.92	0.96	5.4	6.5°	16°

Table Ap.A 2 Non-dimensional geometrical parameters of the basic nozzle configuration at different CR and for β =15˚.

CR	$\frac{R_{in}}{R_{max}}$	$\frac{l_{plug}}{R_{max}}$
1.291426	0.42313	1.57853
1.397102	0.45226	1.68716
1.534572	0.48188	1.79769
1.594400	0.49281	1.83849
1.663344	0.50435	1.88163
1.745329	0.51602	1.92526

Table Ap.A 3 Non-dimensional geometrical lead parameters of the core-nozzle configuration at different CR and for β =15˚.

cCR	$\frac{R_{in}}{R_{max}}$	$\frac{l_{plug}}{R_{max}}$
1.35000	0.43774	1.64314
1.43003	0.45120	1.69145
1.49893	0.46366	1.73976
1.57000	0.47581	1.78743

1.67000	0.48919	1.83505
1.77440	0.50206	1.88286

A.2 Additional figures

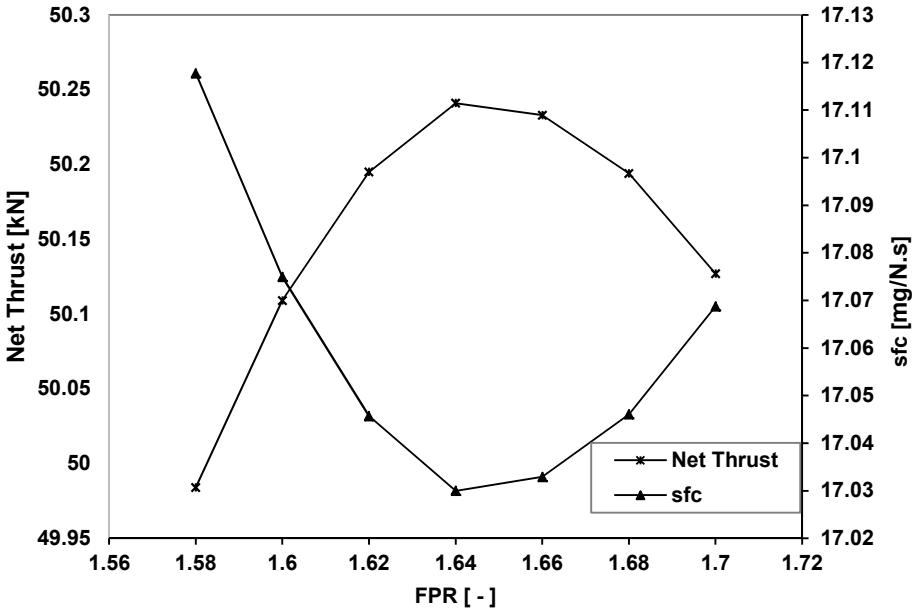

Figure Ap.A 2 Optimum net thrust and SFC of the engine model similar to the GE CF6-80E1 engine.

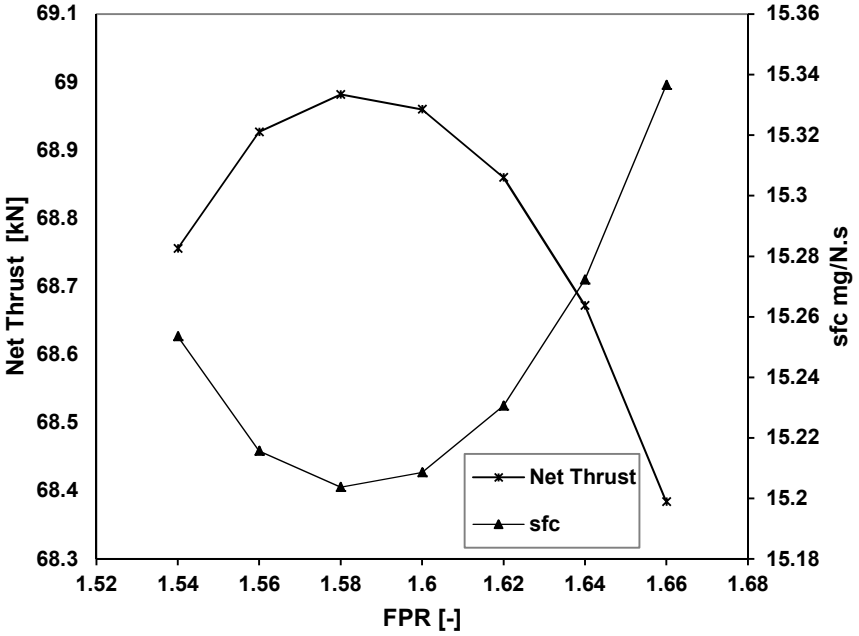

Figure Ap.A 3 Optimum net thrust and SFC of the engine model similar to the GE90-B85 engine.

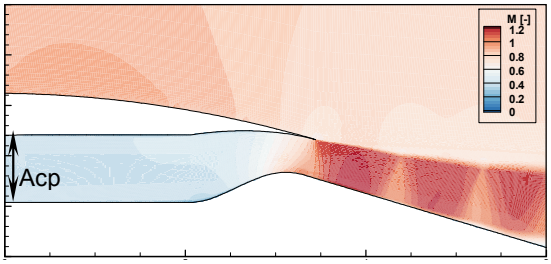

Figure Ap.A 4 Mach number contour of the nozzle configuration with CR=1.6, in operating conditions of NPR =2.5.

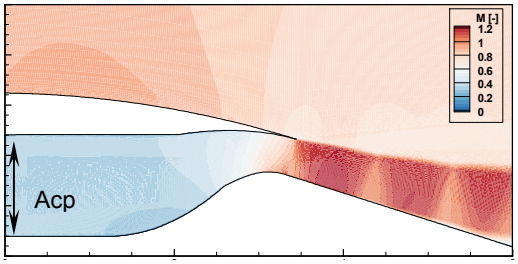

Figure Ap.A 5 Mach number contour of the nozzle configuration with CR=2.0, in operating conditions of NPR =2.5.

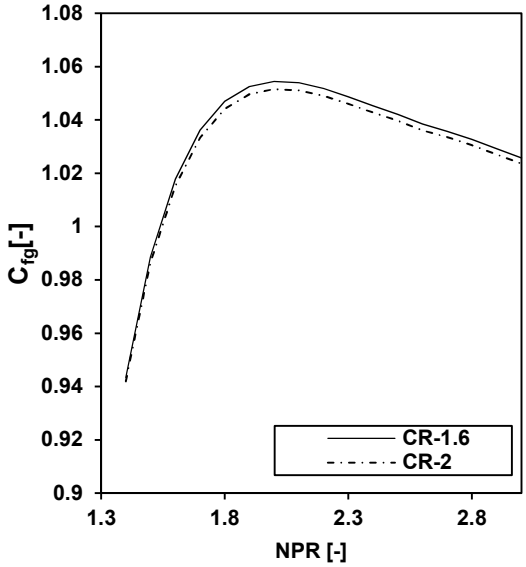

Figure Ap.A 6 Nozzle gross thrust coefficient (C_{fg}) comparison between two nozzle CR 1.6 and 2.0.

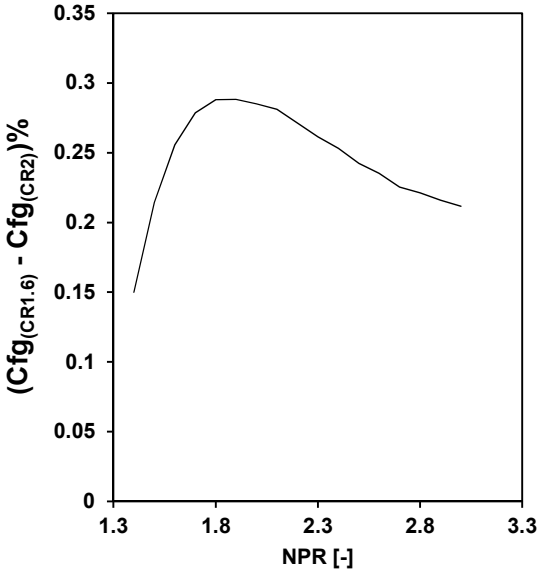

Figure Ap.A 7 Nozzle gross thrust coefficient percentage difference ($C_{fg(CR1.6)}$ - $C_{fg(CR2)}$)%, between two nozzle CR of 1.6 and 2.0 as a function of the NPR.

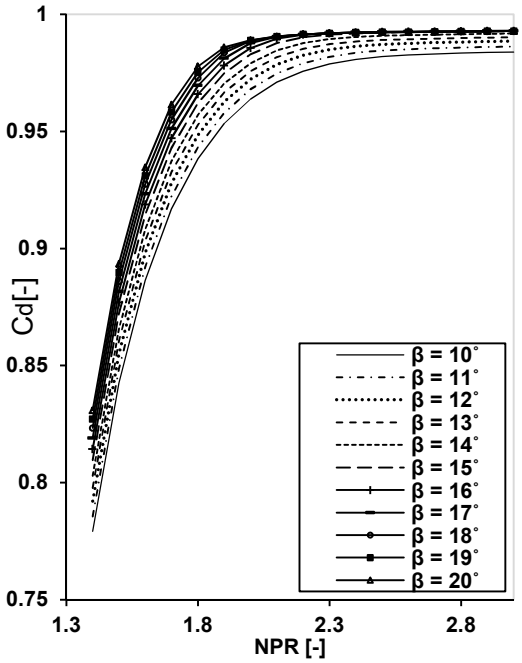

CR =1.30

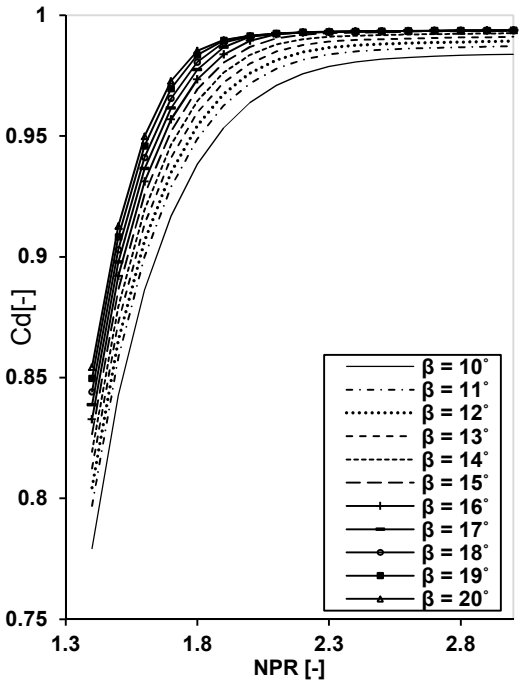

CR =1.54

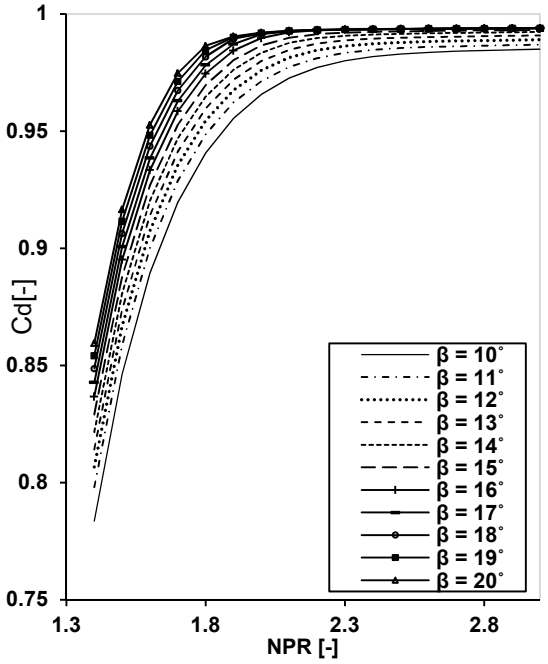

CR =1.60

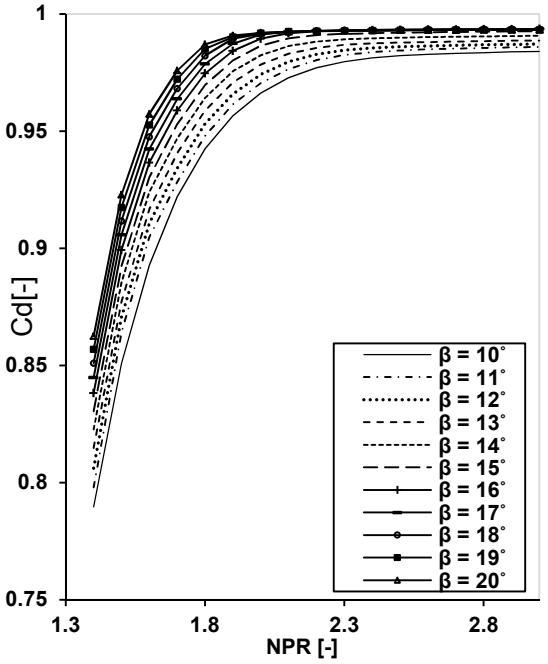

CR =1.66

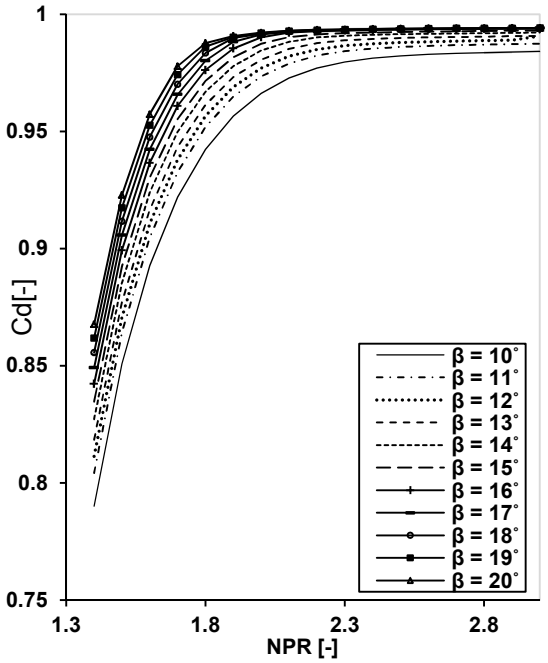

CR =1.75

Figure Ap.A 8 Nozzle discharge coefficient (Cd) maps as a function of the NPR and β for the chosen CR at mid-cruise operational conditions.

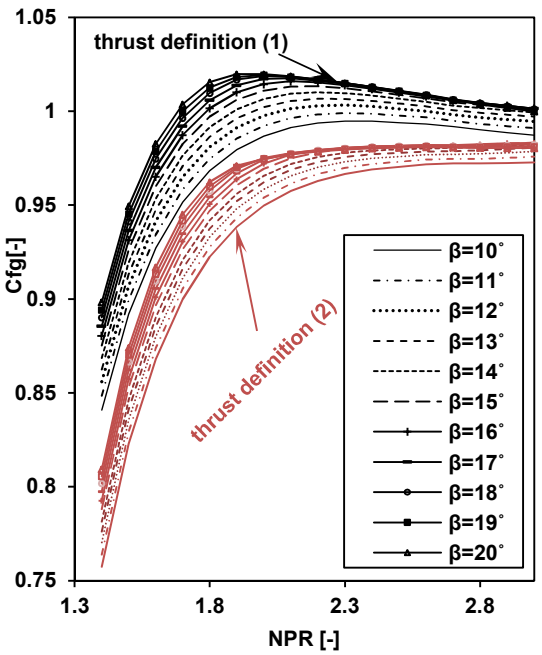

CR =1.30

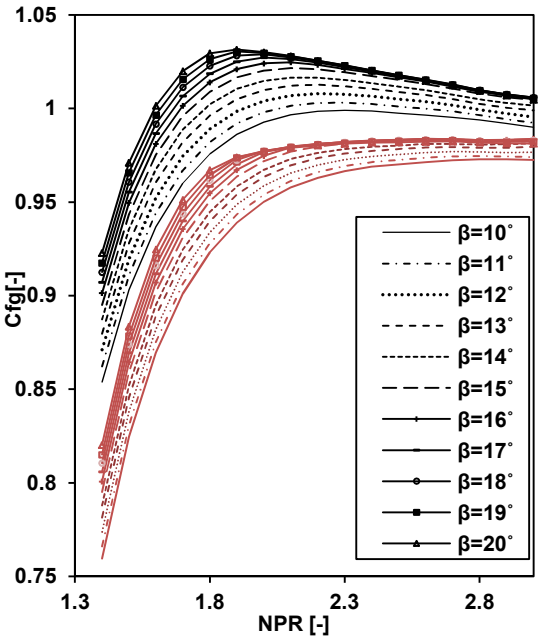

CR =1.40

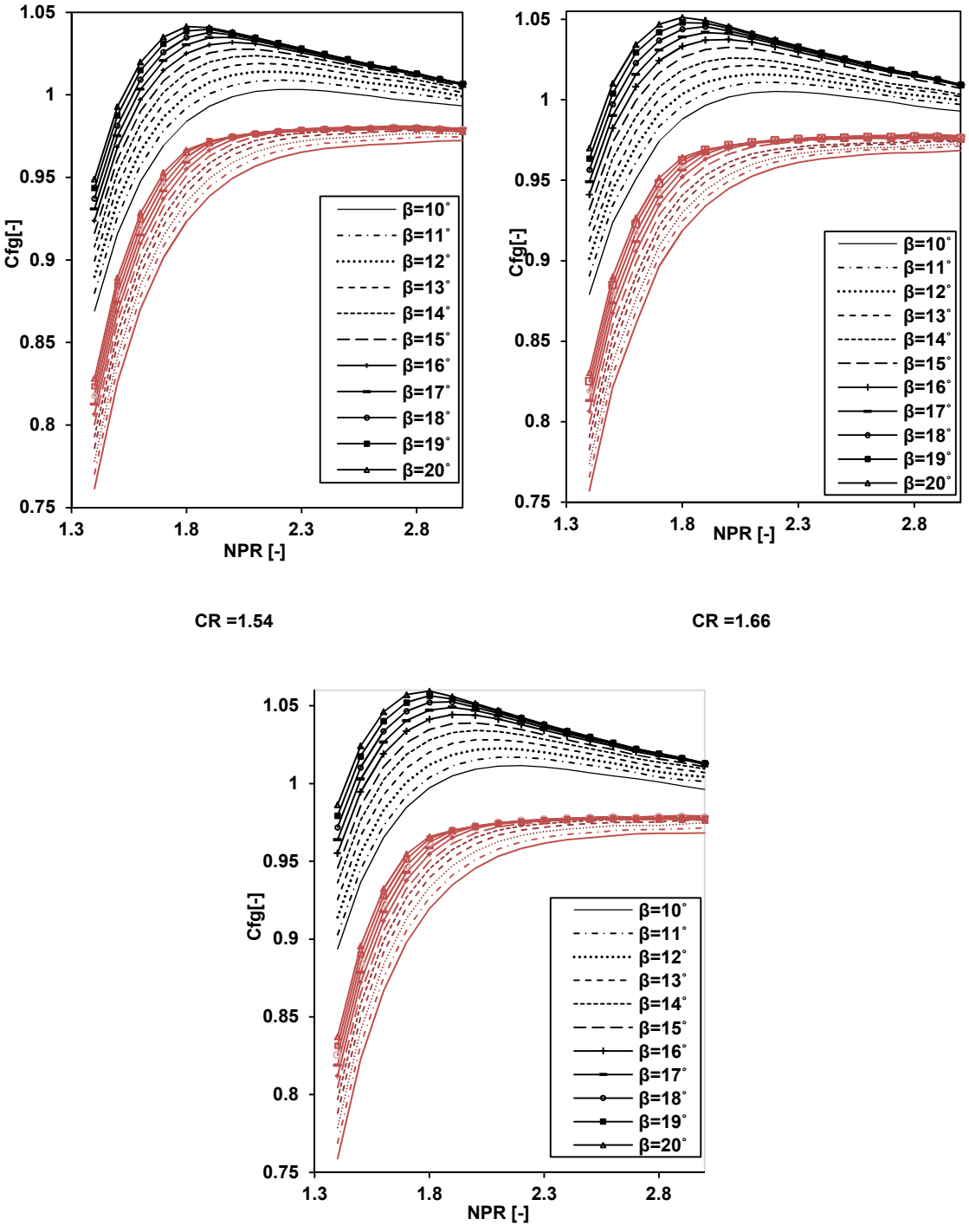

Figure Ap.A 9 Nozzle gross thrust coefficient (C_{fg}) maps as a function of the NPR and β for the chosen CR at mid-cruise operational conditions.

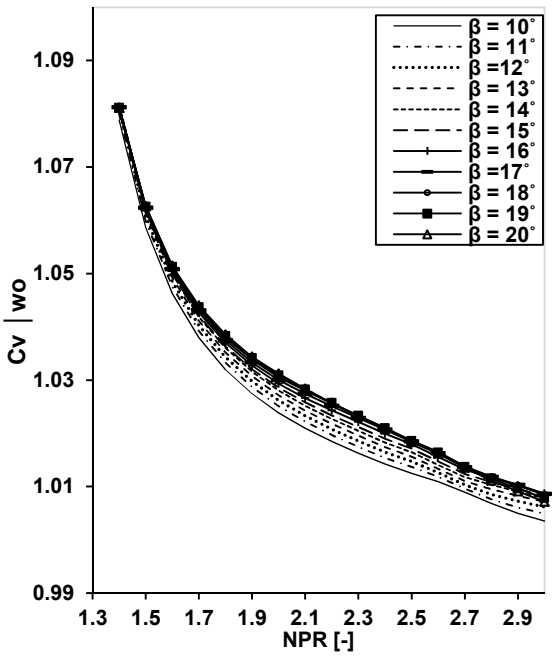

CR =1.30

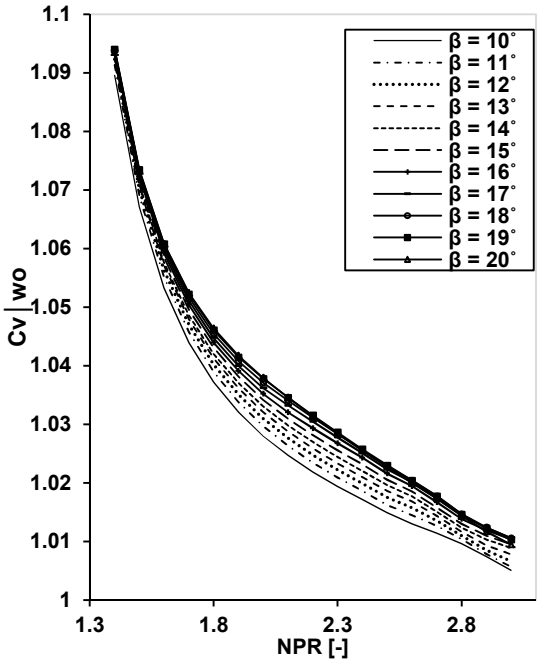

CR =1.40

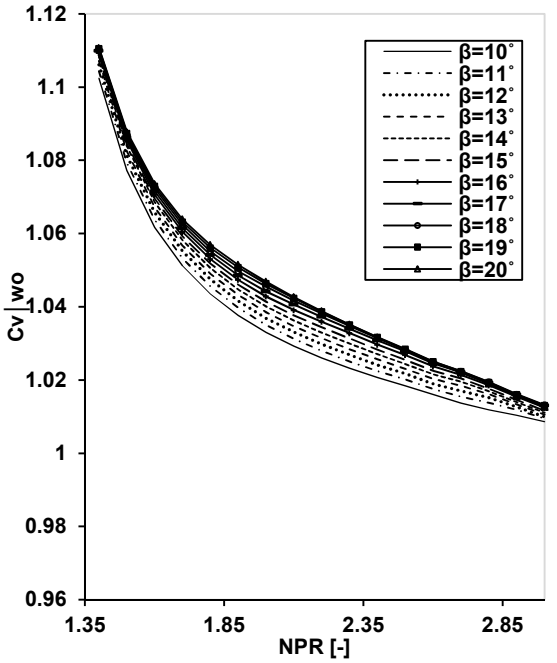

CR =1.54

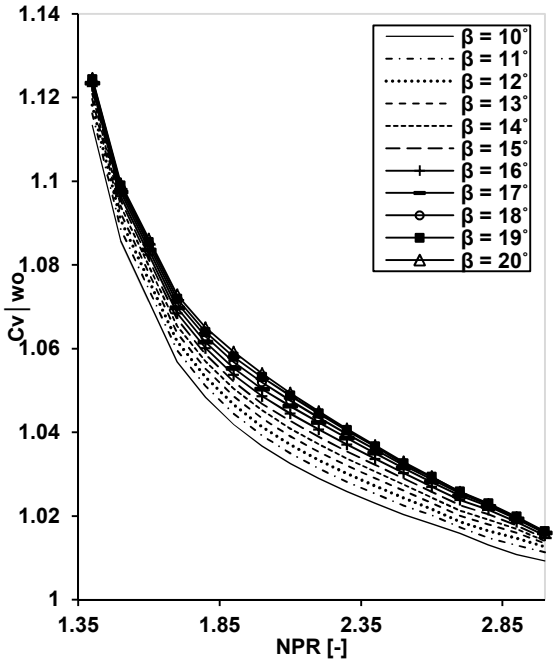

CR =1.66

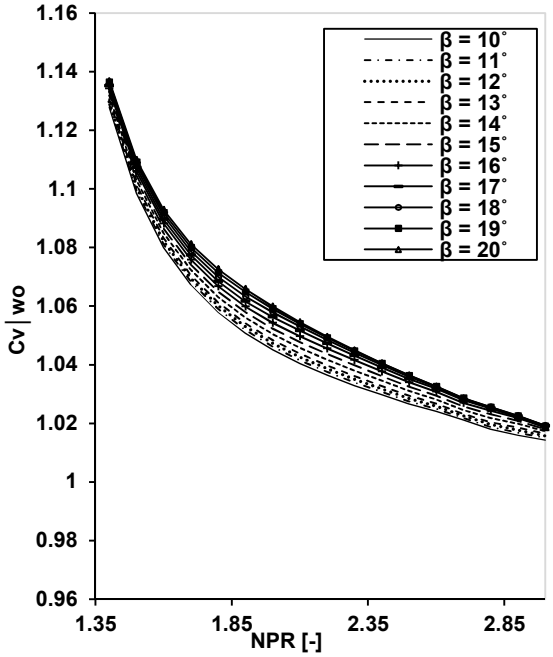

CR =1.75

Figure Ap.A 10 Nozzle velocity coefficient (Cv | wo) (without the cowl afterbody) maps as a function of the NPR and β for the chosen CR at mid-cruise operating conditions.

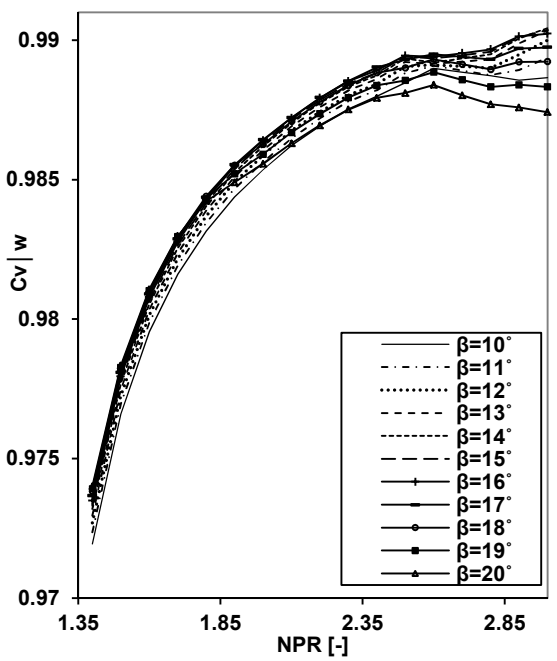

CR =1.30

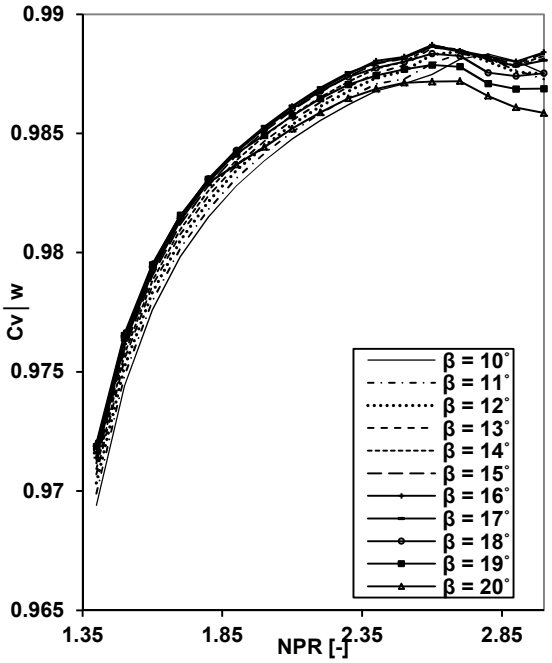

CR =1.40

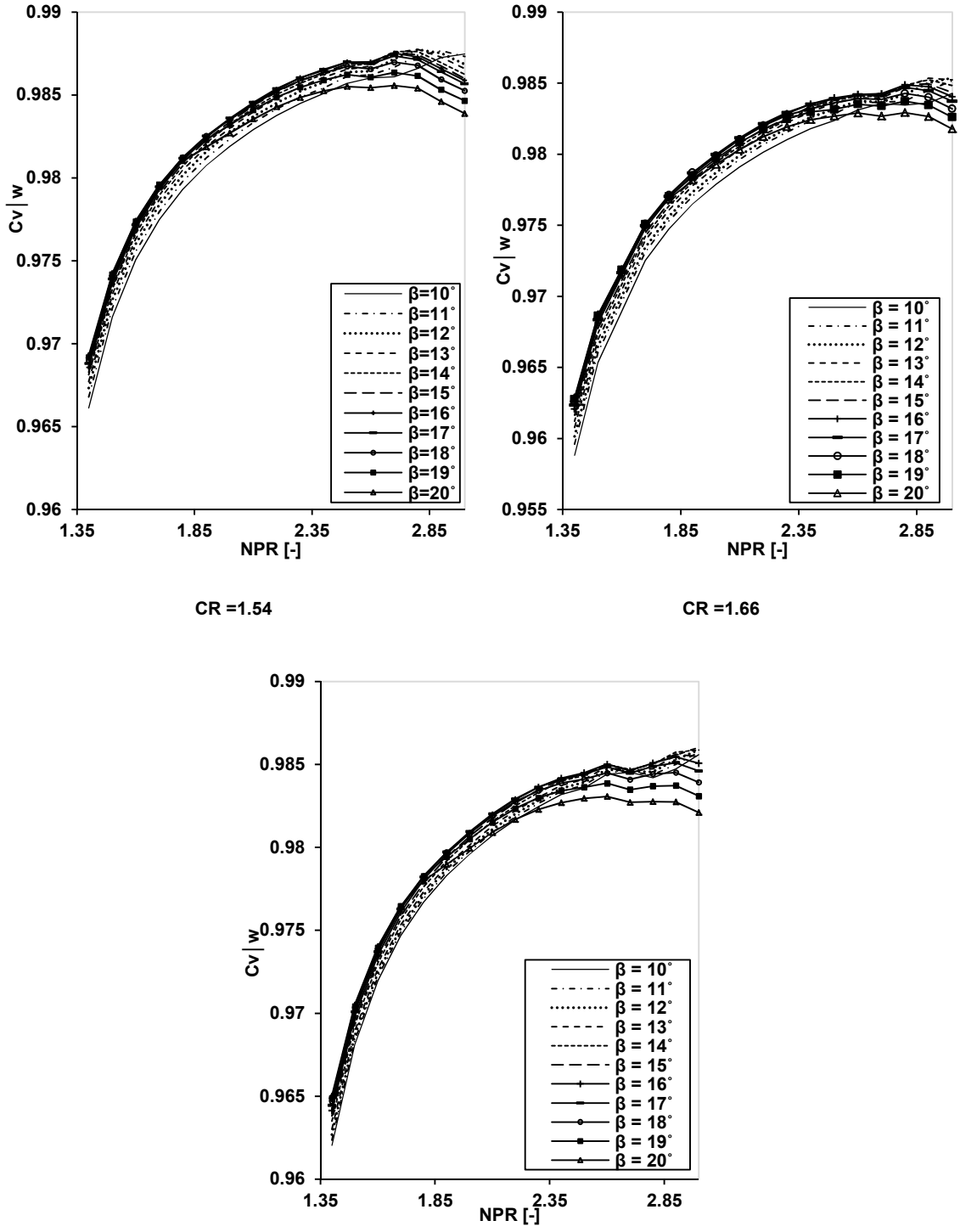

Figure Ap.A 11 Nozzle velocity coefficient ($C_v | w$) (with the cowl afterbody) maps as a function of the NPR and β for the chosen CR at mid-cruise operating conditions.

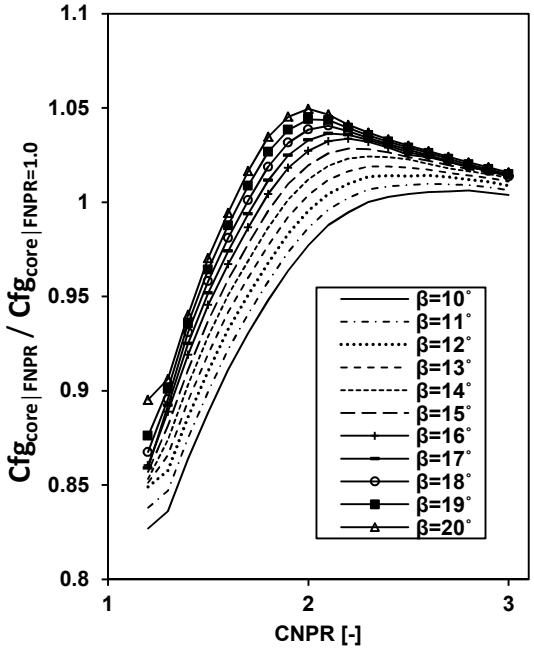

cCR =1.35; FNPR= 2.0

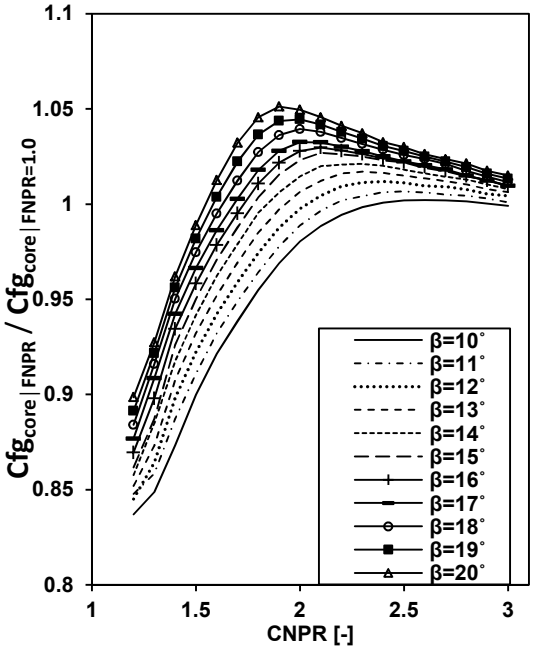

cCR =1.35; FNPR= 2.2

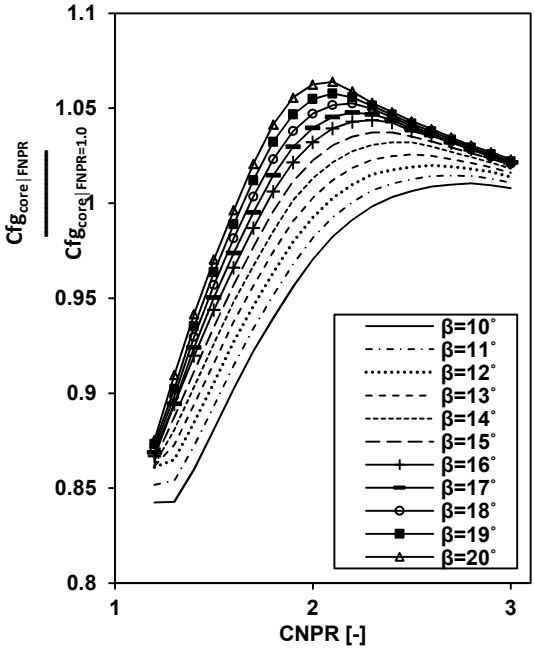

cCR =1.35; FNPR= 2.5

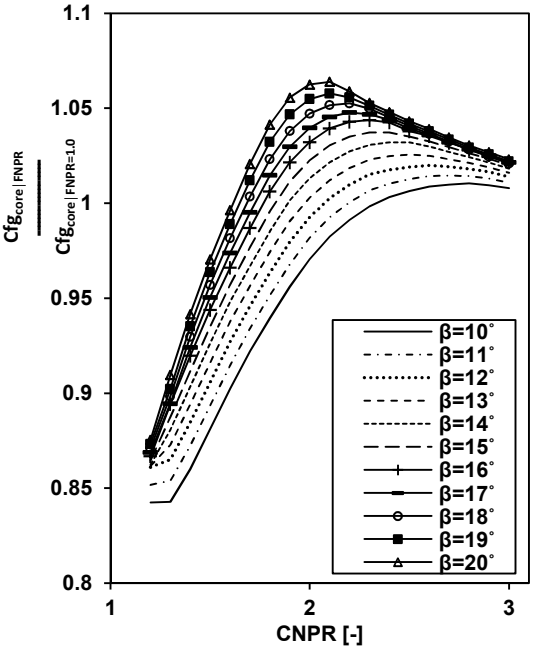

cCR =1.35; FNPR= 2.8

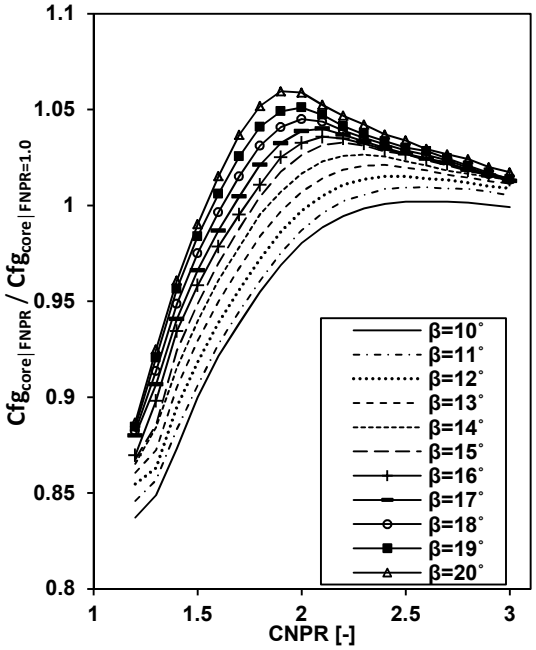

cCR =1.43; FNPR= 2.0

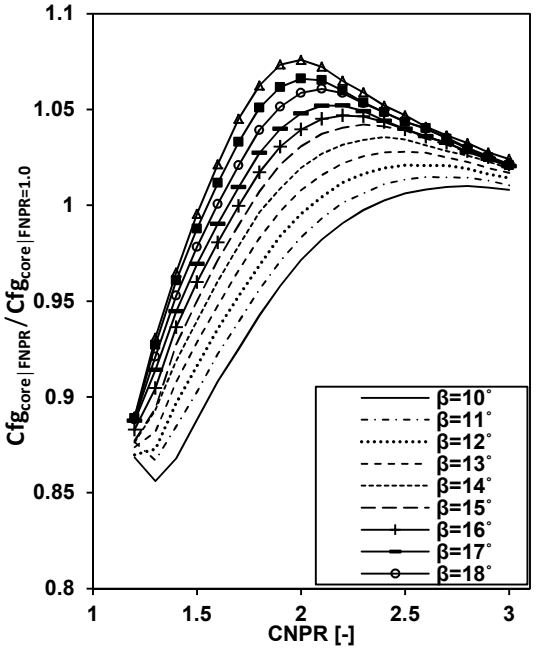

cCR =1.43; FNPR= 2.2

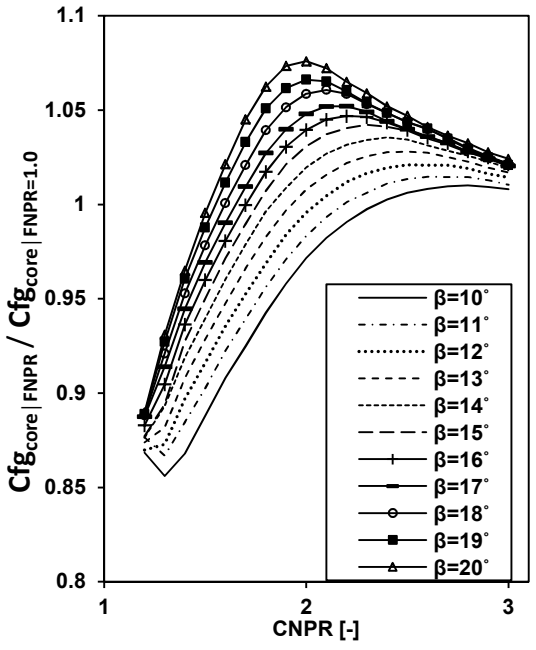

cCR =1.43; FNPR= 2.5

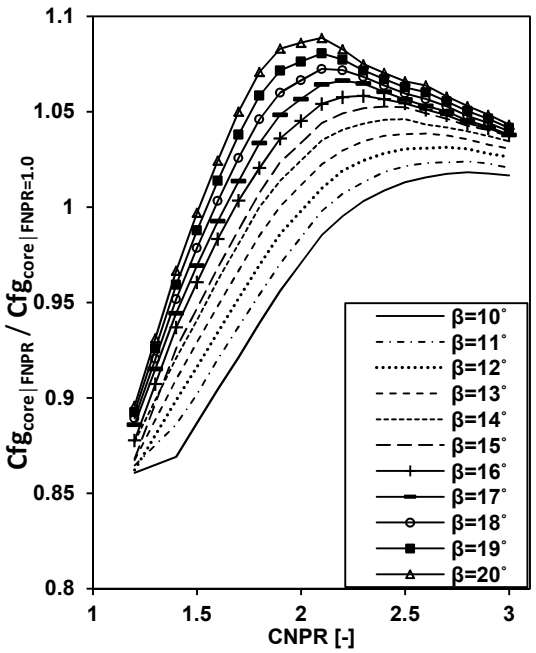

cCR =1.43; FNPR= 2.8

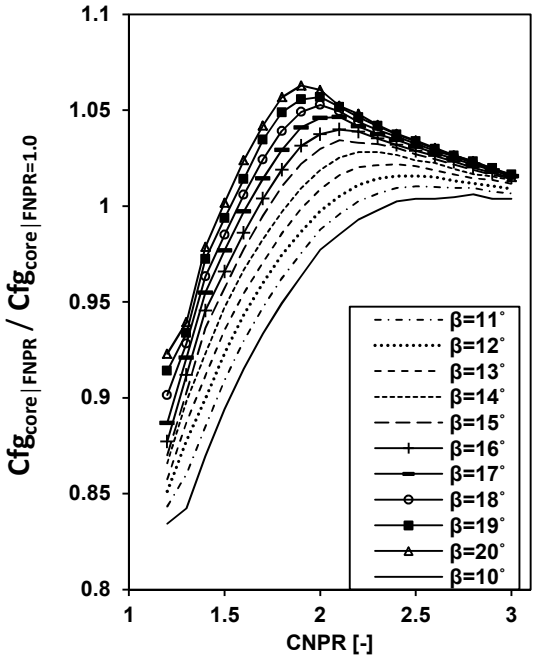

cCR =1.50; FNPR= 2.2

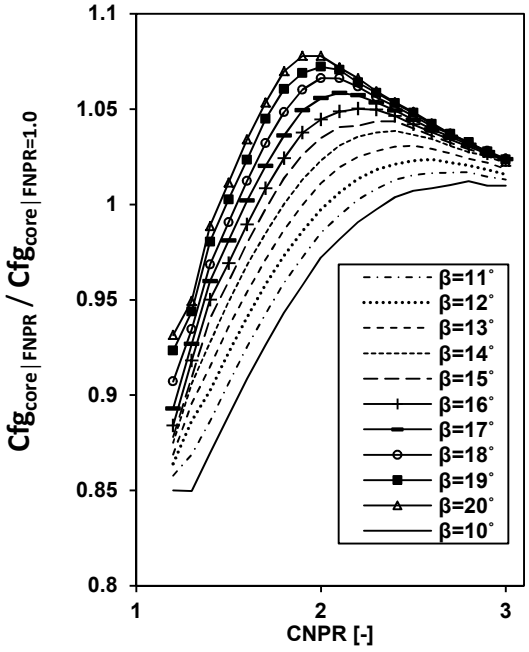

cCR =1.50; FNPR= 2.5

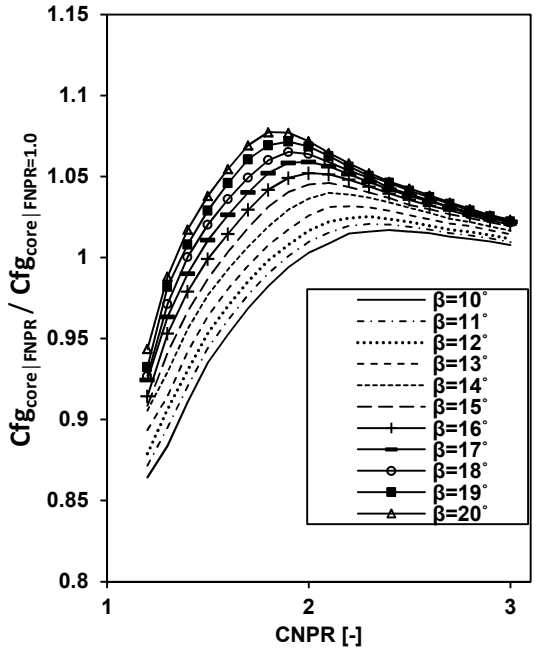

cCR =1.57; FNPR= 2.0

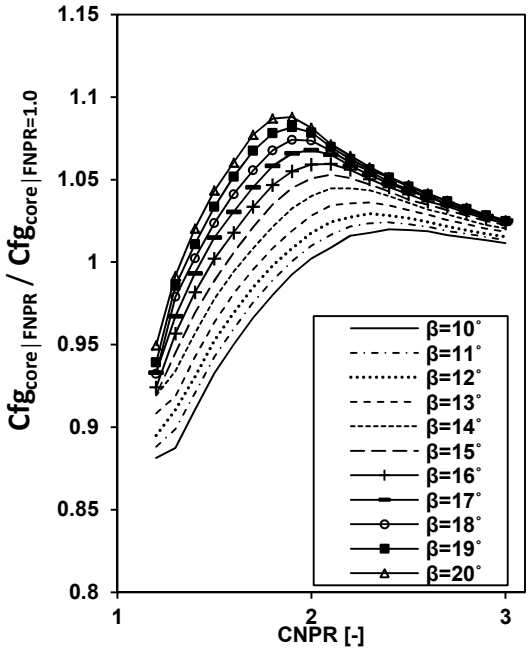

cCR =1. 57; FNPR= 2.2

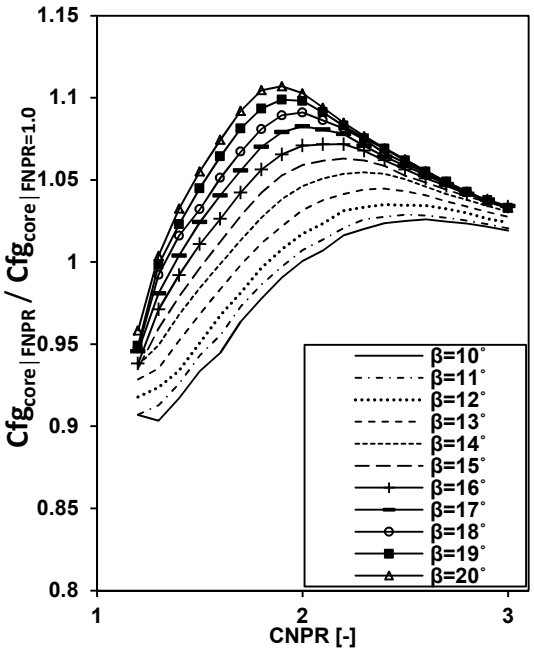

cCR =1. 57; FNPR= 2.5

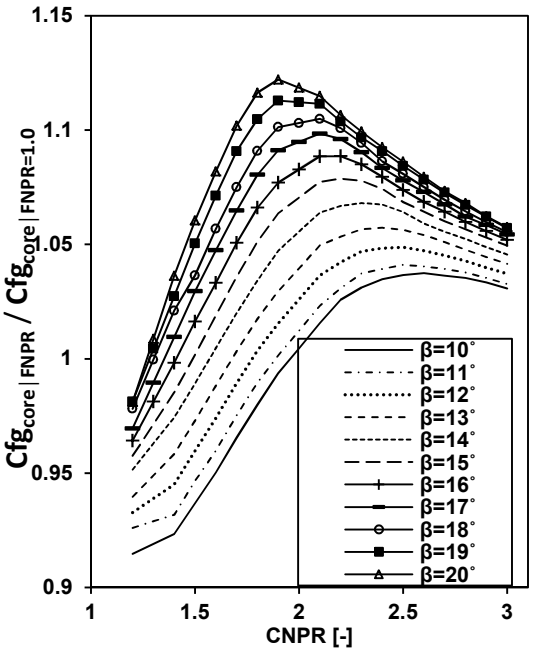

cCR =1. 57; FNPR= 2.8

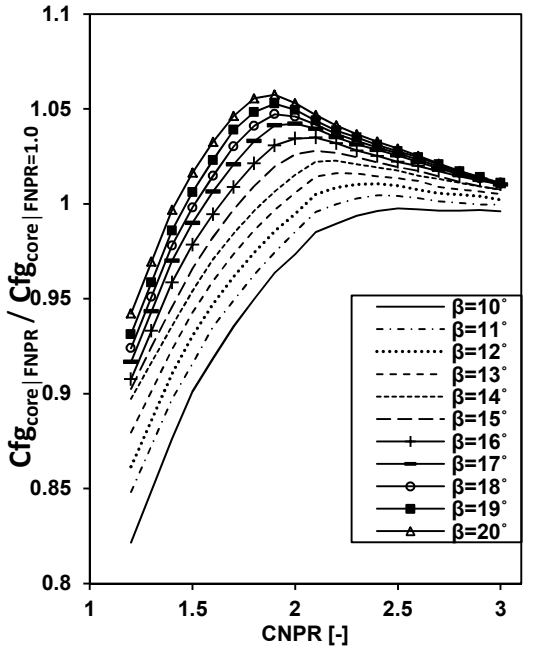

cCR =1.67; FNPR= 2.0

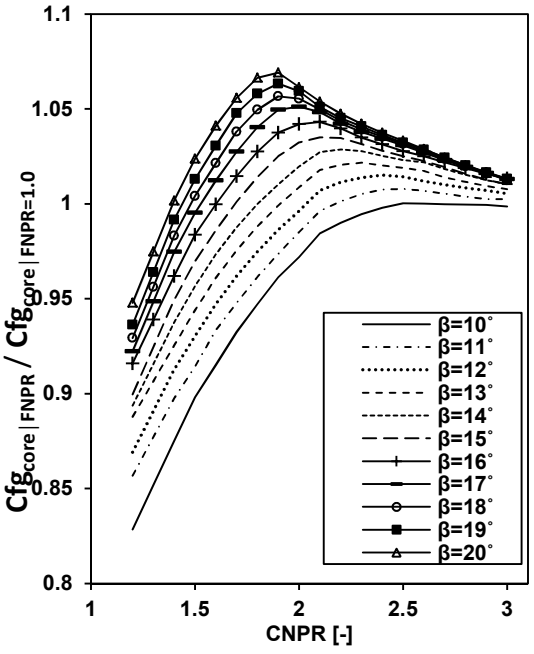

cCR =1. 67; FNPR= 2.2

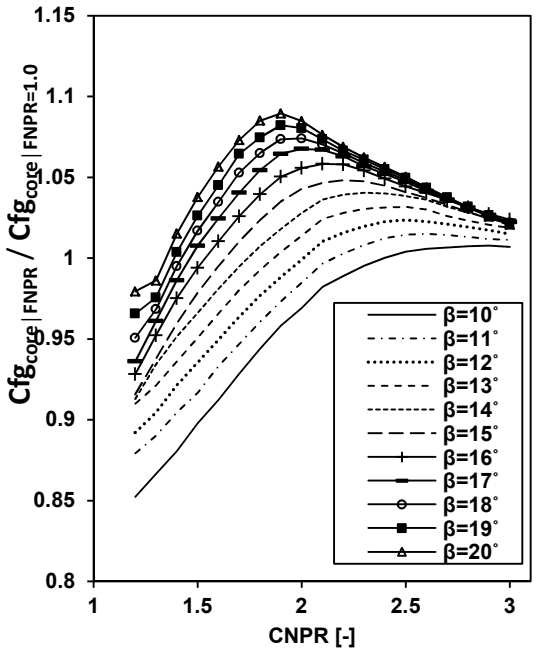

cCR =1.67; FNPR= 2.5

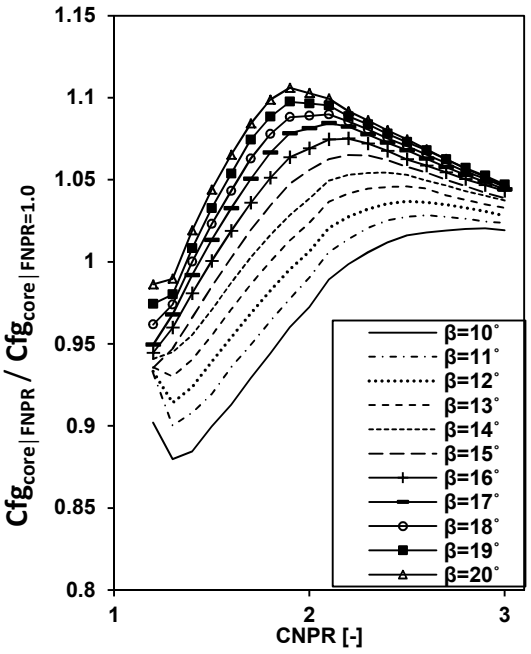

cCR =1.67; FNPR= 2.8

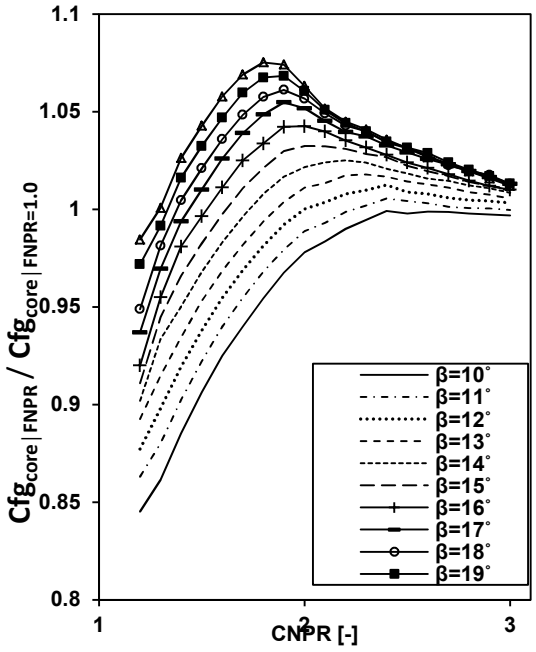

cCR =1.77; FNPR= 2.0

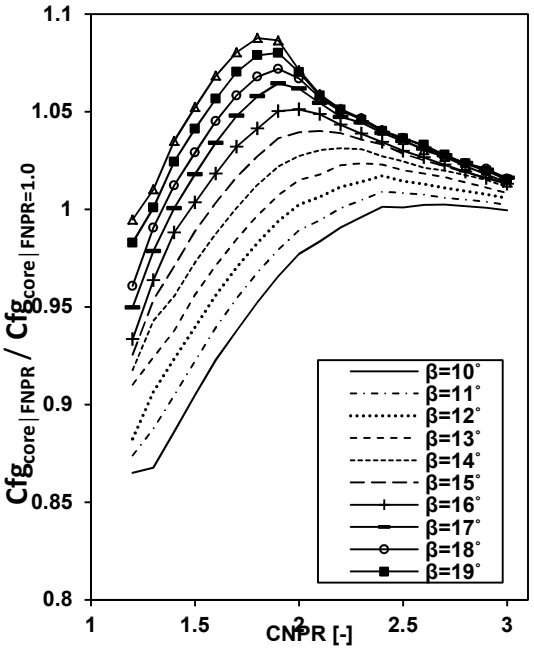

cCR =1.77; FNPR= 2.2

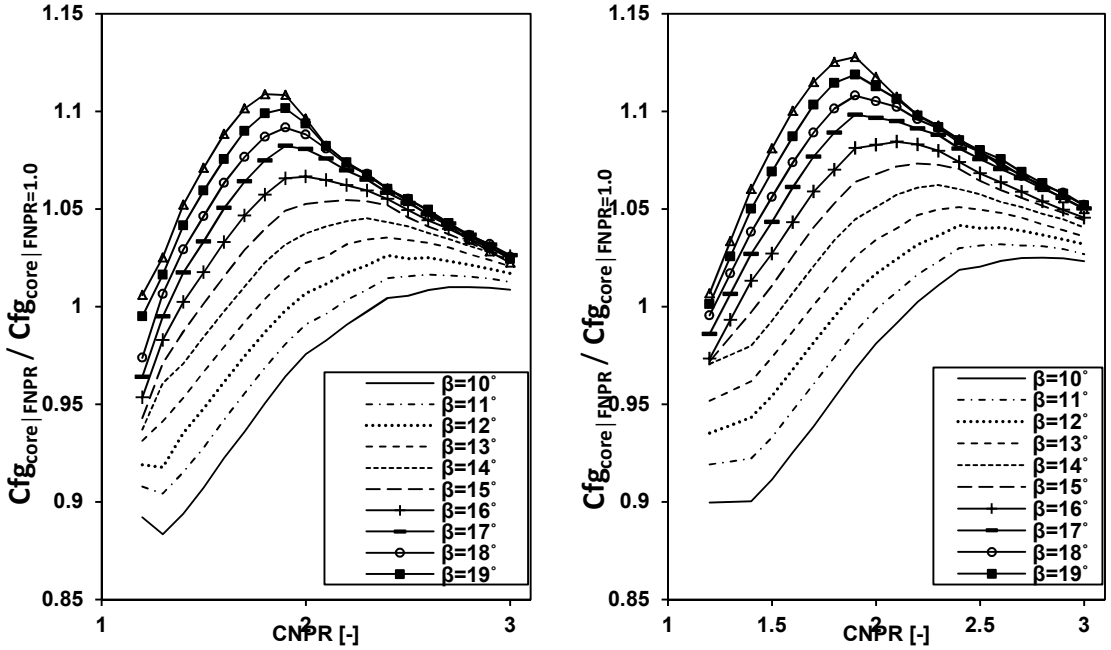

cCR =1.77; FNPR= 2.5

cCR =1.77; FNPR= 2.8

Figure Ap.A 12 Extracted corrections of the core nozzle gross thrust coefficient, for the chosen FNPR and cCR.

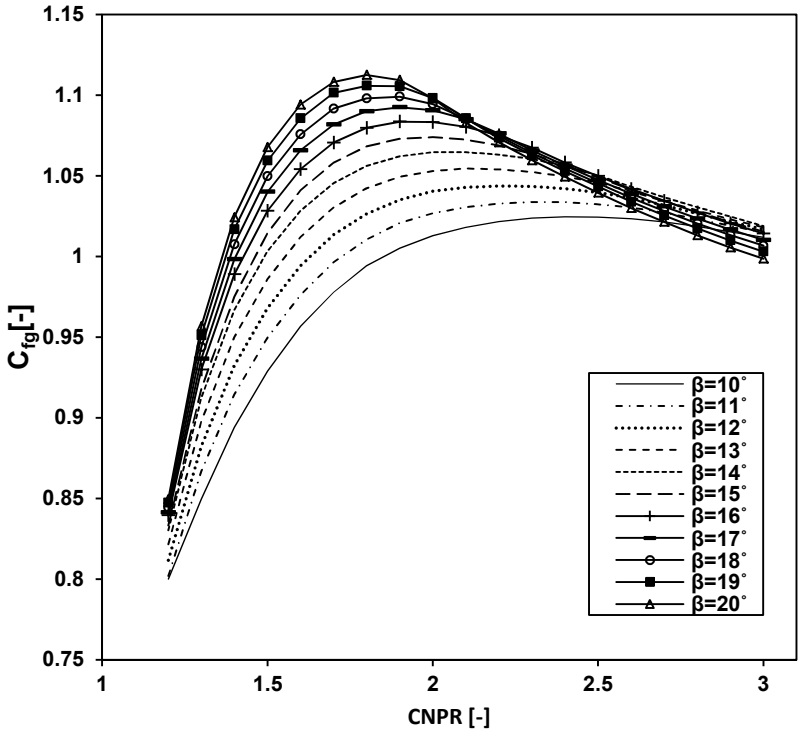

Figure Ap.A 13 Core nozzle gross thrust coefficient as a function of the CNPR for the chosen plug half angle.

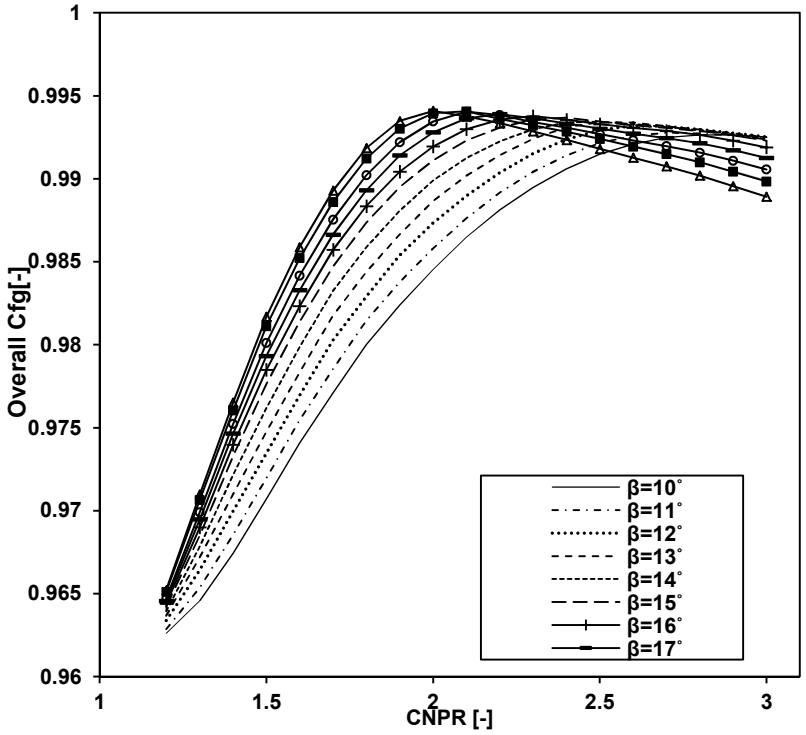

Figure Ap.A 14 Overall dual-stream nozzle gross thrust coefficient as a function of the CNPR for the chosen plug half angle, for nozzle configuration of cCR =1.50 and FNPR =2.50.

Appendix B Employed computational Domains and Meshes description and sensitivity study

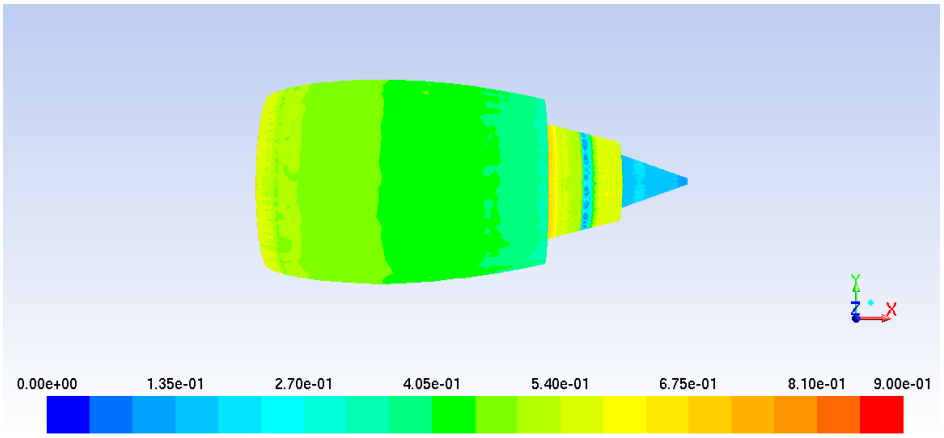

Figure Ap. B 1 Y^+ contour over isolated nacelle surface, at operating conditions of M_∞ = 0.82, Alt = 11000 m and zero $AoA_{A/C}$.

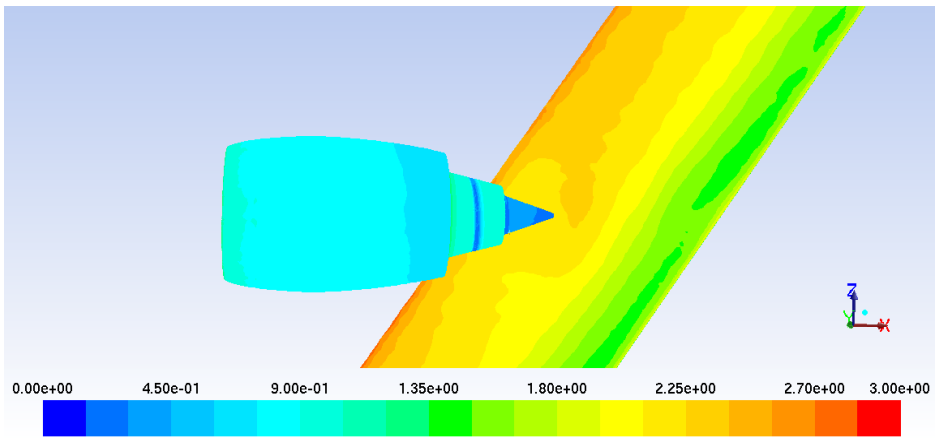

Figure Ap. B 2 Y^+ contour over installed nacelle and the wing surface, at operating conditions of M_∞ = 0.82, Alt = 11000m and zero $AoA_{A/C}$ the engine placed at P02.

$$p = \frac{\ln\left[\frac{f_3 - f_2}{f_2 - f_1}\right]}{\ln r} \quad \text{.....B 1}$$

$$GCI_{12} = \frac{F_s\left[\frac{f_2 - f_1}{f_1}\right]}{r^p - 1} \quad \text{.....B 2}$$

$$GCI_{23} = \frac{F_s\left[\frac{f_3 - f_2}{f_1}\right]}{r^p - 1} \quad \text{.....B 3}$$

$$r_{eff} = \left(\frac{finer\ mesh\ No.of\ elements}{coarser\ mesh\ No.of\ elements}\right)^{1/D} \quad \text{.....B 4}$$

It should be noted that for unstructured mesh only r_{eff} has been used. All the equations have been drawn from Roach [100]

Where:

p: grid convergence index

f: refers to any physical value of interest

r: Grid refinement ratio

Fs: safety factor, it is equal to 1.25 for three meshes [100]

D: dimensional of the problem, for 3-D cases it equals to 3.0[100]

Table Ap.B 1 GCI values for the coarse and fine mesh of the isolated nacelle simulated at M_∞=0.82, Alt=11000 m, MFCR = 0.73, FNPR = 2.45, CNPR = 1.9 at zero $AoA_{A/C}$, nacelle drag coefficient based on the maximum nacelle diameter.

#	No.of elements	C_{Dnac} [-]	r_{eff12}	r_{eff23}	r	p	GCI_{12}	GCI_{23}	$\frac{GCI23}{r^p GCI12}$
1	11.2 x 10^6	0.055	1.16	1.26	1.2	5.8	0.002668	0.0079	0.996
2	7.11 x 10^6	0.0551							
3	3.77 x 10^6	0.056							

Table Ap.B 2 GCI values for the coarse and fine mesh of the isolated nacelle simulated at M_∞=0.82, Alt=11000m, MFCR = 0.73, FNPR = 2.45, CNPR = 1.9 at zero $AoA_{A/C}$, nacelle C_{fg} was calculated using thrust definition (1).

#	No.of elements	C_{fg} [-]	r_{eff12}	r_{eff23}	r	p	GCI_{12}	GCI_{23}	$\frac{GCI23}{r^p GCI12}$
1	11.2x 10^6	1.021	1.2	1.26	1.23	22	0.000308%	0.0002%	1.0
2	7.11x 10^6	1.02105							
3	3.77x 10^6	1.031							

Table Ap.B 3 GCI values for the coarse and fine mesh of the infinit swept wing simulated at M_∞=0.82, Alt=11000 m, MFCR = 0.732, FNPR = 2.45, CNPR = 1.9 at $AoA_{A/C}$= 2.5°; the lift coefficient was calcualted based on the wing platform area.

#	No. of elements	C_L[-]	r_{eff12}	r_{eff23}	r	p	GCI_{12}	GCI_{23}	$\frac{GCI23}{r^p GCI12}$
1	12.2 x 10^6	0.304	1.16	1.24	1.20	6.3	0.00734311	0.022884	0.99
2	7.86 x 10^6	0.30785							
3	4.11 x 10^6	0.32							

Table Ap.B 4 GCI values for the coarse and fine mesh of the SW and nacelle configuration, simulated at M_∞=0.82, Alt =11000 m and MFCR = 0.73, FNPR = 2.45, CNPR = 1.90 at Zero $AoA_{A/C}$, C_{Dnac} was calculated based on the maximum diameter of the nacelle.

#	No. of elements	C_{Dnac} [-]	r_{eff12}	r_{eff23}	r	p	GCI_{12}	GCI_{23}	$\frac{GCI23}{r^p GCI12}$
1	31.5 x 10^6	0.03905	1.2	1.23	1.215	6.3	0.0134	0.044291	0.975013
2	18.8 x 10^6	0.04005							
3	10.6x 10^6	0.04344							

Table Ap.B 5 GCI values for the coarse and fine mesh of the SW and nacelle configuration, simulated at M_∞=0.82, Alt =11000m and MFCR = 0.732, FNPR = 2.45, CNPR = 1.9 at Zero $AoA_{A/C}$, C_{fg} was calculated based on thrust defintion (1).

#	No. of elements	C_{fg} [-]	r_{eff12}	r_{eff23}	r	p	GCI_{12}	GCI_{23}	$\frac{GCI23}{r^p GCI12}$
1	31.5×10^6	1.0300	1.21	1.2	1.21	1.9	0.0015172	0.0021677	1.0
2	18.8×10^6	1.0295							
3	10.6×10^6	1.0287							

Table Ap.B 6 GCI values for the coarse and fine mesh of the CRM WB and nacelle configuration, simulated at M_∞=0.82, Alt. =11000m and MFCR = 0.72, FNPR = 2.51, CNPR = 1.9 at zero $AoA_{A/C}$, nacelle C_{Dnac} was calculated based on the maximum diameter of the nacelle.

#	No. of elements	C_{Dnac}[-]	r_{eff12}	r_{eff23}	r	p	GCI_{12}	GCI_{23}	$\frac{GCI_{1,2}}{r^p GCI_{2,3}}$
1	31.8×10^6	0.063	1.2	1.23	1.21	5	0.02645	0.06410	1.0
2	18.2×10^6	0.065							
3	10.8×10^6	0.07							

Table Ap.B 7 GCI values for the coarse and fine mesh of the CRM WB and nacelle configuration, simulated at M_∞=0.82, Alt. =11000m and MFCR = 0.72, FNPR = 2.51, CNPR = 1.9 at Zero $AoA_{A/C}$; C_{fg} was calculated based on thrust defintion (1).

#	No.of elements	C_{fg}	r_{eff12}	r_{eff23}	r	p	GCI_{12}	GCI_{23}	$\frac{GCI_{1,2}}{r^p GCI_{2,3}}$
1	31.8×10^6	1.02854	1.2	1.23	1.21	14.3	0.0000283%	0.00042%	1.0
2	18.2×10^6	1.02851							
3	10.8×10^6	1.028							